

---

# Optical Nanoantennas for Ultrafast Nonlinear Spectroscopy of Individual Nanosystems

---

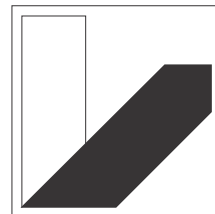
Von der Fakultät für Mathematik, Physik und Informatik  
der Universität Bayreuth zur Erlangung des Grades eines  
Doktors der Naturwissenschaften (Dr. rer. nat.)  
genehmigte Abhandlung

vorgelegt von  
**Thorsten Schumacher**  
geb. in Esslingen am Neckar

Angefertigt am  
Max-Planck-Institut für Festkörperforschung in Stuttgart,  
und dem Lehrstuhl für Experimentalphysik III  
der Universität Bayreuth



**Max Planck Institute  
for Solid State Research**



**Experimental Physics III  
University of Bayreuth**

Hauptberichter:

Prof. Dr. M. Lippitz

Mitberichter:

Prof. Dr. J. Köhler

Prof. Dr. B. Hecht

Prüfungsvorsitz:

Prof. Dr. V. M. Axt

Erweiterte Prüfungskommission:

Prof. Dr. A. Köhler

Tag der Einreichung:

29. Januar 2014

Tag des Kolloquiums:

23. Juli 2014





*Für meine Familie*



## ABSTRACT

---

This thesis considers the ultrafast nonlinear dynamics of various processes in individual metallic and semiconductor nanostructures without averaging over ensembles. Single nanoobjects with a size of a few nanometers show exceptional linear and nonlinear optical behavior. Ultrafast nonlinear spectroscopy investigates the time dependent deviations from linear light-matter interaction with sub-picosecond temporal resolution. The already weak nonlinear response of bulk matter is reduced further when single nanoobjects such as quantum dots, molecules, or nanoparticles are investigated. Optical nanoantennas, composed of plasmonic nanostructures, are a novel tool to investigate previously unattainable dimensions in the nanocosmos by locally increasing the light-matter interaction. We aim for the theoretical development and first experimental realization of an optical antenna to enhance the ultrafast nonlinear response of a single nanoobject. This requires highly sensitive experimental methods and efficient modeling and optimization techniques by applying various numerical methods and models.

First, we introduce our method of highly sensitive and shot-noise limited transient differential transmission spectroscopy, followed by the implementation of a time-resolved single photon counting photoluminescence setup and dark-field spectroscopy setup. We provide an overview on the developed and applied numerical models which form the basis of our theoretical work. In particular, we introduce a model to predict the polarization dependent higher harmonic emission of complex nanostructures.

In the next part, we demonstrate for the first time how an extremely weak nonlinear signal can be enhanced by an optical nanoantenna. For this purpose we use the transient optical response of a mechanically oscillating single gold nanodisc. The antenna is a second gold nanodisc with a larger diameter and placed closely to the particle under study. In this configuration, the antenna enhancement can be understood in the plasmon hybridization framework, where the antenna-nanoparticle interaction modulates the weak nonlinear response of the nanoparticle on the much stronger antenna signal. We provide a detailed introduction to the theoretical modeling and the experimental analyses. The good agreement supports the picture of modulating the desired signal of a tiny nanoparticle on a strong carrier signal of the antenna, in analogy to radio-frequency equivalents.

Furthermore, our sensitive pump-probe setup allows us to investigate for the first time spectrally resolved ultrafast carrier dynamics in quantum confined states of a single CdSe nanowire. We measure the pump induced bleaching of several excitonic transitions which gives insight into previously hidden processes and numbers such

as the time dependent population of various states. We discuss the observed characteristic short and long living phenomena and find indications for re-absorption processes of emitted photons. Finally, we investigate and discuss the interaction between a single CdSe wire and a plasmonic nanoantenna.

In the last part of the thesis we provide a general discussion about optical nanoantennas. For this purpose, we introduce a point dipole approach, based on the discrete dipole approximation method, and focus on the fundamental interaction mechanisms between nanoparticle and antenna. Furthermore, the strongly reduced computation effort allows us to analyse previously unattainable, large parameter spaces. The method is applied to investigate the crucial antenna parameters to achieve maximum efficiency. By implementing a genetic algorithm we provide a first step to find optimized many-particle antenna geometries.

## ZUSAMMENFASSUNG

---

Die vorliegende Arbeit befasst sich mit der ultraschnellen nichtlinearen Dynamik verschiedener Prozesse in individuellen metallischen und halbleitenden Nanostrukturen, ohne die Mittlung über Ensembles. Nanoobjekte mit einer Größe von nur wenigen Nanometern zeigen außergewöhnliche lineare wie auch nichtlineare optische Eigenschaften. Die zeitabhängige Abweichung von linearer Licht-Materie Wechselwirkung wird mittels ultraschneller nichtlinearer Spektroskopie untersucht, bei einer Zeitauflösung von weniger als einer Pikosekunde. In der Erforschung einzelner Nanoobjekte, wie Quantenpunkte, Moleküle oder Nanopartikel, ist das bereits schwache nichtlineare Signal von makroskopischer Materie weiter verringert. Optische Nanoantennen, bestehend aus plasmonischen Nanoobjekten, erhöhen lokal die Licht-Materie Wechselwirkung und bieten ein neues Hilfsmittel um zuvor unzugängliche Größen des Nanokosmos zu untersuchen. Die Entwicklung und Anwendung solcher Antennen zur Verstärkung ultraschneller nichtlinearer Signale von einzelnen Nanoobjekten soll erstmalig umgesetzt werden und erfordert hochsensitive experimentelle Methoden und eine gezielte Modellierung und Optimierung wobei numerischen Lösungsverfahren und Modellbildung zum Einsatz kommen.

Im ersten Teil der Arbeit wird auf unsere Methode der hochsensitiven 'zeitabhängigen differentiellen Transmissions-Spektroskopie' eingegangen, gefolgt von den Erweiterungen für zeitaufgelösten 'Einzelphotonen Photolumineszenz-Spektroskopie' und 'Dunkelfeld-Spektroskopie'. Weiterhin bieten wir einen Überblick über die entwickelten und angewandten numerischen Modelle, welche als Basis unserer theoretischen Arbeit dienen. Im Besonderen wird ein Modell zur Vorhersage der polarisationsabhängigen Emission höherer Harmonischer von komplexen Nanostrukturen vorgestellt und diskutiert.

Der nächsten Abschnitt befasst sich mit der erstmaligen Realisierung einer optischen Nanoantenne zur Verstärkung eines extrem schwachen nichtlinearen Signals. Zu diesem Zweck verwenden wir die zeitabhängige Modulation der optischen Eigenschaften eines einzelnen Gold-Nanopartikels, verursacht durch dessen mechanische Oszillationen. Die Antenne wird durch eine zweite, größere Nanostruktur realisiert und befindet sich im Abstand von nur wenigen Nanometern zum untersuchten Nanopartikel. Die Wechselwirkung zwischen beiden Nanoobjekten und die angestrebte Antennenverstärkung kann im Rahmen der Plasmonhybridisierung verstanden werden. Dabei wird das schwache, nichtlineare Signal des Nanopartikels auf das starke Trägersignal der Antenne moduliert. Wir bieten eine detaillierte Einführung in die theoretische Modellierung und experimentelle Analyse. Die gute Übereinstimmung bestätigt die Analogie zu bekannten Radiofrequenzantennen die bei niedrigeren Frequenzen arbeiten.

Im Weiteren ermöglicht unsere hochsensible Methode zum ersten Mal die spektral aufgelöste Untersuchung von ultraschnellen Ladungsträgerdynamiken innerhalb quantisierter Zustände eines einzelnen CdSe Nanodrahtes. Wir messen das anregungsinduzierte Bleichen unterschiedlicher Exzitonenübergänge und erhalten Einsicht in zuvor versteckte Prozesse und Größen wie zum Beispiel die zeitabhängige Population verschiedener Zustände. Die beobachteten Phänomene spielen sich auf unterschiedlichen Zeitskalen ab und werden im Einzelnen diskutiert. Weiterhin finden wir Hinweise für Reabsorptionsprozesse von emittierten Photonen. Zuletzt untersuchen und diskutieren wir die Wechselwirkung zwischen einem einzelnen CdSe Nanodraht und einer plasmonischen Antenne.

Der letzte Teil der Arbeit bietet eine allgemeine Diskussion von optischen Nanoantennen. Zu diesem Zweck verwenden wir einen Punkt-Dipol Ansatz auf Basis der 'Discrete Dipole Approximation', um im Weiteren besonderen Wert auf die elementaren Wechselwirkungsmechanismen zwischen Nanopartikel und Antenne zu legen. Weiterhin erlaubt uns der stark reduzierte Rechenaufwand riesige, zuvor unzugängliche Parameterräume zu analysieren. Wir verwenden die Methode und diskutieren die relevanten Eigenschaften einer optischen Nanoantenne mit maximaler Effizienz. Mittels der Implementierung eines genetischen Algorithmus bieten wir einen ersten Schritt zum Auffinden optimaler Mehr-Teilchen Antennengeometrien.





## PUBLICATIONS AND PRESENTATIONS

---

### ARTICLES IN SCIENTIFIC JOURNALS

1. T. Schumacher, K. Kratzer, D. Molnar, M. Hentschel, H. Giessen, and M. Lippitz, *Nanoantenna-enhanced ultrafast nonlinear spectroscopy of a single gold nanoparticle*, **Nature Communications** **2**, 333 (2011)
2. T. Schumacher, H. Giessen, and M. Lippitz, *Ultrafast spectroscopy of quantum confined states in a single CdSe nanowire*, **Nano Letters** **13**, 1706 (2013)
3. B. Metzger, M. Hentschel, T. Schumacher, M. Lippitz, X. Ye, C. B. Murray, B. Knabe, K. Buse, and H. Giessen, *Doubling the efficiency of third harmonic generation by positioning ITO nanocrystals into the hot-spot of plasmonic gap-antennas*, **Nano Lett.** **14**, 2867 (2014)
4. B. Metzger, T. Schumacher, M. Hentschel, M. Lippitz, and H. Giessen, *Third harmonic mechanism in complex plasmonic Fano structures*, **ACS Photonics** **6**, 471 (2014)
5. C. Dicken, T. Schumacher, D. Ullrich, K. Lindfors, H. Giessen, and M. Lippitz, *The Role of the scattering phase in the interferometric detection of single nanomagnets*, **in preparation**
6. T. Schumacher, D. Ullrich, and M. Lippitz, *A point dipole approach for the fast computation and optimization of optical nanoantennas*, **in preparation**

### CONTRIBUTIONS ON INTERNATIONAL CONFERENCES

1. T. Schumacher, H. Giessen, and M. Lippitz, *Ultrafast dynamics of quantum confined carriers in a single CdSe nanowire*, **Talk**  
CLEO: QELS 2013 - Munich/Germany
2. T. Schumacher, H. Giessen, and M. Lippitz, *Optical antennas for ultrafast spectroscopy of single CdSe nanoobjects*, **Talk**  
DPG Frühjahrstagung 2013 - Regensburg/Germany
3. T. Schumacher, H. Giessen, and M. Lippitz, *Ultrafast Spectroscopy of excitonic states in an individual CdSe nanowire*, **Poster**  
DPG Frühjahrstagung 2013 - Regensburg/Germany

4. T. Schumacher, H. Giessen, and M. Lippitz, *Ultrafast spectroscopy of individual CdSe nanowires*, **Talk**  
SPP1391: Student Seminar on Ultrafast Nanooptics 2012 - Lauterbad/Germany
5. T. Schumacher, D. Ullrich, M. Hentschel, H. Giessen, and M. Lippitz, *Optical Nanoantennas for Nonlinear Spectroscopy of a Single Nanoobject*, **Poster**  
Ultrafast Phenomena 2012 - Lausanne/Switzerland
6. T. Schumacher, D. Ullrich, M. Hentschel, H. Giessen, and M. Lippitz, *Optical Nanoantennas for Ultrafast Spectroscopy of Single Nanoparticles*, **Talk**  
DPG Frühjahrstagung 2012 - Berlin/Germany
7. T. Schumacher, M. Hentschel, H. Giessen, and M. Lippitz, *A Point-Dipole Model for fast Computation of Plasmonic Structures and Nanoantennas*, **Poster**  
DPG Frühjahrstagung 2012 - Berlin/Germany
8. T. Schumacher, D. Ullrich, M. Hentschel, H. Giessen, and M. Lippitz, *Nanoantenna-enhanced ultrafast spectroscopy of a single nanoparticle*, **Poster**  
SPP1391: Second Summer School - Bad Honnef/Germany
9. T. Schumacher, M. Brandstetter, M. Esslinger, C. Sönnichsen, R. Vogelgesang, and M. Lippitz, *Optical mapping of the elasto-mechanical response in nanostructures*, **Poster**  
Annual SPP1391 Meeting 2011 - Bad Honnef/Germany
10. T. Schumacher, K. Kratzer, D. Ullrich, M. Hentschel, H. Giessen, and M. Lippitz, *Nanoantenna-enhanced ultrafast nonlinear spectroscopy of a single plasmonic nanodisc*, **Talk**  
CLEO: QELS 2011 - Baltimore/United States
11. T. Schumacher, D. Ullrich, K. Kratzer, M. Hentschel, H. Giessen, and M. Lippitz, *Optical Nanoantennas for Ultrafast Spectroscopy of Single Nanoparticles*, **Talk**  
DPG Frühjahrstagung 2011 - Dresden/Germany
12. T. Schumacher, K. Kratzer, M. Hentschel, H. Giessen, and M. Lippitz, *Optical nanoantennas enhance ultrafast nonlinear spectroscopy of single nanodiscs*, **Talk**  
Nanometa 2011 - Seefeld/Austria
13. T. Schumacher, K. Kratzer, M. Hentschel, H. Giessen, and M. Lippitz, *Plasmon Hybridization Enhances Nonlinear Responses of Single Metal Nanoparticles*, **Talk**  
SSP1391: First Student Seminar on Ultrafast Nanooptics 2010 - Kiel-Sehrendorf/Germany

14. T. Schumacher, K. Kratzer, M. Hentschel, and M. Lippitz, *Plasmon Hybridization Enhances Nonlinear Responses of Single Metal Nanoparticles*, **Talk**  
SSP1391: Second International Workshop on Ultrafast Nanooptics 2010 -  
Bad Dürkheim/Germany
15. T. Schumacher, K. Kratzer, D. Molnar, M. Hentschel, and M. Lippitz, *Plasmon Hybridization Enhances the Nonlinear Response of Single Metal Nanoparticles*, **Talk**  
DPG Frühjahrstagung 2010 - Regensburg/Germany

#### CONTRIBUTIONS OF COLLABORATORS

1. B. Metzger, M. Hentschel, T. Schumacher, M. Lippitz, and H. Giessen *Third harmonic spectroscopy of complex plasmonic Fano structures*, **Talk**  
CLEO: QELS 2013 - Munich/Germany
2. B. Metzger, M. Hentschel, T. Schumacher, and H. Giessen *Third harmonic spectroscopy of complex plasmonic Fano structures*, **Talk**  
6th International conference on surface plasmon photonics - Ottawa/Canada
3. C. Dicken, T. Schumacher, D. Ullrich, K. Lindfors, H. Giessen, and M. Lippitz, *The Role of the Scattering Phase in Single Particle Spectroscopy*, **Talk**  
DPG Frühjahrstagung 2013 - Regensburg/Germany
4. D. Ullrich, T. Schumacher, H. Giessen, and M. Lippitz, *Modelling of Optical Nanoantennas for Nonlinear Spectroscopy*, **Poster**  
DPG Frühjahrstagung 2011 - Dresden/Germany
5. K. Kratzer, T. Schumacher, and M. Lippitz, *Acousto-Plasmonic Properties of Single Metal Nanoparticles*, **Poster**  
DPG Frühjahrstagung 2010 - Regensburg/Germany

#### OTHER CONTRIBUTIONS

1. **Annual Report 2010 of the Max-Planck-Institute for Solid State Research**  
*An optical nanoantenna enhances ultrafast nonlinear spectroscopy of a single nanoparticle*
2. **Annual Report 2014 of the Max-Planck-Institute for Solid State Research**  
*Ultrafast spectroscopy of quantum confined states in a single CdSe nanowire*



# CONTENTS

---

Abstract	vii
Zusammenfassung	ix
Publications	xiii
1 INTRODUCTION AND OUTLINE	3
2 ULTRAFAST NONLINEAR NANOOPTICS: PRINCIPLES OF THEORY AND EXPERIMENT	7
2.1 Light-matter interaction on the nanoscale	7
2.1.1 Linear material response	8
2.1.2 Mie theory and plasmons in spherical nanoparticles	9
2.1.3 Optical response of semiconductor nanostructures	12
2.2 Ultrafast nonlinear response of single nanoobjects	16
2.2.1 Nonlinear material polarization density	16
2.2.2 Ultrafast nonlinear spectroscopy and optical antennas	17
2.3 Transient differential transmission spectroscopy	19
2.3.1 Experimental realisation	20
2.3.2 Dark-field spectroscopy	25
2.3.3 Photoluminescence lifetime and single photon counting	27
3 NUMERICAL SIMULATION METHODS AND MODELS	31
3.1 Finite element method (FEM)	32
3.1.1 Fundamentals	32
3.1.2 Formulation of Maxwell's equations	33
3.2 Scattered field components as independent variables	34
3.2.1 Isolated nanostructures	34
3.2.2 In periodic boundary conditions	39
3.3 Nonlinear response of complex plasmonic structures	44
3.3.1 Numerical model for third harmonic generation	44
3.3.2 Theoretical prediction for a dolmen-type structure	46
3.3.3 Conclusion	51
3.4 The total field components as independent variables	51
3.5 Implementation of the constitutive equations for optical chirality simulations	54
4 ANTENNA ENHANCED ULTRAFAST ACOUSTO-OPTICAL RESPONSE OF A SINGLE GOLD NANOPARTICLE	57
4.1 Motivation and Introduction	57
4.2 Pump excitation of acoustical vibrations	58
4.3 Modeling of the ultrafast response	61
4.3.1 Theoretical prediction for the experimental results	64

## Contents

4.4	Single particle response	65
4.4.1	Sample fabrication and characterization	65
4.4.2	Ultrafast nonlinear response and data evaluation	67
4.4.3	Spectrally resolved response	70
4.4.4	Mechanical properties	72
4.4.5	Conclusion of single particle experiments	74
4.5	Signal enhancement utilizing an optical nanoantenna	74
4.5.1	Antenna mediated excitation enhancement	77
4.5.2	Enhanced nonlinear response and antenna optimization	78
4.5.3	Experimental investigation of the antenna-nanoparticle pair	81
4.5.4	Comparison of single and antenna enhanced particle	84
4.6	Conclusion and Outlook	85
5	QUANTUM CONFINED CARRIER DYNAMICS IN A SINGLE CDSE NANOWIRE	87
5.1	Introduction	87
5.2	Quantized electron and hole states	89
5.2.1	One band effective mass theory for electron states	89
5.2.2	Six band effective mass theory for hole states	90
5.2.3	Overlap matrix elements and allowed transitions	92
5.3	Sample characterization	94
5.3.1	Polarization dependent absorption of wires	95
5.4	Ultrafast carrier dynamics in quantum confined states	97
5.4.1	Nonlinear response of a single CdSe nanowire	97
5.4.2	Population of exciton states	101
5.4.3	Investigation of transitions and photoemission lifetimes	103
5.4.4	Re-absorption processes in an individual nanowire	106
5.4.5	Conclusion and outlook of single wire experiments	107
5.5	Interaction of a CdSe nanowire and a plasmonic nanoobject	108
5.5.1	Theoretical prediction of the nonlinear response	108
5.5.2	Ultrafast spectroscopy of the hybrid system	113
5.6	Conclusion and outlook	116
6	A POINT DIPOLE APPROACH FOR THE FAST COMPUTATION AND OPTIMIZATION OF MANY-PARTICLE ANTENNAS	119
6.1	Point dipole approximation	120
6.1.1	Fundamentals and the discrete dipole approximation	120
6.1.2	Range of validity	124
6.2	Signal enhancement via an optical antenna	127
6.2.1	Strong perturbation case	128
6.2.2	Weak perturbation case	133
6.2.3	Conclusion	135
6.3	Optimization of many-particle optical antennas	136
6.3.1	Evolutionary computation as optimization routine	137
6.3.2	Optimum antenna geometries	140

6.4 Conclusion	142
7 CONCLUSION AND OUTLOOK	145
Bibliography	151
A APPENDIX	167



## INTRODUCTION AND OUTLINE

---

Nanoobjects which consist of a few hundreds to a few hundreds of thousands of atoms bridge the gap between atomistic and bulk behavior. At these scales, single mesoscopic nanostructures with a size of a few nanometers show exceptional linear and nonlinear properties which make them to essential objects in fundamental research, novel technologies, and future applications. Among the wide field of nanoscale science, nanooptics investigates the linear and nonlinear light-matter interaction of subwavelength nanosystems in the visible spectrum. One of the most fundamental and amazing topics of this field of research is the ability of shaping the interaction of light and matter, especially the linking of different nanosystems via their electromagnetic interaction to complex networks.

Sophisticated fabrication techniques and methods such as electron beam lithography or chemical synthesis allow the production of a wide range of nanoobjects. Prominent examples of particular interest are plasmonic nanostructures and metamaterials, artificial atoms such as semiconductor nanocrystals and epitaxial semiconductor quantum dots, but also carbon nanotubes, graphene nanodots, single molecules, or dielectric microcavities [1–9]. Besides the fundamental physical interest in metal and semiconductor nanosystems, which we are going to investigate in greater detail, first applications in optical sensors and filters or bio-medical imaging and diagnostics have been developed [10–14]. The great success of these nanoobjects for this kind of applications is due to their linear optical properties and the wide spectral tunability of absorbing but also emitting states dependent on the material and geometric properties of the nanoparticle.

Artificial atoms such as nanoscopic semiconductor quantum systems show discrete electron and hole state energies, strongly deviating from the bulk band structure [4]. The quantum confinement, determined by the geometrical properties of the nanosystem, allows the tailoring of specific spectral properties. Simultaneously, their longevity and stability are clear advantages compared to single molecules and are essential for technological applications. In the age of quantum information, artificial atoms provide a basis for optical integrated circuits and quantum networks [15]. At ultra-low temperatures, the elementary building blocks such as single photon sources, but also simple quantum gates have been experimentally demonstrated [16, 17]. In cavity quantum electrodynamics, strong coupling between a single emitter and a cavity system is investigated and provides the basis for quantum information processing [18]. Semiconductor nanowires are novel one-dimensional nanostructures which combine the quantum properties with strongly anisotropic

behavior at room temperature. This makes them very appealing systems for fundamental research, future technologies, and next generation solar cells [19–22].

Localized surface plasmons are the classical coherent oscillation of the quasi free conduction band electrons in the confinement of a metal nanoparticle. Different plasmon mode resonances shape the spectral response of subwavelength structures and are determined by the dielectric constants of the used metal but also by the size, shape, excitation properties, and environment of the nanoobject [23]. In resonance, the periodic displacement of the free carriers with respect to the quasi static ionic lattice, combined with the large free carrier density leads to strong dipole moments and efficient far-field coupling and emission [24]. The corresponding electric near-fields can exceed the excitation field intensity by orders of magnitude and allows the electromagnetic interaction of individual metal nanostructures [25, 26]. In analogy to molecular orbital theory, plasmon hybridization gives an intuitive description for the mixing of elementary plasmonic modes into new hybrid modes with corresponding eigenenergies [27, 28]. This provides additional parameters to shape the optical properties and electric near-fields of complex metallic nanosystems as shown in many fascinating examples [29, 30]. Plasmonic metamaterials are artificial large area structures with engineered optical properties which cannot be found in natural matter. Common examples are negative refractive index media, superlenses, and optical cloaking [31–33]. Furthermore, sharp plasmon resonances and their sensitivity to the environment make them to popular candidates for optical sensors [11, 34, 35].

Although the linear properties of these nanosystems are mainly well understood, the nonlinear and especially ultrafast processes are still under discussion and content of current research. Ultrafast nonlinear spectroscopy investigates the deviations from linear light-matter interaction appearing on sub-picosecond timescales. However, even with the best preparation methods, the individual objects of interest differ from each other in size, shape, or local environment, rendering the necessity of single object experiments. Here, the weak nonlinear response is reduced further and becomes almost impossible to detect due to the tiny interaction cross sections of the nanoobjects and the incident light field [36–39]. Surface enhanced Raman spectroscopy uses the surface roughness of metals to increase the Raman scattering of single molecules or other nanostructures by random local field enhancement [40, 41]. Optical antennas are contrived metal nanostructures based on plasmonic objects and promise controlled signal enhancement to open a new regime in linear and nonlinear spectroscopy on the nanoscale [42, 43]. The conversion of the incoming light into strongly amplified and localized fields enhances the light-matter interaction within the volume of a nanofocus. Different antenna designs are suggested to achieve strong field, signal, or directivity enhancement, inspired by radio-frequency equivalents to link various subsystems over large distances [24, 44, 45]. However, the fabrication limitations and especially the characteristic properties of metals in the optical spectrum complicate the downscaling into the nanometer regime [46].

In this thesis, we aim for the investigation of different ultrafast nonlinear processes in individual metallic and semiconductor nanostructures without averaging over ensembles. For this purpose, we want to theoretically study, develop, and apply optical antennas for nonlinear spectroscopy, based on plasmonic nanostructures. Chapter 2 will provide an introduction into the theoretical and experimental concepts of ultrafast nonlinear nanooptics. We will introduce the basic set of differential equations and use the example of gold to consider the linear material response of noble metals. Mie theory will be applied to describe the scattering of a plane wave by a spherical particle and to introduce the fundamentals of localized surface plasmons which shape the linear spectral response of metal nanoparticles. Furthermore, we will present a classical model for the light-matter interaction of semiconductor nanostructures and excitonic transitions, followed by a review about ultrafast nonlinear optics. At the end of this chapter, we will introduce the applied experimental techniques of transient transmission spectroscopy, time-resolved photoluminescence measurements, and dark-field microscopy.

Chapter 3 will briefly introduce the finite element method and present the developed and applied numerical models which allow us to compute the scattering of different types of nanosystems in specific boundary conditions. In particular, we will discuss our model for the computation of the higher harmonic generation in complex coupled nanostructures which allows the prediction of the polarization resolved higher harmonic emission. In order to compute the interaction of chiral media and plasmonic antennas, we will show the implementation of the constitutive material equations into our model.

In chapter 4 we will present the first realization of an optical nanoantenna for ultrafast nonlinear spectroscopy and investigate the time resolved acousto-plasmonic response of single tiny metal nanoparticles. The partial absorption of the excitation laser pulse launches mechanical vibration of the structure's lattice which leads to a perturbation of the optical properties. We will give a full theoretical description of the optical excitation and interrogation processes. This will allow us to investigate the size dependent mechanical properties and the mechanical mode spectrum of tiny metal nanoparticles. However, the rapidly reducing signal intensity for decreasing particle sizes limits our investigations of smaller structures and requires the application of an optical nanoantenna. Based on plasmon hybridization, we will discuss the antenna mechanisms and their influences on the excitation and interrogation process. We will theoretically optimize the antenna structure and present the experimental realization of an optical nanoantenna for ultrafast spectroscopy, which enhances the nonlinear response of a single nanoparticle by one order of magnitude.

The ultrafast carrier dynamics in quantum confined states of a single CdSe nanowire will be investigated in chapter 5. Semiconductor nanostructures which are on the size of the exciton Bohr radius show quantum confined states of the electron and the hole. We will experimentally determine the population of the several states and

apply a six-band-effective mass model to predict the optically allowed transition energies. This will give us insight into previously unattainable carrier dynamics in quantized states of a semiconductor nanowire. We will separately discuss the observed characteristic short and long living features in the transient absorption spectra and directly extract the lifetime of various transitions. Furthermore, we will discuss the correlations between state populations, quantum efficiency, and time resolved photoluminescence measurements of different single wires. It will be shown that the discrepancy between the number of excited and radiatively decayed excitons gives us hints on re-absorption processes, after emission of a photon. Finally, we will present our theoretical and experimental work of coupling a single CdSe nanowire to a plasmonic antenna.

In the last part of this thesis, in chapter 6, we will generally discuss the crucial parameters for an optical nanoantenna to achieve maximum efficiency and signal enhancement of the linked nanosystem. For this purpose, we will introduce a point dipole approximation model for the fast computation and optimization of complex plasmonic antennas so that large parameter spaces can be investigated. We will show that our model can predict the linear and nonlinear response of complex coupled plasmonic nanostructures. Furthermore, we will consider the limitations of our model. The method will be applied to discuss the optimum antenna parameters for the cases when the nanoobject does significantly influence the overall response or not. Finally, we will discuss the implementation of an evolutionary algorithm to find advanced antenna geometries, consisting of several nanoparticles.

ULTRAFAST NONLINEAR NANOOPTICS:  
PRINCIPLES OF THEORY AND EXPERIMENT

---

2.1 LIGHT-MATTER INTERACTION ON THE NANOSCALE

Nanoobjects with sizes between 1 nm and 100 nm are mesoscopic systems showing fascinating optical properties, strongly deviating from their pure atomistic or bulk behavior. As long as the quantum mechanical character can be neglected, the light matter interaction and resulting electromagnetic phenomena are fully described by Maxwell's equations [47, 48]

$$\nabla \times \mathbf{E} + \frac{\partial}{\partial t} \mathbf{B} = \mathbf{0} \quad (2.1)$$

$$\nabla \times \mathbf{H} - \frac{\partial}{\partial t} \mathbf{D} = \mathbf{J} \quad (2.2)$$

$$\nabla \cdot \mathbf{D} = \rho_e \quad (2.3)$$

$$\nabla \cdot \mathbf{B} = 0 \quad (2.4)$$

with  $\mathbf{E}$  and  $\mathbf{H}$  being the complex electric and magnetic vector fields,  $\rho_e$  the electric charge density and  $\mathbf{J}$  the current density. For simplicity, the contribution of different media is embedded in the displacement field  $\mathbf{D}$  and magnetic flux density  $\mathbf{B}$ . The constitutive equations for optically inactive materials are defined as

$$\mathbf{D} = \epsilon_0 \underline{\underline{\epsilon_r}} \mathbf{E} = \epsilon_0 \mathbf{E} + \mathbf{P} \quad (2.5)$$

$$\mathbf{B} = \mu_0 \underline{\underline{\mu_r}} \mathbf{H} = \mu_0 \mathbf{H} + \mathbf{M} \quad , \quad (2.6)$$

where the relative permittivity  $\underline{\underline{\epsilon_r}}$  and permeability  $\underline{\underline{\mu_r}}$  tensors are introduced to describe the material properties. The separation of the incident electromagnetic field allows the definition of the electric polarization density  $\mathbf{P}$  and magnetization  $\mathbf{M}$ , both expressing the density of induced or oriented electric and magnetic dipole moments, respectively. In general, the material response is a function of frequency so that either experimentally determined data [49, 50] or physical models [51–53] for  $\underline{\underline{\epsilon_r}}(\omega)$  and  $\underline{\underline{\mu_r}}(\omega)$  have to be applied. At photon energies between 1.5 eV and 3.5 eV, the electric response  $\underline{\underline{\epsilon_r}}(\omega)$  of most materials is shaped by the response of electrons, and the contribution of vibrational and rotational modes can be neglected. Furthermore the magnetic response vanishes ( $\mu_r = 1$ ) for most materials and the complex refractive index  $n + i\kappa$  at optical wavelengths is given by

$$n^2 = \frac{1}{2} \left( \sqrt{\epsilon'{}^2 + \epsilon''^2} + \epsilon' \right) \quad (2.7)$$

$$\kappa^2 = \frac{1}{2} \left( \sqrt{\epsilon'{}^2 + \epsilon''^2} - \epsilon' \right) \quad . \quad (2.8)$$

### 2.1.1 Linear material response

In solid state physics, isolators, semiconductors, and metals differ in their electronic band structure. The Drude-Lorentz theory [52] offers a simple classical model to describe the frequency dependent dielectric response function  $\epsilon_r(\omega) = \epsilon'(\omega) + i\epsilon''(\omega)$  of an isotropic medium. While the Lorentz term describes electrons bound to spatially fixed atom cores under the assumption of a harmonic potential, the Drude term considers a free electron gas to approximate the behavior of quasi free electrons in the conduction band of a metal. Optical transitions as for example between the valence and conduction band in semiconductors, or higher band excitations are not described by this theory. The linear equation of motion for a bound electron driven by a monochromatic field with amplitude  $\mathbf{E}_0$  and frequency  $\omega$  is given by

$$\frac{d^2\mathbf{r}}{dt^2} + \gamma_L \frac{d\mathbf{r}}{dt} + \omega_0^2 \mathbf{r} = \frac{e}{m_e} \mathbf{E}_0 \cdot \exp(i\omega t) \quad (2.9)$$

with  $\mathbf{r}$  being the displacement from the electron's equilibrium position,  $\gamma_L$  and  $\omega_0$  the decay rate and eigenfrequency of the oscillator,  $e$  the elementary charge, and  $m_e$  the free electron mass. With the solution of equation 2.9, the induced local dipole moment is given by  $\mathbf{p}_{loc}(t) = -e \cdot \mathbf{r}(t)$ . Consequently the electric polarization density

$$\mathbf{P} = -n_e \cdot \mathbf{p}_{loc} = -n_e \frac{e^2/m_e}{(\omega_0^2 - \omega^2) + i\omega\gamma_L} \cdot \mathbf{E}_0 \cdot \exp(i\omega t) \quad (2.10)$$

can be derived, by taking the electron density  $n_e$  into account. Following equation 2.5, the complex relative permittivity  $\epsilon_{r,L} = \epsilon'_{r,L} + i\epsilon''_{r,L}$  is given by

$$\epsilon_{r,L} = 1 + \frac{n_e}{\epsilon_0} \frac{e^2/m_e}{(\omega_0^2 - \omega^2) + i\omega\gamma_L} \quad (2.11)$$

or decomposed into real and imaginary part by

$$\epsilon'_{r,L} = 1 + \left( \frac{n_e e^2}{m_e \epsilon_0} \right) \frac{\omega_0^2 - \omega^2}{(\omega_0^2 - \omega^2)^2 + \omega^2 \gamma_L^2} \quad (2.12)$$

$$\epsilon''_{r,L} = \left( \frac{n_e e^2}{m_e \epsilon_0} \right) \frac{\omega/\tau}{(\omega_0^2 - \omega^2)^2 + \omega^2 \gamma_L^2} \quad (2.13)$$

A quasi free electron follows the same equation of motion but without restoring force ( $\omega_0 = 0$ ). Hence equations 2.12 and 2.13 are simplified to

$$\epsilon'_{r,D} = 1 - \frac{\omega_p^2}{\omega^2 + \gamma_D^2}; \quad \epsilon''_{r,D} = \frac{\omega_p^2 \gamma_D}{\omega^3 + \omega \gamma_D^2} \quad (2.14)$$

by introducing the plasma frequency

$$\omega_p = \sqrt{\frac{n_e e^2}{m_e \epsilon_0}} \quad (2.15)$$

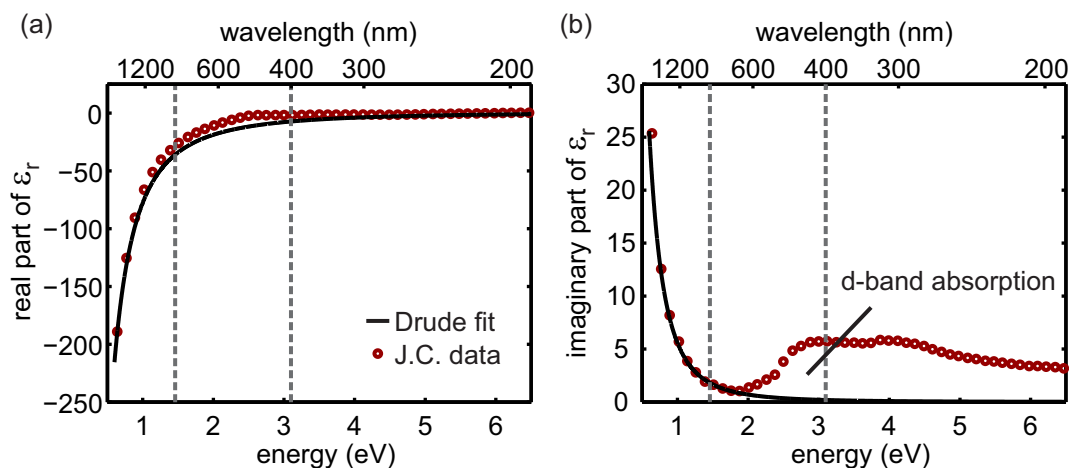


**Figure 2.1**

Comparison of the Drude-model fit and experimentally determined real (a) and imaginary part (b) of the dielectric function of gold. For orientation, the vertical dashed lines at 850 nm and 400 nm mark the spectral region of interest for this work.

and the Drude damping  $\gamma_D$ . The red circles in figure 2.1 show the real (a) and imaginary part (b) of the dielectric function  $\epsilon_r$  of gold, measured by Johnson and Christy [49]. For comparison, the model solution of  $\epsilon_{r,D}$  with  $\omega_p = 8.89$  eV and  $\gamma_D = 7.088 \cdot 10^{-2}$  eV are superimposed (black curves) and in a very good agreement for energies below  $\approx 2$  eV. The deviation, especially in the imaginary part, for larger energies stems from the d-band absorption of gold, that is not taken into account in the Drude model. As a consequence, the numerical simulations presented in this work are computed with the optical constants determined by Johnson and Christy. However, the model gives the correlation to elementary physical values and allows the prediction of small perturbations in the material properties. In chapter 4 it is used to approximate the nonlinear response of gold nanoparticles, excited by an ultrashort laser pulse.

### 2.1.2 Mie theory and plasmons in spherical metal nanoparticles

The derivation of the linear optical properties  $\epsilon_r$  of a metal, following the Drude approach, assumes an infinitely extended quasi free electron gas without restoring forces. This corresponds to an infinitely large material volume and models the bulk optical properties. Surface plasmons are resonant coherent electron oscillations within a typical skin depth, for example at a metal-dielectric interface [54]. However, by decreasing the structure size to particles much smaller than the excitation wavelength  $\lambda_0$ , the electron movement is restricted by the particle boundaries. In analogy to a single particle in a potential well, the plasma oscillation in a metal particle has certain discrete eigenenergies. The 'quantum' of the confined electron gas oscillation is called particle plasmon or localized surface plasmon and defined by its resonance energy, plasmon mode, and eigenfunction.

A fully analytical solution of Maxwell's equation 2.1- 2.4 for a monochromatic plane wave, scattered by a spherical object was derived by Gustav Mie in 1908 [55]. The theory allows the extraction of three characteristic geometrical values namely scattering, absorption and extinction cross section which are defined as follows.

$$\sigma_{scat} = \frac{P_{scat}}{I_{inc}} \quad \sigma_{abs} = \frac{P_{abs}}{I_{inc}} \quad (2.16)$$

$$\sigma_{ext} = \frac{P_{ext}}{I_{inc}} \quad (2.17)$$

$$= \sigma_{scat} + \sigma_{abs} \quad (2.18)$$

$I_{inc}$  is the incident energy flux density of the excitation wave and  $P_i$  the scattered, absorbed or extinct energy of the particle. In case of the spherical scatterer, the scattering and extinction cross section can be written as the infinite series

$$\sigma_{scat} = \frac{2\pi}{k^2} \sum_{n=1}^{\infty} (2n+1)(|a_n|^2 + |b_n|^2) \quad (2.19)$$

$$\sigma_{ext} = \frac{2\pi}{k^2} \sum_{n=1}^{\infty} \text{Re}[a_n + b_n] \quad (2.20)$$

where  $k = 2\pi \cdot n_{med}/\lambda$  is the wavenumber of the excitation wave, and  $n_{med}$  the refractive index of the environment. Further, the parameters  $a_n$  and  $b_n$  are given by

$$a_n = \frac{m\psi_n(mx)\psi'_n(x) - \psi_n(x)\psi'_n(mx)}{m\psi_n(mx)\xi'_n(x) - \xi_n(x)\psi'_n(mx)} \quad (2.21)$$

$$b_n = \frac{\psi_n(mx)\psi'_n(x) - m\psi_n(x)\psi'_n(mx)}{\psi_n(mx)\xi'_n(x) - m\xi_n(x)\psi'_n(mx)}$$

with  $m = \sqrt{\epsilon_p/\epsilon_{med}} = n_p/n_{med}$  being the ratio of the refractive indices of particle and environment ( $\mu_p = \mu_{med} = 1$ ). In addition,  $\psi_n$  and  $\xi_n$  are the n-th order Riccati-Bessel functions, and  $x = k \cdot R$  a size parameter depending in the sphere radius  $R$ .

For simplicity, the d-band absorption of gold is neglected and we use the Drude model, discussed previously, to describe the optical properties. The upper graph in figure 2.2(a) contains the normalized extinction cross section  $C_{ext}$  spectrum of a spherical particle with 100 nm in radius. The surrounding medium is vacuum with  $n_{med} = 1$ . Several pronounced plasmon resonances are observed. The broad linewidths reveal the fast dephasing of the plasmon, with lifetimes on the order of some tens of femtoseconds. The fundamental plasmon mode, labeled  $n = 1$  is in the optical regime at 2 eV (600 nm), followed by higher order modes, reaching deep into the UV. The size dependence of the plasmon modes for sphere radii, ranging from 1 nm to 100 nm, is presented through the normalized extinction spectra in the

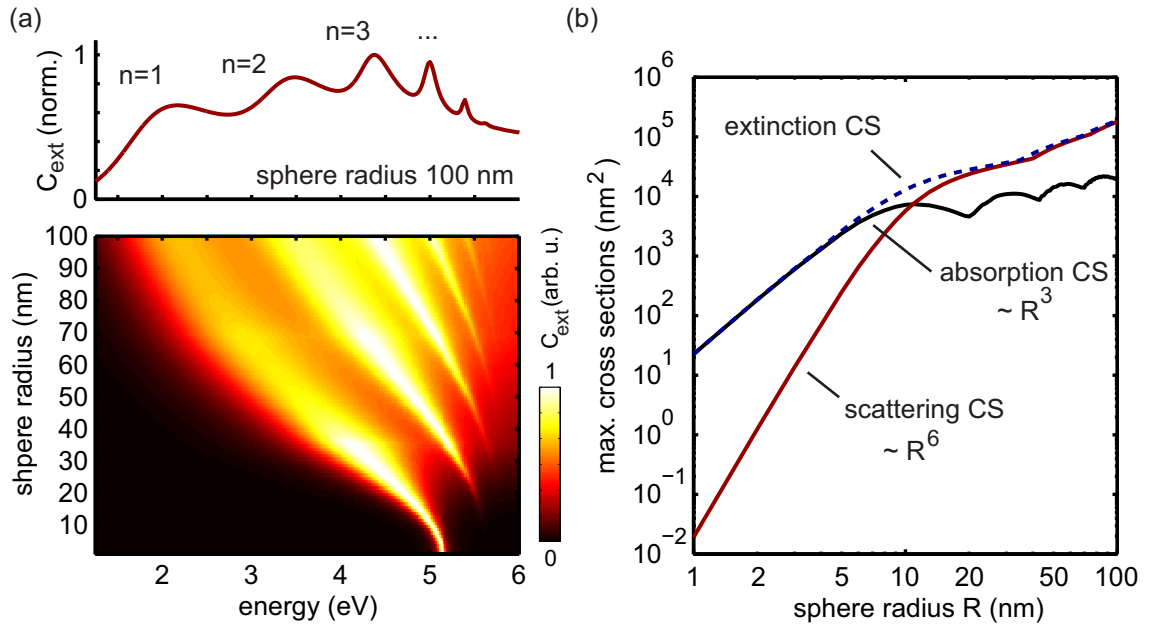


**Figure 2.2**

(a) Normalized extinction spectra of a spherical nanoparticle with 100 nm radius and for sphere radii between 1 and 100 nm, showing the characteristic plasmon mode dependence. (b) Maximum absorption (black), scattering (red), and extinction (blue dashed) cross section as a function of particle radius in a double-logarithmic plot. For small sphere radii, absorption goes linearly with the volume ( $R^3$ ), scattering with volume squared ( $R^6$ ).

lower graph. We observe a shift of the modes to higher energies by decreasing the particle size. The spectrum of the 1 nm sphere is dominated by the fundamental mode resonance.

In figure 2.2(b) the maximum scattering and absorption cross section is plotted over the particle radius. At radii below 5 nm, the maximum absorption cross section goes linearly with the particle volume, the scattering cross section with volume squared. This behavior changes when  $C_{scat}$  becomes the dominant contribution of  $C_{ext}$ . Here the modes broaden due to increasing radiation losses and a shift to spectral regions with higher material losses, resulting in a complex behavior. Furthermore, for realistic optical properties of gold, higher energetic plasmon modes above  $\approx 2.25$  eV vanish in the d-band absorption. Plasmons in gold nanoparticles show good tunability over wide ranges in the optical and near infrared spectrum. In the most general case, plasmons depend on material, size, shape, and polarization [34, 56]. They can be degenerated in polarization (s-, p- polarization for a spherical particle) or dipole forbidden (quadrupolar mode), showing negligible far-field interaction and radiative decay. However, the electron movement causes high electric near-fields (see subsection 3.2.1) and allows strong plasmon-plasmon interaction between separated metallic particles on a nanometer scale. These properties

open almost infinite possibilities for sub-wavelength optical devices [57–59], sensing or labeling applications [34, 60–62]. The combination of high electric near fields, spectral tunability, and strong far field interaction makes plasmonic nanostructures to prominent candidates for optical antennas in fundamental nanoscience. Nevertheless, the scattering contribution for small particle sizes is negligible. Thus optical antennas that have to direct photons from a local source into a certain direction have to exceed a certain volume to work reasonably. Otherwise the dominant dissipative losses prevent elastic scattering. In cases where the antenna serves to increase the absorption cross section, the far field radiation plays a subordinate role which will be discussed in more detail in chapter 6.

### 2.1.3 Optical response of semiconductor nanostructures

In contrast to the quasi free electrons in metals, semiconductors have an empty conduction band at 0 K. But also at higher temperatures the Fermi-Dirac distribution allows only an insufficiently low density of free carriers for plasmonic phenomena. However, the band gap energy  $E_{gap}$  often lies in the optical or near infrared spectrum [63, 64]. As a consequence, their optical properties are dominated by interband transitions of electrons. Table 2.1 gives an overview about the band gaps for some elementary and combined semiconductors at room temperature (300K) and around 0K. A photon with energy larger than  $E_{gap}$  can excite an electron from the valence into the conduction band, while a vacancy or hole remains in the valence band. If electron and hole are unbound they serve as quasi free charge carriers. However, due to the attractive Coulomb interaction they can bind and form an exciton. In analogy to the Bohr model of a hydrogen atom, the Bohr radius  $r_B$  of the exciton can be approximated by

$$r_B = \frac{4\pi\epsilon_0\hbar^2}{e^2} \left( \frac{m_e^*m_h^*}{m_e^* + m_h^*} \right)^{-1} \quad (2.22)$$

where  $\hbar = h/2\pi$  is the Planck constant,  $m_e^*$  and  $m_h^*$  the effective masses of electron and hole in the crystal environment. The effective masses depend on the curvature of the band structure, and can be described by an effective mass theory as applied in chapter 5. Typically  $r_B$  is on the order of a few nanometers.

	CdSe	GaAs	Si	InP	CdTe	ZnO
$T = 300^\circ K$	1.74	1.43	1.11	1.27	1.44	3.20
$T \approx 0^\circ K$	1.84	1.52	1.17	1.42	1.61	3.44

**Table 2.1**

Band gap energies (in eV) at room temperature and around 0K for a selection of elementary and combined semiconductors.

In semiconductor nanostructures with sizes around or smaller than the Bohr radius, the electrons and holes are confined by the boundaries of the nanocrystal. Here, the quantum mechanical character can no longer be neglected, and a transition from the band structure to discrete states takes place. The behavior of the single electron and hole is described separately, by the time dependent Schrödinger equation (SE)

$$i\hbar \frac{\partial}{\partial t} \Psi_i(\mathbf{r}_i, t) = \left[ -\frac{\hbar^2}{2m_i^*} \nabla^2 + V_i(\mathbf{r}_i, t) \right] \Psi_i(\mathbf{r}_i, t) \quad (2.23)$$

with  $\Psi_i$  being the wavefunction,  $m_i^*$  the effective mass of the free particle in the potential  $V_i(\mathbf{r}, t)$ . In order to solve equation 2.23 in steady state, several approximations are possible. An atomistic approach via pseudopotentials takes each atom of the quantum dot or nanocrystal into account and avoids the approximation via effective masses of the bulk material band structure. However, these methods are content of current theoretical research and limited due to the huge computational effort. In chapter 5 we apply a single band model for the electrons and six-band effective mass theory for the holes to describe the band properties of bulk CdSe. Thus we separately solve the Schrödinger equation for both charge carriers independently. However, the steady state two particle SE for the exciton is given by

$$-E_X \Psi_X(\mathbf{r}_e, \mathbf{r}_h) = \left[ -\frac{\hbar^2}{2m_e^*} \nabla_{\mathbf{r}_e}^2 + V_e(\mathbf{r}_e) - \dots -\frac{\hbar^2}{2m_h^*} \nabla_{\mathbf{r}_h}^2 + V_h(\mathbf{r}_h) - \frac{e^2}{\epsilon |\mathbf{r}_e - \mathbf{r}_h|} \right] \Psi_X(\mathbf{r}_e, \mathbf{r}_h) \quad (2.24)$$

with  $E_X$  being the exciton energy, which differs from the energy that can be calculated from the single particle Hamiltonians due to the Coulomb term in equation 2.24. But the solution for the exciton can be approximated from the single particle solutions. The resulting eigenenergy can be written to

$$E_X = E_e + E_h + E_{Coul} \quad (2.25)$$

where  $E_e$  and  $E_h$  are the steady state eigenenergies of the single particle solution. The binding energy  $E_{Coul}$  is typically negative due to the attractive Coulomb interaction, leading to a small energy reduction with respect to the free carriers. From first order perturbation theory, the exciton-photon interaction follows Fermi's Golden Rule. Hence, the dipole allowed transition probability rate  $\gamma_{0,X}$  is given by

$$\gamma_{0,X} = \frac{2\pi}{\hbar} |d_{0,X}|^2 \delta(E_0 - (E_X + E_{gap}) - \hbar\omega) \quad (2.26)$$

with

$$d_{0,X} = \int \Psi_X^* \hat{\mathbf{d}} \Psi_0 d^3r = \langle \Psi_X | \hat{\mathbf{d}} | \Psi_0 \rangle \quad (2.27)$$

being the transition dipole matrix element with the dipole operator  $\hat{\mathbf{d}}$ , and  $\Psi_X$ ,  $\Psi_0$  the exciton (final) and crystal ground state (initial). The bandgap energy is added to the exciton energy since it is not considered in equation 2.24. In general,  $E_{gap}$  is a function of temperature but almost invariant for small temperature fluctuations, especially at room temperatures. While the binding energy  $E_{Coul}$  is typically on the order of some tens of meV, the eigenenergies of electrons  $E_e$  and holes  $E_h$  are widely tunable via their potentials and confinement. According to equation 2.26, this allows the synthesis of artificial atoms and nanocrystals, with defined ground state transitions over the whole optical and NIR spectrum. In analogy to the plasmonic nanoparticles, these properties offer a wide range of possibilities for labeling and imaging applications [13, 14] and as local probe [65]. But especially as single photon sources, semiconductor quantum dots are prominent candidates for future telecommunication applications [66, 67]. In quantum information science they can be used as qubits, due to their long coherence time at lower temperatures [15].

Although the exciton transitions in semiconductor nanostructures have to be considered quantum mechanically, their spectral dependence of the absorption cross section can be approximated classically as summarized by Karrai and Warburton [68]. For a known exciton transition energy  $\hbar\omega_X$  and dephasing rate  $\Gamma$ , the absorption cross section can be written as

$$\sigma_{abs} = \sigma_0 \frac{(\Gamma/2)^2}{(\omega - \omega_X)^2 + (\Gamma/2)^2} \quad (2.28)$$

$$\text{with } \sigma_0 = \frac{e^2 f}{\epsilon_0 c_0 m_0 n \Gamma} \quad (2.29)$$

where  $f$  is the oscillator strength which can be related to the optical dipole moment of the excitonic transition [69], and  $n$  the refraction index of the surrounding medium. For a purely radiative decay of the exciton via spontaneous emission, the dephasing rate is

$$\Gamma_{sp} = n \frac{2\pi}{3\lambda_0^2} \frac{e^2 f}{\epsilon_0 c_0 m_0} \quad (2.30)$$

$$= \frac{8\pi^2 n}{3\lambda_0^2} \frac{d_{12}^2}{\hbar \epsilon_0} \quad (2.31)$$

with  $\lambda_0$  being the emitter wavelength and  $d_{12}$  the dipole moment [70, 71]. Plugged into equation 2.29, we obtain the maximum absorption cross section  $\sigma_{0,sp}$  as function of the emission wavelength  $\lambda_0$

$$\sigma_{0,sp} = \frac{3}{2\pi} \left( \frac{\lambda_0}{n} \right)^2, \quad (2.32)$$

independent of the oscillator strength. Graph 2.3(a) shows the calculated absorption spectrum of a single emitter in vacuum at  $\lambda_0 = 600$  nm with purely radiative lifetime  $\tau_{sp}$  of 10 ns, respectively  $\Gamma_{sp} = 0.1$  GHz =  $0.41$   $\mu$ eV. The calculated peak

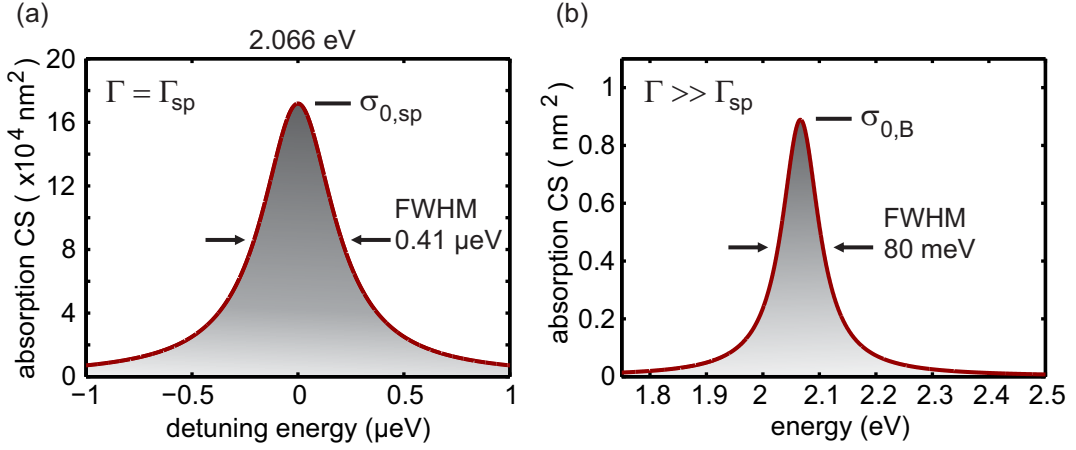


**Figure 2.3**

(a) Absorption cross section  $\sigma_{abs}$  with peak absorption  $\sigma_{0,sp}$  of an ideal emitter with purely spontaneous emission decay at a wavelength of 600 nm and a lifetime of 10 ns. (b) For additional dephasing the spectrum broadens, while the integrated absorption stays constant, leading to a drastic reduction of the peak absorption cross section  $\sigma_{0,B}$ .

absorption is  $\sigma_{0,sp} = 17.2 \cdot 10^4 \text{ nm}^2$ , the oscillator strength  $f = 1.62$  (equation 2.30). This corresponds to a dipole moment of  $d = 8.3$  Debye or an elementary charge separation of 0.17 nm.

The high absorption peak and narrow linewidth of the considered idealized system deviate strongly from measured values [72]. Especially at room temperatures the emission spectrum of a single quantum dot shows a linewidth in the order of 100 meV. Responsible are dephasing effects such as scattering with phonons in the crystal lattice. To circumvent the missing information of the statistical broadening, a value only dependent on the oscillator strength  $f$ , which is responsible for the absorption, is introduced. The integral absorption  $\sigma_i$  is defined by the integral of equation 2.28 over the whole spectral range.

$$\sigma_i = \int \sigma(\omega) d\omega \quad (2.33)$$

$$= \sigma_0 \pi \frac{\Gamma}{2} \quad (2.34)$$

$$= \frac{3}{4} \left( \frac{\lambda_0}{n} \right)^2 \Gamma_{sp} \quad (2.35)$$

The product of  $\sigma_{0,sp}$  and  $\Gamma_{sp}$  or any other  $\sigma_0, \Gamma$  pair

$$\sigma_{0,sp} \Gamma_{sp} = \sigma_0 \Gamma = \frac{e^2 f}{n \epsilon_0 c_0 m_0} \quad (2.36)$$

shows the desired  $f$  dependence. As a consequence, the integral absorption stays invariant for a single emitter, independent of the spectral broadening components and we can write the relation

$$\sigma_{0,B} = \sigma_{0,sp} \frac{\Gamma_{sp}}{\Gamma_B} = \sigma_{0,sp} \eta \quad (2.37)$$

between ideal emitter and a realistic system with peak absorption  $\sigma_{0,B}$  and emission linewidth  $\Gamma_B$ . Furthermore we define the broadening parameter  $\eta$  (with  $\eta < 1$ ) by  $\Gamma_{sp} = \eta \Gamma_B$ . For the emitter considered previously, with  $\lambda_0 = 600$  nm and  $\Gamma_{sp} = 0.41$   $\mu$ eV, the integral of absorption is calculated to  $\sigma_{i,sp} = 112$  nm<sup>2</sup> meV. At room temperature, a typical emission linewidth of a quantum dot is  $\Gamma_B = 80$  meV given by additional dephasing. By equation 2.37 we model the corresponding absorption spectrum which is shown in figure 2.3. According to equation 2.37, the absorption peak is reduced by the factor  $\eta = 5.2 \cdot 10^{-6}$  to  $\sigma_{0,B} = 0.89$  nm<sup>2</sup>. Under the assumption of a homogeneously illuminated laser spot area  $A_{spot} = \pi \cdot 400^2$  nm<sup>2</sup>, the absorbing emitter leads to a maximum signal change of  $\sigma_{0,B}/A_{spot} = 1.77 \cdot 10^{-6}$ . For comparison, the plasmon absorption maximum of a spherical gold nanoparticle with 1.5 nm in radius is on the same order.

## 2.2 ULTRAFAST NONLINEAR RESPONSE OF SINGLE NANOOBJECTS

### 2.2.1 Nonlinear material polarization density

We discussed the linear material response of metallic and semiconductor nanoobjects in the previous sections. There, a proportionality of polarization density  $\mathbf{P}_{lin}$  and excitation field  $\mathbf{E}$  is assumed and defined via the susceptibility  $\chi^{(1)}$ .

$$\mathbf{P}_{lin} = \epsilon_0 \chi^{(1)} \mathbf{E} \quad (2.38)$$

$$\text{with } \chi = (\epsilon_r - 1) \quad (2.39)$$

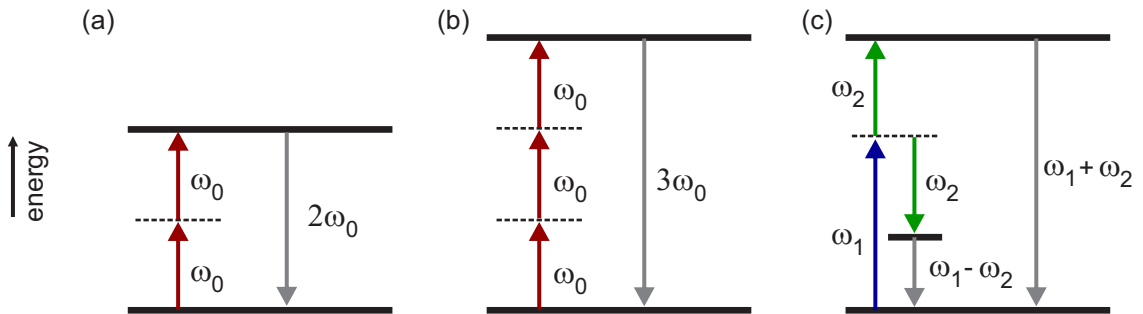


**Figure 2.4**

Second harmonic (a), third harmonic (b), and sum frequency generation (c) in a multi-photon energy conservation scheme. The gray arrows represent the emission frequencies.

However, the material response is much more complex than the linear approximation of equation 2.38. Bulk material [73, 74], as well as plasmonic nanostructures [38, 75], can show inelastic light scattering at higher frequencies than the monochromatic excitation field  $\omega_0$ . These higher order nonlinear optical processes are many photon processes with virtual energy levels as shown in figure 2.4 and depend on the crystalline or molecular structure and symmetry. Prominent examples are the second (SHG) and third harmonic generation (THG) in plasmonic nanostructures. The latter is further discussed in section 3.3, where we introduce a numerical model to describe the polarization dependent correlation between linear plasmonic response and THG in complex nanostructures. For two or many color excitation at  $\omega_1$  and  $\omega_2$ , as sketched in figure 2.4(c), further emission lines at  $(\omega_1 + \omega_2, 2\omega_1 \pm \omega_2, \dots)$  appear. In all cases, the polarization density  $\mathbf{P}$  deviates from the linear approximation. Hence we introduce the definition

$$\mathbf{P} = \mathbf{P}_{lin} + \Delta\mathbf{P} \quad (2.40)$$

where the polarization density is separated into a linear  $\mathbf{P}_{lin}$  and nonlinear  $\Delta\mathbf{P}$  part. Consequently the previously discussed phenomena are covered if the polarization density is extended by

$$\Delta\mathbf{P} = \underbrace{\epsilon_0\chi^{(2)}\mathbf{E}^2 + \epsilon_0\chi^{(3)}\mathbf{E}^3 + \dots}_{\text{nonlinear response}} \quad (2.41)$$

with  $\chi^{(i)}$  being the higher order susceptibility components. As the nonlinear terms are functions of  $\mathbf{E}^i$ , their contribution can be neglected for small electric field amplitudes. For the interaction with ultrashort laser pulses, the high field amplitude leads to higher harmonic generation.

### 2.2.2 Ultrafast nonlinear spectroscopy and optical antennas

Nonlinear spectroscopy investigates the deviations from linear light-matter interaction [39, 74, 76, 77]. Most common is the time independent investigation of the nonlinear response  $\Delta\mathbf{P}$  of a material, as discussed previously. As the crucial value is the peak electric field amplitude, these experiments are usually performed using broadband ultrashort laser sources, leading to photon conversion with higher harmonic and sum frequency emission. As the excitation and emission fields are spectrally separated, the measurement is almost background free and allows long integration times.

More complex are multiple pulse experiments to investigate the temporal behavior of ultrafast processes and phenomena [78, 79]. In the case of incoherent systems and two laser pulses, the first one at frequency  $\omega_1$  and time  $t_1$  serves as pump pulse to induce the process, the second one at  $\omega_2$  and  $t_2$  as probe which is detected to interrogate its time dependent response. Since excitation and response are energy dependent processes, we write the nonlinear polarization density as

$$\Delta\mathbf{P}(\omega_1, \omega_2, \tau_{2,1}) = \mathbf{P}(\omega_1, \omega_2, t_2 - t_1) - \mathbf{P}_{lin}(\omega_2) \quad (2.42)$$

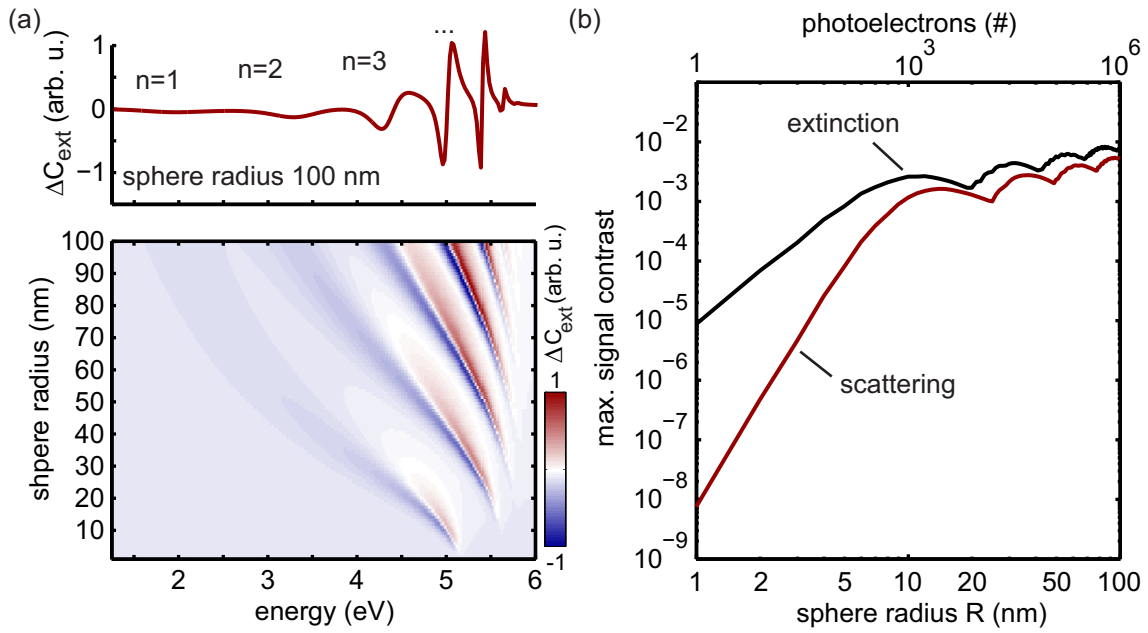


**Figure 2.5**

Comparison to the linear optical response, shown in figure 2.2. Change of extinction cross section after excitation (a). The modes are influenced differently by the perturbation of the material properties, especially the narrow resonances show high sensitivity. The theoretical signal contrast in the discussed ionization experiment ranges from  $10^{-8}$  to  $10^{-2}$  for the scattering and  $10^{-5}$  to  $10^{-2}$  for the absorption measurement.

where  $\tau_{2,1} = t_2 - t_1$  is the temporal evolution, and  $\mathbf{P}_{lin}$  the linear response without pump pulse. In 2D-spectroscopy, pump and probe wavelength are tuned independently to obtain the full two pulse response.

Particle plasmons have widely tunable resonances as introduced in subsection 2.1.2. Due to their strong correlation to the dielectric function and confinement, they show high sensitivity to any kind of perturbation. An example for the spectrally resolved nonlinear response is summarized in figure 2.5. In a Gedankenexperiment we use the pump pulse to induce photoelectron emission from a Drude-gold nanoparticle. Following the previous equation we compute the linear particle response  $\mathbf{P}_{lin}(\omega_2)$  of the probe pulse as described in subsection 2.1.2. For the polarization density  $\mathbf{P}(\omega_1, \omega_2, t_2 - t_1)$  after pump excitation we assume a time independent perturbation of the plasma frequency of  $\Delta\omega_p = -0.2\%$ . This corresponds to one photoemitted electron for the gold particle with 1 nm radius, and  $10^6$  electrons for the 100 nm particle. Further we assume an invariant Drude damping parameter  $\gamma_D$ . The nonlinear response  $\Delta P$  of a 100 nm sphere in arbitrary units is plotted in graph 2.5(a). The missing electrons change the dielectric function, resulting in a perturbation of the plasmon resonances. The differential signal  $\Delta \mathbf{P}$  is strongest where the spectral gradient is highest (see figure 2.2(a) for comparison), and the linear plasmon modes

have a high q-factor combined with a high peak extinction. Graph (b) depicts the normalized nonlinear response for different sphere radii. The comparison with figure 2.2 supports the previously discussed results. The maximum differential signal contrast  $\Delta C_{max}/A_{spot}$  for a spotsize of  $A_{spot} = \pi \cdot 400^2 \text{ nm}^2$  as function of the sphere radius is plotted in (c). The upper scale shows the number of emitted electrons corresponding to the sphere radius. We find nonlinear signals from below  $10^{-5}$  for the smallest sphere and a single emitted electron to approximately  $10^{-2}$  for larger particles of 100 nm radius and  $10^6$  emitted conduction electrons.

In analogy to the presented example, ultrafast nonlinear processes in metal nanoobjects can be mapped via plasmon resonances [80]. The process has to disturb the optical properties of the particle itself or its environment. In the latter case, the plasmonic nanoparticle acts as a local probe or optical antenna. In chapter 4 we investigate mechanical vibrations of metal nanoparticles. Here, the signal contrast is on the order of  $\approx 10^{-5}$  for particle sizes of a few tens of nanometers. Furthermore, to increase the signal of even smallest gold particles, we develop and use an optical nanoantenna as discussed in section 4.5. Here the nanoobject of interest as well as the antenna are plasmonic nanostructures and interact strongly via their near fields. Plasmon hybridization can transfer the weak perturbation information to a much stronger oscillator respectively carrier signal. The same holds true for semiconductor nanostructures. Transition bleaching of a single exciton as introduced in section 2.1.3 leads to relative signals of  $\approx 10^{-6}$ . In chapter 5 we investigate ultrafast carrier dynamics in quantum confined states in a single CdSe nanowire. In contrast to a plasmonic nanoobject, the dipole strength of the exciton is very small and has less influence on an antenna plasmon. Furthermore the combination of classical and quantum mechanical system leads to additional effects which will be discussed in section 5.5.

### 2.3 TRANSIENT DIFFERENTIAL TRANSMISSION SPECTROSCOPY

From theory, we expect relative signals of a single nanoobjects being on the order of  $10^{-4}$  or below. In combination with the high temporal resolution and detectivity over a broad spectral range, several optical and electronic noise reducing techniques have to be applied. Transient differential transmission spectroscopy is a nonlinear two pulse technique, and allows direct extraction of the time dependent nonlinear response of a system. Different pump wavelengths are required to excite various nanosystems as presented in the chapters 5 and 4. The probe pulse interrogates the system response as a function of time after excitation. In the presented setup, the measurements are performed in transmission and the nanoobjects are positioned on 200  $\mu\text{m}$  thin glass substrates. High resolution electron-beam-lithography enables design and fabrication of planar structures down to sizes of approximately 10 nm. The sample is mounted vertically on a 3D piezo table which allows accurate scanning and positioning in the laser focus between two high NA objectives. The differential signal (eq: 2.42), caused by an intensity modulated pump pulse, is recorded by a low

noise balanced detection amplifier with serially connected lock in amplifier. A dark-field and photoluminescence setup supports the localization and additional analyses the nanostructures. The experimental setup with its many degrees of freedom and detectors is synchronized via real time electronics (*ADwin - Jäger*) and controlled by an universal software package for Labview.

### 2.3.1 *Experimental realisation*

Here we focus on the optical realisation of the pump-probe spectroscopy experiment [80, 81]. The achieved temporal resolution and noise limitation are separately discussed afterwards. The implemented dark-field microscopy and spectroscopy setup is discussed in greater detail in subsection 2.3.2, followed by the time and spectrally resolved photoluminescence setup in subsection 2.3.3.

#### *Optical setup*

A simplified sketch of the setup containing all relevant optics and detectors is depicted in figure 2.6. As pump source we use a frequency doubled CW high-power Nd:YVO<sub>4</sub> solid-state laser (*Coherent Verdi V18*) operating at 532 nm wavelength and 10 W output power. Ultrashort laser pulses are provided by the pumped 76 MHz Ti:Sa oscillator in femtosecond configuration (*Coherent Mira 900*), equipped with a *Xwave* mirror set for spectral tunability between 700 nm and 1050 nm. The output pulses are set to  $\approx 795$  nm center wavelength and have energies of  $\approx 20$  nJ/pulse and pulse durations below 150 fs. A lambda-half plate rotates the linear polarized Ti:Sa output and defines the intensity relation of pump and probe branch which is separated by a polarizing beam splitter (PBS). The length of the optical pump-path is controlled by a high precision mechanical delay line (*OWIS - Limes 150*) with mounted retroreflector. This allows the variation of the path by  $2 \times 15$  cm with a resolution below 10  $\mu\text{m}$ , corresponding to a temporal range of  $\Delta t = \Delta s \cdot c_0^{-1} = 1000$  ps and reproducible sub 70 fs resolution. Dependent on the system under investigation, the pump photon energy can be doubled by a phase-matched Beta-Bariumborat (BBO) crystal. Upcoming focus drifts, caused by the delay line, are negligible for temporal scans up to  $\approx 500$  ps where the effect is in the order of 3%. For larger scans, a normalization becomes necessary. In case of frequency doubled pump pulses, the remaining fundamental light is removed by the short pass filter *AHF BrightLine HC 390/18*, with OD6 at 785 nm and above. In order to apply the lock-in technique, we modulate the pump beam intensity with 22.5 kHz by collecting the first diffraction order behind an acousto optical modulator (AOM).

The probe beam is guided into an optical parametric oscillator (OPO) with periodically poled lithium niobate crystal in a ring cavity configuration (*APE, OPO PP Auto*). It supports Fourier limited photon energy conversion into the visible spectrum from 505 nm to 790 nm, by crystal temperature controlled phase matching. The resulting pulse train passes a linear polarizer, followed by a Soleil Babinet

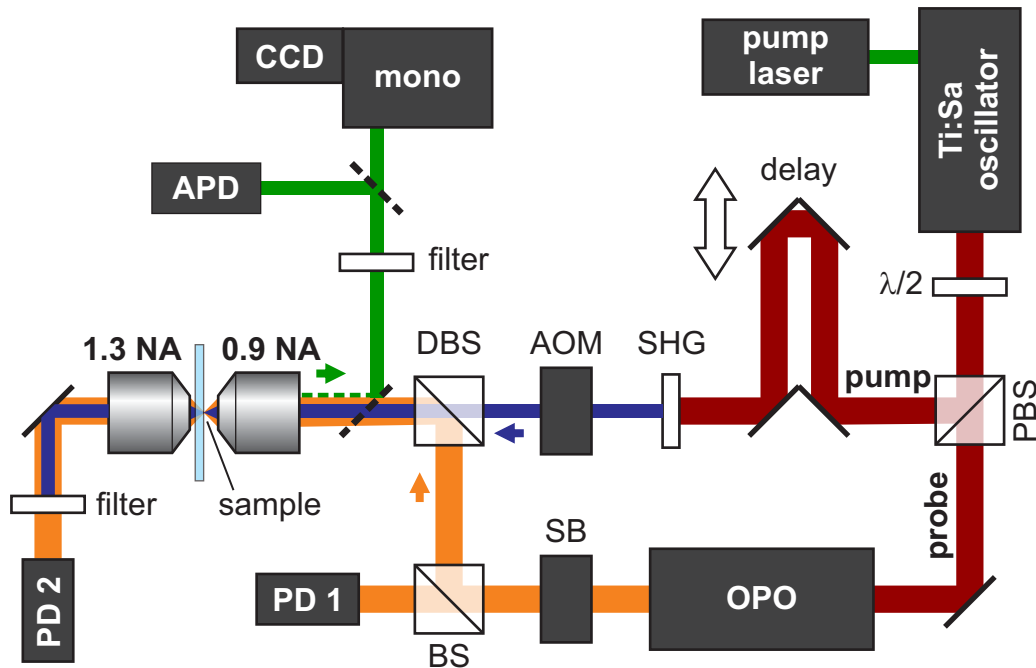


**Figure 2.6**

Ultrafast laser pulses provided by a Ti:Sa oscillator are split into a pump and a probe branch. The pump pulses are temporally shifted with a mechanical delay line and afterwards frequency doubled (SHG) by a BBO crystal. An AOM modulates the pump beam intensity. The probe pulses are frequency converted by an OPO and cover the visible and NIR spectrum from 520 nm to 740 nm. Pump and probe beam are superimposed with a dichroic beam splitter (DBS) before they are focused through a microscope (NA 0.9) onto the sample. The transmitted light is collected by a high NA oil immersion objective and filtered afterwards to suppress the modulated pump pulses. Additional noise reduction is achieved using a balanced detection scheme. The implemented microscope (represented by the NA 0.9 objective) together with the attached APD and monochromator allows dark-field and time resolved photoluminescence measurements in reflection.

Compensator (SB) which allows an almost loss-less definition of the probe polarization. For the balanced detection we separate 50% of the probe beam intensity by a beam splitter (BS) and collect a reference signal at the photo detector (PD1).

After their preparation, both pulse trains are superimposed by the dichroic beam splitter (DBS). We use an *AHF Beamsplitter 460 DCSPXR-UV*, which efficiently reflects the probe pulses in the range from 440 nm to 740 nm. The pump pulse transmission strongly depends on the chosen wavelength. While the fundamental Ti:Sa output shows transmission above 90%, the frequency doubled pulses in the near UV have higher but still tolerable losses. The collinear pulse trains pass an implemented dark-field microscope and are focused by a high NA objective (*Olympus MPlanFL (N) 100x/0.90 BD P*) onto the sample. A closed loop 3D piezo scanner (*Piezosystem Jena*) allow the accurate positioning of the desired nanoobject in the Abbé limited foci. The transmitted light is collected by a cover glass corrected 1.3 NA oil immersion objective. To extinguish the modulated pump pulses, we use the *AHF - Edge Basic 488 LP* long pass filter for the frequency doubled, or *AHF - RazorEdge SP 785 RS* short pass filter for the pump pulses at 795 nm. The transmitted probe intensity is measured by the photo detector PD2 of the balanced detector (*Femto - OE100*). Its differential output PD2 - PD1, of the signal and reference path, compensates intensity fluctuations of the laser on low frequencies. An internal low-noise amplifier increases the signal by seven orders of magnitude which is fed into lock-in amplifier (*Stanford Research SR830*). This reduces the noise by narrowband Fourier filtering.

### *Noise limitations*

Incoherent noise has various sources, for example laser intensity fluctuations or mechanical movement. In frequency domain, they appear on different frequency scales with characteristic distributions as for example the 1/f noise. The implemented lock-in technique, operated at 22.5 kHz, eliminates highly efficient the noise outside a narrow bandwidth that depends on the integration time. In advance, the balanced detector reduces low frequency noise and supports the fourier filtering by signal preparation. However, shot-noise cannot be overcome and is the overall limiting noise.

Shot-noise exists due to the quantized nature of detected photons and electrons. The noise width  $\sigma_{SN}$  for a photodiode, which measures the overall energy of absorbed photons per second  $P_{det}$ , is calculated by

$$\sigma_{SN} = \sqrt{2\Delta\nu_{BW} \cdot P_{det} \cdot \frac{h c_0}{\lambda}} \quad (2.43)$$

with  $\Delta\nu_{BW} = \frac{5}{64 \cdot \tau_{int}}$ .

with  $h$ ,  $c_0$  and  $\lambda$  being the Planck constant, the vacuum speed of light and the measured wavelength. Further,  $\Delta\nu_{BW}$  is the noise equivalent bandwidth for a slope

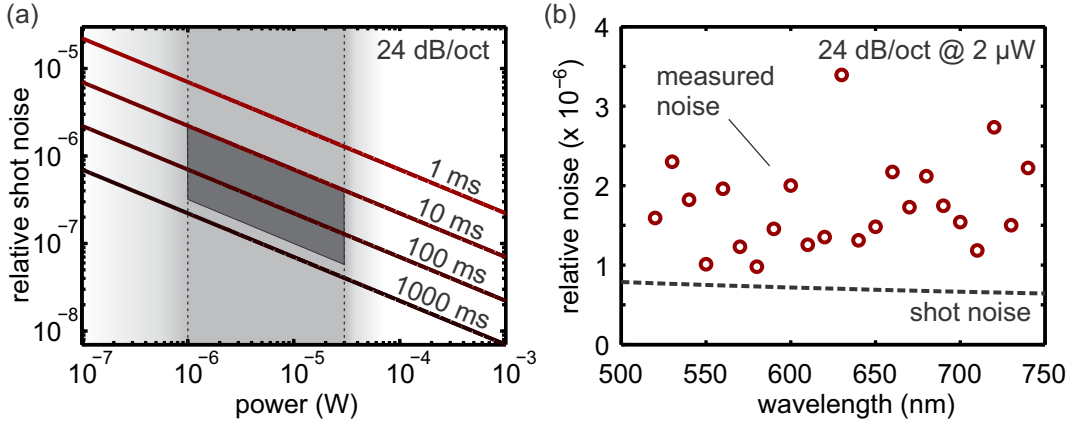


**Figure 2.7**

(a) Calculated relative noise of the lock-in amplifier as function of the time-averaged laser power for different integration times. (b) Measured noise as a function of wavelength, with 50 ms integration time and 2  $\mu\text{W}$  power at the detector. We find a shot noise limited behavior over the whole spectral range.

of 24 dB/oct as used in the experiment, and depends on the integration time  $\tau_{int}$  of the lock-in amplifier [82]. Since  $\sigma_{SN}$  depends on the detector power  $P_{det}$ , we write

$$\begin{aligned}\sigma_{relSN} &= \frac{\sigma_{SN}}{P_{det}} \\ &\propto \sqrt{P_{det}}^{-1} \\ &\propto \sqrt{\tau_{int}}^{-1}\end{aligned}\tag{2.44}$$

and obtain the relative noise, limiting our experimental resolution. As shown by equation 2.44, shot noise reduction at a fixed photon energy ( $h c_0/\lambda$ ) can be achieved by either increasing the integration time or the laser power. Figure 2.7(a) shows the theoretical shot noise limit of our experiment at 630 nm wavelength as function of detected laser power and for the integration times of 1, 10, 100 ms and 1000 ms. The light grey marked interval shows the probe power limitations in our experiment. Here, the upper limit is given by the sample destruction or its ending linear behavior. The lower value is open but actually limited by the expected signal to noise ratio. Furthermore, integration times between  $\approx 10$  ms and 500 ms have to be applied where setup and sample stability limits the overall measurement time and thus the integration time of each pixel. As a consequence of these limitations, the typical operating parameters of our experimental setup are indicated by the dark grey area.

In order to prove a shot-noise limited setup, we compare the theoretical limit with experimental data presented in chapter 5. There we use a lock-in integration time of 50 ms and measure a probe power at the detector of 2  $\mu\text{W}$ . The red circles in figure 2.7(b) show the determined relative noise as function of probe wavelength.

The dashed black curve marks the theoretical shot noise limit at the different wavelengths. We find an almost shot-noise limited experiment. The slightly higher noise of the setup can be explained by the two diodes of the balanced detector.

### *Spectral and temporal performance*

The finite lengths of the pump and probe pulses blur the desired temporal information in the experiment. Consequently, the time resolution of incoherent measurements is limited by the width of the convolution

$$I_{conv}(t) = \int_{\tau} E_{pump}(\tau)^2 E_{probe}(t - \tau)^2 d\tau , \quad (2.45)$$

of pump and probe pulse intensity. Under the assumption of Gaussian shaped envelope intensities

$$E_{pulse}^2(t) \propto \exp\left(\frac{-t^2}{2 \cdot \sigma_{pulse}^2}\right)^2 , \quad (2.46)$$

of  $E_{pump}(t)$  and  $E_{probe}(t)$ , equation 2.45 is written to

$$I_{conv}(t) \propto \exp\left(\frac{-t^2}{2 \cdot \sigma_{conv}^2}\right) \quad \text{with} \quad \sigma_{conv} = \sqrt{\sigma_{pump}^2 + \sigma_{probe}^2} . \quad (2.47)$$

For the excitation pulse we choose between the fundamental (794.4 nm) and frequency doubled (397.4 nm) Ti:Sa output. Figure 2.3.1(a) shows the spectra of both, measured in front of the focusing objective. We determine a bandwidth  $\Delta\nu$  of 2.5 GHz for the fundamental output. From the time-bandwidth product

$$\Delta\nu \cdot \Delta t \geq 0.441 \quad (2.48)$$

for Gaussian shaped pulses, with  $\Delta t$  being the pulse duration, we calculate the Fourier limited pulse duration to 176 fs at the fundamental wavelength. In addition, we directly measure the pulse duration  $I_{pump}(t) = E_{pump}(t)^2$  of the fundamental Ti:Sa output with an autocorrelator. The measured FWHM of the coherent nonlinear autocorrelator function intensity

$$I_{ACF}(t) = \int_{\tau} |(E_{pump}(\tau) + E_{pump}(t - \tau))^2|^2 d\tau \quad (2.49)$$

is 200 fs. From equation 2.47, the deconvolution factor for Gaussian pulses is  $1/\sqrt{2}$ , resulting in a measured pump pulse duration of 141 fs. The comparison with the Fourier limited pulse duration implies a small deviation from the assumed Gaussian shape but can be neglected in our experiments. For the second harmonic pump pulses we assume slightly shorter pulse durations due to the involved nonlinear process.

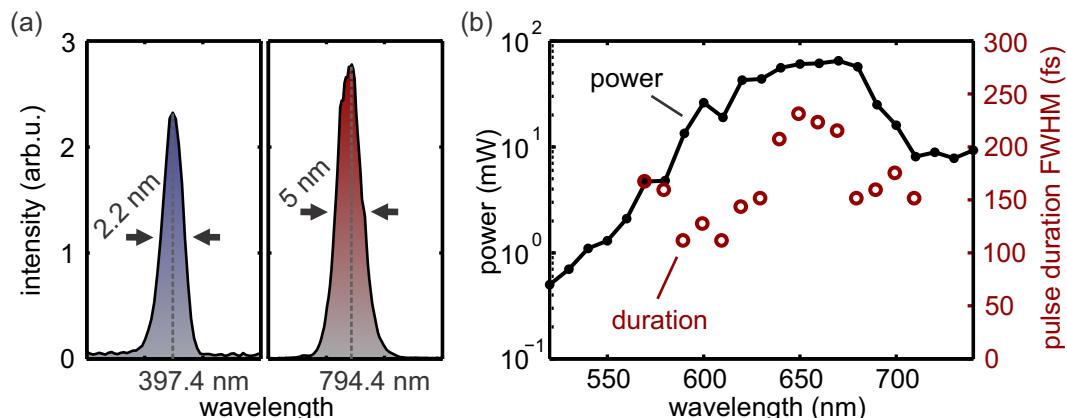


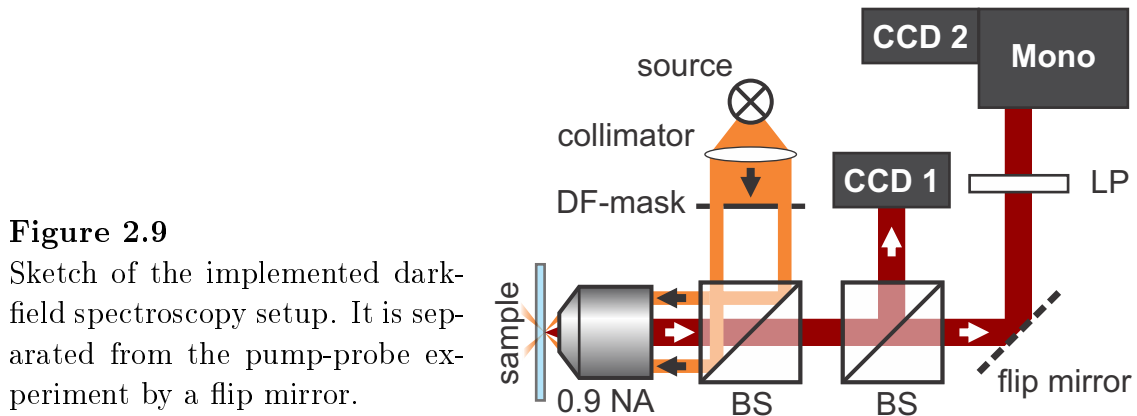
**Figure 2.8**

(a) **Pump:** Ti:Sa laser emission spectrum with sub 150 fs pulses (794.4 nm) and its corresponding second harmonic spectrum (397.4 nm) on different intensity scales. (b) **Probe:** Wavelength dependent output power and pulse duration of the OPO, pumped with the fundamental Ti:Sa output of a constant crystal temperature of 7°C.

In analogy, we analyze the probe pulses as function of wavelength. Figure 2.3.1(b) depicts the measurement results. The red circles show the pulse durations, the black curve the average OPO output power. For wavelengths below 570 nm and above 710 nm the weak autocorrelation signal prevents the extraction of accurate durations. Within the measured range, we find an average probe pulse length of 165 fs. All measurements are performed at a constant crystal temperature of 7°C as used in the experiment. We resign on crystal temperature adaptation due to the long stabilization time, leading to long term drifts of the setup or mode hopping during a scan if the equilibrium state is not fully reached. Finally, to approximate the temporal resolution of the experimental setup, we apply equation 2.47 to calculate the FWHM of the integral of equation 2.45. Under the assumption of Gaussian shaped laser pulses the temporal resolution is determined to  $\approx 215$  fs (NIR pump).

### 2.3.2 Dark-field spectroscopy

Dark-field microscopy and spectroscopy are powerful methods to investigate the scattering properties of even smallest objects. Due to the characteristic sample illumination we obtain a background free image where only scattered light is collected. This offers the possibility of long integration times without saturating highly sensitive detectors and allows the localization of objects of a few tens of nanometers in size. In addition, the scattering spectrum contains information about the nanoobject itself. Thus, dark-field spectroscopy in combination with numerical models offers a fast method for the characterization, and optimization of plasmonic nanos-



structures. A sketch of the implemented dark-field setup is depicted in figure 2.9. The microscope is a slightly modified *Olympus BXFM system-microscope*. Both beam splitters (BS) are mounted movably and can be removed from the optical path of pump-probe or photoluminescence measurements. A halogen lamp serves as unpolarized light source, emitting from the near-UV up to the near-IR. After collimation, the beam profile is shaped by the typical dark-field aperture. The light-beam is focused with the same high NA dark-field objective, which is used in the other experiments. Due to the characteristic illumination, only backscattered light is collected and transmitted through the first beam splitter. CCD 1 is used to find the sample region of interest in dark-field or bright-field configuration. For more sensitive measurements, the second beam splitter is removed and the full backscattered light is guided into the spectrometer (*Princeton Instruments - Acton SP-2150*). An optional linear polarizer (LP) allows polarization resolved analysis. The spectrometer (Spec) is equipped with a mirror for imaging and a grating (300

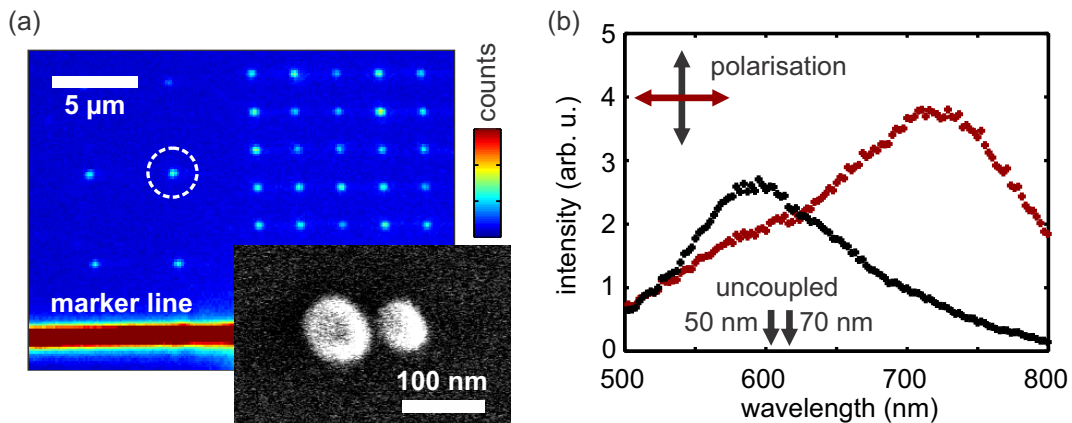


**Figure 2.10**

(a) Dark field image of an array of gold disk pairs. The inset shows the SEM image of the marked disk pair with a 50 nm and a 70 nm disk, separated by 15 nm. Marker lines help to identify the individual pairs on the large glass substrate. (b) Polarization dependent dark-field spectra of the marked disc pair. The black arrows indicate the measured resonances of another single 50 nm and 70 nm disc.

grooves/mm and 500 nm blaze) for spectral analyses. The attached liquid nitrogen cooled backplane illuminated CCD (1340 px  $\times$  400 px) records the image or spectrum respectively. In the used configuration, the setup covers a spectral range of  $\approx 350$  nm in a single exposure and a spectral resolution of  $\approx 0.26$  nm.

Figure 2.10 shows a measurement performed with the dark-field setup. The sample consists of periodic arrays of gold disk pairs as further discussed in chapter 4. Markers help to identify the disk pair of interest as presented in the dark-field image 2.10(a), measured with the nitrogen cooled CCD. The inset shows an SEM image of the structure, highlighted by the white circle in the array. The larger disk has a diameter of 70 nm, the smaller one of 50 nm. Both have a height of 30 nm and are separated by 15 nm, promising strong near field coupling and polarization dependent plasmon hybridization. Graph 2.10(b) shows the scattered spectra along the symmetry axis of the structure (red) and perpendicular to it (black). For comparison, the plasmon resonances of a single 70 nm and 50 nm disc are marked on the wavelength axis of the graph. We find the expected behavior of plasmon hybridization (see section 4.5.2 for more details).

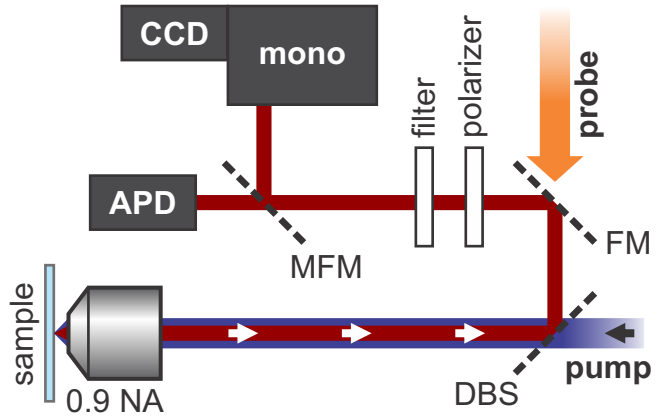
### 2.3.3 Photoluminescence lifetime and single photon counting

After a photon is absorbed by a material, its energy can dissipate via several non-radiative ( $\Gamma_{nrad}$ ) and radiative ( $\Gamma_{rad}$ ) decay channels. Photoluminescence is the spontaneous emission of a photon from a dipole allowed transition and carries information about the emitter system. Semiconductor nanostructures, as presented in chapter 5, show emission around their excitonic ground state or band-gap energy. Similar to dark-field microscopy, the spectrally resolved photoluminescence method is an almost background free measurement technique with the opportunity of long integration times without background noise or detector saturation. This allows the localization and even characterization of single nanoobjects with small absorption and scattering cross sections.

A sketch of the implemented photoluminescence setup is shown in figure 2.11. We use the frequency doubled Ti:Sa output as excitation pulses ( $\lambda \approx 390$  nm), shown in figure 2.3.1(a). In analogy to the pump-probe experiments, the pulse train is transmitted through the dichroic beam splitter (DBS) and focused with the high NA objective. The redshifted photoluminescence photons are collected by the same objective and efficiently reflected by the DBS for wavelengths between 440 nm and 740 nm. A flip mirror reflects the luminescence beam in direction of the monochromator (Mono) and single photon counting avalanche photo diode (APD). The advantage of the configuration is a fast switching between pump-probe and photoluminescence measurements by flipping only one mirror. Before entering the detection hardware, remaining pump photons are suppressed by a bandpass. An optional linear polarizer allows polarization dependent photoluminescence measurements. A motorized flip mount (MFM) directs the remaining photons into the avalanche photodiode with

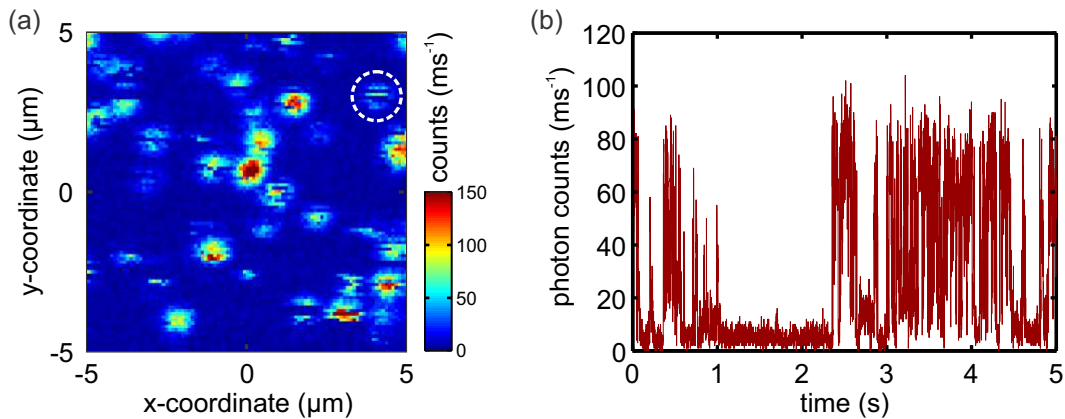
**Figure 2.11**

Sketch of the implemented photoluminescence setup. A flip mirror (FM) directs the luminescence photons to the detection hardware. A motorized flip mirror (MFM) allows the fast switching between a single photon counting photodiode with connected lifetime analyzer and a monochromator.



attached *PicoHarp*, which supports time-correlated single photon counting. The spectrometer allows the measurement of photoluminescence spectra. The switching between APD and spectrometer works fast and reproducible without the need of readjustment.

In order to test the performance of the photoluminescence setup, we measure individual CdSe nanocrystals, randomly distributed on the glass substrate. The core-shell quantum dots are spherically shaped and have a diameter of roughly 5 nm. Quantum confinement leads to discrete states with the ground state absorption peak around 600 nm. Figure 2.12(a) shows a  $10 \mu\text{m} \times 10 \mu\text{m}$  scan over the sample surface. The background count rate is on the order of  $\approx 3.5$  counts/ms and comes from the substrate and leftovers of solvent (Toluene). For comparison, the dark-count rate is  $\approx 0.05$  counts/ms, measured with an open optical path to the APD but without pumping. The 2D luminescence map shows Abbé limited signals of different

**Figure 2.12**

(a) Photoluminescence map of a test sample with CdSe nanocrystals. (b) Photoluminescence counts of the marked nanocrystal over 5 s and 1 ms resolution. The blinking behavior proves the ability of single nanocrystal photoluminescence measurements.

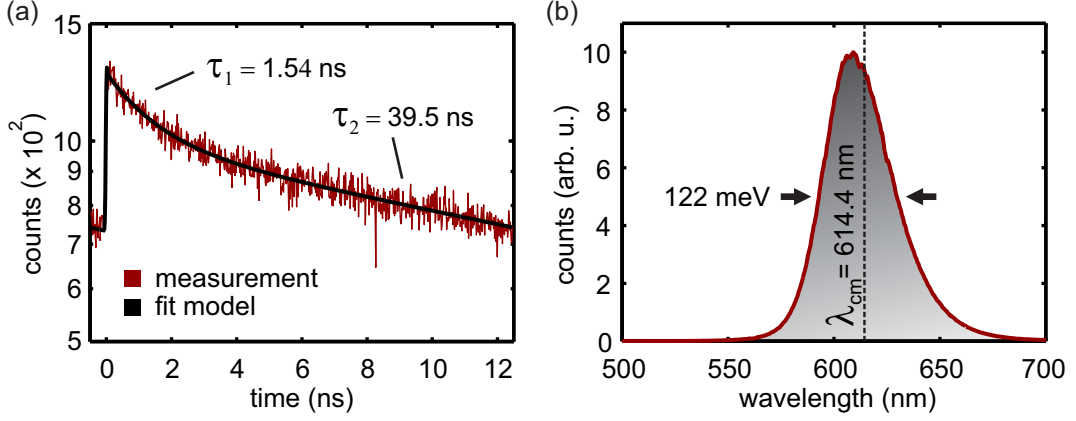


**Figure 2.13**

(a) Time-resolved photoluminescence measurement of the single nanocrystal presented in figure 2.12. The fitting model including the APD response and a biexponential decay shows a very nice agreement. (b) Photoluminescence spectrum with the center of mass at 614.4 nm and a width of 122 meV.

amplitudes. We find blinking for the signals with lower intensity, indicated by dark lines crossing the spots. The photoluminescence emission of the marked signal is measured over 5 seconds with a temporal resolution of 1 ms and plotted in 2.12 (b). We observe a clear blinking behavior between two excitonic states, a fast decaying bright transition, and a long living trapped state which blocks the quantum-dot emission. Furthermore, we measure the luminescence lifetime with 16 ps resolution as shown in figure 2.13(a). The high repetition rate of 76 MHz of the laser system limits the measurable photoluminescence time to 13.2 ns. Counts at negative times arise from leftovers of the previous excitation. To model the actual photoemission function  $c_{QD}(t)$  we consider a detector response function  $r_{det}(t)$ , dark-counts containing the substrate background  $c_{dark}$  as well as pump pulse leakage  $c_{leak}$ . For the detector response we assume the normalized Gaussian distribution

$$r_{det}(t) = \exp\left(\frac{-t^2}{2\sigma_{det}^2}\right) \quad (2.50)$$

with  $\sigma_{det} = 21.2$  ps, corresponding to a  $FWHM_{det} = 50$  ps. The laser leakage has a temporal length of  $\approx 150$  fs and is described by a delta peak  $c_{leak}$  at  $t = 0$  ns. It is included in the overall decay function  $c(t) = c_{leak} + c_{QD}$  together with a biexponential function  $c_{QD}$  to describe the quantum dot photoluminescence response from two uncorrelated emitting states. The final fitting function

$$c_{fit}(t) = c_{dark} + \dots \int_{\tau} (c_{leak} + c_f \exp(-\tau \Gamma_f) + c_s \exp(-\tau \Gamma_s)) \cdot r_{det}(t - \tau) d\tau \quad (2.51)$$

is the convolution of the overall decay function  $c(t)$  and detector response function  $r_{det}(t)$  on a constant background  $c_{dark}$ . As fit result we obtain the background count

rate  $c_{dark}$ ,  $c_f$  and  $c_s$  as the fast and slow decay amplitudes, and  $\Gamma_f$  and  $\Gamma_s$  the fast and slow decay rates. For the presented quantum dot we find a fast decay component with  $\tau_f = \Gamma_f^{-1} = 1.5$  ns, observable within the first nanoseconds, and a slowly decaying component with  $\tau_s = \Gamma_s^{-1} = 39.5$  ns. The contribution of the slowly decaying component ( $c_s$ ) is three times larger than the fast decaying one ( $c_f$ ). Finally, we measure the luminescence spectrum of the nanocrystal. Figure 2.13(b) shows the spectrum for an exposure time of 240 seconds. The broad emission spectrum with FWHM = 122 meV is characteristic for room temperature measurement, where the emission linewidth is broadened by exciton-phonon scattering.

A single particle in a potential is described by the Schrödinger equation, and shows quantized behavior for strong confinement. Nanoobjects consisting of a few hundred to a few hundred thousand atoms fill the gap between atomistic and bulk behavior and increase in complexity. Ab-initio calculations offer an atomistic approach to approximate the electronic and thus optical properties of nanostructures but are limited by the number of considered atoms due to the enormous computation effort [83]. Particle plasmons also show quantized behavior but as fully classical phenomena described by Maxwell's equations. Only on lengthscales below  $\approx 5$  nm, the quantum character must be taken into account to describe surface or tunneling effects, for example by time dependent density functional theory (TDDFT) [84–86]. As a consequence of the different behavior and physical descriptions, the theoretical prediction of nanoscopic light-matter interaction is challenging if we consider coupling of several different sized nanoobjects or systems. However, all investigated plasmonic nanoobjects in this work are above 10 nm in size with surface distances larger than the quantum tunneling regime so that their interaction with light can be computed by solving Maxwell's equations [87]. In cases of semiconductor nanostructures the quantum character must be taken into account. In order to model their interaction with plasmonic systems, we separately solve the Schrödinger equation for the subsystem and implement its quasi classical properties into the model. Neglected effects will be discussed in the corresponding chapters.

Mie theory gives the full analytic solution of classical Maxwell's equations for a plane wave scattered by a spherical object of arbitrary size and material [55]. This contains the complex electromagnetic field in- and outside the scatterer as well as spectral information of scattering, absorption, and extinction cross section. However, already the inclusion of an additional interface, for example the substrate under a spherical nanoparticle, makes the solution no longer valid. Effective medium theory can partially approximate the spectral response but not the local electromagnetic field distribution [88]. At the latest when the quantitative calculation of the optical response of arbitrarily shaped or coupled structures is necessary, numerical techniques have to be applied. Computational electromagnetics offer a wide range of different integral (DDA, MMP, ... ) and differential (FEM, FDTD, ...) equation solvers to compute the desired electromagnetic field distribution [89–92]. However, not all fulfill the requirements of non-periodic coupled nanoobjects and complex geometries. Especially structures in close vicinity with different size, shape and rounded edges due to the fabrication technique demand a good discretisation of space by flexible meshing. The finite element method in frequency domain gives

access to all relevant physical values and allows meshing based on tetrahedral, cubic or combined building blocks [92]. In the following we briefly introduce the fundamentals of the Finite-Element-Method and the implementation of Maxwell's equations. Different models are discussed in order to compute the linearly scattered field (sec. 3.2) or total field distribution (sec. 3.4) under various conditions. In section 3.3 we introduce our model to predict the nonlinear optical response of complex plasmonic structures. The constitutive relations of the electric displacement field and magnetic flux in their most general form are implemented and discussed in section 3.5. The model allows the calculation of chiral and optically active behavior without an approximation via the permittivity tensors.

### 3.1 FINITE ELEMENT METHOD (FEM)

#### 3.1.1 Fundamentals

The mathematical problem is described by a set of partial differential equations (PDE) in a given boundary value problem. The finite element method is a numerical technique to approximate the solution  $\Psi_{Gl}(\mathbf{x})$  for the given system with the degrees of freedom  $\mathbf{x}$  [93]. After transformation into a minimization problem, for example known from the theory of Euler Lagrange, stationary solutions of the system are given by the local extrema. In order to find them, the system is disassembled into  $n$  subdomains

$$\Psi_{Gl}(\mathbf{x}) = \bigcup_{i=1}^n \psi_i(\mathbf{x}) \quad , \quad (3.1)$$

with  $\psi_i$  being the finite elements. In contrast to the commonly used Finite-Difference-Time-Domain method (FDTD), these elements are relatively flexible in shape, orientation and size within the same model. In addition, FEM offers the continuous solution in the whole simulation space and is not limited to discrete meshpoints. The local solution of each element is composed by a linear superposition

$$\psi_i(\mathbf{x}) = \sum_{k=1}^m a_{k,i} \cdot \Phi_{k,i}(\mathbf{x}) \quad (3.2)$$

of  $m$  base functions  $\Phi_k$ , being linearly independent, differentiable and fulfilling the boundary conditions. In order to minimize the error function and approximate  $\Psi_{Gl}(\mathbf{x})$ , different variational methods for the coefficients  $a_{k,i}$  can be applied. For example, if we consider the boundary value problem

$$\nabla^2 \psi(x) - b(x_0) = 0 \quad (3.3)$$

with  $b(x_0)$  being the boundary condition and plug in the discussed ansatz, we find as error the so called residue

$$R = \nabla^2 \Psi_{Gl}(\mathbf{x}) - b(x_0) \quad . \quad (3.4)$$

The elements have to fulfill the boundary conditions of its neighbors. In the Galerkin method, the residue is multiplied with test functions  $\theta_j$  and integrated over the solution space

$$\int_V (\nabla^2 \Psi_{Gl}(\mathbf{x}) - b(x_0)) \cdot \theta_j dV = 0 \quad , \quad (3.5)$$

leading to a linear equation system for the unknown coefficients  $a_{k,i}$  of the overall solution. For a good set of testfunctions  $\theta_j$ , a sparse matrix is obtained and reduces the required computation power [93]. In this work we use the software package *Comsol Multiphysics* as FEM solver, which contains a pre-processor, the FEM-solver with implemented equation system, and a simple post-processor [89]. A Matlab interface allows almost unrestricted data processing.

### 3.1.2 Formulation of Maxwell's equations

In 3-D vector notation, the time dependent Maxwell's equations in their differential form are given by the equations 2.1- 2.4. By transforming them into a diffusion equation, the required minimization formulation is achieved. The ansatz

$$\mathbf{E}(\mathbf{r}, t) = \mathbf{E}(\mathbf{r}) \cdot \exp(i\omega t) \quad (3.6)$$

separates the spatial and temporal component and the diffusion equation in Helmholtz representation can be written as [47, 94, 95]

$$\nabla \times \frac{1}{\mu_r(\mathbf{r})} (\nabla \times \mathbf{E}(\mathbf{r}, \omega)) - \frac{\omega^2}{c_0^2} \left( \epsilon_r(\mathbf{r}) - \frac{i \cdot \sigma(\mathbf{r})}{\omega \cdot \epsilon_0} \right) \mathbf{E}(\mathbf{r}, \omega) = 0 \quad (3.7)$$

with  $\mu_r$ ,  $\epsilon_r$ , and  $\sigma$  being the relative permeability, permittivity and the conductivity as functions of frequency  $\omega$  and position  $\mathbf{r}$ . As a consequence of the separation ansatz, the complex electric vector field  $\mathbf{E}(\mathbf{r}, \omega)$  has to be calculated separately for each frequency  $\omega$ . Furthermore it can be useful or even necessary to separate the purely scattered field  $\mathbf{E}_{scat}(\mathbf{r}, \omega)$  and the excitation field  $\mathbf{E}_{back}(\mathbf{r}, \omega)$ . The total field  $\mathbf{E}(\mathbf{r}, \omega)$  is defined as the superposition

$$\mathbf{E}(\mathbf{r}, \omega) = \mathbf{E}_{scat}(\mathbf{r}, \omega) + \mathbf{E}_{back}(\mathbf{r}, \omega) \quad (3.8)$$

of both fields. Plugged into equation 3.7, the boundary value problem changes and the scattered vector field components directly become the independent variables [96]. In addition, numerical errors are reduced since the known background field is not part of the solution and does not suffer from its computation.

## 3.2 SCATTERED FIELD COMPONENTS AS INDEPENDENT VARIABLES

### 3.2.1 Isolated nanostructures

The wavefront in the focal plane of a high NA objective is approximated by a plane wave with wavenumber  $k = n \cdot 2\pi/\lambda_0 = n \cdot \omega/c_0$ . This is valid for structure sizes much smaller than the applied wavelength, where the superposition of many  $k$  components, symmetrically distributed around the optical axis, shows an almost constant spatial phase over the whole nanoobject. Further we follow the ansatz of equation 3.8 to calculate the scattered electric field  $\mathbf{E}_{scat}$  in frequency domain and an effective medium ( $n_{eff}$ ) approach. The used background field  $\mathbf{E}_{back}(\mathbf{r}, \omega)$  with perpendicular incidence is given by the plane wave

$$\mathbf{E}_{back}(\mathbf{r}, \omega) = \begin{pmatrix} E_{x,0} \\ E_{y,0} \\ 0 \end{pmatrix} \cdot \exp\left(-i \cdot n_{eff} \cdot \frac{\omega}{c_0} \cdot z\right) \quad , \quad (3.9)$$

propagating in negative z-direction. Linearly, circularly and elliptically polarized illumination is defined by the complex values of  $E_x$  and  $E_y$  with

$$E_0 = \sqrt{|E_{x,0}|^2 + |E_{y,0}|^2} \quad (3.10)$$

being the excitation field amplitude and

$$\alpha = \arctan\left(\frac{E_{y,0}}{E_{x,0}}\right) \quad \text{with} \quad E_x, E_y \in \mathbb{R} \quad (3.11)$$

the polarization angle for linearly polarized light. In case of an effective medium  $n_{eff}$  with spherical scatterer, the system allows the comparison with analytical Mie theory. A more generalized background field including a substrate is discussed in the following subsection 3.2.2. More complex systems where the separation of the background field is almost impossible are discussed in the sections 3.4 and 3.5.

Figure 3.1 depicts a cut through the model geometry to compute the electromagnetic scattering of an isolated nanostructure with arbitrary shape in an effective medium. The spherical scatterer (SC) is located in the model center, surrounded by various shells, forming the environment (light blue) and integration surface (IS). Further, the model is closed by perfectly matched layers (PML) with spherical wave scattering conditions  $\mathbf{k}_{dir}(\mathbf{r}) = -\mathbf{n}(\mathbf{r})$  at the outer PML surface. Consequently, remaining fields are directed outwards, parallel to the surface normal  $\mathbf{n}$ . For analysis, we include a permeable integration sphere (IS), providing a well defined and meshed surface outside the near-field. If possible, the model can be split along its symmetry axis, to reduce computation time and increase the accuracy of the solution. Real and imaginary part of the dielectric function of  $\epsilon_r(\omega)$  are given by the data of Johnson and Christy [49] or other databases [50], the one of the effective medium by

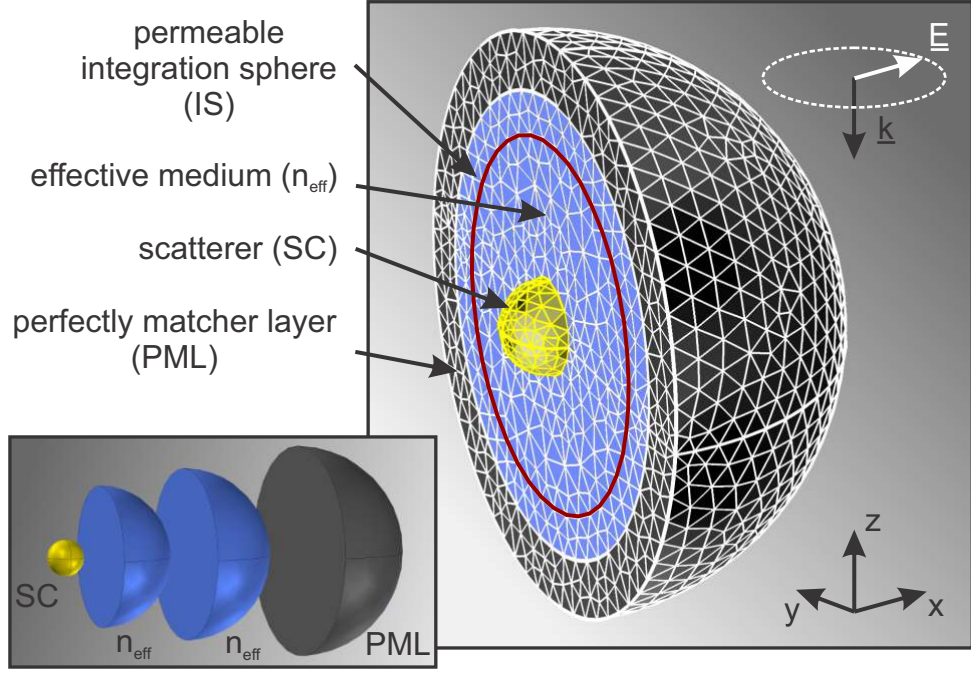


**Figure 3.1**

Cross section through the geometric constitution of the Mie scattering model. The spherical scatterer (SC) with 50 nm in radius is located in the center. It is surrounded by a spherical shell and refractive index  $n_{eff}$ . The model is limited by perfectly matched layers and scattering boundary conditions at the outer surface. A meshed permeable integration sphere (IS) within the effective medium allows the calculation of the scattering and absorption cross section.

equation 2.7. We use the *parallel direct sparse solver interface method (PARDISO)* as direct solver or the *generalized minimal residual method (GMRES)* as indirect solver. Their accuracy and computation time, especially for the iterative solver, strongly depend on the spatial discretisation. Here, we typically use free tetrahedral meshing with an overall number of elements between  $5 \cdot 10^4$  to  $9 \cdot 10^4$ .

In the following we consider a spherical gold nanoparticle with 50 nm radius in an effective medium environment with  $n_{eff} = 1.4$ . The PML shell radius ranges from 300 nm to 350 nm, the integration sphere (IS) is defined outside the near-field at 250 nm. As background field we use equation 3.9 with  $E_x = 1$  V/m and  $E_y = 0$  V/m. Figure 3.2 shows the imaginary part of the separated complex field components for an excitation wavelength of 585 nm. The background wave shown in figure 3.2(a) propagates from left to right with a polarization in the plotted x-z-symmetry plane. In the hot spots of the scattered near field (b) we observe a six times higher field amplitude than in the excitation field. With equation 3.8 we obtain the total field distribution  $E_x$  as superposition of the separated fields as shown

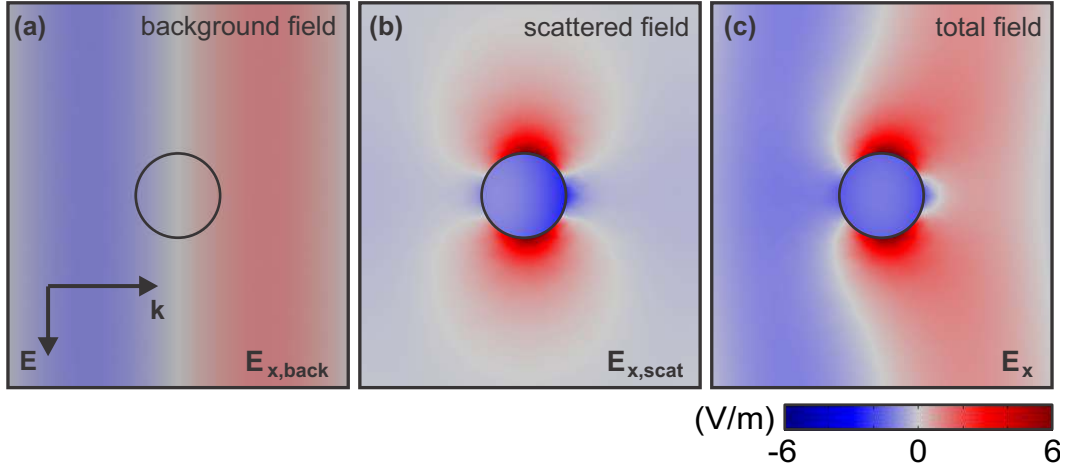


**Figure 3.2**

Electric field distribution of background (a), scattered (b) and total field (c), plotted in an area of  $600 \times 600$  nm in the x-z symmetry plane. All graphs show the imaginary part of the x-component for an excitation wavelength of 585 nm. The scattered near-field distribution (b) reveals high field amplitudes, known as plasmonic hot spots.

in (c). In order to calculate  $C_{abs}$ ,  $C_{scat}$ , and  $C_{ext}$  (see subsection 2.1.2), we consider the energy flux density  $\mathbf{S}(\mathbf{r}, t)$  given by equation 3.12. The separation of spatial and temporal components allows the transformation into a time independent and time dependent term as shown in eq. 3.14 [47].

$$\mathbf{S}(\mathbf{r}, t) = \mathbf{E}(\mathbf{r}, t) \times \mathbf{H}(\mathbf{r}, t) \quad (3.12)$$

$$= \text{Re} [\mathbf{E}(\mathbf{r}, \omega) \cdot e^{i\omega t}] \times \text{Re} [\mathbf{H}(\mathbf{r}, \omega) \cdot e^{i\omega t}] \quad (3.13)$$

$$= \frac{1}{2} \text{Re} [\mathbf{E}(\mathbf{r}, \omega) \times \mathbf{H}^*(\mathbf{r}, \omega)] + \frac{1}{2} \cdot \text{Re} [\mathbf{E}(\mathbf{r}, \omega) \times \mathbf{H}(\mathbf{r}, \omega) \cdot e^{2i\omega t}] \quad (3.14)$$

The time averaged energy flux density  $\langle \mathbf{S}(\mathbf{r}, \omega) \rangle$  is given by the integral 3.15 over a whole period  $T$ . Due to periodicity, the second term of equation 3.14 vanishes and we obtain eq. 3.16 as the time averaged energy flux.

$$\langle \mathbf{S}(\mathbf{r}, \omega) \rangle = \int_0^T \mathbf{S}(\mathbf{r}, t) dt \quad (3.15)$$

$$= \frac{1}{2} \text{Re} [\mathbf{E}(\mathbf{r}, \omega) \times \mathbf{H}^*(\mathbf{r}, \omega)] \quad (3.16)$$

We implement the Poynting vector components for the scattered field as follows.

$$\langle S_{x,scat}(\mathbf{r}, \omega) \rangle = \frac{1}{2} \cdot \text{Re} [E_{y,scat} \cdot H_{z,scat}^* - E_{z,scat} \cdot H_{y,scat}^*] \quad (3.17)$$

$$\langle S_{y,scat}(\mathbf{r}, \omega) \rangle = \frac{1}{2} \cdot \text{Re} [E_{z,scat} \cdot H_{x,scat}^* - E_{x,scat} \cdot H_{z,scat}^*] \quad (3.18)$$

$$\langle S_{z,scat}(\mathbf{r}, \omega) \rangle = \frac{1}{2} \cdot \text{Re} [E_{x,scat} \cdot H_{y,scat}^* - E_{y,scat} \cdot H_{x,scat}^*] \quad (3.19)$$

The normalized energy flux density through an arbitrary surface with normal vector  $\mathbf{n}(\mathbf{r})$  is given by

$$\langle S_{scat}(\mathbf{r}, \omega) \rangle = \sum_{i=x,y,z} n_i(\mathbf{r}) \cdot \langle S_{i,scat}(\mathbf{r}, \omega) \rangle \quad (3.20)$$

Due to the definition of the normal vector for interior boundaries in Comsol, we correct  $n_i$  if necessary with a sign flip, pointing always into the outward direction on any boundary. In analogy, the Poynting vector  $\langle S_{tot}(\mathbf{r}, \omega) \rangle$  for the total electromagnetic field is defined. A special case is the time averaged energy flux density of the background plane wave, as defined in equation 3.9. It can be simplified to

$$\langle S_{back} \rangle = \frac{1}{2} \cdot E_0^2 \cdot n_{eff} \cdot c_0 \cdot \epsilon_0 \quad (3.21)$$

being space and frequency independent [48]. With the equations for  $\langle S_{tot}(\mathbf{r}, \omega) \rangle$  and  $\langle S_{scat}(\mathbf{r}, \omega) \rangle$  we calculate the total and scattered energy propagating through the permeable integration sphere (IS) by integrating over their surface. The integral normalization via the excitation flux density  $\langle S_{back} \rangle$  leads directly to the absorption and scattering cross sections

$$C_{abs}(\omega) [\text{m}^2] = \frac{1}{\langle S_{back} \rangle} \cdot \iint_{IS} \langle S_{tot}(\mathbf{r}, \omega) \rangle dS \quad (3.22)$$

$$C_{scat}(\omega) [\text{m}^2] = \frac{1}{\langle S_{back} \rangle} \cdot \iint_{IS} \langle S_{scat}(\mathbf{r}, \omega) \rangle dS \quad (3.23)$$

as function of the excitation wave frequency  $\omega$ . An alternative way to determine the absorption cross section is given by

$$C_{abs,diss}(\omega) = \frac{1}{\langle S_{back} \rangle} \cdot \sum_{i=1}^n \underbrace{\iiint_{V_i} Q_{diss}(\mathbf{r}, \omega) dV}_{=P_{i,diss}(\omega)} \quad (3.24)$$

where the *total dissipative loss density*  $Q_{diss}(\mathbf{r}, \omega)$  is integrated over the volumes  $V_i$  of all  $n$  domains within the integration sphere. The result is identical to the surface integral 3.22 but allows to distinguish between the contributions  $P_{n,diss}(\omega)$  of various particles in more complex and coupled nanostructures.

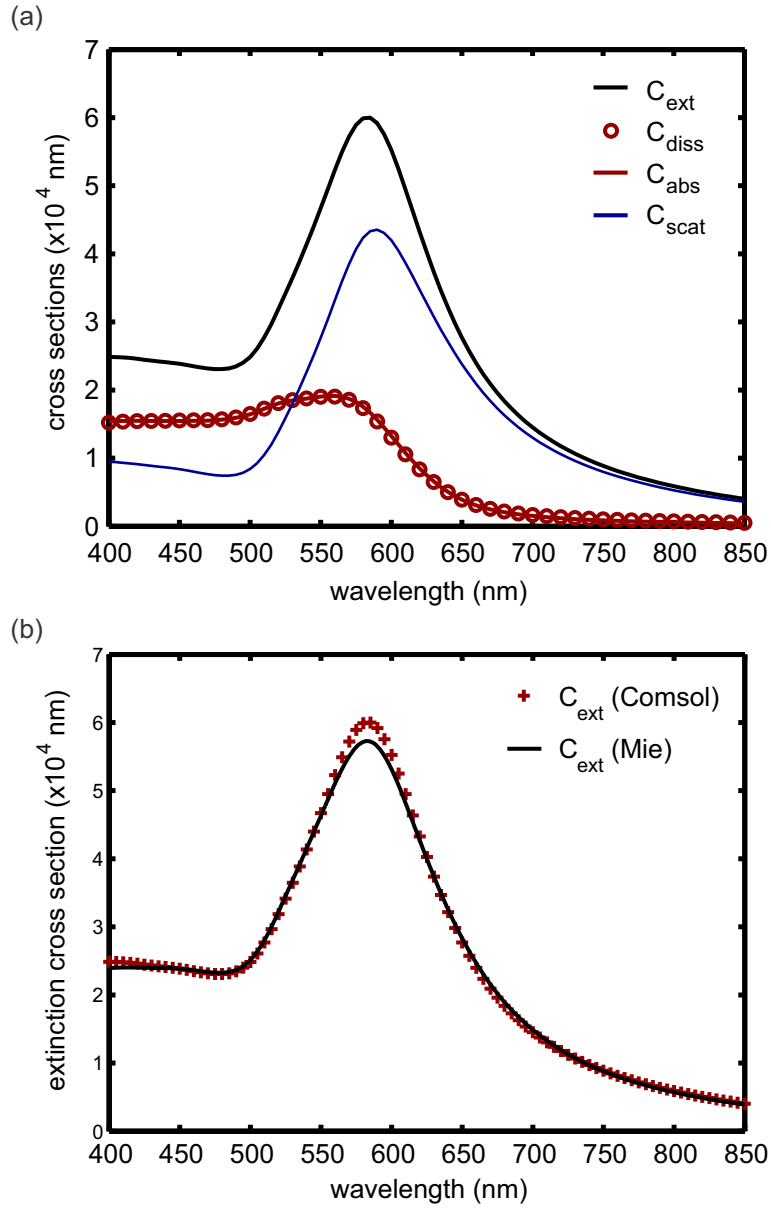


**Figure 3.3**

Results of the FEM simulation of scattering  $C_{scat}$  (blue) and absorption cross section  $C_{abs}$  (red) as a function of the excitation wavelength (a). The red circles show the result of the absorption cross section  $C_{abs,diss}$  on a 10 nm grid, computed by the alternative method of equation 3.24. The extinction spectrum  $C_{ext}$ , computed with the presented model, is compared with a 50th order Mie calculation (b). The results are in excellent agreement.

Figure 3.3(a) shows  $C_{abs}(\omega)$  and  $C_{scat}(\omega)$  in the spectral range from 400 nm to 850 nm in 5 nm steps. For comparison, the red circles are the solutions of equation 3.24 with the gold sphere as only integration domain. They show excellent agreement with the result of eq. 3.22 and energy dissipation in the gold sphere and not in the environment with purely real refractive index. The extinction cross section  $C_{ext}(\omega)$  is calculated as sum of both cross sections and plotted as black curve. Finally, the result of the extinction cross section  $C_{ext}$  calculated with Comsol is compared with a 50th order Mie calculation, following equations 2.20 and 2.21. Both solutions are plotted in figure 3.3(b) and are in excellent agreement. The small deviation around the plasmon resonance can be explained by the non-perfect spherical shape of the gold scatterer, caused by the tetrahedral meshing in Comsol. Consequently the model allows the calculation of the linear properties of arbitrarily shaped nanostructures. However, it can be important to distinguish between the integration over all directions and real experimental conditions, for example given by the numerical aperture of the light harvesting objective. In case of small particles, the scattered light contribution can be almost neglected and transmission experiments are described without taking the objective into account. For larger particles, the scattered field becomes more important and can be no longer neglected. Since the light propagation direction destroys the symmetry at the  $x - y$  plane, reflection and transmission show different behavior. This can be taken into account by splitting the integration sphere into two half spheres. For integrating over a conic section with an opening angle corresponding to the numerical aperture, even the collection properties of certain objectives could be approximated. However, this was never taken into account in the performed simulations.

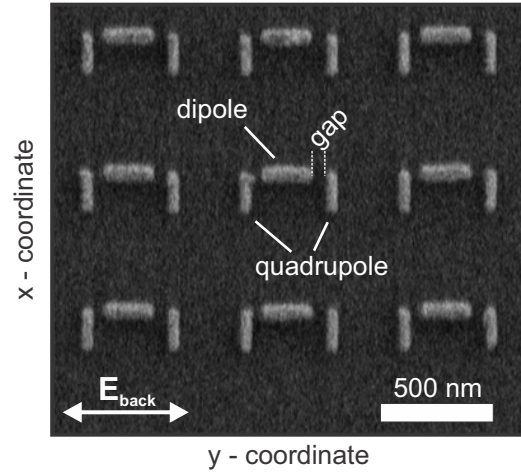
### 3.2.2 In periodic boundary conditions

Metamaterials are artificial large area structures with engineered optical properties [97, 98]. The material usually consist of coupled or uncoupled nanostructures, arranged in a periodic pattern. In addition to many applications, for example filters and polarizers [99, 100], sensors [101], and even cloaking [3, 102], metamaterials can be considered as an ensemble of almost identical nanostructures. Inhomogeneous broadening gives a smoothed or distorted response compared to the single particle, but their experimental investigation is less challenging. In order to simulate the optical response, the structure periodicity must be taken into account. Here, the interaction over several unit cells can lead to grating or far field coupling effects.

Figure 3.4 shows an SEM image of a periodically arranged dolmen type plasmonic nanostructure, consisting of three rod-type elements in the unit cell. The labeling of *dipole* and *quadrupole* is related to the plasmon modes and only reasonable for a far-field excitation, polarized parallel to the long dipole axis. The near-field coupling strength between dipole and quadrupole can be tuned by a symmetric change of the gap distance. As already discussed, metamaterials as particle ensembles can help

**Figure 3.4**

SEM image of a dolmen type plasmonic nanostructure arranged in a periodic pattern. The structure is decomposed into two subdomains called dipole and quadrupole. For the sketched polarisation of the excitation field  $E_{back}$ , dipole and quadrupole form a coupled bright and dark mode plasmonic system. Their electromagnetic coupling strength is defined by their gap distance.



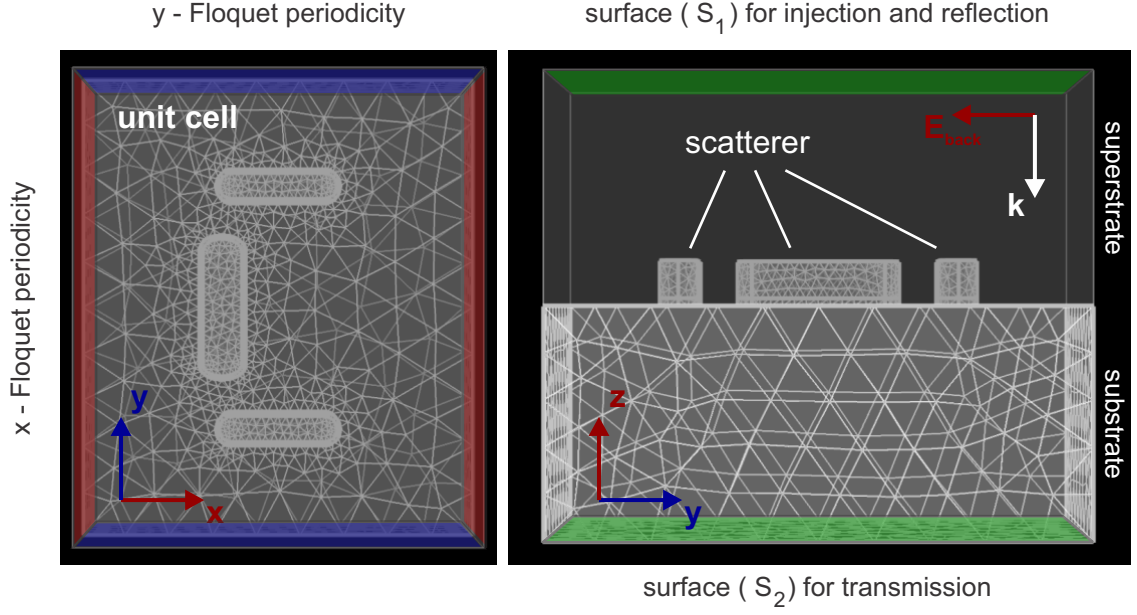
to understand fundamental processes in complex nanostructures. Bernd Metzger uses the shown geometry to investigate third harmonic generation and emission in a coupled bright and dark plasmon system [103], known as the classical analogue of electromagnetically induced transparency (EIT) [30, 104]. In section 3.3 we introduce our theoretical model to compute the polarization resolved nonlinear third harmonic generation, supporting the experimental findings. Here we focus on the linear response of arbitrary nanostructures in periodic boundary conditions, including a substrate interface.

Figure 3.5 depicts the geometric model with centered dolmen (EIT) structure. The top view on the unit cell with 700 nm y-periodicity and 600 nm x-periodicity is shown on the left. We use Floquet periodicity boundary conditions, defined by

$$E_{scat,source}(\mathbf{r}, \omega) = E_{scat,destination}(\mathbf{r}, \omega) \quad (3.25)$$

where source and destination being opposite boundaries, marked red and blue. Thus, each unit cell side-boundary has the field distribution of the opposite side, imitating the neighbor cell. This kind of boundary condition is typical for the combination of plane wave excitation and periodic structure [89]. To achieve continuous conditions, opposite boundaries are identically discretized. The side view on the z-y plane is shown in the right image, with only the structure and substrate being meshed. To include the interface at  $z = 0$  nm we define the complex refractive index of the environment by

$$n(\mathbf{r}) = \begin{cases} n_{sup}, & \text{if } z > 0, \\ n_{sub}, & \text{if } z < 0. \end{cases} \quad (3.26)$$

**Figure 3.5**

Unit cell of the periodic EIT structure in the finite element model. The left figure shows the top view of the x-y-plane. The red and blue boundaries mark periodic boundary conditions with copied mesh-surfaces to obtain a continuous meshing. The structure is located in the center. A side view of the z-y-plane of the model geometry is shown on the right. For visualization, only the scatterers and substrate are meshed. The superstrate - substrate interface is clearly defined. The green areas show scattering boundary conditions and the integration surfaces for injected, reflected, and transmitted energy.

as a function of space. The background field with continuous interface conditions follows Fresnel's equations. For the special case of perpendicular incidence, the field components  $E_{x,back}(\mathbf{r}, \omega)$  and  $E_{y,back}(\mathbf{r}, \omega)$  are written to

$$E_{x \vee y, back}(\mathbf{r}, \omega) = \begin{cases} E_{x \vee y, 0} \cdot \left( \exp\left(-i \cdot n_{sup} \cdot \frac{\omega}{c_0} \cdot z\right) + \dots \right. \\ \left. \dots + \frac{n_{sub} - n_{sup}}{n_{sub} + n_{sup}} \cdot \exp\left(+i \cdot n_{sup} \cdot \frac{\omega}{c_0} \cdot z\right) \right), & \text{if } z > 0, \\ E_{x \vee y, 0} \cdot \frac{2n_{sub}}{n_{sub} + n_{sup}} \cdot \exp\left(-i \cdot n_{sup} \cdot \frac{\omega}{c_0} \cdot z\right), & \text{if } z < 0 \end{cases} \quad (3.27)$$

with  $E_{x,0}$ ,  $E_{y,0}$  being again the complex polarization components and the wave propagating in negative  $z$  direction [47]. However, we choose

$$\frac{n_{sub} - n_{sup}}{n_{sub} + n_{sup}} = 0 \quad \text{and} \quad \frac{2 \cdot n_{sup}}{n_{sub} + n_{sup}} = 1 \quad (3.28)$$

and consider a fully transmitting background field. As the solver searches the correct solution for the given system, the solution for the scattered field  $E_{scat}$  contains the reflection from the interface. This simplifies the calculation for reflectivity. From the ratio of backscattered power and injected power

$$R(\omega) = \frac{\iint_{S1} \langle S_{scat}(\mathbf{r}, \omega) \rangle dS}{\iint_{S1} \langle S_{back} \rangle dS} \quad (3.29)$$

at the green colored surface S1, we obtain the experimentally easily accessible reflectance  $R$  of interface and scatterer. In analogy we calculate the transmittance

$$T(\omega) = \frac{\iint_{S2} \langle S_{tot}(\mathbf{r}, \omega) \rangle dS}{\iint_{S1} \langle S_{back} \rangle dS} \quad (3.30)$$

as ratio of transmitted power through surface S2 and injected power at S1.

We discuss the linear response and different plasmonic modes of the shown structure in more detail, since it is fundamental for the following section and chapter 6. The geometric parameters for the model are slightly modified within the accuracy of the SEM measurement. As structure height we use 60 nm. The dipole size is 190 nm  $\times$  50 nm, the quadrupole arms are each 220 nm  $\times$  40 nm and displaced by gaps of 20 nm. The structures have rounded edges (extruded half ellipses with 20 nm  $\times$   $width/2$  as semi-axes) as shown in the model figure 3.5. This renders the geometry presented in the SEM image and further reduces numerical and unphysical errors at sharp corners. We assume a lossless substrate with flat dispersion and purely real refractive index  $n_{sub} = 1.5$ . For the other half space we use  $n_{sup} = 1$ . Figure 3.6 shows the comparison between measured and calculated linear transmittance spectrum (a,b). Both are in very good agreement, showing the typical EIT mode splitting into repulsive and attractive mode at  $\lambda_1$  and  $\lambda_3$  with a narrow-band transparency window in between at  $\lambda_2$ . For better insight, subfigure (c) depicts the  $z$ -component of the scattered near field at the three wavelengths, 20 nm above the upper structure surface. Since the solution is phase dependent, we plot the field distribution at two orthogonal phases  $\Phi = \pi/2$  and  $\Phi = 0$ . We find dipolar near field pattern for all structure components, oscillating with different phases. The bright in-phase mode of the two quadrupole arms is symmetry forbidden. Furthermore, the behavior of a driven harmonic oscillator is nicely reproduced, where the bright plasmon drives the dark mode in the quadrupole. For wavelengths below 930 nm,

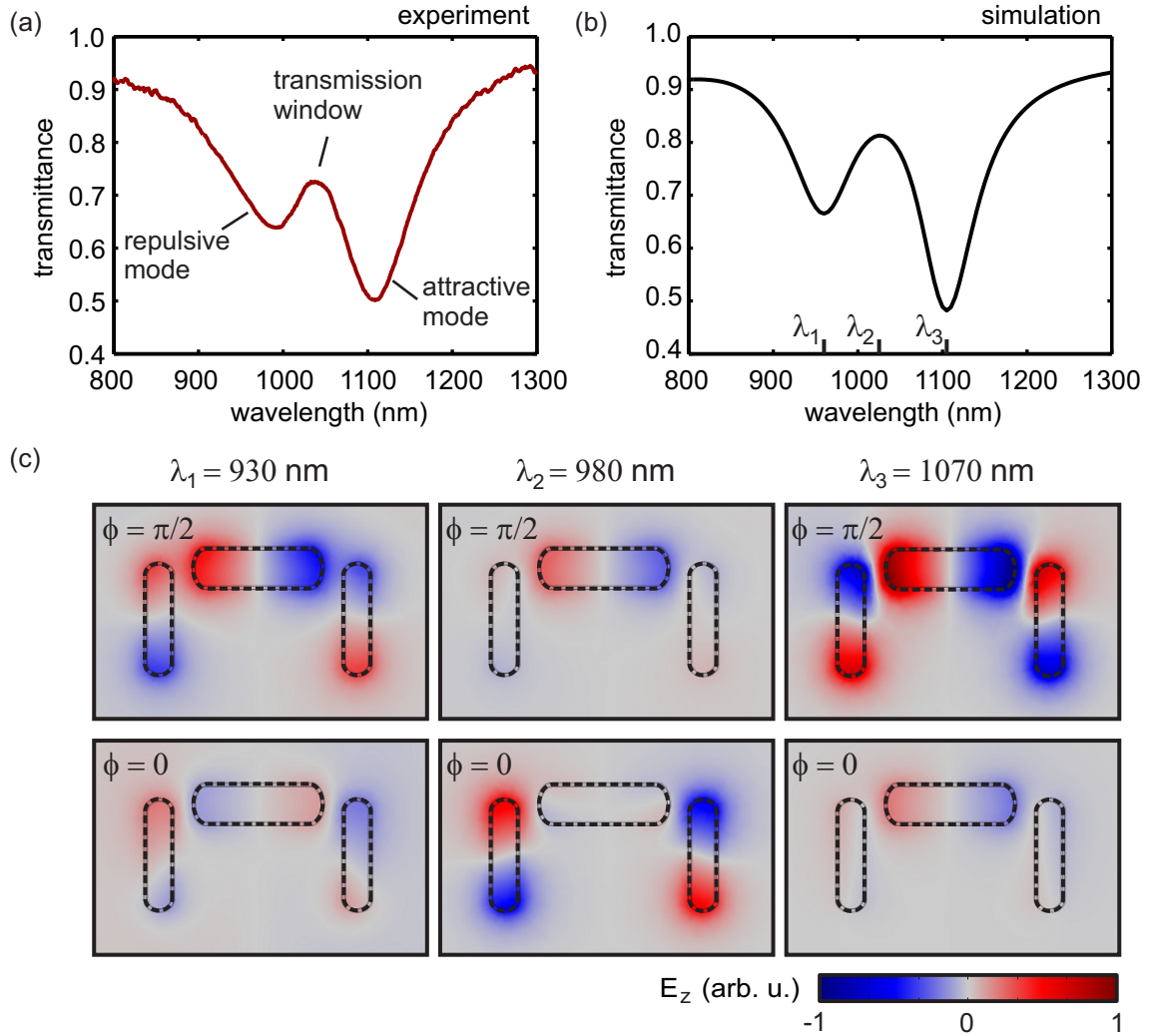


**Figure 3.6**

(a) Measured spectrum of the EIT structure depicted in figure 3.4. The fundamental dipole resonance shows a splitting into a repulsive and attractive mode, with an upcoming transparency window in between. The calculated transmittance spectrum is in good agreement (b). The  $z$ -component of the scattered near-field for different phases is shown in (c), giving more insight into the different modes and the phase behavior of the coupled plasmons.

the quadrupole-dipole oscillation is phase shifted by  $\pi$ , forming the repulsive mode. The attractive mode is above ( $\lambda_3$ ) with in-phase oscillation. The transparency window is caused by plasmon hybridization that shifts the two modes to a higher and a lower energy, respectively. Between the two modes, the oscillation is shifted by  $\pi/2$  and the quadrupole resonantly driven. The narrowband transmission window is due to the non-radiative damping of the quadrupole, shaping the coupled response.

### 3.3 NONLINEAR RESPONSE OF COMPLEX PLASMONIC STRUCTURES

Linear light-matter interaction assumes the proportionality between material response and incident electromagnetic field. In fact, this approximation holds true for small electric fields and intensities. Ultrashort laser pulses as used by Bernd Metzger compress the time averaged intensity into very short temporal intervals, leading to high pulse energies and fields. Plasmons can resonantly enhance the nonlinear response of metal nanostructures [105]. However, the source and prediction of the nonlinear emission in complex plasmonic structures is approached by various theories and part of current research [106–109]. In the following we introduce our numerical model to predict the polarization dependent nonlinear response of arbitrarily shaped and coupled structures to support the experimental findings of Metzger [103].

#### 3.3.1 Numerical model for third harmonic generation

As already discussed in the fundamentals chapter 2.2.1, the polarization density can be expanded to

$$\mathbf{P} = \epsilon_0 \sum_n \chi^{(n)} \mathbf{E}^n = \underbrace{\epsilon_0 \chi^{(1)} \mathbf{E}}_{\text{linear response}} + \underbrace{\epsilon_0 \chi^{(2)} \mathbf{E}^2 + \epsilon_0 \chi^{(3)} \mathbf{E}^3 + \dots}_{\text{nonlinear response}} \quad (3.31)$$

with  $\chi^n$  being the n-th order susceptibility and  $E$  the incident field. However, the direct implementation of equation 3.31 into our linear model (see subsection 3.2.2) is not applicable. The solution for the nonlinear polarization density exists on several frequencies, what is not covered by the diffusion equation in Helmholtz representation. Here, time domain solvers such as FDTD have a clear advantage. Several groups use a hydrodynamical approach to describe the nonlinear current flow and nonlinear dielectric properties. However, we use an alternative model to describe the nonlinear response. As illustrated in figure 3.7(a), we follow the discrete dipole approximation (DDA) where each material and structure is decomposed into single dipolar scatterers. Each dipole with dipole moment  $d$  describes the local material response in dependence of the incident electric field  $\mathbf{E}_{back}$  and the scattered field from other parts of the structure. A more detailed introduction to the method can be found in chapter 6.

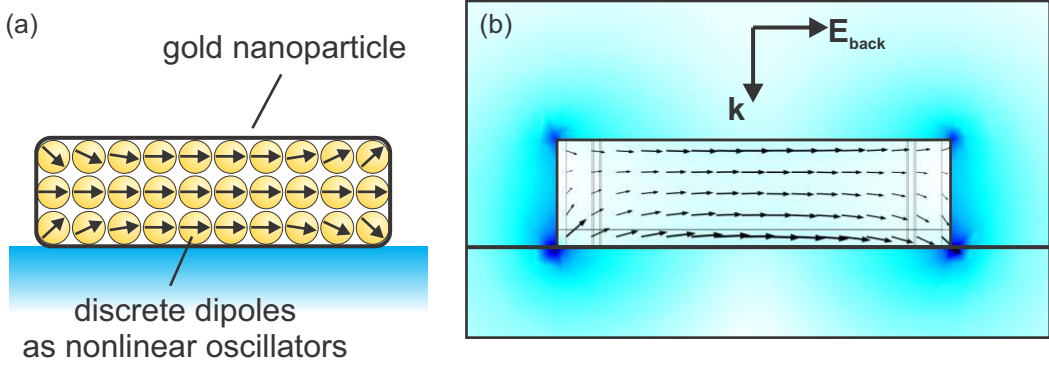


**Figure 3.7**

Visualization of the Discrete Dipole Approximation (a). Each scatterer is decomposed into small discrete dipoles. The correlation to electromagnetics is given by the polarization density. Subfigure (b) shows the dipoles in the symmetry plane of a rod type scatterer, calculated by FEM.

The correlation between DDA and electromagnetics is given by the linear polarization density  $\mathbf{P}^{(1)}$  which is defined as the average electric dipole moment  $\langle d \rangle$  in the considered volume  $V$ , given by

$$\mathbf{P}^{(1)}(\mathbf{r}, \omega) = \frac{\langle d \rangle}{V} . \quad (3.32)$$

From previous work we know that a harmonic oscillator model expanded by a cubic perturbation term can be used to describe the third harmonic behavior of simple gold nanostructures [75, 110]. For materials with no second harmonic generation the oscillator model gives a third harmonic generation that goes with the third power of the linear dipole moment. However, the model needs to be fitted to experimental data. Further its accuracy is limited since it uses the averaged dipole moment of the whole plasmon mode, neglecting local properties and effects. At least if complex and randomly shaped structures are investigated, the model fails. These limitations can be overcome if we assume that each discrete dipole serves as nonlinear oscillator and source for third harmonic generation. We follow equation 3.32 and consider the local dipole moment via its correlation to the linear polarization density. The spatial distribution in frequency domain is computed by

$$\mathbf{P}^{(1)}(\mathbf{r}, \omega) = \mathbf{D}(\mathbf{r}, \omega) - \epsilon_0 \cdot \mathbf{E}(\mathbf{r}, \omega) \quad (3.33)$$

$$= (\mathbf{D}(\mathbf{r}) - \epsilon_0 \mathbf{E}(\mathbf{r})) \cdot \exp(i\omega t) , \quad (3.34)$$

with  $\mathbf{D}(\mathbf{r}, \omega)$  being the displacement field and  $\mathbf{E}(\mathbf{r}, \omega)$  the electric field. In analogy to the illustration in figure 3.7(a), the average dipole moment within identical volume elements in a rod type structure is shown in (b). The integral of  $\mathbf{P}^{(1)}(\mathbf{r}, \omega)$  over the particle volume leads to the average dipole moment that is used in the oscillator

model. However, we follow the oscillator model on a microscopic scale and define the third harmonic generation density proportional to the third power of the linear polarization density with

$$\mathbf{P}^{(3)}(\mathbf{r}, \omega) \propto (\mathbf{P}^{(1)}(\mathbf{r}, \omega))^3 \quad (3.35)$$

$$\propto (\mathbf{D}(\mathbf{r}) - \epsilon_0 \mathbf{E}(\mathbf{r}))^2 \cdot (\mathbf{D}(\mathbf{r}) - \epsilon_0 \mathbf{E}(\mathbf{r})) \cdot \exp(i3\omega t) \quad . \quad (3.36)$$

Here we assume a flat or normalized dispersion of the third order susceptibility. Otherwise the proportionality changes to a function of frequency ( $N(\omega)$ , in equation 3.37), containing the nonlinear material properties. Furthermore,  $\mathbf{P}^{(3)}(\mathbf{r}, \omega)$  is a complex vector which carries polarization, amplitude and phase information, and oscillates with  $3\omega$ . The overall THG generation of a structure is computed, by integrating the function for the third order polarization density over all  $n$  domains, each with volume  $V_i$ . From

$$\begin{pmatrix} d_x^{(3)}(\omega) \\ d_y^{(3)}(\omega) \\ d_z^{(3)}(\omega) \end{pmatrix} \propto \sum_{i=1}^n N_i(\omega) \cdot \iiint_{V_i} (\mathbf{P}^{(1)}(\mathbf{r}, \omega))^2 \cdot \begin{pmatrix} P_x^{(1)}(\mathbf{r}, \omega) \\ P_y^{(1)}(\mathbf{r}, \omega) \\ P_z^{(1)}(\mathbf{r}, \omega) \end{pmatrix} dV \quad (3.37)$$

we obtain the third order dipole moment  $d_i^{(3)}$ , with  $N_i(\omega)$  being the third harmonic material parameter of the domain. Neglecting the directivity and re-absorption processes of the generated radiation, we approximate the emission intensity by

$$I_{THG,i}(\omega) \propto d_i^{(3)}(\omega) \cdot d_i^{(3)*}(\omega) \quad , \quad (3.38)$$

in analogy to the radiated power of a dipole [47].

### 3.3.2 Theoretical prediction for a dolmen-type structure

We apply the model to support the experimental findings of the dolmen-type structure, introduced in the previous subsection 3.2.2. Metzger uses ultrashort laser pulses generated by a broad band laser source combined with a pulse shaping technique to measure polarization resolved third harmonic emission [75, 111]. As control parameter for the coupling between bright and dark mode, we vary the gap distance (see SEM image 3.4) in 10 nm equidistant steps between 30 nm and 100 nm. For the simulation geometry we use the parameters determined by SEM measurements [103]. The experimental findings are normalized by the response of a gold film. Thus, artifacts of the experiment are canceled out and we obtain a spectrally flat material parameter  $N_i(\omega) = const.$  for the simulation.

Figure 3.8 summarizes the theoretical predictions for gap sizes between 30 nm and 100 nm. The linear and nonlinear spectral response in case of the 30 nm and 100 nm gap distance is shown in (a) and (b). Here, the linear extinction spectra are plotted as black curves, calculated by

$$E(\lambda) = -\ln(T(\lambda)) \quad , \quad (3.39)$$

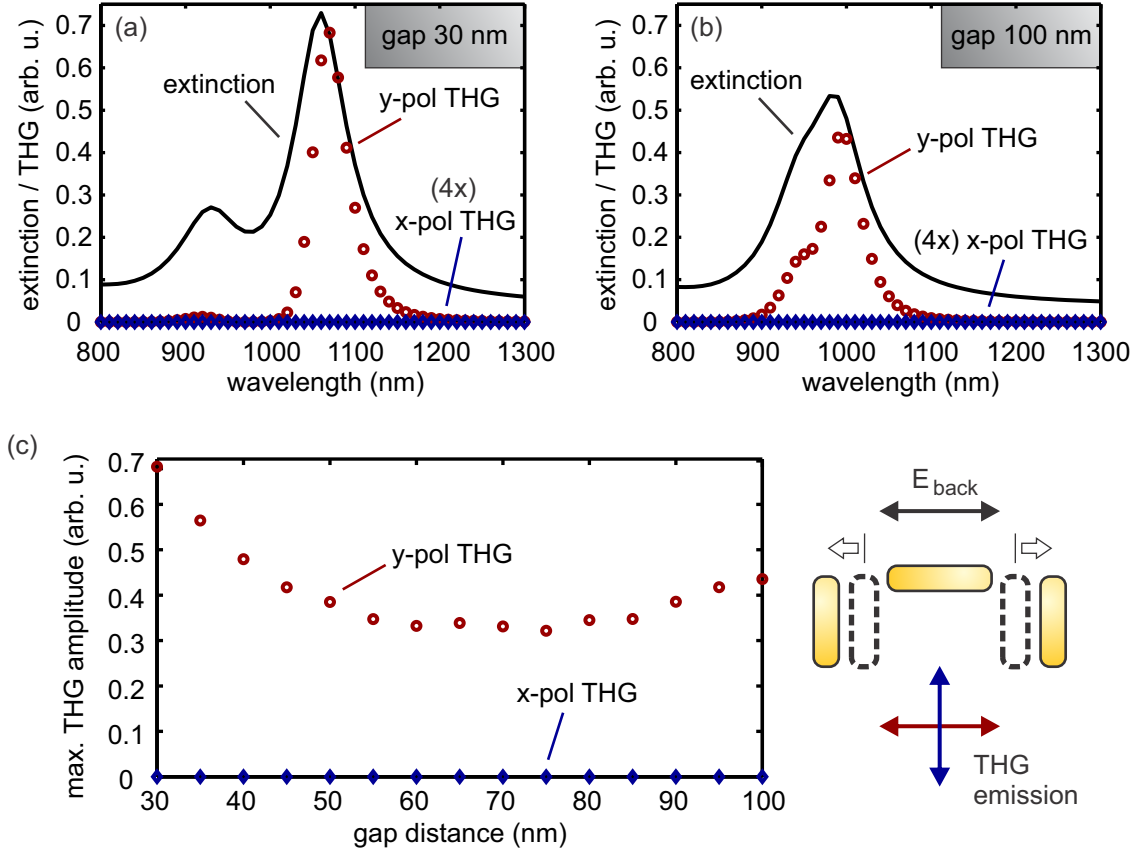


**Figure 3.8**

Simulated extinction and polarization resolved THG emission spectra for a gap distance of 30 nm (a) and 100 nm (b). The wavelength axis of the THG spectra is projected on the fundamental wavelength for a better comparison. To visualize the sweep parameter dependence, the maximum third harmonic generation for both polarizations is plotted in (c), as a function of gap distance.

with  $T$  being the transmittance. In case of the 30 nm gap distance, the extinction spectrum shows two clearly separated resonances. For the 100 nm gap, the mode splitting is almost gone due to the weak coupling between bright and dark mode. From equation 3.38 we obtain the nonlinear emission intensity at  $3\omega$ . For a better comparison, the nonlinear response is plotted as a function of the excitation wavelength  $\omega$  and overlaid to the linear response. First, we consider the third harmonic emission component  $I_{y,THG}$  parallel to the excitation field (red circles). The emission shows an unbalanced behavior at the two modes with strongest emission at the lower energy mode. Furthermore, the THG emission is slightly displaced with respect to the linear response. This is found for all gap distances and in agreement with the oscillator model. Emission with a perpendicular polarization (blue) is constantly zero. In subfigure (c), the maximum THG emission for both polarizations is

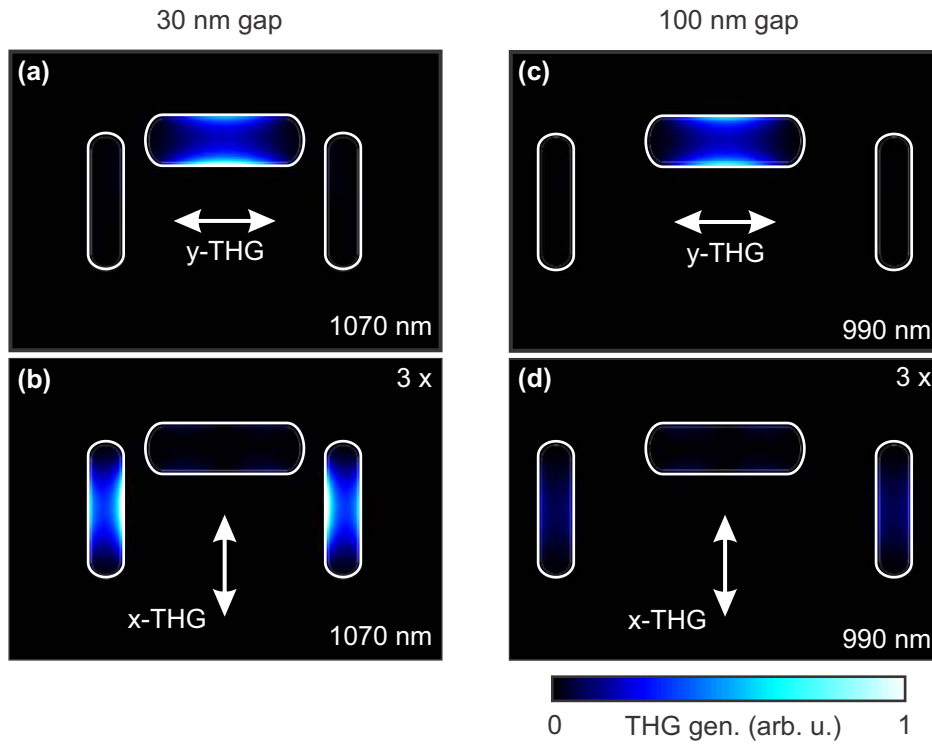


**Figure 3.9**

Polarization resolved third harmonic generation, plotted at the center height of the structure. The parallel component is generated in the dipole particle (a,c). For better visibility, the perpendicular polarized THG (b,d) is multiplied by a factor of 3.

plotted as a function of gap distance. We find no third harmonic emission along the perpendicular polarization, independent of the gap distance. The behavior of the y-polarization, especially for smaller gap values is more complex and not directly intuitive. Most responsible for the maximum nonlinear emission intensity seems the combination of high oscillator strength and high quality factor (Q-factor), leading to high polarization values. The first parameter can be increased by the particle volume, while the Q-factor is increased by reducing the losses in the plasmon oscillation. Here, intrinsic losses depend on the resonance position of the linear plasmon mode and the corresponding dielectric function  $\epsilon_r(\omega)$ . The complex interplay between shape, geometry, dielectric function and ensuing radiation damping makes numerical simulations necessary to predict the nonlinear emission behavior of complex nanostructures. This limits the validity of more simple models, where radiation losses and geometry effects are neglected. However, a quantitative comparison of experiment and simulation is almost impossible, since already small deviations in the linear spectra lead to a distorted nonlinear response and eventually wrong interpretations. In our case, experiment and model are in very good agreement and

support the concept of the model with nonlinear local dipoles as source of third harmonic emission. As a consequence, we can calculate and visualize the spatial distribution of third harmonic generation in the nanostructure.

Given by the absolute value  $|P_i^{(3)}|$ , the polarization resolved third harmonic generation along the x-y-plane is plotted in the figures 3.8(a) - (d). For orientation, the white contours mark the gold boundaries, showing the structures with 30 nm (a,b), and 100 nm (c,d) gap distance. In all cases, the wavelength is chosen to be at the maximum THG emission. Independent of the gap distance we find the dipole element as the source of the nonlinear emission parallel (y-THG) to the excitation polarization (a,c). Only the overall amplitude slightly changes. For the perpendicular polarization (x-THG) we obtain the distributions shown in (b) and (d), multiplied by a factor of 3 for better comparison. Here, the third harmonic generation in the quadrupole strongly depends on the transferred energy, given by the gap distance. Especially the 30 nm gap structure shows strong third harmonic generation in both quadrupole branches. Nevertheless, experiment and model show no emission for the x-polarization. This is due to the coherent nature of the nonlinear process. While the absolute value of  $P_i^{(3)}(\mathbf{r}, \omega)$  gives the local amount of third harmonic generation, the radiation phase is defined by the angle. Consequently, the integral 3.37 takes the out of phase oscillation of the quadrupole arms into account, leading to interference effects in the far field. Angular dependent measurements or a disturbance of the quadrupole properties allows further investigation of the coherent behavior. The latter case requires no change of the experimental setup and can be realized by influencing the counter phase oscillation of the quadrupole arms, or by increasing the averaged dipole moment of one of the arms. Both is done simultaneously by shifting the bright dipole out of the symmetry plane of the structure, leading to retardation effects as well as an unbalanced energy transfer to the arms. Thus we expect third harmonic emission for the perpendicular polarization. Figure 3.10 summarizes the theoretical predictions for a structure with an averaged gap distance of 50 nm and shifted dipole (see lower right sketch). The results are in good agreement with the experiment. The symmetric structure (a,b) shows the previously discussed behavior and no third harmonic emission along the perpendicular polarization. In (c) and (d) the case for the dipole shifted by 30 nm is shown. We directly observe the unbalanced nonlinear generation in the two quadrupole branches, leading to emission in x-polarization (c). Retardation plays a minor role. The maximum emission is between the two EIT modes, slightly blue shifted with respect to the low energy mode. With equation 3.24 we separate the absorption spectra of quadrupole and dipole in the coupled system. The absorption maximum of the quadrupole mode is marked in (c). We find the characteristic redshift of the third harmonic emission in respect to the quadrupole absorption resonance. This determines the detuned quadrupole as source of the perpendicular polarized third harmonic emission.

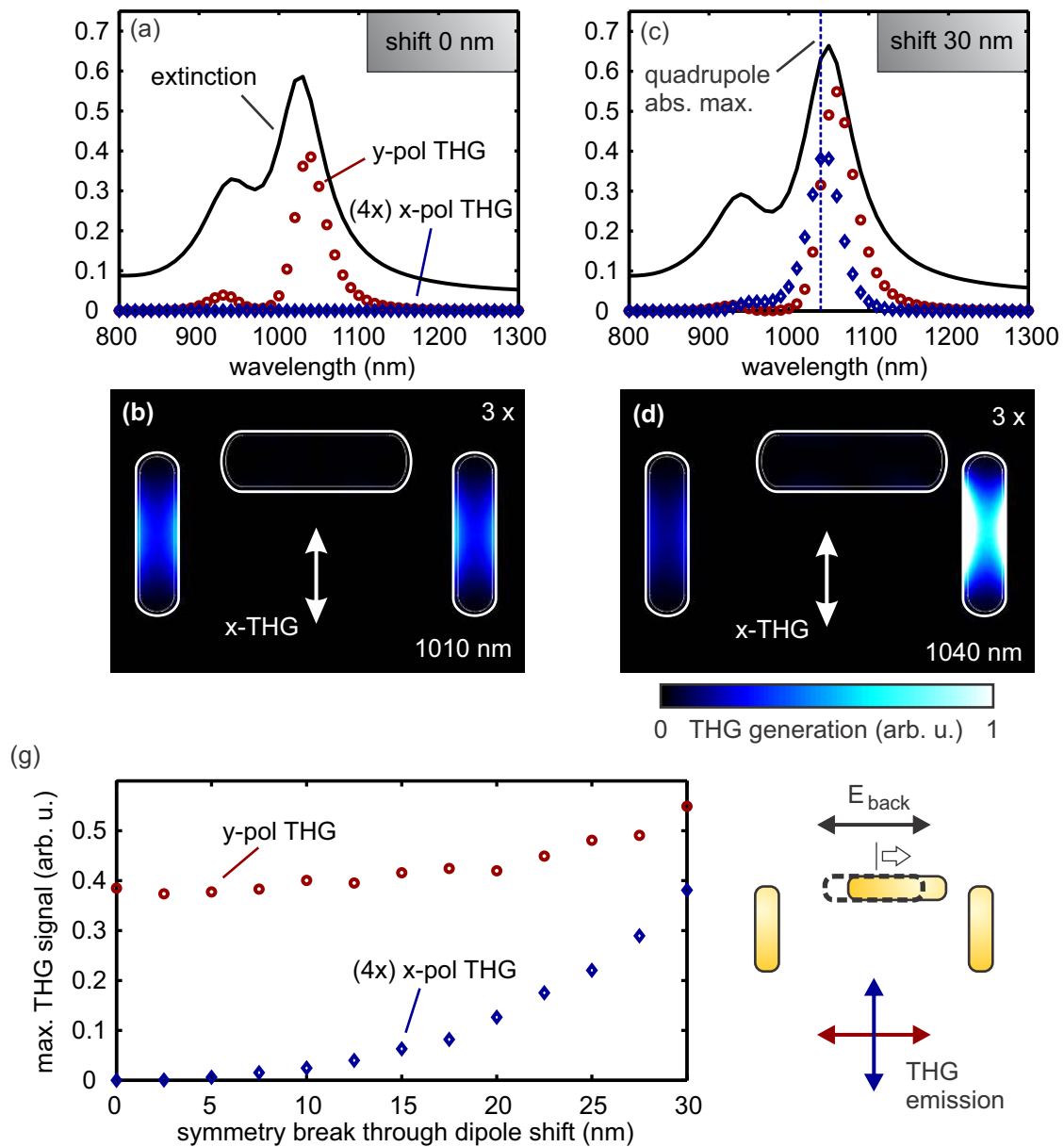


**Figure 3.10**

(a,c) Simulated extinction and polarization resolved THG emission spectra for the symmetric and broken symmetry case with the corresponding THG generation plots (b,d). The scale is identical to figure 3.8. It can be seen that the increase of x-polarized THG emission is directly correlated with the unbalanced generation in the two quadrupole branches, leading to radiation losses. (g) Maximum third harmonic generation for both polarizations as a function of gap distance. All graphs are plotted in the x-y-plane at the center height of the gold structure.

### 3.3.3 Conclusion

In this section we presented our numerical model for third harmonic generation. In addition to the discussed structure, we find good agreement of our model and experiments for other geometries, for example L-shaped structures and ITO filled double rod nanoantennas [112]. In summary we developed a simple model to compute the nonlinear optical response of complex coupled nanostructures. However, further experiments especially on *random* shaped particles have to be performed to confirm the validity of the model and its limits. As further optimization one could take emission and reabsorption properties into account. Therefore we would calculate the inverse behavior of the photoemission at  $3\omega$  by illuminating the structure from the detector side and weight the previously calculated third harmonic emission with the local field. This promises an even more precise model, including radiation effects. In order to enhance the nonlinear response of single nanoobjects, for example the previously mentioned ITO spheres in a double rod antenna gap, high fields can help but the desired signal is superimposed by a huge antenna background. Here, intelligent antenna designs or other materials showing less nonlinearity can help to overcome this challenge and separate the desired signals. Finally the interpretation of our model predicts a minor role of high gap fields for the case of third harmonic generation in purely plasmonic structures but rather a strong dependence on the spectral resonance and the corresponding dielectric function and radiation damping, as already discussed.

### 3.4 THE TOTAL FIELD COMPONENTS AS INDEPENDENT VARIABLES

In the previously discussed models we are able to use the field separation ansatz of equation 3.8. This approach breaks down when no simple analytical solution for the background field can be found. An example is a particle separated by a spacer layer from a non-perfect mirror with losses and penetration depth. In this configuration, the particle is influenced by its own backreflected scattered field, leading to a complex interplay and multiple reflections between mirror and particle. In addition, the overall scattered field  $E_{scat}$  of the particle interferes with the reflected excitation field of the mirror  $E_{ref}$ . In a far field reflection measurement, the intensity on a detector is given by

$$I_{det} = |E_{ref} + E_{scat}|^2 \quad (3.40)$$

$$= |E_{ref}|^2 + \underbrace{|E_{scat}|^2 + 2 \cdot \text{Re}[E_{ref} \cdot E_{scat}]}_{\text{modulated components in homodyne detection}} \quad (3.41)$$

where both field contributions have to be described by their amplitude and phase. In homodyne detection, the scattered field  $E_{scat}$  is modulated. Thus the measured signal is given by the last two terms of equation 3.41 and allows signal enhancement by the multiplication of weak scattering component and strong reference field in the interferometry term [113]. Figure 3.11(a) shows the simplified sketch of a

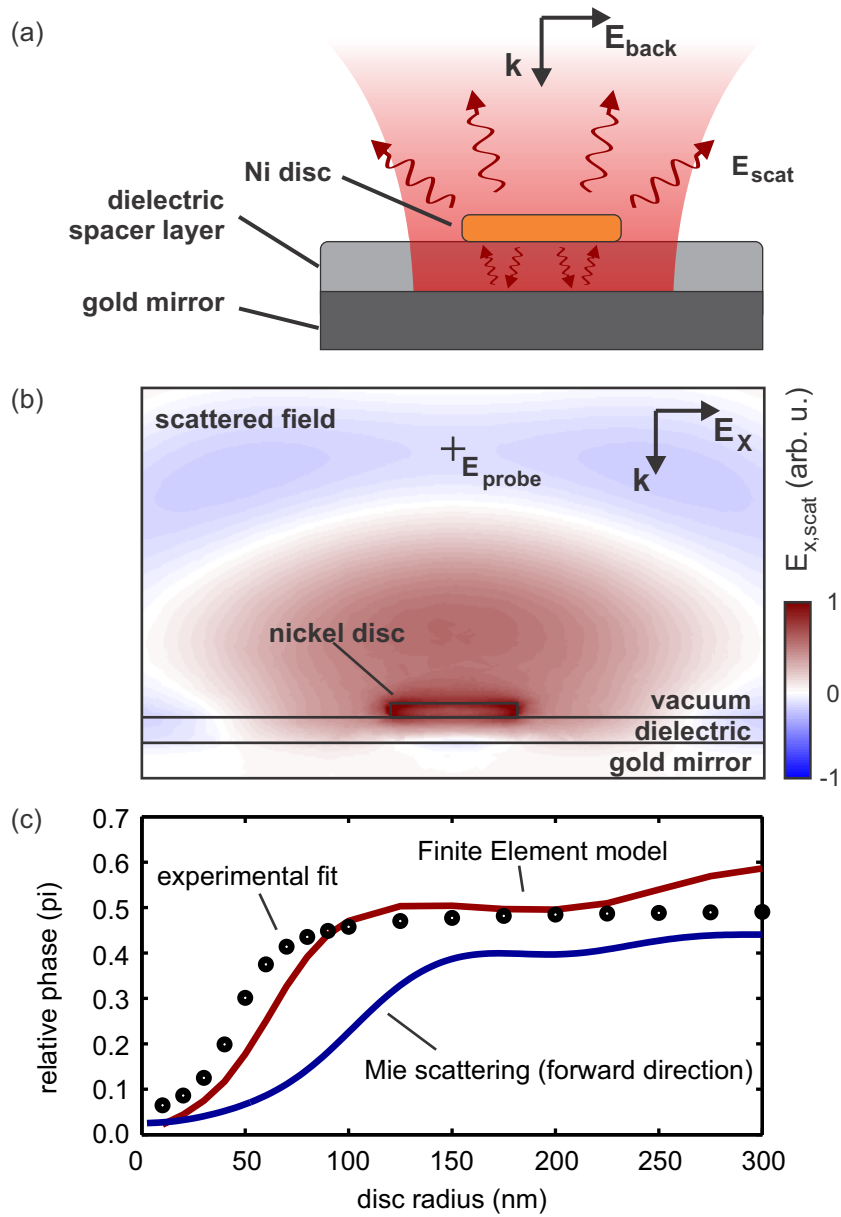


**Figure 3.11**

Sketch of an interferometric structure consisting of a nickel disc in front of a gold mirror. (b) Real part of the x-component of the electric field  $E_x$  in the x-z-plane. The complex field  $E_{probe}$  outside the near-field can be used to calculate the amplitude and relative phase for the interferometric model. (c) Calculated relative phase from the finite element model and Mie scattering. The black circles show a simplified arctangent model-fit to the experimental data.

magneto-optical nanostructure in front of a gold mirror as used in the experiments of Christian Dicken. He uses a Sagnac-Interferometer at 800 nm wavelength to investigate the Kerr rotation of a single nickel nanostructure in reflection, as a function of the applied magnetic DC-field [114]. He applies an analytical interferometric model to describe the experimentally found signal amplitude. However, the critical unknown parameter in the model is the scattered field  $E_{scat}$ , where simple models fail to describe the varying amplitudes and phases in dependence of the nickel particle's size. In addition, multiple reflections with the non-perfect gold mirror potentially change the spectral and scattering properties of the system and numerical simulations have to be performed.

We solve the full electromagnetic field  $\mathbf{E}(\mathbf{r}, \omega)$  in analogy to the model for periodic boundary conditions, depicted in figure 3.5. The scattering boundary condition at the injection surface (S1) is defined to

$$\begin{pmatrix} E_{x,0} \\ E_{y,0} \end{pmatrix} = E_{x,0} \cdot \underbrace{\begin{pmatrix} 1 \\ 0 \end{pmatrix}}_{\text{linear polarization}} + E_{y,0} \cdot \begin{pmatrix} 0 \\ 1 \end{pmatrix}, \quad (3.42)$$

$$= \underbrace{\frac{E_0}{\sqrt{2}} \cdot \begin{pmatrix} i \\ 1 \end{pmatrix}}_{\text{circular polarization}} \quad \text{or} \quad \frac{E_0}{\sqrt{2}} \begin{pmatrix} -i \\ 1 \end{pmatrix} \quad (3.43)$$

leading to plane wave excitation in the given Floquet periodicity. Although the Sagnac interferometer works with circularly polarized light, we can solve the system for a single linear polarization ( $E_{x,0} \neq 0, E_{y,0} = 0$ ) due to the symmetry of the structure. The side view of the model geometry containing vacuum superstrate, nickel disc (height = 25 nm), spacer layer ( $n = 1.5$ ) and gold mirror is depicted in figure 3.11(b). To approximate the field distribution around a single nickel disc we choose a large unit cell size of  $1.5 \mu\text{m} \times 1.5 \mu\text{m}$ . The computed total electric field distribution contains the unknown background and scattered field. Here, their separation is done by solving the same structure without disc. For this purpose we keep the particle volume but with the optical properties of vacuum, in order to use the same meshing and reduce discretisation errors. The scattered field distribution  $E_{scat}(\mathbf{r})$  including multiple interactions between particle and mirror is calculated from the difference of the two solutions.

Figure 3.11(b) shows the real part of  $E_{scat}$  for an excitation wavelength of 800 nm. In order to extract the desired scattered field amplitude and phase information we use a local probe  $E_{probe}$ , placed 800 nm above the spacer layer-vacuum surface in the far field and on the optical axis. The result for the relative phase in units of  $\pi$  as a function of the disc radius is plotted as red curve in (c). It changes from 0 to  $\pi/2$  if the radius is tuned from 10 nm to above 100 nm. Within this range, the fundamental particle plasmon resonance is tuned over the 800 nm excitation wavelength. From a simple driven oscillator model, we expect a phase change by  $\pi$ . The reason for

the smaller shift in our calculation is the changing particle size, leading to increased scattering and additional broadening of the plasmon resonance of nickel. Here, a slow transition from scatterer to reflector influences the scattered field, disturbing the simple oscillator behavior. For other materials such as gold, a clear phase shift from 0 to  $\pi$  is observed. For comparison, the Mie scattering solution for a spherical particle in forward direction without mirror and spacer layer is plotted as blue curve. We find a similar but stretched behavior, shifted to larger sphere radii. The reason is the blue shifted plasmon resonance for spherical nanoparticles where larger radii are required to pass the 800 nm. A phenomenological arc tangent model to fit the experimental data by the analytical model is represented by the black circles. The slight deviations are explained by fabrication errors. However, we find a very good agreement of the complex finite element model and the phenomenological fit.

### 3.5 IMPLEMENTATION OF THE CONSTITUTIVE EQUATIONS FOR OPTICAL CHIRALITY SIMULATIONS

The most general form of the constitutive relations for a bi-anisotropic medium is given by the equation

$$\begin{pmatrix} \mathbf{D} \\ \mathbf{B} \end{pmatrix} = \begin{pmatrix} \underline{\underline{\epsilon}} & \underline{\underline{\xi}} \\ \underline{\underline{\zeta}} & \underline{\underline{\mu}} \end{pmatrix} \cdot \begin{pmatrix} \mathbf{E} \\ \mathbf{H} \end{pmatrix} \quad (3.44)$$

with  $\underline{\underline{\epsilon}}$  and  $\underline{\underline{\mu}}$  being the permittivity and permeability tensors,  $\underline{\underline{\xi}}$  and  $\underline{\underline{\zeta}}$  additional magneto-electric coupling tensors, cross-linking the electric and magnetic response [115]. For bi-isotropic media they can be reduced to the complex scalar values

$$\xi = (\chi - i\kappa) \cdot \sqrt{\epsilon_0\mu_0} \quad (3.45)$$

$$\zeta = (\chi + i\kappa) \cdot \sqrt{\epsilon_0\mu_0} \quad (3.46)$$

where  $\chi$  defines the degree of inherent reciprocity and  $\kappa$  the degree of chirality [115, 116]. The latter gives the difference of the refractive index for left (LCP) and right circularly polarized light (RCP)

$$n_{\pm} = n \pm \kappa \quad (3.47)$$

of a chiral medium. Consequently, a linearly polarized plane wave, which can be decomposed into the base-functions LCP and RCP, changes its polarization angle while propagating through the material. The angle of polarization rotation can be calculated analytically and is given by

$$\Phi_{rot} = \kappa \cdot \frac{2\pi}{\lambda_0} \cdot l \quad (3.48)$$

with  $\lambda_0$  being the free space wavelength and  $l$  the propagation length in the chiral medium [117]. However, the values for  $\kappa$  of organic and inorganic materials are

typically on the order of  $10^{-4}$  to  $10^{-7}$  [118]. Thus, linearly polarized light with  $\lambda_0 = 700$  nm has to propagate through  $\approx 2$  mm of the chiral medium to perform a rotation by  $1^\circ$ . This requires long propagation distances for qualitative analysis and makes measurements with small volumes of molecules or even of a single one almost impossible. However, in analogy to molecules, plasmonic nanostructures can also show optical chirality and are prominent candidates for chiral sensitive optical antennas [25, 119, 120]. Circular dichroism (CD), which refers to the differential absorption  $\Delta A$  of LCP and RCP light, is a common value to define the chiral response of such structures. Due to experimental circumstances we consider the differential transmittance  $\Delta T$ , given by

$$\Delta T(\omega) = T_{LCP}(\omega) - T_{RCP}(\omega) \quad . \quad (3.49)$$

For the computation of  $\Delta T$ , we can use the previously described model of section 3.4. However, to study the interplay between plasmonic nanostructures and chiral molecules or media, the constitutive equations 3.45 in the following form

$$\mathbf{D} = \epsilon \mathbf{E} + (\chi - i\kappa) \cdot \sqrt{\epsilon_0 \mu_0} \mathbf{H} \quad (3.50)$$

$$\mathbf{B} = (\chi + i\kappa) \cdot \sqrt{\epsilon_0 \mu_0} \mathbf{E} + \mu \mathbf{H} \quad (3.51)$$

have to be implemented. As a consequence of the solver and the computation in frequency domain, Maxwell's equations in their constitutive form must be expressed

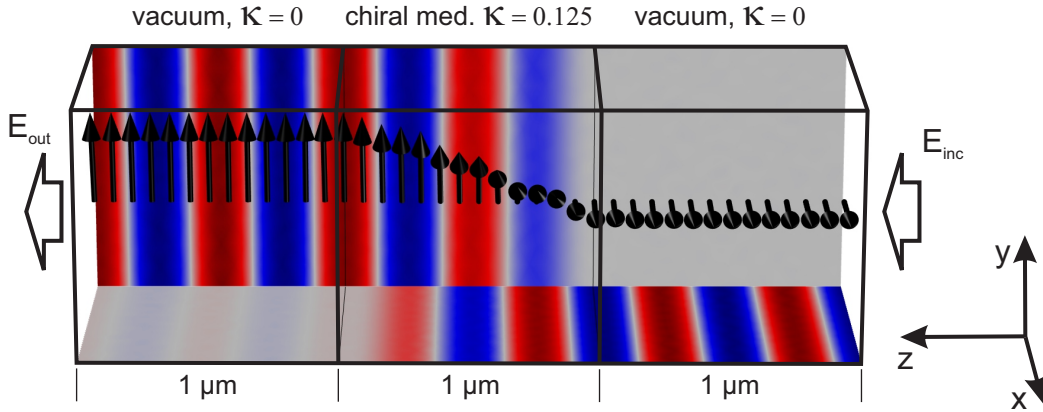


**Figure 3.12**

Control model to compute the plane-wave propagation through a chiral layer. The system consists of three lined up sections, each  $1 \mu\text{m} \times 1 \mu\text{m} \times 1 \mu\text{m}$  in size, all with purely real refractive index 1. The middle layer is chiral with  $\kappa = 0.125$ . The rear model boundary shows the  $y$ -, the lower the  $x$ -real part component of the electric field. In addition, the black arrows point along electric field. The calculation shows the expected  $\pi/2$  rotation of a linearly polarized plane wave, propagating from right to left.

as a function of the electric field components without direct time derivatives. Thus we write for the magnetic field

$$\mathbf{H} = \mu^{-1} \cdot (\mathbf{B}(\mathbf{E}) - (\chi + i\kappa) \cdot \sqrt{\epsilon_0 \mu_0} \mathbf{E}) \quad (3.52)$$

with  $\mu^{-1}$  being the inverse permeability.  $\mathbf{B}(\mathbf{E})$  is the magnetic flux, derived from the Maxwell-Faraday equation 2.1 and

$$\frac{\partial \mathbf{H}}{\partial t} = \mu^{-1} \frac{\partial \mathbf{B}}{\partial t} - \mu^{-1} (\chi + i\kappa) \sqrt{\epsilon_0 \mu_0} \cdot \underbrace{i\omega \cdot \mathbf{E}}_{=\frac{\partial \mathbf{E}}{\partial t}} \quad (3.53)$$

where the temporal derivative of the electric field is directly derived from the separation ansatz eq. 3.6. With knowledge of  $\mathbf{H}$ , equation 3.50 can be directly implemented and the model contains the constitutive equations for bi-isotropic media without approximation.

Figure 3.12 depicts the control model in order to check the implemented equations. It consists of three  $1 \mu\text{m} \times 1 \mu\text{m} \times 1 \mu\text{m}$  cubes, all with real refractive index  $n = 1$ . A plane wave with wavelength 500 nm, polarized along the x-coordinate, propagates from the right boundary into positive z-direction. We follow equation 3.48 to obtain a  $90^\circ$  polarization rotation, and choose a fictive  $\kappa$  of 0.125 for the center layer. The environment shows no chirality, leading to a plane wave propagation in the first section, illustrated by the black arrows and the projection of the field components (see figure caption). After the plane wave reaches the chiral layer, a significant rotation sets in. Behind the center section, the polarization is rotated by  $\pi/2$  and agrees nicely with the prediction of the analytical solution. Further we found the postulated rotation independence of the refractive index and the wavelength dependence of equation 3.48. Furthermore, we performed first calculation to investigate the interaction between a chiral medium and a planar chiral plasmonic antenna. However, to observe a measurable signal in the differential transmittance  $\Delta T$  we have to assume a  $\kappa$  which is approximately 3 to 4 orders of magnitude larger than the typical values for chiral media. As a next step we suggest to investigate the interaction with three dimensional plasmonic structures, showing a global chirality and possibly larger signal enhancement [25].

ANTENNA ENHANCED  
ULTRAFAST ACOUSTO-OPTICAL RESPONSE  
OF A SINGLE GOLD NANOPARTICLE

---

#### 4.1 MOTIVATION AND INTRODUCTION

Nanostructures of a few ten nanometers in size can perform mechanical oscillations and follow the laws of continuum mechanics, where the discretized nature of the material is neglected [39, 122, 123]. Figure 4.1 shows an arbitrary selection of classical mechanical modes of a disc-shaped gold nanoparticle lying on an inelastic substrate. The computation is done using the structural mechanics module of Comsol Multiphysics [121]. Similar to particle plasmons, the mechanical eigenmodes are defined by the boundary conditions of the nanoparticle and are characterized by a mode profile with corresponding eigenfrequency. However, the validity of the bulk mechanical and classical properties are limited to structure sizes above  $\approx 10$  nm [124, 125]. A further decrease of the structure size reveals the discrete atomistic nature of matter, which differs from the continuum approximation. The investigation of this transition at mesoscopic systems promises deep insight into the involved physical processes [124–128].

Metal nanoparticles with several ten nanometers in size have their fundamental eigenfrequency above 10 GHz, dependent on material, size, and shape [39, 129–131]. This corresponds to an oscillation period of less than 100 ps. In order to resolve these dynamics, a temporal resolution of a few picoseconds or better is required, making optical pump-probe experiments necessary. However, the tiny interaction

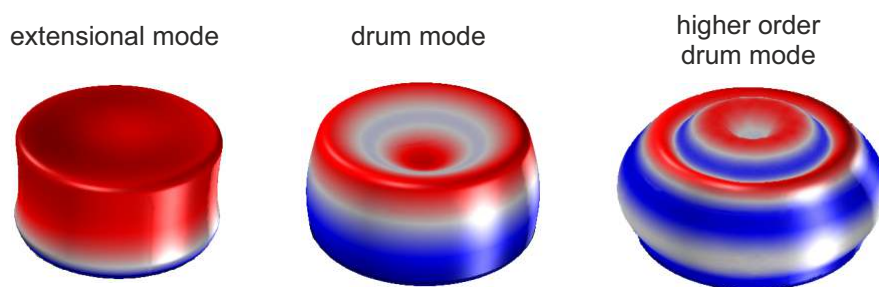


**Figure 4.1**

Symmetric mechanical eigenmodes of a gold nanodisc with a radius of 35 nm and height of 30 nm, in contact with an inelastic substrate. The computation is done with the structural mechanics module of the finite elements solver [121].

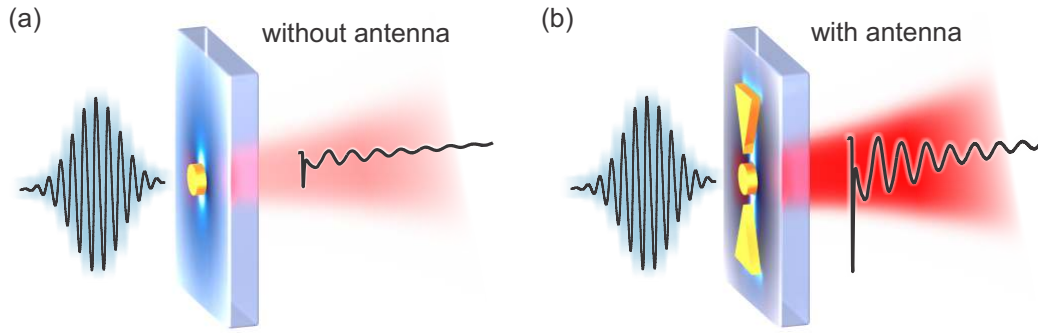


**Figure 4.2**

Illustration of an optical nanoantenna enhancing the nonlinear response of a single nanoobject. On the left side, a gold nanodisc of few nanometers in size is probed by an ultrashort laser pulse. The resulting nonlinear response is extremely weak but carries information about the involved physical processes. Shown on the right side, the response of the same nanoparticle is enhanced by the nanoantenna (represented by the bow-tie structure).

cross section of the plasmonic nanostructure complicates single particle experiments. Especially the nonlinear response, which is already weak for bulk material, becomes difficult if not impossible to detect. A resonant optical nanoantenna that concentrates the optical field on the individual nanoobject promises enhancement of the weak nonlinear signal as illustrated in figure 4.2 [11, 132, 133].

In the following we discuss how mechanical vibrations are launched by the energy deposited by an ultrashort laser-pulse. The oscillation state is monitored by the perturbation of the plasmon resonance, similar to the example introduced in subsection 2.2.2. We present a numerical model to compute the expected signal intensity. Later in the chapter, the experimental results and data evaluation at the example of single gold nanoparticles is discussed and compared with the theoretical predictions. This proves the validity and limitations of our model and allows the simulation and optimization of optical nanoantennas to enhance the signal of previously barely detectable particle sizes. Finally, the first experimental realization of an optical nanoantenna for ultrafast spectroscopy is shown and discussed [80].

## 4.2 PUMP EXCITATION OF ACOUSTICAL VIBRATIONS

We consider a noble metal nanoparticle with volume  $V_p$  in a highly focused laser beam consisting of ultrashort laser pulses. The pulse duration is around a hundred femtoseconds and the spot size in the focal plane has a radius of  $\approx 400$  nm. The laser pulse is partly absorbed by the particle. From subsection 2.1.2, we assume the maximum absorption cross section in the order of  $10^4$  nm<sup>2</sup> for particles of a few ten nanometers in size. As a consequence, approximately 2% of the pulse energy is transferred to the electron-gas. The deposited energy is distributed over several radiative and non-radiative processes, appearing on different timescales [134–136].

Figure 4.3 gives an overview about the relevant non-radiative processes and their temporal appearance. After instantaneous excitation by the femtosecond laser pulse, the coherent oscillation of the conduction electrons dephases on a 10–20 fs timescale and an incoherent hot electron-gas remains [137, 138]. For an assumed pulse energy of  $W_p = 1$  pJ, the energy stored in the electron-gas  $W_{abs}$  is approximately 20 fJ. In order to describe the energy transfer between the electron-gas and the material lattice, a simple two-temperature model can be applied [139]. However, we neglect the temporal evolution and focus on the quasi equilibrium state after excitation. Therefore, the maximum electron-gas temperature is approximated via the heat capacity parameter  $\alpha = 65 \text{ Jm}^{-3}\text{K}^{-2}$ , which gives the linear correlation of heat capacity and electron-gas temperature by  $C_{e,V} = \alpha T$  [134]. With  $T_i$  being the initial (room temperature) and  $T_{f,e}$  the maximum electron-gas temperature without energy transfer to the lattice, we write

$$W_{abs} = \alpha V_p \int_{T_i}^{T_{f,e}} T dT \quad (4.1)$$

$$= \frac{1}{2} \alpha V_p (T_{f,e}^2 - T_i^2) \quad (4.2)$$

and solve for

$$T_{f,e} = \sqrt{\frac{2W_{abs}}{\alpha V_p} + T_i^2} \quad (4.3)$$

As a consequence, we obtain the upper limit for the electron-gas temperature with  $T_{f,e} \approx 2300$  K, assuming an initial gas temperature of  $T_i = 300$  K. Simultaneously to the gas heating, energy is transferred to the lattice, mediated by electron-phonon scattering. This leads to a fast cooling of the electrons after passing their peak temperature  $< 2300$  K. The duration until electron-gas temperature and lattice temperature are in thermal equilibrium at  $T_{eq}$  depends on the scattering rate but

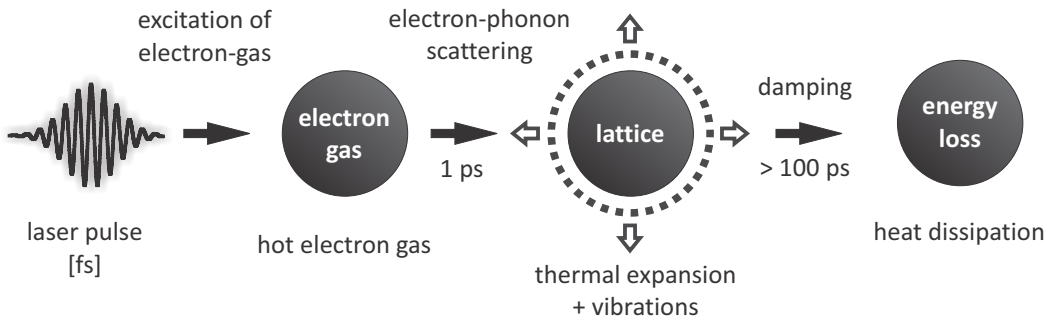


**Figure 4.3**

Nonradiative decay processes and their temporal behavior in a metal nanoparticle, after partial absorption of an ultrafast laser pulse.

is typically in the order of 1 ps. This is much faster than the period of the fundamental mechanical mode of the nanoparticle. As the lattice is not able to follow the impulsive heating adiabatically, it overshoots its new equilibrium state and acoustic vibrations are excited. As the energy loss  $\Delta W_e$  of the electron-gas is equal to the energy gain of the lattice  $\Delta W_l$ , we write  $\Delta W_l = -\Delta W_e$  and solve for the equilibrium temperature  $T_{eq}$ . We obtain

$$T_{eq} = -\frac{C_l}{\alpha} + \sqrt{\left(\frac{C_l}{\alpha}\right)^2 + \frac{2C_l}{\alpha}T_i + T_{f,e}^2} \quad (4.4)$$

with  $C_l = C_{l,V}V_p$  being the heat capacity,  $T_i$  the initial temperature of the lattice, and  $T_{f,e}$  the electron-gas temperature, calculated from equation 4.3. For gold, with  $C_{l,V} = 2.415 \cdot 10^6 \text{ Jm}^{-3}\text{K}$ , we obtain an equilibrium temperature of  $T_{eq} = 371 \text{ K}$  which is approximately 70 K above the initial room temperature. For comparison, if we consider a  $15\times$  higher pulse energy, the equilibrium lattice temperature is at 1350 K and exceeds the melting point of gold. As a consequence, the pump-pulse excitation is limited by the deformation or the solid-liquid phase transition and the destruction of the particle. The thermal background typically decays on a timescale of several hundred picoseconds due to heat dissipation losses to the environment. The decay of the mechanical oscillations occurs on the same timescale through intrinsic losses. For times  $> 1 \text{ ns}$ , the excitation energy is dissipated in the environment. This guarantees the full relaxation of the system into its initial state for the repetition rate of 76 MHz of our pulse source.

The structures of investigation are gold nanodiscs with various radii but constant height. Their fabrication and characterization is further discussed in section 4.4. Here, we numerically investigate the pump excitation of mechanical oscillations for disc shaped gold nanoparticles. We apply the T-Matrix method in order to compute the absorption spectra for discs with a constant height of 30 nm and radii ranging from 10 nm to 70 nm [140]. The effective medium for the structures at the glass-air interface is chosen to  $n_{eff} = 1.4$ , showing best agreement for the experimentally determined scattered spectra. The optical constant of gold is given by the data of Johnson and Christy [49]. Figure 4.4(a) shows the calculated absorption cross section as a function of the disc radius. We observe the expected redshift of the fundamental plasmon mode with increasing disc size. Higher order modes are extinct by the d-band absorption of gold. Most efficient excitation is achieved for pump wavelengths at the absorption maxima and thus dependent on the disc size. However, in the experiment we use a constant wavelength of 800 nm as we have enough pump power for off resonant excitation. As a consequence, the absorbed pulse energy  $W_{abs}$ , as a function of the disc radius  $r$ , is given by  $C_{abs}(r, 800 \text{ nm})$ . Furthermore, we assume a spot radius of 500 nm being  $\approx 10\%$  above the diffraction limit of the 0.9 NA objective. The red curve in figure 4.4(b) shows the absorbed energy as a function of the disc radius. The absorbed energy varies over three orders of magnitude, due to the large volume changes and the inefficient pumping of the smaller discs but almost resonant excitation for the bigger ones. However,

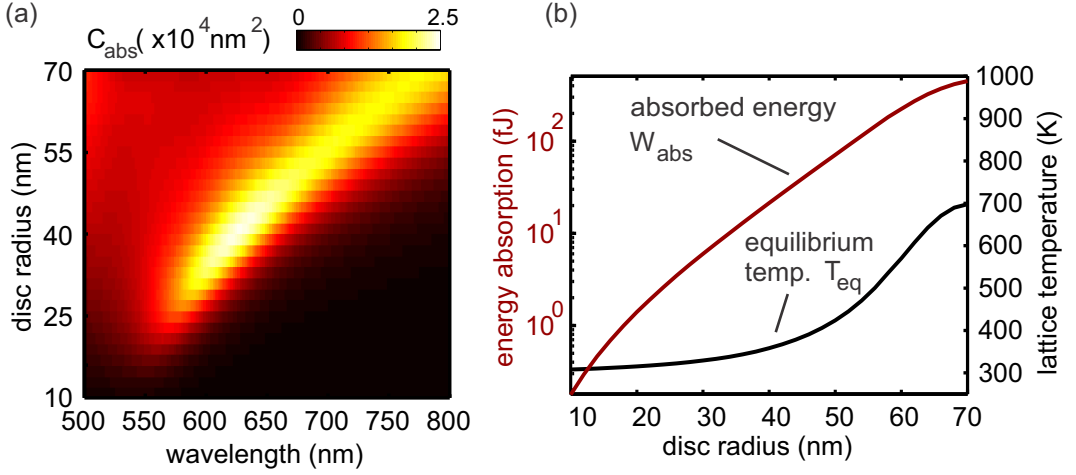


**Figure 4.4**

Radius dependent absorption cross section  $C_{abs}$  of a single gold nanodisc with 30 nm height, in the spectral range between 500 nm and 800 nm. In combination with the pump spot size, the absorbed energy for an excitation wavelength of 800 nm is calculated and plotted as red curve in (b). From this, the maximum lattice temperature  $T_{eq}$  (black) is approximated, utilizing a two-temperature model.

equation 4.4 is a function of the particle volume since more energy is required to heat up a larger particle volume. Consequently, the equilibrium temperature  $T_{eq}$  is affected much less by the amount of absorbed energy. Furthermore we find an excitation maximum for particle radii around 70 nm. Particles with larger radii are again off-resonant and less excited although they are larger in size. Finally, we conclude that the excitation properties vary with disc size and must be taken into account when the nonlinear response amplitude of different disc sizes is compared, as we discuss in the following section.

### 4.3 MODELING OF THE ULTRAFAST RESPONSE

In subsection 2.2.2, we discussed how an ultrafast nonlinear process can be mapped via the perturbation of a plasmon resonance. In contrast to the given example, where the perturbation is caused by the emission of photoelectrons, the number of conduction electrons  $N$  is constant during a mechanical oscillations. Here, the perturbation is caused by a change of the electron-gas and lattice temperature as well as the geometric extension from its equilibrium. The Drude model, given by

$$\epsilon'_{r,D} = 1 - \frac{\omega_p^2}{\omega^2 + \gamma_D^2}; \quad \epsilon''_{r,D} = \frac{\omega_p^2 \gamma_D}{\omega^3 + \omega \gamma_D^2}, \quad (4.5)$$

has two parameters  $\omega_p$  and  $\gamma_D$  which are related to the physical properties of the material. While the damping parameter  $\gamma_D$  increases for larger temperatures due to phonon scattering, the plasma frequency  $\omega_p$  is influenced by the variation of the particle volume during the oscillation [141].

Our model to describe the dielectric function variation during an oscillation is based on linear thermal expansion and completely neglects the response of the hot electron gas during the first picoseconds after excitation. For simplification we assume that the change of the damping parameter  $\gamma_D$  is negligible for temperatures below 800 K ( $\approx 500^\circ\text{C}$ ). The plasma frequency of the excited gold  $\omega_p^* = \sqrt{n_e^* e^2 \cdot (m_e \epsilon_0)^{-1}}$  is computed from the new equilibrium electron density  $n_e^* = N/V^*$  via the linear thermal expansion of the particle. A temperature increase of  $\Delta T$  leads to a equilibrium volume  $V^*$  of

$$V^* = (1 + \alpha_V \Delta T) \cdot V_0 \quad (4.6)$$

with  $\alpha_V$  being the volumetric thermal coefficient and  $V_0$  the initial volume of the unpumped particle. Furthermore, the volume  $V_0$  of a disc with height  $h_0$  and radius  $r_0$  can be calculated by  $V_0 = h_0 \pi r_0^2$ . If we assume an isotropic expansion, the new particle axes

$$h^* = h_0 \cdot \xi \quad r^* = r_0 \cdot \xi \quad (4.7)$$

are expanded by the parameter  $\xi$ . Combining equation 4.6, 4.7 and the volume equation we obtain the modified electron density

$$n_e^*(\Delta T) = \frac{N}{V^*} = \frac{N}{(1 + \alpha_V \Delta T)^{1/3} h_0 \cdot (1 + \alpha_V \Delta T)^{2/3} r_0^2} \quad (4.8)$$

as a function of the induced temperature change  $\Delta T = T_{eq} - T_i$  and expansion parameter  $\xi = (1 + \alpha_V \Delta T)^{1/3}$ . With this, the optical and geometric properties can be modeled as function of the excitation process discussed previously. However, the described model fully neglects the d-band absorption of gold and already fails to compute the linear absorption and extinction spectra in or close to the band transition. This makes it impossible to predict the nonlinear response of the considered discs.

In order to take the missing d-band beneath  $\approx 600$  nm (see subsec. 2.1.1) into account, we define the difference between experimental data  $\epsilon_{r,JC}$  and unperturbed Drude function  $\epsilon_{r,D}$  as

$$\Delta\epsilon_r = \left( \epsilon'_{r,JC} - \epsilon'_{r,D} \right) + i \cdot \left( \epsilon''_{r,JC} - \epsilon''_{r,D} \right), \quad (4.9)$$

with  $\omega_p = 8.89$  eV and  $\gamma_D = 7.088 \cdot 10^{-2}$  eV. The dielectric function  $\epsilon_r^*$  as function of  $\Delta T$  can be written as

$$\epsilon_r^*(\Delta T) = \epsilon_{r,D}^*(\Delta T) + \Delta\epsilon_r \quad (4.10)$$

where  $\epsilon_{r,D}^*$  is the Drude model with  $\omega_p^*$  and the unperturbed  $\gamma_D$ . In the following we consider a gold particle with a height of 30 nm and a radius of 35 nm and the excitation intensities discussed previously. The pump induced change of the lattice

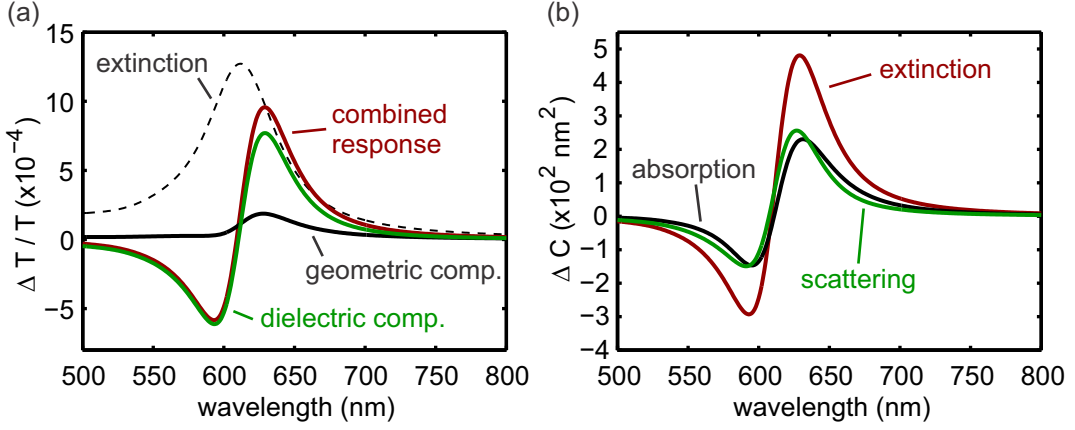


**Figure 4.5**

Model prediction of the nonlinear response by the perturbation of the fundamental plasmon resonance. The contributions of purely geometric (black), dielectric (green), and the combined perturbation to the nonlinear extinction signal is shown in (a). The linear extinction spectrum (dashed black curve) is plotted as reference in arbitrary units. In case of the discussed 35 nm disc, the perturbation of scattering and absorption cross section contribute equally to the overall nonlinear extinction signal (b).

temperature is 40 K and extracted from figure 4.4(b). The thermal expansion coefficient for gold is  $\alpha_V = 42.6 \cdot 10^{-6} \text{ K}^{-1}$  [142]. Under the assumption of a constant probe spot size of  $A_{probe} = \pi 400^2 \text{ nm}^2$ , the nonlinear response is calculated from  $\Delta T/T = \Delta C_{ext}/A_{probe}$ . We follow equation 4.7 and obtain a change of the disc size by  $\Delta r = 0.2 \text{ \AA}$  and  $\Delta h = 0.17 \text{ \AA}$ , for  $\Delta T = 40 \text{ K}$ . Corresponding to these values, the new equilibrium plasma frequency  $\omega_p^* = (1 + \alpha_V \Delta T)^{-1} \omega_p$  is calculated and reduced by 0.085% with respect to the undisturbed gold. Figure 4.5(a) summarizes the several contributions of the response. For comparison, the extinction spectrum (dashed) is plotted in arbitrary units. The solid black curve shows the nonlinear response caused by the change of the particle size by keeping the undisturbed dielectric function of gold. The green curve shows the response of the electron-gas without changing the particle size. The red curve gives the combined nonlinear response by taking the change of the particle size and its dielectric properties into account. Furthermore, the combined response differs from the sum of both partial effects. However, we find that the dominant contribution of the response is given by the perturbation of the dielectric function. The volume change increases the asymmetry of the dispersive line shape. In addition, it must be mentioned that the predicted response fails for wavelengths  $< 600 \text{ nm}$ , due to the d-band absorption. We assumed that the maximum oscillation signal is equal to the maximum thermal signal. Under real conditions, the expected response signal is smaller than the plotted one defining an upper limit. In figure 4.5(b), the change of extinction, scattering, and absorption cross section for the combined response is plotted. In case

of the disc with 35 nm radius, both contribute equally, what changes for different particle sizes (see figure 2.2(b)).

#### 4.3.1 Theoretical prediction for the experimental results

In order to compute the expected signal for our pump-probe experiment as function of the particle size, we combine the models for size dependent excitation and spectrally resolved nonlinear response. Therefore, the size dependent temperature change  $\Delta T = T_{eq} - 300$  K is used to modify the electron density and corresponding optical properties, respectively. Figure 4.6(a) depicts the linear extinction cross section  $C_{ext}$  for the simulation parameters discussed previously. Higher order plasmon

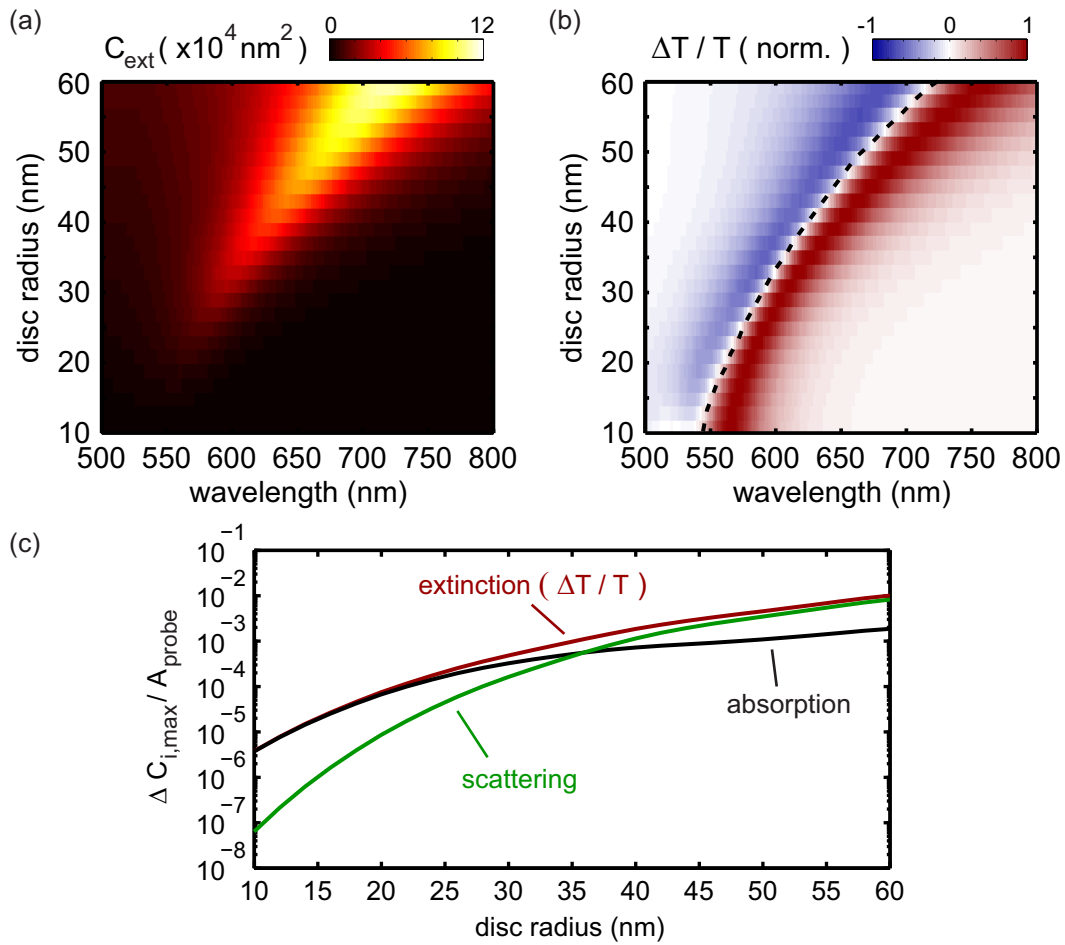


**Figure 4.6**

Linear extinction cross section  $C_{ext}$  as a function of disc radius (a). The plasmon resonance position of (a) is plotted as reference in the simulated nonlinear response in (b). For better comparability, each nonlinear spectrum is normalized to its maximum. The maximum values are extracted separately and plotted in (c). As shown in the previous section, we find an equal contribution of scattering and absorption at a disc radius of  $\approx 35$  nm.

modes are damped out due to the included d-band absorption. The corresponding nonlinear response is plotted in (b), where each spectrum is normalized to its maximum value for better comparability. We find the dispersive response around the fundamental plasmon resonance, independent of the particle size. Furthermore, the asymmetry of the line shape for particle radii  $< 25$  nm is more pronounced and also an effect of the d-band. This is in contrast to a simple derivative of the extinction spectrum which suggests a more symmetric behavior. Figure 4.6(c) shows the maximum signal contrast  $|C_i/A_{spot}|_{max}$  in extinction, absorption, and scattering, by taking the pump excitation at 800 nm into account. In the experiment we investigate discs with radii between 20 nm and 45 nm. We expect relative signals between  $7 \cdot 10^{-5}$  and  $10^{-3}$ .

#### 4.4 SINGLE PARTICLE RESPONSE

##### 4.4.1 Sample fabrication and characterization

Electron beam lithography allows the fabrication of extended two-dimensional structures of almost arbitrary shape and sizes down to a few nanometers in size [143, 144]. The ultra high resolution is slightly reduced as our substrate is non-conductive and has to be transparent. For the given conditions and technology, we reach structure sizes and distances down to 10 – 20 nm with good reproducibility [26, 144].

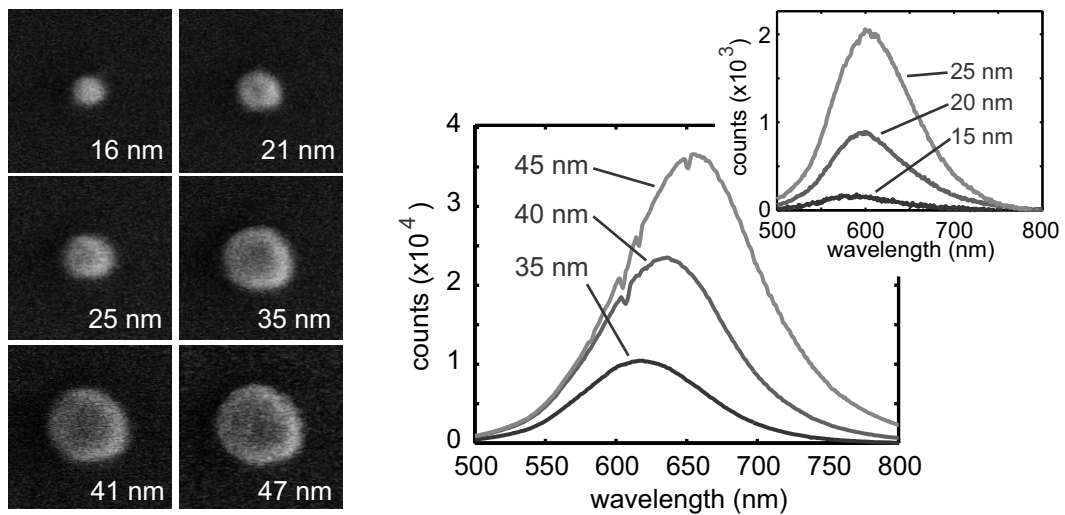
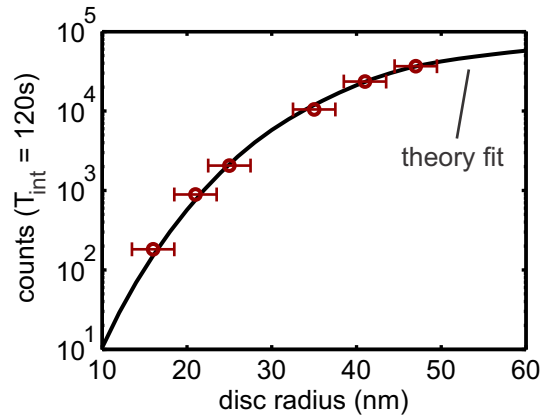


**Figure 4.7**

SEM images of single gold nanodiscs, fabricated by electron-beam lithography. Their height is constant at 30 nm. The measured radii are given in the lower right corners and have an error of  $\pm 2.5$  nm. The corresponding dark-field spectra are plotted on the right side, showing the expected blueshift and a rapid decrease of the scattering amplitude when the disc radius is reduced.

**Figure 4.8**

Scattered spectrum amplitudes as function of particle size. The measured data with errorbars are represented by the red circles, the theory-fit in arbitrary units by the black curve.



As substrate we use a cover glass of  $200 \mu\text{m}$  thickness. The single gold discs are designed in a two dimensional periodic pattern ( $5 \times 20$  discs) with  $2.5 \mu\text{m}$  lattice constant. This allows the optical far-field measurements of individual nanoparticles. Furthermore, each structure can be clearly identified by its column and row number and characterized by SEM, AFM or dark-field spectroscopy. Large marker structures help to locate the disc arrays on the glass substrate. The sample design is written in a layer of PMMA photo resist. After developing the mask, a 3 nm chromium layer is evaporated what guarantees a good adhesion of the gold on the glass substrate. Its contribution to the optical response for structure heights of 30 nm and more is negligible [145]. Finally, the gold structure with the desired height is evaporated and the remaining photoresist is removed. Here I want to thank Mario Hentschel for his great support and contribution to the sample fabrication. The whole preparation process after the design with the eLine software was performed by him. A more detailed description of the several fabrication steps containing all chemical components can be found in his dissertation [146].

Scanning electron microscope images of the fabricated single gold nanodiscs are shown on the left-hand side of figure 4.7. All are on the same substrate and have a constant height of 30 nm. The measured radii, with an assumed error of  $\pm 2.5$  nm, are in excellent agreement with the design values of 15, 20, 25 nm and 35, 40, 45 nm. On the right side of figure 4.7, the corresponding dark-field spectra are plotted. The exposure time for each measurement is kept constant at 120 s. We find clearly shaped plasmon resonances, redshifting and rising in intensity for increasing disc radius. Furthermore, we obtain good agreement for the simulated scattered spectra  $C_{\text{scat}}$ , calculated with an effective medium of  $n_{\text{eff}} = 1.4$  (not shown). The comparison of dark-field spectra and the T-Matrix simulation reveals a slightly broader linewidth in the experiment. We attribute this deviation to the differences between our evaporated gold and the reference material, fabricated under optimal conditions. However, the response amplitude behavior for different disc radii is nicely predicted and shown in figure 4.8. The Lorentz amplitude of the dark-field spectra is plotted as function of the disc radius (red circles). The black curve shows the theory curve in arbitrary units, to fit the integration time of the measurement. Both datasets are

in excellent agreement and verify the numerical model for the linear response and support our predictions for the nonlinear signals. But, as the experimentally determined linewidths are broadened with respect to simulation results, the expected nonlinear responses of section 4.3 are further reduced.

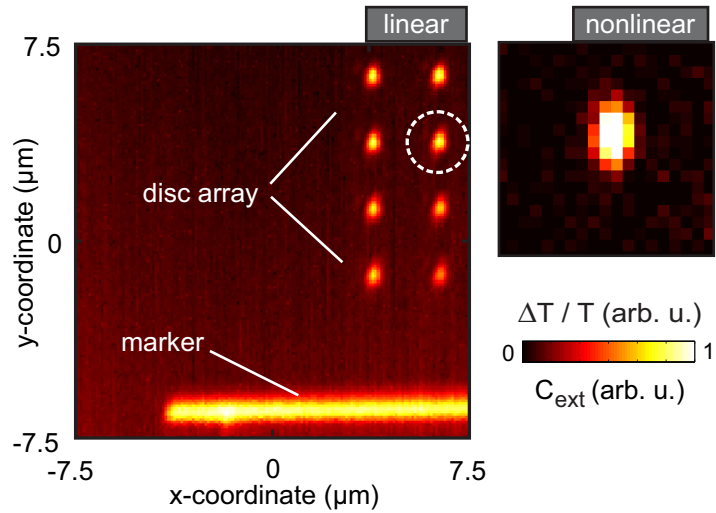
#### 4.4.2 *Ultrafast nonlinear response and data evaluation*

In the following we consider the sample area with single discs of 35 nm radius. The pump pulses have 20 pJ at 800 nm wavelength and launch the acoustic vibrations. From our theory, we expect the maximum nonlinear response at  $\approx 635$  nm and use this as probe wavelength. As the measurements were performed in an earlier phase of the experimental setup, the probe pulses were generated by a white light fiber in combination with a pulse shaper instead of the OPO. The time delay between excitation and interrogation is set to 20 ps. An  $15 \times 15 \mu\text{m}^2$  extinction map of the sample surface with a lateral pixel size of 100 nm is plotted in figure 4.9. The measurement was performed with the confocal sample scanning microscope with balanced detection and a pixel integration time of 20 ms. In the lower part of the image we see part of a marker line which helps for the orientation on the sample. In the upper right, a section of the diffraction limited disc array with  $2.5 \mu\text{m}$  lattice distance can be seen. The right image shows the corresponding nonlinear response of a  $2.5 \times 2.5 \mu\text{m}^2$  area around the marked particle (linear response map). We find a background free signal with the nonlinear response of the particle located in the center. The lateral size of the feature is smaller than the linear response, due to the convolution of the two pulses. In order to obtain the temporal behavior, the particle position is set and optimized to the maximum nonlinear response. Finally, the time delay between pump and probe pulse is tuned. The measured relative transmission change  $\Delta T/T$  over 400 ps in 500 fs steps is shown as black curve in figure 4.10(a). For a time delay of 0 ps, pump and probe overlap temporally. At negative times, the nonlinear response is zero and guarantees that the system fully decays between the pump pulses. Within the first picosecond after excitation, a sharp dip is observed, caused by the hot electron-gas as discussed in section 4.2. After 1 – 2 ps, electron-gas and lattice are in thermal equilibrium, leading to the discussed thermal response. Superimposed to the thermal background, the mechanical oscillations are clearly observable. Both phenomena decay on different timescales. While the oscillation component disappears after  $\approx 300$  ps, the thermal background is still present at the end of the measured trace.

The Fourier space of the mechanical oscillation signal contains information about the vibration modes, their eigenfrequency, damping, and excitation strength (or more precise, their excitation combined with the perturbation strength of the plasmon). In order to extract the optomechanical information of the particle, several data evaluation steps have to be performed. We already discussed the various features in the temporal response, plotted in figure 4.10(a). To extract the pure oscillation feature, we separate the time interval of interest between the green marker lines. For

**Figure 4.9**

Two dimensional extinction map ( $\lambda = 635$  nm) of the sample surface with disc array and marker structure. The nonlinear response in arbitrary units around the marked particle is zoomed and shown at the right side.



the comparison of different measurements, we use the temporally invariant electron response dip as reference to cut at a constant delay after excitation [122]. Here, we typically use times between 10 ps and 20 ps, where the equilibrium state is guaranteed. Within the extracted time interval, we use a monoexponential fit to model the thermal decay (red curve). After its subtraction, we obtain the separated mechanical oscillation trace, plotted in (b). It shows the behavior of a damped oscillator. The transformation into the frequency domain is performed numerically, using the discrete (fast) Fourier transformation (FFT) [147, 148]. The result, consisting of real and imaginary part, contains two mechanical mode properties. In polar coordinates, this is the absolute value which gives the amplitude of a certain frequency, contributing to the overall signal, the other one is its phase. The mechanical spectrum, given by the absolute values, is depicted in figure 4.10(c). We observe one dominant mechanical mode at  $\approx 22$  GHz. From numerical simulations (see figure 4.1) we assign this frequency to the fundamental 'drum' mode, calculated to be at approximately 20 GHz. The higher frequency components are mainly attributed to noise, the lower components to the leftovers of the thermal background separation. The resonance linewidth of  $\approx 5$  GHz reflects the oscillation damping time of  $\approx 200$  ps and can't be improved by additional datapoints or higher integration times, which in best case would lead to a background reduction in the mechanical spectrum. Furthermore, we compare the oscillation amplitude ( $\Delta T/T \approx 12.5 \cdot 10^{-5}$ ) at a small delay time in (b) with the FFT peak amplitude of  $\approx 2.2 \cdot 10^{-5}$  and find a strong deviation. This is a result of the Fourier transformation, where the maximum amplitude in the frequency domain is a function of the oscillation decay. For a given decay time of 200 ps, this corresponds to a factor of 5 between maximum oscillation amplitude and FFT maximum and agrees well with our findings. However, due to the large error in the resonance linewidth, we relinquish on this back scaling in our data evaluation.

In order to prove the reproducibility, all measurement are performed six times in a row. In addition, it allows the calculation of a statistical error. The inset of figure 4.10(c) shows the complex solution of the Fourier transformation in polar co-

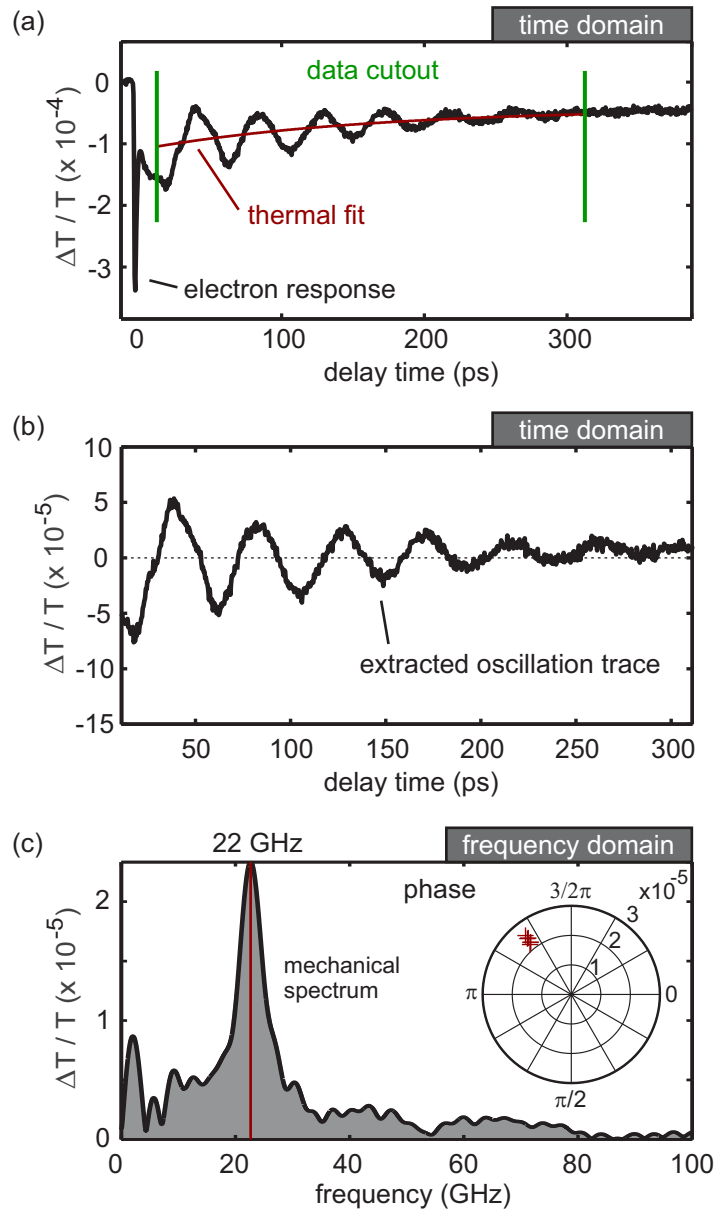


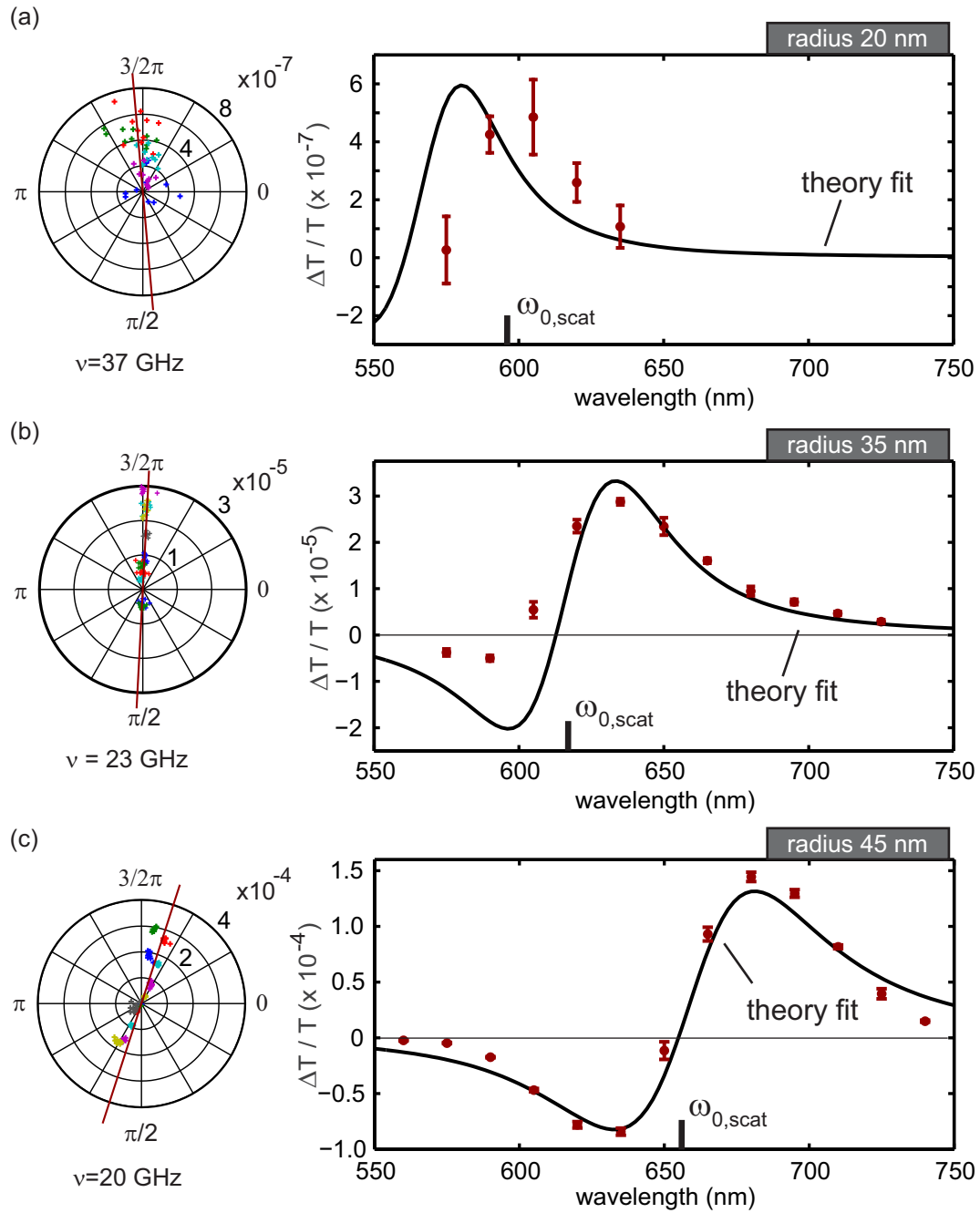
**Figure 4.10**

Data evaluation of the measured mechanical oscillation signal (a), containing the electron-gas response and a thermal background signal. The electron dip is used as temporal reference to obtain a constant data cutout region. Within this section, the thermal background is fitted by a monoexponential function and allows the separation of the pure mechanical oscillation signal (b). The mechanical mode spectrum (c), showing one dominant mode, is given by the absolute value of the discrete Fourier transformation. In addition, the complex solution allows the extraction of the oscillation phase (at 22 GHz). Amplitude and phase are both confirmed and reproduced by 6 identical measurements as shown in the polar plot.

ordinates for all six performed measurements, extracted at 22 GHz. We find a good reproducibility of amplitude and phase, which is given relative to the electron-gas dip. This allows the comparison of the oscillation excitation phase, in case of different probe wavelengths and particle sizes. Furthermore, we compare the measured noise with the shot noise limit. While the average probe power at the sample is  $\approx 4\mu\text{W}$ , the power at the detector is reduced by 50 % to  $2\mu\text{W}$ , due to optical elements in between. With a noise bandwidth of  $\Delta\nu_{BW} = 26\text{ Hz}$  and a pixel dwell time of 50 ms, we calculate a shot noise per pixel of  $\Delta T/T = 2.9 \cdot 10^{-6}$ . The measured noise per pixel is slightly above the shot noise as  $\Delta T/T = 6 \cdot 10^{-6}$  and in agreement with our noise analyses in subsection 2.3.1.

#### 4.4.3 Spectrally resolved response

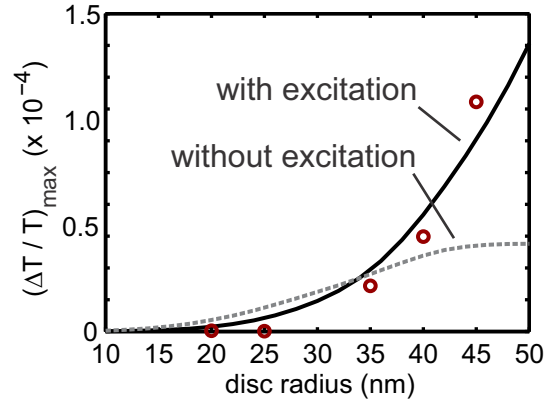
We investigate the discs shown in the SEM images of figure 4.7. The ultrafast nonlinear responses are measured over a spectral range from 560 nm to 740 nm in 15 nm steps. The pump excitation is linearly polarized and fixed at 800 nm. The probe pulses are circularly polarized to average over all polarization angles, as the actual shape differs from a perfectly symmetric disc. For the signal amplitude we use the absolute value of the fundamental mechanical drum-mode, extracted at their resonance position as depicted in figure 4.10(c). Furthermore, the constant excitation process allows us to use the mechanical oscillation phase from the complex Fourier spectrum to define the sign of the response. Consequently, we reconstruct the predicted dispersive lineshape, caused by the sign flip of the gradient around the plasmon resonance. Figure 4.11(a) shows the spectrally resolved nonlinear response amplitude for the disc with 21 nm radius. In order to partially compensate the off-resonant excitation, we use a higher pump intensity with a time average pump power of 5 mW. For comparison we normalize the response to an average pump power of 1.5 mW, afterwards. The polar plot contains all measured data points. Crosses with the same color correspond to a certain probe wavelength. We find a constant oscillation phase at the mechanical resonance at 37 GHz over the whole measured spectrum which proves the origin of the signal. The red line represents the average phase, including the phase shift of  $\pi$ . However, due to the very small signals, slightly above the noise limit, only 5 datapoints are analyzed. The remaining probe wavelengths show neither an oscillation trace, nor the typically strong electron peak. Furthermore, all datapoints have the same phase and sign, respectively. As a consequence, the measured transient transition spectrum, plotted as red curve on the right, has only positive values. For comparison, the model response of section 4.3.1 is scaled by a factor of  $8 \cdot 10^{-3}$  and plotted as black curve. The spectral shift can be explained by the rough approximation with the effective medium. In addition, the response lies in the d-band absorption, leading to further deviations and signal suppression. The scattered spectrum resonance  $\omega_{0,scat}$  is slightly redshifted with respect to the simulated zero crossing. The response of the disc with 35 nm and 45 nm radius is depicted in (b) and (c). In both cases we see the negative sign response on the blue side of the plasmon resonance. The theory fitting factors are

**Figure 4.11**

Spectrally resolved nonlinear response of a single nanodisc with a radius of 20 nm (a), 35 nm (b), and 45 nm (c). Each datapoint (red circle) in the spectra is calculated from the average of 6 identical measurements. The polar plots contain the amplitude and phase of the mechanical mode of all measurements. The constant phase proves the measurement of a real mechanical signal, since the oscillation is independent of the probe process. The black curves are theory fits with different scaling factors.

**Figure 4.12**

Model prediction of the maximum non-linear response with (black) and without (gray) taking the varying excitation conditions into account. The red circles mark the experimental results and show the importance of the excitation process. The simulation fails to model the response of the 20 nm and 25 nm discs, due to the unmodeled d-band absorption.



$3 \cdot 10^{-2}$  for the 35 nm and  $4 \cdot 10^{-2}$  for the 45 nm disc. While the deviation from the missing d-band modeling is still visible for the 35 nm disc, the simulation and measurement results of the 45 nm disc are in excellent agreement. We conclude that the model allows the prediction of the optomechanical response of single gold nanoobjects. However, due to the neglect of the d-band perturbation, the model fails for wavelengths below 610 nm. In figure 4.12 we compare the maximum non-linear response of measurement (red circles) and simulation. Here, the fitting factor for the theory, plotted as solid black curve and including the excitation process, is  $4 \cdot 10^{-2}$ . The gray dashed curve shows the maximum response, neglecting the size dependent pump-absorption and assuming a constant lattice heating ( $T_{eq} = const.$ ). The comparison shows the necessity of taking the excitation process into account, especially if coupled structures of different size are investigated. Furthermore, we assumed constant lifetimes for all modes, which would also influence the maximum signal amplitudes due to the Fourier processing. This assumption is supported by the almost constant linewidths of the mechanical oscillation resonances, shown in the following subsection.

In addition to the presented acousto-optical signals of single gold nanodiscs, their polarization dependence and corresponding asymmetry, as well as the statistical behavior and different particle geometries and materials are investigated. Furthermore, we find an approximately linear behavior of the pump power and even melting or particle deformation processes are observed. The work was done together with Kai Kratzer and Daniela Ullrich. Here, I want to thank them both for the great collaboration and refer to their diploma theses for a detailed discussion of the mentioned investigations [149, 150].

#### 4.4.4 Mechanical properties

Finally in this section, the mechanical spectra of the shown discs are discussed. Figure 4.13(a) shows the mechanical oscillation spectra of the 20 nm, 35 nm, and 45 nm disc in the range of 0 GHz and 100 GHz, extracted at their maximum nonlinear response wavelength. In analogy to the plasmon blueshift for the stronger

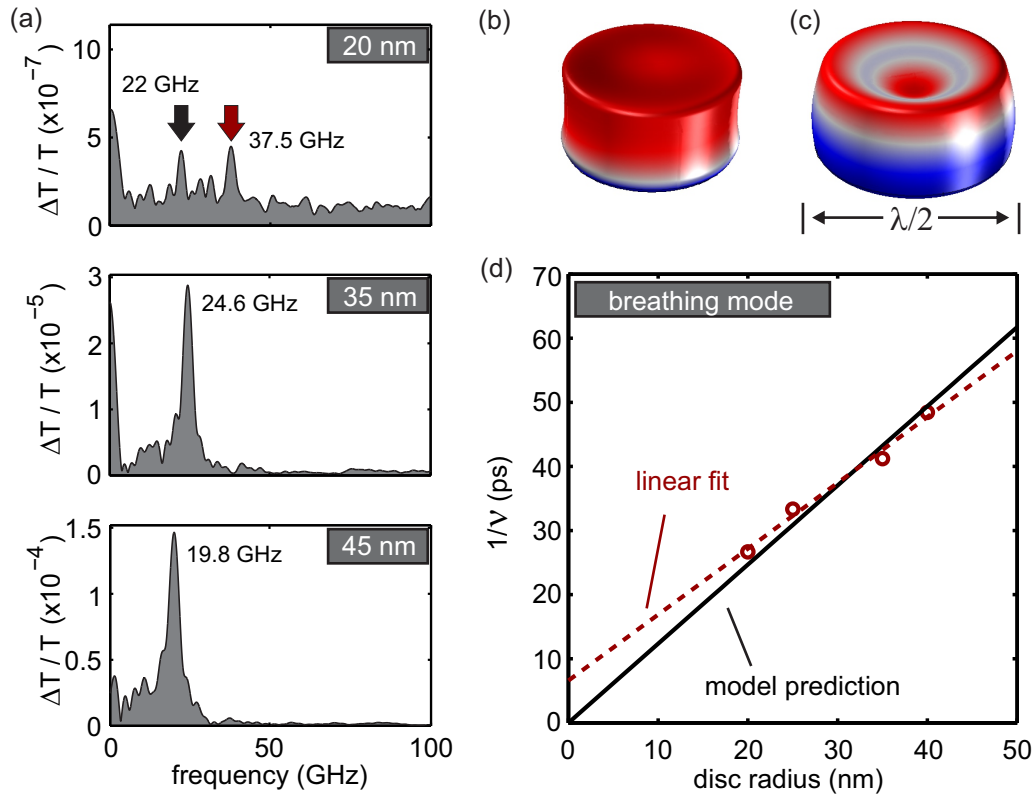


**Figure 4.13**

Mechanical spectra of the presented discs of figure 4.11, taken at their maximum signal wavelength. The black arrow in the 20 nm disc plot marks the extensional mode (b). In addition, the investigated higher frequency drum mode (c) can be observed. A simple model, plotted as black curve in (d), contains the sound velocity of gold and is in good agreement with our experimental results (linear fit in red).

confined electron-gas, the mechanical eigenmodes shift to higher frequencies. The mode spectrum of the 20 nm disc reveals two clear resonances at  $\approx 22.0$  GHz (black marker) and  $\approx 37.5$  GHz (red marker). While both modes are distinguishable in the 20 and 25 nm disc spectra, the larger discs show one dominant resonance, with a barely resolvable mode at the lower frequency tail. We assume that the lower frequency mode corresponds to the 'extensional mode' shown in (b), as its eigenfrequency is almost independent on the disc radius. The higher frequency mode shifts to higher frequencies for decreasing radius and is thus attributed to the 'drum mode', sketched in (c). However, this is just an assumption and cannot be exactly proven as too many unknown parameters, especially for the influence of the substrate, are given in the simulation. However, in order to approximate the first order drum mode eigenfrequency, we follow the sketch of figure 4.13(c) and assume

$$\lambda/2 = 2r_d \quad (4.11)$$

with  $\lambda$  being the mechanical mode wavelength and  $r_d$  the disc radius. With the correlation  $\lambda/c = 1/\nu$  we write

$$\frac{1}{\nu_{dm}} = T_{dm} = 4 \cdot \frac{r_d}{c} \quad (4.12)$$

where  $c = 3240$  m/s is the speed of sound in gold,  $\nu_{dm}$  the eigenfrequency, and  $T_{dm}$  the period of the mode [151]. The black curve in figure 4.13(d) gives the predicted mode frequency as a function of the disc radius. The red circles are the measured values and in good agreement with the simple model. Furthermore, we fit the experimental data with a linear function and allow an offset which considers a constant wave reflection behavior at the gold-air interface. We find a best fitting result for  $c_{fit} = 3891$  m/s. The fit is plotted as dashed red curve. In contrast to the size dependent mechanical eigenfrequencies, the linewidth stays approximately constant within the spectrum resolution. As a consequence, a direct comparison of the peak amplitudes is possible, as discussed in the previous subsection.

#### 4.4.5 Conclusion of single particle experiments

We introduced ultrafast nonlinear spectroscopy of the mechanical oscillations of single gold nanoparticles. After partial absorption of the pump pulse, the impulsive heating of the lattice, mediated by electron-phonon scattering, launches acoustical vibrations which can be detected via the perturbation of the particle plasmon resonance. We discussed a spectrally and size dependent numerical model for the excitation and probe process. The experimentally investigated sample, consisting of gold nanodiscs of 30 nm height and different radii, shows significant mechanical eigenmodes with different size dependence. We apply a simple model, containing the sound velocity of gold, to fit the measured frequency dependence of the higher energy mode and find very good agreement. Furthermore, the data evaluation via the complex Fourier components allows the detailed reconstruction of the spectrally resolved nonlinear response of a single gold nanoparticle. The comparison of simulation and experiment shows a good agreement if the excitation process is taken into account and the nonlinear response is at wavelength  $> 610$  nm, where the influence of the d-band can be neglected. Additional studies such as the pump power dependence and different particle geometries are discussed in the diploma theses of Kai Kratzer and Daniela Ullrich [149, 150]. However, the particles with 20 nm radius are at the detection and shot noise limit. In order to reach particles of smaller sizes, an optical antenna must be applied.

### 4.5 SIGNAL ENHANCEMENT UTILIZING AN OPTICAL NANOANTENNA

The near field of a plasmonic nanostructure, acting as optical nanoantenna, can exceed the amplitude of the incident light field by orders of magnitude [152, 153]. Consequently, the light-matter interaction of a nanoobject which is placed in the close vicinity of the nanoantenna, is enhanced but also correlated to the optical

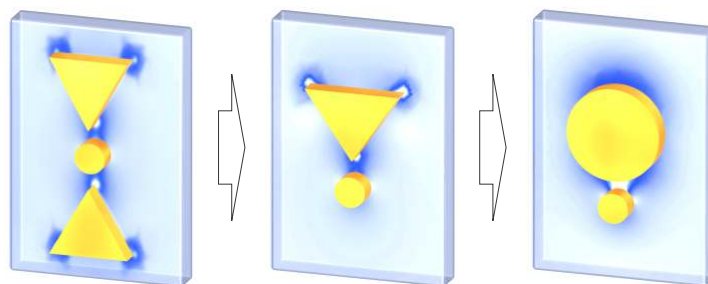


**Figure 4.14**

Illustration of simplifying the antenna geometry to avoid higher order mechanical modes of the antenna which overlap with the desired nanoparticle signal.

properties of the antenna. Furthermore, the electromagnetic interaction leads to a coupling of the two subsystems and results in a combined response with characteristic new optical properties [27, 29, 30]. The coupling depends on geometric and material properties, as well as the oscillator and coupling strength. This offers a huge parameter space for the antenna design. In chapter 6, we introduce a point dipole approximation approach to numerically optimize complex antenna geometries and discuss the different behavior with and without back coupling of the nanoobject. In this section we demonstrate the first realization of an optical nanoantenna to enhance the ultrafast nonlinear response of a gold nanodisc of 20 nm radius [80].

Different antenna geometries are under development, ranging from simple dipoles to complex Yagi-Uda antennas [45, 154–157]. However, in order to distinguish between the nonlinear response of nanoparticle and antenna, we have to use the signal identification via their different mechanical eigenmodes in the Fourier spectrum. For example a bow-tie geometry, known for a high electro-magnetic field enhancement in the feed gap, shows several mechanical modes between 10 GHz and 100 GHz [150, 153]. As a consequence, we are limited in the antenna design and simplify the geometry as illustrated in figure 4.14. The concept of signal enhancement is summarized in figure 4.15. The electric near-field distribution of a disc-shaped antenna, taken at its plasmon resonance, is plotted in the subfigure (a). According to the incident field polarization, two hot spots with high field amplitudes are observed. These hot spots act similar to a nano-lens by concentrating the field in a small volume. The nanoparticle of interest is placed into one of these nanofoci to enhance its light matter interaction via the antenna. Here, the backscattering of the nanoparticle cannot be neglected in the coupled response as the mode pattern and eigenenergy of the coupled system changes significantly as shown in subfigure (b). In analogy to orbital hybridization in molecular physics, the coupling of plasmonic modes can be described by plasmon hybridization [27]. In the case of two particles with one plasmonic mode, a symmetric and an antisymmetric eigenmode with new corresponding eigenenergies is formed as sketched in subfigure (d). In the

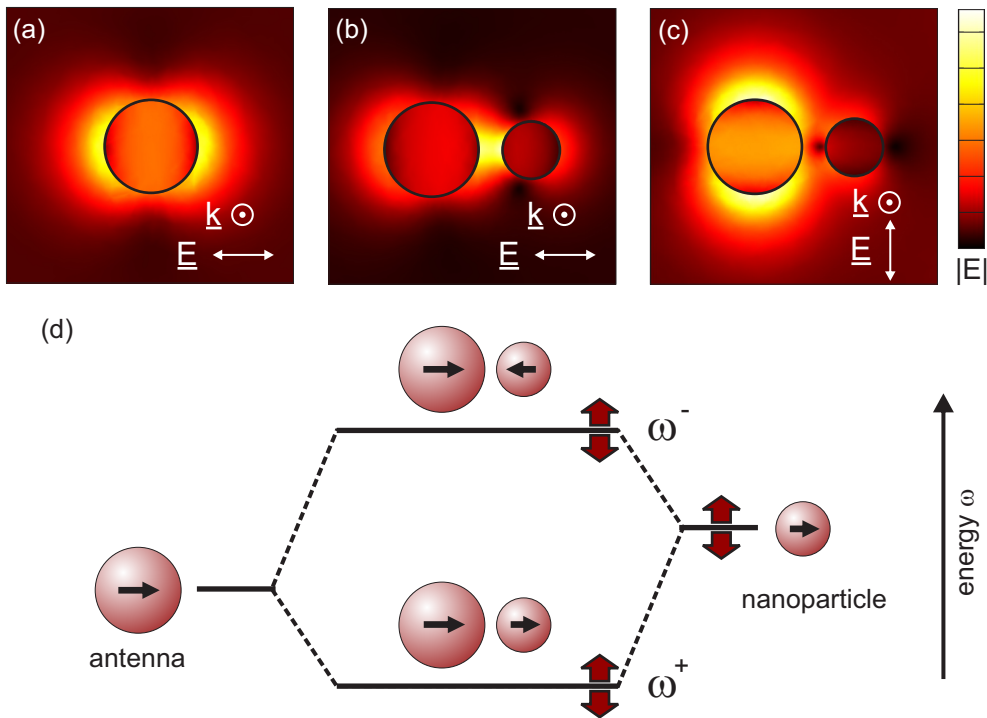


**Figure 4.15**

Basic concept of an antenna for a plasmonic particle. Absolute value of the electric field in the top plane of the structure of the bare antenna (a) and particle-antenna pair system (b). The wavelength is in each case adjusted to the resonance. In the latter case, plasmon hybridization leads to a symmetric  $\omega^+$  and antisymmetric  $\omega^-$  eigenmode with corresponding eigenenergies as shown in (d). A perturbation of the optical properties of the nanoparticle modulates the hybrid modes, promising the desired signal enhancement. For comparison, a polarization rotation by  $\pi/2$  reduces the near-field coupling (c), and an almost negligible antenna effect.

symmetric mode, the plasmon oscillations of antenna and nanoparticle are in phase and attract each other, resulting in an energy reduction of the hybrid mode. Furthermore the mode shows an increased effective dipole moment and couples strongly with the external light field (b). In case of the antisymmetric mode, the energy is blue shifted due to the repulsive near-field forces. The counter phase oscillation leads to a weak effective dipole moment and an almost dark plasmon mode [158].

The perturbation by mechanical oscillations of the nanoparticle influences the hybrid modes of the antenna-nanoparticle pair. As a consequence, the weak oscillation information of the nanoparticle is modulated on a much stronger carrier signal of the antenna. Maximum signal enhancement is achieved for a compromise between spectral overlap (modulation strength) and antenna oscillator strength. A theoretical and experimental study of various antenna geometries, concerning different materials and antenna-particle arrangements, can be found in the diploma thesis of

Daniela Ullrich [150]. A more generalistic model to find optimum antenna geometries and to understand the involved mechanisms is presented in chapter 6. Here, we consider the excitation as well as response enhancement by a disc shaped gold nanoantenna. We consider the excitation and detection polarization being parallel to the long pair axis. This leads to a strong coupling with the bright symmetric plasmon mode at  $\omega^+$ . For comparison, a polarization rotation of the probe pulses by  $\pi/2$  reduces the near-field coupling as depicted in subfigure (c). Here, the strong symmetric mode is shifted to slightly higher, the weak asymmetric mode to lower energies. However, the less efficient coupling decreases the desired antenna effect.

#### 4.5.1 Antenna mediated excitation enhancement

In analogy to section 4.2, we investigate the excitation of mechanical oscillations in the gold structure, consisting of the coupled antenna-nanoparticle pair. In order to separate the energy absorbed by the two substructures, we use the numerical model introduced in section 3.2 and integrate the dissipative loss density over the nanoantenna and particle volumes, respectively. The excitation enhancement  $f_{NP,pump}$  as a function of the antenna radius  $r_a$  and particle surface distance  $g$  is defined as

$$f_{NP,pump}(\lambda, g, r_a) = \frac{P'_{NP,diss}(\lambda_{pump}, g, r_a)}{P_{NP,diss}(\lambda_{pump})} \quad (4.13)$$

with  $P'_{NP,diss}$  being the absorbed power of the nanoparticle in the close vicinity of the antenna, and  $P_{NP,diss}$  the absorbed power of the single nanoparticle. In analogy, the excitation of the optical nanoantenna is influenced as well by the presence of the nanoparticle. In the following we consider a nanoparticle radius of 20 nm and a

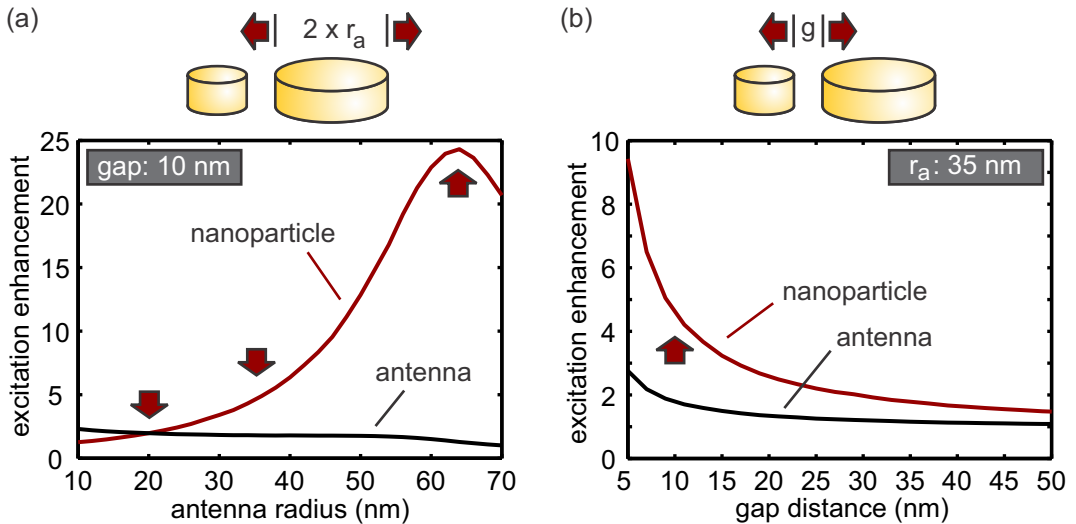


**Figure 4.16**

Excitation enhancement of nanoparticle and optical-antenna as function of antenna radius (a) (gap = const.), and gap distance (b) (antenna radius = const.).

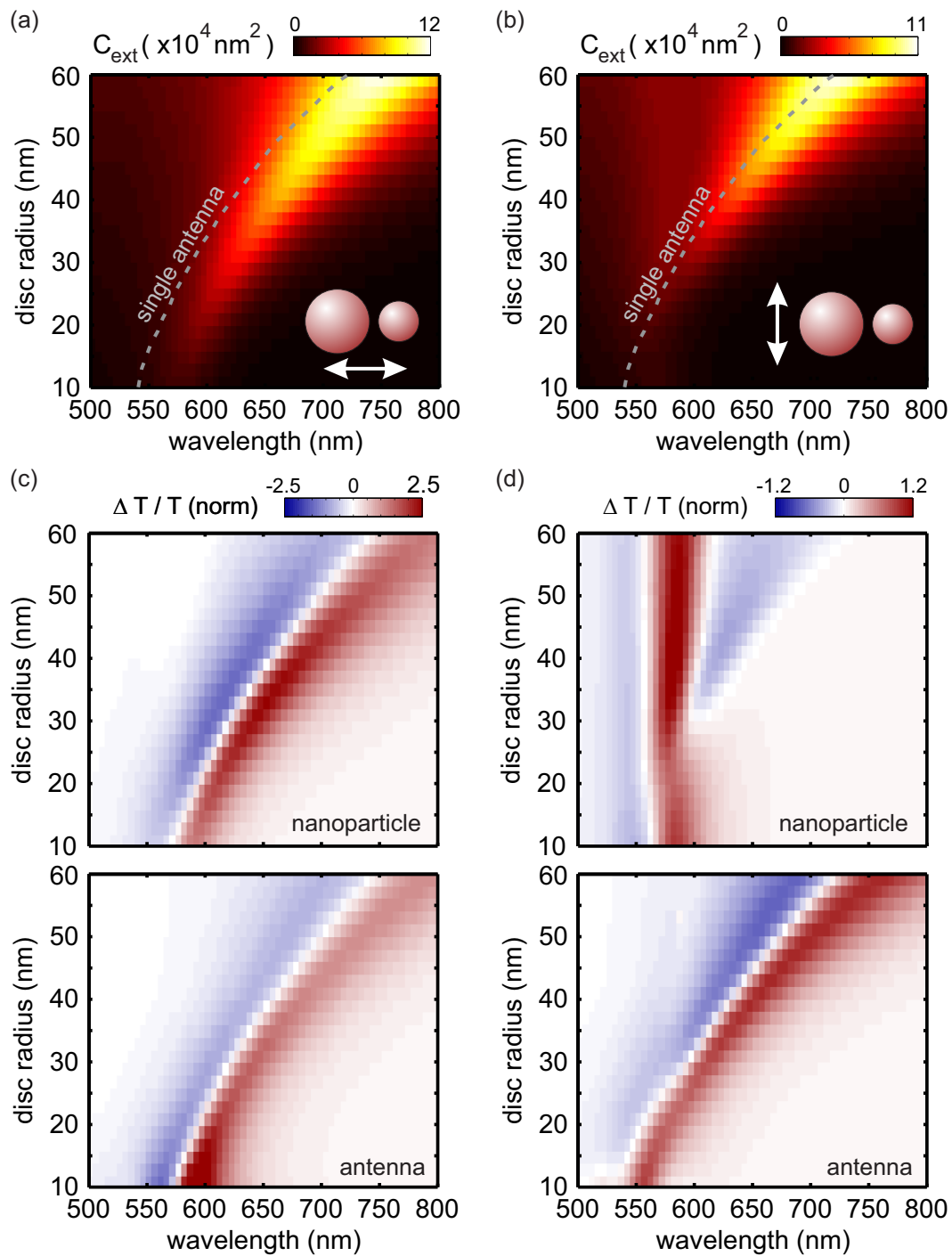
constant structure height of 30 nm. The calculations are performed in an effective medium of  $n_{eff} = 1.4$  at the pump wavelength  $\lambda_0 = 800$  nm. Figure 4.16(a) shows the excitation enhancement of nanoparticle and antenna for a constant gap distance of  $g = 10$  nm and antenna radii between 10 nm and 60 nm. We find a different behavior for the excitation enhancement. In case of two identical nanoparticles with radii of 20 nm, the redshift of the hybrid mode resonance leads to an excitation enhancement by a factor of  $\approx 2$  for each particle (left red arrow). A further increase of the antenna size, for example at  $r_a = 35$  nm (middle red arrow), leads to stronger excitation enhancement for the nanoparticle but decreasing antenna excitation. Here we find an excitation enhancement of the nanoparticle by  $\approx 4.5$  and of the antenna by 1.8. The optimum excitation is found for an antenna radius of 64 nm where the absorption resonance of the coupled system exceeds the pump pulse wavelength. The gap dependent excitation enhancement for a 35 nm antenna is plotted in 4.16(b). We find stronger enhancement for decreasing distances.

#### 4.5.2 Enhanced nonlinear response and antenna optimization

The nonlinear response is influenced by the coupling as well. We discussed how the mechanical oscillation information of nanoparticle and antenna are both projected on the combined hybrid modes. Experimentally, their contribution to the overall signal can be separated by the Fourier decomposition, since both have different mechanical eigenfrequencies. In our theory, the separation can be done directly. In order to investigate the perturbation of the hybrid mode by the nanoparticle, we change its dielectric properties and size as described in the single particle section and keep the antenna properties undisturbed. In analogy, the contribution of the antenna is calculated. The geometry is identical to the previous subsection. Furthermore we consider the pure probe response and neglect the excitation enhancement under the assumption of a constant lattice temperature increase of 100 K. The plots 4.17(a,b) show the linear extinction spectra of the coupled system for a probe polarization along the symmetry axis (a) and perpendicular to it (b). For comparison, the resonance position of the single antenna is plotted as dashed curve. The deviations are due to the interaction with the nanoparticle and show the behavior expected from the plasmon hybridization picture. The nonlinear response of the nanoparticle and the antenna is shown in (c). For both, we find a similar spectral behavior what supports the picture of a signal modulation on the hybrid mode. The amplitudes are normalized to the maximum nonlinear response of the single nanoparticle  $(\Delta T/T)_{NP,max}$  or the single antenna, respectively. Hence we obtain the probe enhancement by

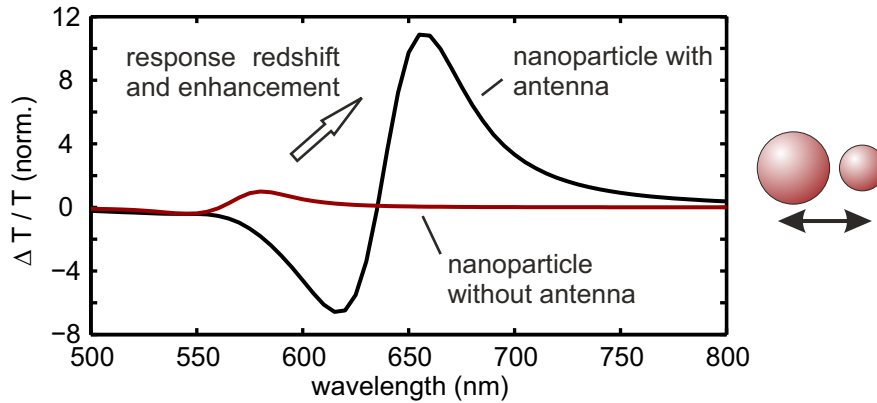
$$f_{NP,probe}(\lambda, g, r_a) = \frac{\Delta T/T}{(\Delta T/T)_{NP,max}} \quad . \quad (4.14)$$

Furthermore, we determine the optimum antenna radius to be at  $\approx 32.5$  nm where the signal of the nanoparticle is enhanced by a factor of  $\approx 2.5$ . The antenna signal is increased by a factor of 1.4. Antennas with smaller radii show better spectral



**Figure 4.17**

Linear response of the antenna-nanoparticle pair as function of the antenna radius for parallel (a) and perpendicularly polarized light (b). Nanoparticle and antenna signal show the same nonlinear spectral behavior (c). The predicted antenna radius optimum for the 20 nm particle lies at  $\approx 32.5$  nm. For the perpendicular polarization (d), nanoparticle and antenna are almost decoupled and no signal enhancement is achieved.

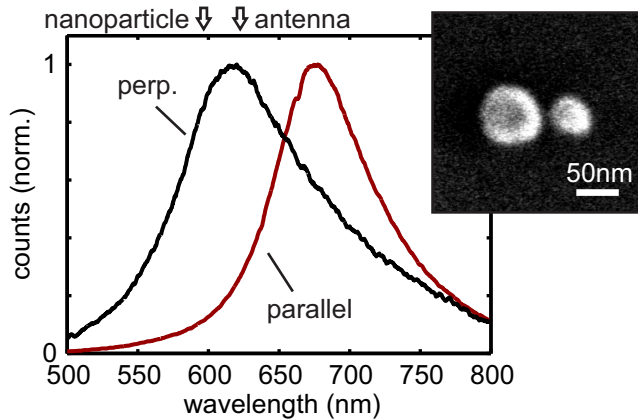


**Figure 4.18**

Comparison between the theoretically predicted single nanoparticle response and the antenna enhanced response, taking excitation and response enhancement into account. The signal is redshifted to the hybrid mode and enhanced by a factor of  $\approx 10$ .

overlap, but have less oscillator strength. For larger radii, the effects are vice versa. Figure 4.18(d) shows the results for the perpendicular polarization. We find the almost uncoupled behavior and thus no antenna effect.

Finally, we compare the single particle with the enhanced response in the case of the antenna with a radius of 35 nm. The simulation results are summarized in figure 4.18. We find a characteristic redshift of the whole signal to the energy of the hybrid mode and furthermore the desired signal enhancement. For the considered antenna size and gap the excitation enhancement  $f_{pump}$  and probe enhancement  $f_{probe}$  contribute almost equally to the overall signal increase by a factor of  $\approx 11$ . The optimum antenna radius with maximum enhancement is found at around 60 nm as the increase of excitation enhancement overcompensates the decrease of the response enhancement. However, we have to keep in mind that the simulation fully neglects the d-band absorption. In the experiment, we expect a much weaker response for the single particle with 20 nm as predicted by our model (see subsection 4.4.3). Consequently, we have to take into account that the contribution of the probe enhancement is much higher than calculated because the hybrid mode shifts the response away from the d-band where our model fits. In the experiment, we use the presented antenna with a radius of 35 nm, although the theoretical optimum with excitation enhancement would be at larger antenna radii. However, the 35 nm antenna gives the best compromise of maximum probe enhancement but weak background noise in the mechanical spectrum which strongly increases for larger antennas and makes the separation of the nanoparticle mode almost impossible.

**Figure 4.19**

SEM image and measured dark-field spectra for parallel and perpendicularly polarized light. For comparison, the resonances of a single nanoparticle and antenna are marked by the black arrows.

#### 4.5.3 Experimental investigation of the antenna-nanoparticle pair

In the following we verify the theoretical predictions by ultrafast pump-probe spectroscopy. Figure 4.19 shows the SEM image of the investigated structure. The antenna has a radius of  $35 \pm 2.5$  nm, the nanoparticle of  $20 \pm 2.5$  nm. Both are separated by a  $\approx 12.5 \pm 2.5$  nm gap and have a height of 30 nm. The fabrication was done in one step with the single discs, discussed in the previous chapter, to guarantee the comparability. The polarization resolved dark-field spectra are plotted next to the SEM image. For comparison, the resonance positions of the single nanoparticle and antenna are marked by the arrows. We find a clear mode splitting for the polarization along the long structure axis. The perpendicular polarization shows almost the same response as the single antenna. The small blueshift proves the hybridization model and a separation of the two particles.

The spectrally resolved nonlinear response of the antenna-nanoparticle pair is summarized in figure 4.20. The excitation is kept constant at 800 nm wavelength with a time averaged power of 1.5 mW and polarization along the long structure axis. In the left column of the figure, the probe pulses are polarized along the symmetry axis, leading to the strong antenna-nanoparticle coupling. In the right column the polarization is perpendicular to it. The inset in (a) shows the measured temporal response at a probe wavelength of 705 nm. The comparison with the single antenna response of section 4.4.2 shows a clear deviation and implies additional mechanical frequency components. The Fourier decomposition confirms this assumption, showing two clear mechanical modes at the fundamental drum mode resonances of the single nanoparticle (red arrow at 36 GHz) and antenna (black arrow at 22 GHz). Consequently, the mechanical mode spectrum allows us to distinguish between the mechanical signals from antenna and nanoparticle. Subfigure (b) shows the amplitude of both modes as function of the probe wavelength. As expected we find the same spectral behavior of nanoparticle and antenna. Furthermore we compare the mechanical phase for all probe wavelengths as the mechanical oscillations are independent of the optical measurement. The polar plots (a) and (b) in figure 4.21 summarize the results of antenna and nanoparticle, extracted at the correspond-

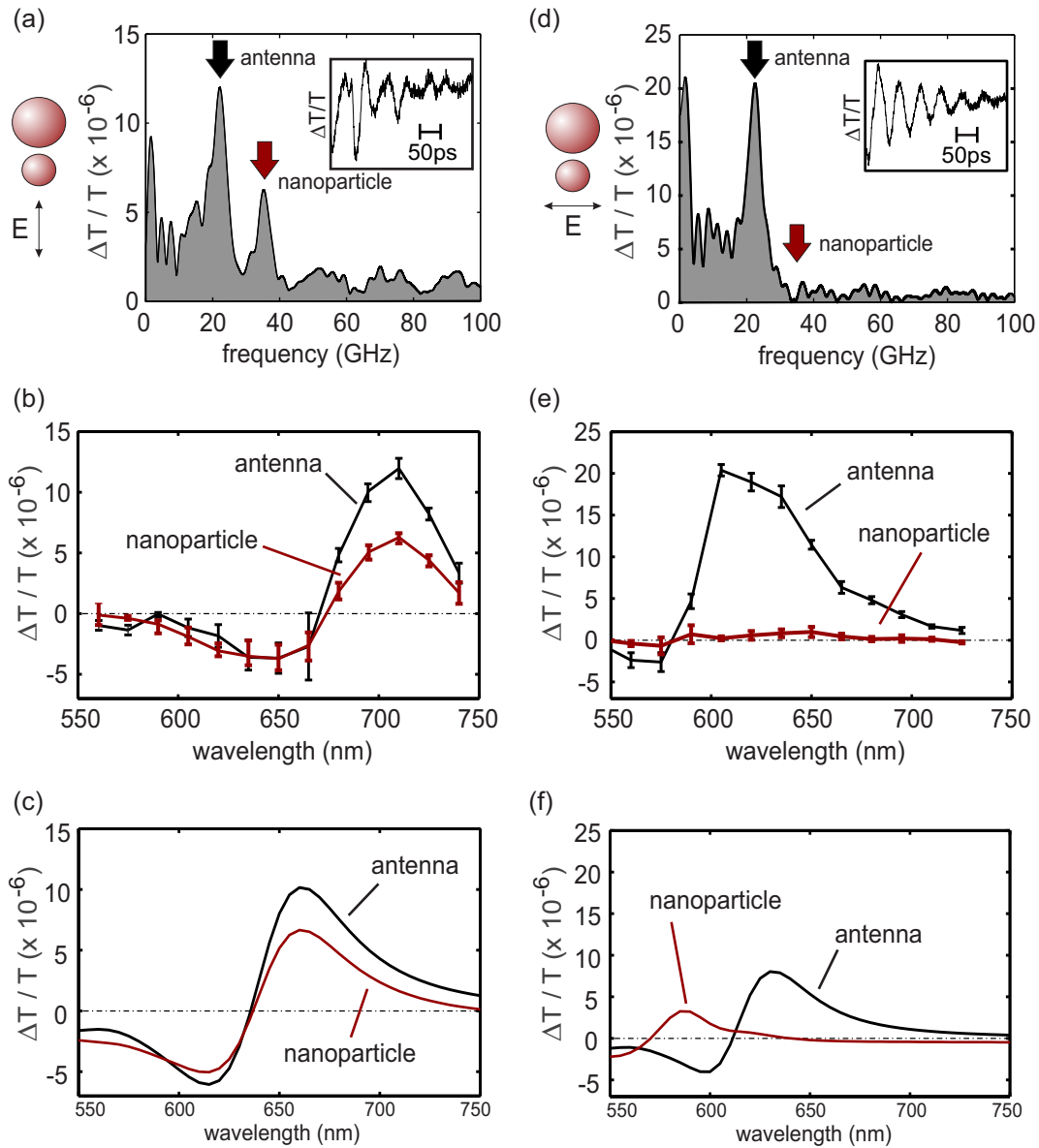


**Figure 4.20**

The polarization of the probe light determines the coupling strength between antenna and nanoparticle. The left column of plots (a,b,c) shows the strong coupling case, the right column (d,e,f) the weak coupling control experiment. The response of the nanoparticle and the antenna are drawn in red and black, respectively. The insets in (a,d) give an example for transient transmission traces, monitoring the mechanical oscillation of the nanoparticles at their maximum signals. The corresponding mechanical spectra (a,d) show always the antenna mode (22 GHz), but only in the strong coupling case (a) also the nanoparticle mode at 36 GHz. (b,e) Oscillation amplitude of both mechanical modes as function of probe wavelength as mean of six consecutive measurements. The error bars give the standard deviation. The line is a guide to the eye. The plots in (c) and (f) show the predicted oscillation amplitudes of the numerical model.

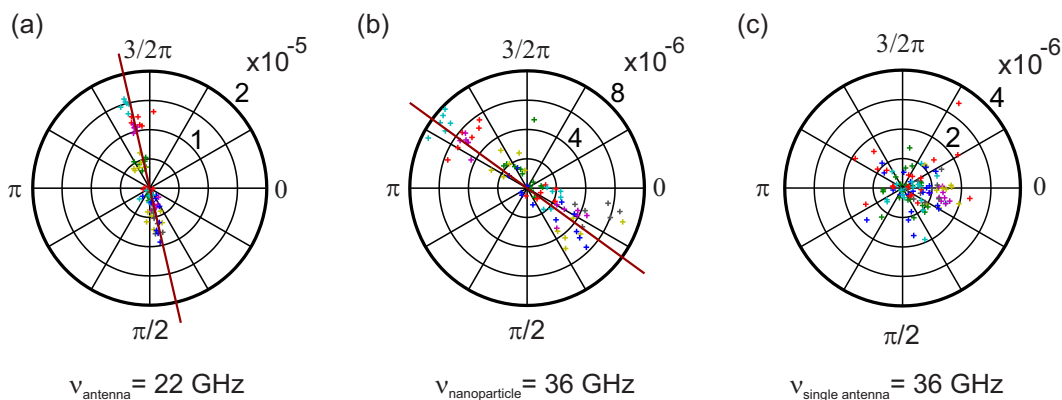


**Figure 4.21**

Complex Fourier values at the mechanical resonances of antenna (a, 22 GHz) and nanoparticle (b, 36 GHz) in the coupled system, both showing phase stability and a good agreement with the single particle measurements. For comparison, the values at 36 GHz of a single antenna are randomly distributed and at the noise limit.

ing mechanical eigenfrequencies. The phases show a constant behavior and are in good agreement with the single particle results. For comparison, the complex Fourier values of the single antenna, taken at the eigenfrequency of the nanoparticle at 36 GHz, are plotted in (c). Finally we compare the experimental data with the previously discussed numerical model. The calculation results are plotted in figure 4.20(c). All spectral features and signal amplitudes as well as the amplitude ratio between antenna and nanoparticle signal are well reproduced. In order to perform a control experiment, the probe polarization is rotated perpendicular to the symmetry axis where we obtain the weak coupling case. Already the detected mechanical oscillation signal, plotted for a probe wavelength of 605 nm in the inset of figure 4.20(d), shows a significant change. The corresponding mechanical mode spectrum shows only one peak, located at the mechanical eigenfrequency of the nanoantenna at 22 GHz. Here, the 36 GHz signal of the small nanoparticle is not recognizable, although the pump excitation process is identical for both probe polarization measurements. This allows the conclusion that the excitation enhancement by the antenna is small with respect to the probe enhancement. Furthermore, a mechanical coupling of the two particles via the substrate would be independent of the probe polarization so the effect is purely optical. The polarization dependent response, based on different plasmonic coupling, proves the concept of resonant antenna enhancement. Again we plot the mechanical oscillation signal of antenna and nanoparticle versus the probe wavelength (e). Here a clear change has taken place, compared to the strong coupling polarization shown in (b). While the nonlinear response of the antenna is still clearly observable over the whole spectral range and located around the uncoupled antenna resonance, the oscillation signal of the small nanoparticle vanishes almost completely. Again, our numerical model predicts the spectral behavior (f) of the signal amplitudes. However, it fails regarding the signal strength of the nanoparticle due to the neglected d-band absorption below 610 nm.

However, the figures (b) and (e) demonstrate clearly that the antenna enhancement can be turned on and off by switching the probe polarization appropriately.

#### 4.5.4 Comparison of single and antenna enhanced particle

Finally we investigate the efficiency and spectral behavior of our antenna. Unfortunately the antenna cannot be removed from the coupled structure without harming the nanoparticle or its close environment. Therefore we compare the response of the presented antenna-enhanced nanoparticle with a single nanoparticle of the same size and shape. However, the nonlinear response of nominally identical nanoparticles varies due to slight variations in size, crystallinity, and environment. Necessarily the statistical distribution of the signal strength must be used to determine the

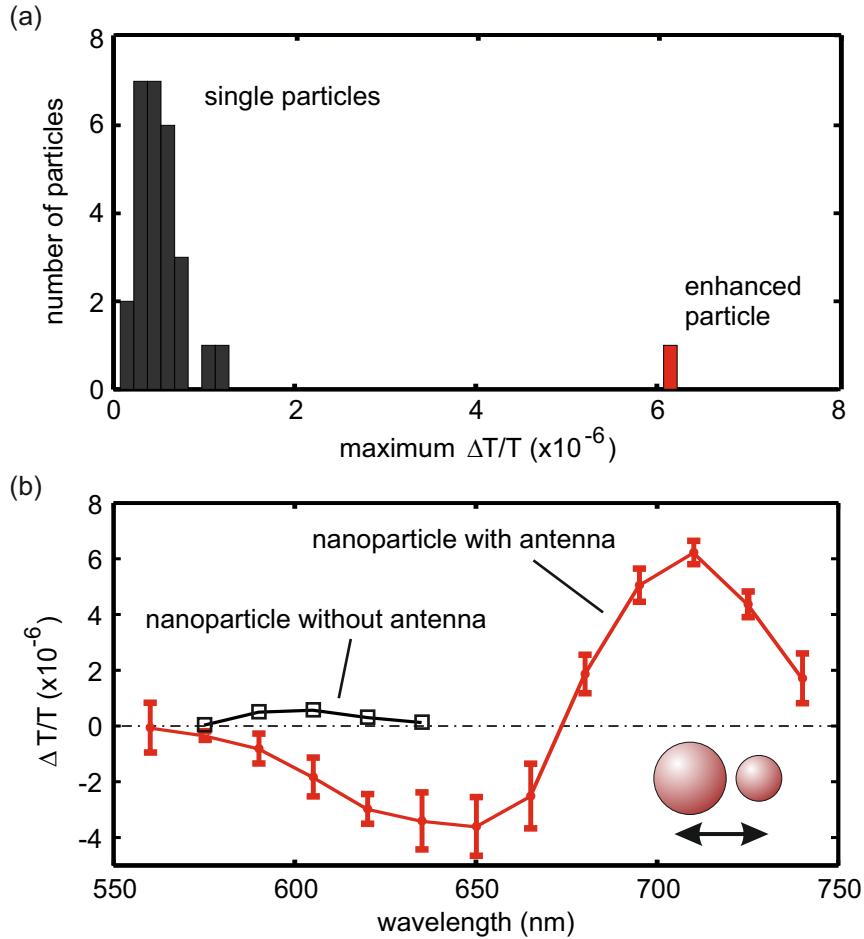


**Figure 4.22**

Histogram of the maximum signal strength of 27 single nanodiscs with 20 nm in radius (black bars). The distribution of the single particles form a Gaussian profile located around  $\Delta T/T \approx 0.5 \cdot 10^{-6}$ . The signal of the antenna-enhanced particle is at  $\Delta T/T \approx 6.1 \cdot 10^{-6}$  which is equivalent to an amplification by a factor of about 10.

antenna enhancement. A histogram of the maximum nonlinear signal response of 27 nanodiscs, normalized to a time averaged pump power of 1.5 mW, is shown in figure 4.22(a). We find a Gaussian distribution of the maximum single nanoparticle response with its mean value at  $\Delta T/T \approx 0.5 \cdot 10^{-6}$  and a width of  $\approx 0.26 \cdot 10^{-6}$ . The disc with 20 nm radius, presented in figure 4.11(a), is in the center of the Gaussian amplitude distribution. Its nonlinear response is plotted as black squares in figure 4.11(b). This reference signal is compared with the antenna-enhanced signal (red dots), which was already shown in 4.20(b). The amplified response is red-shifted and located around the hybrid plasmon resonance  $\omega^+$ . Furthermore we obtain the desired signal enhancement, which is about a factor of ten larger than the signal from the nanoparticle without an antenna. This mechanical oscillation signal is the strongest oscillation we have ever measured of such a small single nanoparticle. For an assumed gap distance of 15 nm we estimate from our model an increase of the excitation by a factor of about 3. The predicted response enhancement gives an additional factor of 3, so that in our model pump and probe enhancement contribute equally for the considered antenna-nanoparticle pair. However, as already discussed in subsection 4.5.2, the prediction for the probe enhancement fails due to the neglected d-band. Consequently, the probe contribution is much stronger with respect to the excitation enhancement and dominates the overall enhancement in the experiment. This is supported by the weak coupling measurements. If the excitation enhancement would contribute equally, we would expect a signal response of the small particle for the perpendicular probe polarization as the excitation process is not changed. This is not the case and we conclude that the probe enhancement plays the dominant role in our experiment as the coupled response is shifted away from the d-band.

#### 4.6 CONCLUSION AND OUTLOOK

In this chapter we presented the first realization of an optical nanoantenna for ultrafast nonlinear spectroscopy at the example of mechanically oscillating gold nanoparticles with frequencies in the GHz region. After the theoretical introduction and modeling of the optical excitation and interrogation of the acoustic vibrations in gold nanostructures, we compared the experimentally determined with the numerically predicted response of single nanodiscs with radii between 20 and 50 nm and a constant height of 30 nm. We found good agreement what allowed us to predict the response of single and coupled nanoparticles with our model, as long as the d-band absorption of gold can be neglected. Furthermore, the mechanical spectra of disc shaped nanoparticles are dominated by the first order drum mode and another, in general weaker extensional mode. In order to enhance the barely detectable 20 nm disc to reach smaller particle sizes, we studied how the excitation and probe processes are influenced by an optical nanoantenna which was realized by a second disc with different radius. A plasmon hybridization picture helps to understand the antenna effect, where the weak nanoparticle signal is modulated on a much stronger hybrid mode. Our model was used to theoretically optimize the antenna-

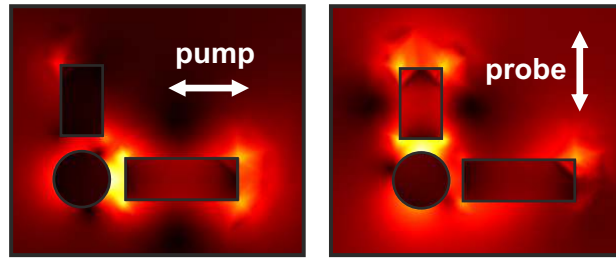


**Figure 4.23**

Complex antenna structure, consisting of two separated antennas where one is optimized for pump excitation of the nanoparticle, the other one for its response enhancement.

nanoparticle structure. The experiment verified the predictions and we achieved an overall enhancement by a factor of ten, compared with the typical response of a single nanoparticle.

Higher enhancement could be realized by resonant excitation with a spectrally tunable pump pulse. While the optimum probe antenna is at a radius of  $\approx 35$  nm, the pump excitation at 800 nm is most efficient for an antenna radius of  $\approx 64$  nm. A complex antenna geometry, for example shown in figure 4.23, can combine maximum pump and probe enhancement. The field distribution shows how a resonant pump antenna (left) can enhance the oscillation amplitude of the nanoparticle by resonant pump excitation, while keeping the other antenna excitation off resonant. The response antenna (right), couples strongly with the nanoobject and enhances its nonlinear response, while the interaction with the pump antenna can be almost neglected. This and several other antenna structures were studied by Daniela Ullrich during her diploma thesis [150]. Even three dimensional structures and antennas composed of different materials are possible and show sharper resonances with respect to the gold discs [159]. Daniela found silver as most promising material for optical antennas. In theory, silver nanoparticles show narrow linewidths without absorption bands in the visible spectrum. Furthermore, it allows spectral overlap with the small gold particles by simultaneously high oscillator strength. This opens a huge parameter space for antenna optimization. However, different antenna geometries and materials are limited by fabrication conditions and the required Fourier decomposition in our analyses. In chapter 6 we present a fast numerical method to approximate plasmon-plasmon interaction which allows, in combination with an evolutionary algorithm, to find optimum parameter settings of many-particle antennas. Furthermore it allows the study of relevant antenna values and their interaction with the nanoparticles. However, an unavoidable circumstance is the Fourier decomposition of the mechanical modes. Here the mechanical background and noise of the antenna is superimposed to the desired nanoparticle signal what limits the capabilities of antenna size and geometric design. A way to circumvent the contribution of the gold antennas could be the usage of dielectric microcavities [160, 161].

QUANTUM CONFINED CARRIER DYNAMICS  
IN A SINGLE CDSE NANOWIRE

---

## 5.1 INTRODUCTION

Semiconductor nanowires bridge the gap between the quantum world and bulk behavior [162, 163]. When the radius of the wire comes into the range of the exciton Bohr radius, the quantum confinement of the electron and hole leads to discrete exciton transition energies what shapes the optical response of the wire [164, 165]. As novel one-dimensional nanostructures, the wires allow the combination of confinement tunability, connectivity to the environment, and polarization dependent behavior. This makes them very appealing nanosystems for fundamental research, next generation solar cells, photodetectors, and future telecommunication applications for example via the coupling to plasmonic nanostructures [19–22, 166, 167]. However, the quantum behavior of these complex systems are still topic of current fundamental research. Spectral diffusion and photobleaching complicate the experiments at room temperature. Furthermore, in the considered size range, the variation of the optical response with the nanowire diameter makes single wire experiments indispensable (see appendix A) [165, 168]. Fluorescence spectroscopy allows insight into the photophysics and emission properties of the nanowires [165, 169, 170]. The ground and higher state absorption of a single nanowire was determined by various techniques [171–173]. However, optical techniques such as transient absorption spectroscopy have to be applied, in order to trace the picosecond resolved quantum confined carrier dynamics before photo-emission. Here, only single wavelength approaches with limited insight to the involved physical processes have been published so far [174, 175].

In this chapter we investigate spectrally resolved ultrafast nonlinear quantum confined carrier dynamics in individual CdSe nanowires with about 10 nm diameter. Figure 5.1 presents the essential idea of the performed experiment. The CdSe nanowire has a diameter of a few nanometers and quantum confined energy states of electrons and holes which are sketched in the inset ladder scheme. A highly focused near-UV pump pulse excites electrons from the valence band above the band gap into the conduction band (blue arrow). On an ultrafast timescale, several of these electron-hole pairs will populate lower energetic exciton states via radiative and non-radiative processes. The probe pulse (red arrow) interrogates the transient bleaching as a function of time delay and probe photon energy. The spectrally resolved bleaching response is correlated with the state population and gives access to previously unattainable processes.

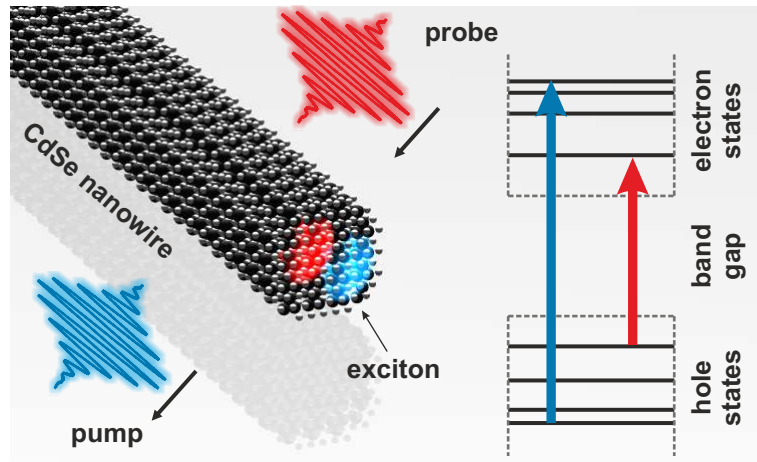


**Figure 5.1**

Illustration of the performed pump-probe experiment of a single CdSe nanowire with a few nanometers in radius. The strong spatial confinement leads to discrete energy states of electrons and holes and thus to discrete optical transitions. The pump pulse in the near UV excites electrons, resulting in an electron and hole state population. The probe pulse interrogates the transition bleaching as a function of time and allows the investigation of ultrafast carrier dynamics in an individual wire. In contrast to zero dimensional nanocrystals, the density of states (DOS) shows no discrete behavior as illustrated, but is similar as known from textbooks.

In the first section we compute the quantized electron and hole states of a CdSe nanowire by effective mass theory [52, 64]. From the solution of the single particle Schrödinger Equation of electron and hole we obtain the wave functions and corresponding eigenenergies, respectively. This allows the calculation of the dipole allowed transition energies and probabilities as a function of the wire radius. After the theoretical overview and its predictions we discuss the sample preparation and wire structure by high resolution transmission electron microscopy (TEM). We perform polarization resolved excitation measurements to characterize the anisotropic properties of individual wires. The findings are supported by our numerical simulations. Finally, we investigate the ultrafast carrier dynamics of quantum confined states of two different wires. We find and discuss characteristic short and long living effects. The direct extraction of the lifetime of various transitions allows the comparison to the corresponding photoluminescence response. We obtain hints on re-absorption processes which can explain the low photoluminescence emission rate of these wires. Finally, we couple a single wire to a plasmonic antenna. We introduce a classical numerical model to predict the coupled response of semiconductor nanostructure and optical antenna. First experimental results of the hybrid system show an enormous increase of the exciton decay rates, what we attribute to the additional decay channels of the plasmon [176, 177].

## 5.2 QUANTIZED ELECTRON AND HOLE STATES

We consider wire radii around or smaller than the exciton Bohr radius of 5.6 nm for bulk CdSe where quantum confinement of electrons and holes leads to discrete eigenstates [171, 178]. The reason for the strong deviation from the bulk semiconductor band structure is the reduced amount of atoms and density of states. Atomistic ab-initio methods allow the precise calculation of the eigenstates of the wire by taking each atom into account [179, 180]. However, the computational effort is huge so that we use an alternative method.

Effective mass approximation is a semiclassical approach to describe a quasi free particle in a lattice environment [52, 181]. In analogy to Newton's second law of motion, the equation of motion of a crystal particle allows the definition of an effective mass

$$\left(\frac{1}{m^*}\right)_{ij} = \frac{1}{\hbar^2} \left[ \frac{\partial^2 \epsilon}{\partial k_i \partial k_j} \right] \quad (5.1)$$

which is correlated with its dispersion relation  $\epsilon(k)$ . For example, a particle in a parabolic shaped band has a constant effective mass. In general the band structure of semiconductors are much more complex. Common methods to describe the nonparabolicities were introduced by Luttinger and Kohn, and Kane [182, 183]. Shabaev et al. and Giblin et al. apply the theory to model excitonic transitions in CdSe nanowires [171, 184]. We follow their detailed introductions to compute the optical properties of our nanowire with radius  $a$ . In contrast to ab-initio calculations, it is assumed that the electron and hole are spatially confined with the bulk band structure properties. The system is reduced and approximated by a two-dimensional model, perpendicular to the wire axis what results in a discrete density of states. The deviations from the extended wire system are neglectable and show good agreement between experiment and theory [171]. Bessel functions  $J_m(\rho) \cdot \exp(im\phi)$  provide the function base, with  $\rho$  being the radial distance from the wire axis and  $\phi$  the angle in polar coordinates. The order of the Bessel function is indicated by  $m$ . In the following we discuss how the equation system with the given boundary conditions is solved and refer to the original paper for more details [184].

### 5.2.1 One band effective mass theory for electron states

The electron states can be found by simple one-band effective mass theory. The complete electron wavefunction  $\Psi_{n|m|}^{(e)}$  is given by

$$\Psi_{n|m|}^{(e)} = \frac{u_{\pm 1/2}^c}{\sqrt{\pi} a J'_{|m|}(a_{n|m|})} J_{|m|} \left( \frac{a_{n|m|}}{a} \rho \right) \exp(im\phi) \quad (5.2)$$

including the conduction band Bloch function  $u_{\pm 1/2}^c$ . Furthermore,  $a_{n|m|}$  is the  $n^{\text{th}}$  root of the  $m^{\text{th}}$  order Bessel function and given by the boundary condition

that the wavefunction  $\Psi(a, \phi) = 0$  has to vanish at the wire radius  $a$ . Defined by the argument of the Bessel function, the radial wavenumber of the electron is  $k_e = a_{n|m|}/a$ . The corresponding energies are derived to

$$E_{n|m|} = \frac{\hbar^2 k_e^2}{m(E_{n|m|})} = \frac{\hbar^2 a_{n|m|}^2}{m(E_{n|m|}) 2a^2} \quad (5.3)$$

with the effective mass

$$m(E_{n|m|}) = m_0 \cdot \left( 1 + 2f + \frac{E_p}{3} \left[ \frac{2}{E + E_g} + \frac{1}{E + E_g + \Delta} \right] \right)^{-1} \quad (5.4)$$

containing the elementary electron mass  $m_0$ , the band-gap energy  $E_g = 1.74$  eV, spin-orbit coupling  $\Delta = 0.42$  eV, and Kane model parameters  $E_p = 19$  eV and  $f = -1.035$ . As  $m(E_{n|m|})$  is a function of the state energy, the combination of the equations 5.3 and 5.4 leads to a recursive function and we have to determine  $E_{n|m|}$  numerically. Therefore, we consider

$$E_{n|m|} - \hbar^2 k_e^2 \cdot (m(E_{n|m|}))^{-1} = 0 \quad (5.5)$$

and compute the first 10 solutions for  $m$ -values from 0 to 5. For our analysis, we typically consider the 20 electron states with lowest energy.

### 5.2.2 Six band effective mass theory for hole states

For the hole states, six-band effective mass theory is applied. The ansatz for the overall wavefunction  $\Psi_{j_z}^{\pm}(\rho, \phi)$  for positive (+) and negative parity (-), is given by the linear combination

$$\Psi_{j_z}^{\pm}(\rho, \phi) = C_h^{\pm} \Psi_{j_z}^{\pm h} + C_l^{\pm} \Psi_{j_z}^{\pm l} + C_s^{\pm} \Psi_{j_z}^{\pm s} \quad (5.6)$$

of the wavefunctions of heavy hole  $\Psi_{j_z}^{\pm h}$ , light hole  $\Psi_{j_z}^{\pm l}$ , and split-off  $\Psi_{j_z}^{\pm s}$  with the corresponding coefficients  $C_h^{\pm}$ ,  $C_l^{\pm}$ , and  $C_s^{\pm}$ . In vector notation, the envelope wavefunctions are given by

$$\begin{aligned} \Psi_{j_z}^{\pm}(\rho, \phi) = & \begin{pmatrix} C_h^{\pm} \\ C_h^{\pm} \\ C_h^{\pm} \end{pmatrix} \begin{pmatrix} \sqrt{3} J_{|j_z \mp 1/2|}(k_h \rho) e^{i(j_z \mp 1/2)\phi} \\ J_{|j_z \pm 3/2|}(k_h \rho) e^{i(j_z \pm 3/2)\phi} \\ 0 \end{pmatrix} \\ & + \begin{pmatrix} C_l^{\pm} \\ C_l^{\pm} \\ C_l^{\pm} \end{pmatrix} \begin{pmatrix} J_{|j_z \mp 1/2|}(k_l \rho) e^{i(j_z \mp 1/2)\phi} \\ -\sqrt{3} J_{|j_z \pm 3/2|}(k_l \rho) e^{i(j_z \pm 3/2)\phi} \\ -i\xi_l(k_l) J_{|j_z \mp 1/2|}(k_l \rho) e^{i(j_z \mp 1/2)\phi} \end{pmatrix} \\ & + \begin{pmatrix} C_s^{\pm} \\ C_s^{\pm} \\ C_s^{\pm} \end{pmatrix} \begin{pmatrix} J_{|j_z \mp 1/2|}(k_s \rho) e^{i(j_z \mp 1/2)\phi} \\ -\sqrt{3} J_{|j_z \pm 3/2|}(k_s \rho) e^{i(j_z \pm 3/2)\phi} \\ -i\xi_s(k_s) J_{|j_z \mp 1/2|}(k_s \rho) e^{i(j_z \mp 1/2)\phi} \end{pmatrix} \end{aligned} \quad (5.7)$$

with

$$\xi_{l,s}(k_{l,s}) = \frac{(\gamma_1^L + 2\gamma^L)\epsilon(k_{l,s}) - E_{l,s}^{(0)}}{\sqrt{2}\gamma^L\epsilon(k_{l,s})} \quad (5.8)$$

being a subfunction for simplicity, and the radial wavenumbers

$$k_h = \frac{2m_0E}{\hbar^2(\gamma_1^L - 2\gamma^L)} \quad (5.9)$$

$$k_{l,s} = \frac{2m_0}{\hbar^2} \left[ \frac{2E(\gamma_1^L + \gamma^L) - \Delta(\gamma_1^L + 2\gamma^L)}{2(\gamma_1^L - 2\gamma^L)(\gamma_1^L + 4\gamma^L)} \right. \\ \left. \pm \frac{\sqrt{(2E(\gamma_1^L + \gamma^L) - \Delta(\gamma_1^L + 2\gamma^L))^2 - 4E(E - \Delta)(\gamma_1^L - 2\gamma^L)(\gamma_1^L + 4\gamma^L)}}{2(\gamma_1^L - 2\gamma^L)(\gamma_1^L + 4\gamma^L)} \right] \quad (5.10)$$

for the different bands. The included Luttinger parameters

$$\gamma_1^L = 2.1 - \frac{E_p}{3E_g} + \frac{E_p}{3(E_g - E)} \\ \gamma^L = 0.55 - \frac{E_p}{6E_g} + \frac{E_p}{6(E_g - E)} \quad (5.11)$$

depend on the energy  $E$  and describe the eigenenergies

$$E_h^{(0)} = (\gamma_1^L - 2\gamma^L) \frac{\hbar^2 k_h^2}{2m_0} \quad (5.12)$$

$$E_{l,s}^{(0)} = (\gamma_1^L + \gamma^L) \frac{\hbar^2 k_{l,s}^2}{2m_0} + \frac{\Delta}{2} \mp \sqrt{\frac{\Delta^2}{4} - \Delta\gamma^L \frac{\hbar^2 k_{l,s}^2}{2m_0} + \left(3\gamma^L \frac{\hbar^2 k_{l,s}^2}{2m_0}\right)^2} \quad (5.13)$$

of the heavy hole, light hole, and split off bands. Finally, the eigenvalue problem of the hole states and wavefunctions is solved in analogy to the states of the electron. The hole wavefunctions  $\Psi_{j_z}^{\pm}(\rho, \phi)$ , given by the linear combination in equation 5.6, have to match the boundary conditions and vanish at the wire edge  $\rho = a$ . As a consequence, the coefficients  $C_h$ ,  $C_l$ , and  $C_s$  can be determined via the transformation of the wavefunction (eq. 5.7 with  $\rho = a$ ) into the homogenous linear equation system  $\underline{\underline{U}}^{\pm} (C_h^{\pm} \ C_l^{\pm} \ C_s^{\pm})^T = \mathbf{0}$ . The relations  $C_h(C_l)$  and  $C_s(C_l)$  are derived to

$$C_h^{\pm} = C_l^{\pm} \left[ \frac{k_s^2((\gamma_1^L + 2\gamma^L) \frac{\hbar^2 k_l^2}{2m_0} - E_l)}{k_l^2((\gamma_1^L + 2\gamma^L) \frac{\hbar^2 k_s^2}{2m_0} - E_s)} - 1 \right] \frac{J_{j_z \mp 1/2}(k_l a)}{\sqrt{3} J_{j_z \mp 1/2}(k_h a)} \quad (5.14)$$

$$C_s^{\pm} = -C_l^{\pm} \frac{k_s^2((\gamma_1^L + 2\gamma^L) \frac{\hbar^2 k_l^2}{2m_0} - E_l)}{k_l^2((\gamma_1^L + 2\gamma^L) \frac{\hbar^2 k_s^2}{2m_0} - E_s)} \frac{J_{j_z \mp 1/2}(k_l a)}{J_{j_z \mp 1/2}(k_h a)} \quad (5.15)$$

Furthermore, the hole wavefunctions have to follow the normalization condition

$$\int_0^a \int_0^{2\pi} \rho |\Psi_{j_z}^{\pm}(\rho, \phi)|^2 d\rho d\phi = 1 \quad (5.16)$$

which allows us to calculate the coefficients and wavefunctions  $\Psi_{n,j_z}^{\pm}$  for a known eigenvalue  $E_{n,j_z}^{\pm}$  of the linear equation system. Furthermore, the eigenenergies are given by the solutions of

$$\begin{aligned} \det(U^{\pm}) &= 0 \\ &= 3\xi_{s,l}(k_{s,l})J_{|j_z \mp 1/2|}(k_h a)J_{|j_z \mp 1/2|}(k_{s,l}a)J_{|j_z \pm 3/2|}(k_{l,s}a) \\ &\quad - \xi_{l,s}(k_{l,s})J_{|j_z \mp 1/2|}(k_{s,l}a)J_{|j_z \mp 1/2|}(k_{l,s}a)J_{|j_z \pm 3/2|}(k_h a) \\ &\quad - 3\xi_{l,s}(k_{l,s})J_{|j_z \mp 1/2|}(k_{l,s}a)J_{|j_z \mp 1/2|}(k_h a)J_{|j_z \pm 1/2|}(k_{s,l}a) \\ &\quad + \xi_{s,l}(k_{s,l})J_{|j_z \mp 1/2|}(k_{s,l}a)J_{|j_z \mp 1/2|}(k_{l,s}a)J_{|j_z \pm 3/2|}(k_h a) \end{aligned} \quad (5.17)$$

and are computed numerically, in analogy to the recursive function of the electron state energies. In our analysis, we typically consider  $j_z$  from 1/2 to 7/2 and solve for the first five energies per angular momentum and parity.

### 5.2.3 *Overlap matrix elements and allowed transitions*

In the previous subsections we introduced the equations to calculate the single particle electron and hole states of a single wire by reducing the system into two dimensions. However, an exciton as bound electron-hole pair requires an interaction term in the Hamiltonian, as given by equation 2.24 in the fundamentals chapter 2.1.3. Nevertheless, we neglect this binding energy which typically reduces the exciton energy  $E_X$  by a few tens of meV [171, 184]. The transition probability for an exciton, when interacting with a photon, is calculated by equation 2.26 (by Fermi's Golden Rule) and the transition dipole matrix element. After the separation of the Bloch functions and the dipole operator, the transition probabilities are calculated by the squared absolute values of the overlap matrix elements

$$K = \left| \int_0^a \int_0^{2\pi} \rho \Psi_{n|m|}^{(e)*}(\rho, \phi) \Psi_{n,j_z}^{\pm}(\rho, \phi) d\rho d\phi \right|^2 \quad (5.18)$$

of the envelope wavefunctions. The corresponding eigenenergies are given by

$$E_{n,m;n,j_z} = E_{n|m|} + E_{n,j_z}^{\pm} + E_g \quad (5.19)$$

with the neglect of the Coulomb binding energy.

Figure 5.2(a) shows an arbitrary selection of electron and hole wavefunctions (absolute values). By equation 5.18 we compute the transition probability between each electron and hole state and obtain the transition matrix. For simplicity, only a part

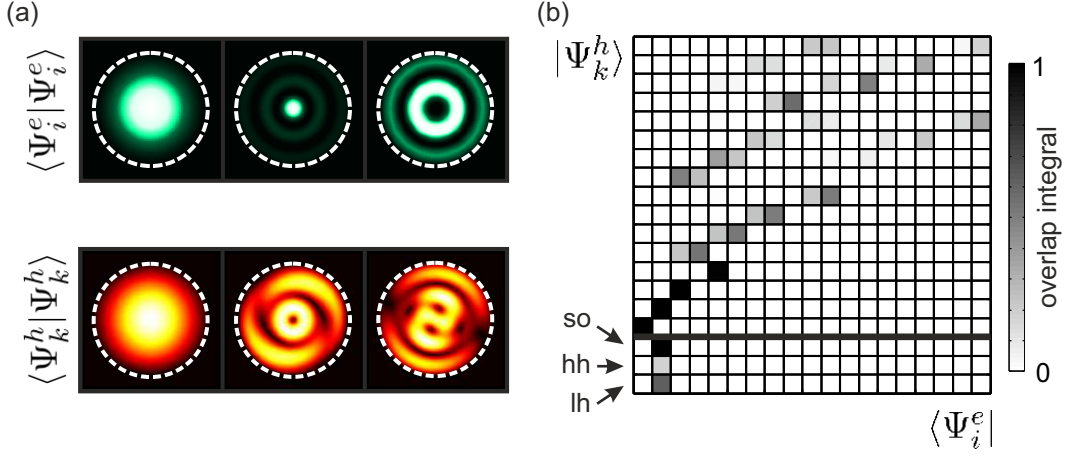


**Figure 5.2**

Calculation of the overlap matrix elements between the computed hole and electron states. The absolute values  $\langle \Psi_i^e | \Psi_i^e \rangle$  and  $\langle \Psi_k^h | \Psi_k^h \rangle$  of a random selection of electron ( $\Psi_i^e$ ) and hole wave functions ( $\Psi_k^h$ ) is plotted in (a). The transition probabilities are given by the square of the overlap matrix elements  $K_{i,k} = \langle \Psi_i^e | \Psi_k^h \rangle$ . A part of the overlap matrix is plotted in (b), with 'lh', 'hh', and 'so' indicating the light hole, heavy hole, and split off bands. We find most transitions being dipole forbidden. However, optically dark states can be populated via decay processes.

of the matrix is visualized in figure 5.2 (b). We find most of the transitions being dipole forbidden and thus not contributing to the optical absorption spectrum. However, although most of the states cannot be directly excited by a photon they can be populated via decay from other states. This is important for our discussion in subsection 5.4.1 where we observe a plasma feature in the ultrafast nonlinear response of a single nanowire.

In order to visualize the optical transitions and approximate the transition spectra as a function of the wire radius, we assume a phonon broadened linewidth (Gaussian distribution) around each transition. Consequently, the absorption spectrum of a wire with radius  $r$  is approximated by

$$\sigma(r, \omega) \propto \sum_{i,k} K_{i,k} \cdot \exp\left(-\frac{1}{2} \left(\frac{E_{i,k} - \omega}{k_B T}\right)^2\right) \quad (5.20)$$

where we sum over all computed transitions, with  $K_{i,k}$  being the transition probability between electron and hole state,  $E_{i,k}$  the transition energy, and  $k_B T$  the approximation for the linewidth broadening by exciton-phonon scattering. Figure 5.3 shows the computed absorption spectra as a function of wire radius. We use  $T = 80$  K for better visibility by thinner absorption linewidths. At room temperature the transitions are barely separable and merge, especially for larger wire radii ( $a > 6$  nm). However, we find the quantized excitonic behavior nicely represented in the spectra. The ground state transition is from the ground state of the hole to the electron's

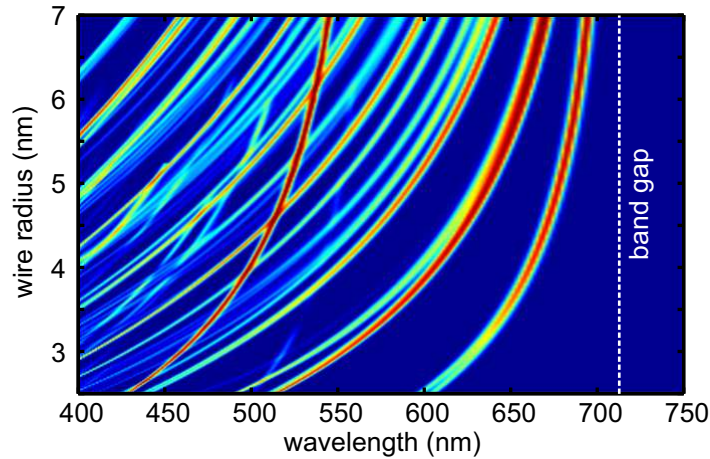


**Figure 5.3**

Radius dependence of the dipole allowed transitions. For better visibility, the linewidths are chosen to 7 meV (80 K).

ground state. Consequently, no lower energetic transitions are possible. Furthermore, the transition probability is large and we expect photon emission as inverse process. We expect good tunability of the ground state absorption line, which red-shifts from about 600 nm wavelength at a wire radius of 2.5 nm and approaches the band gap at approximately 713 nm at larger wire radii.

### 5.3 SAMPLE CHARACTERIZATION

The CdSe nanowires were synthesized by the groups of G.V. Hartland and M. Kuno, using bismuth salts [185]. Their developed method allows easy control about the wire radii combined with almost defect free lattice growth. Here, I want to thank them for their support by providing the sample, containing differently sized wires in a toluene solution.

Atomic resolution of individual wires is achieved by high resolution transmission electron microscopy (TEM) and allows detailed insight into their lattice structure, defects, and geometric properties. We find a constant radius for large parts of a wire and an almost defect free lattice as shown in the TEM image of figure 5.4(a). However, some sections, as imaged in figure 5.4(b), show fluctuations of the radius within an individual wire. Furthermore, wires can be attached to each other and form clusters consisting of two up to a few hundred wires, as depicted in figure 5.4(c). TEM images of dense ensembles of nanowires allow the investigation of the wire radii. Figure 5.4(d) shows the histogram of 40 analyzed wires. We find radii between 2.5 nm and 7 nm, following a Gaussian distribution with a mean value of 4.7 nm. On these lengthscales, we expect quantum confined carriers and discrete exciton transitions as predicted by the discussed theory.

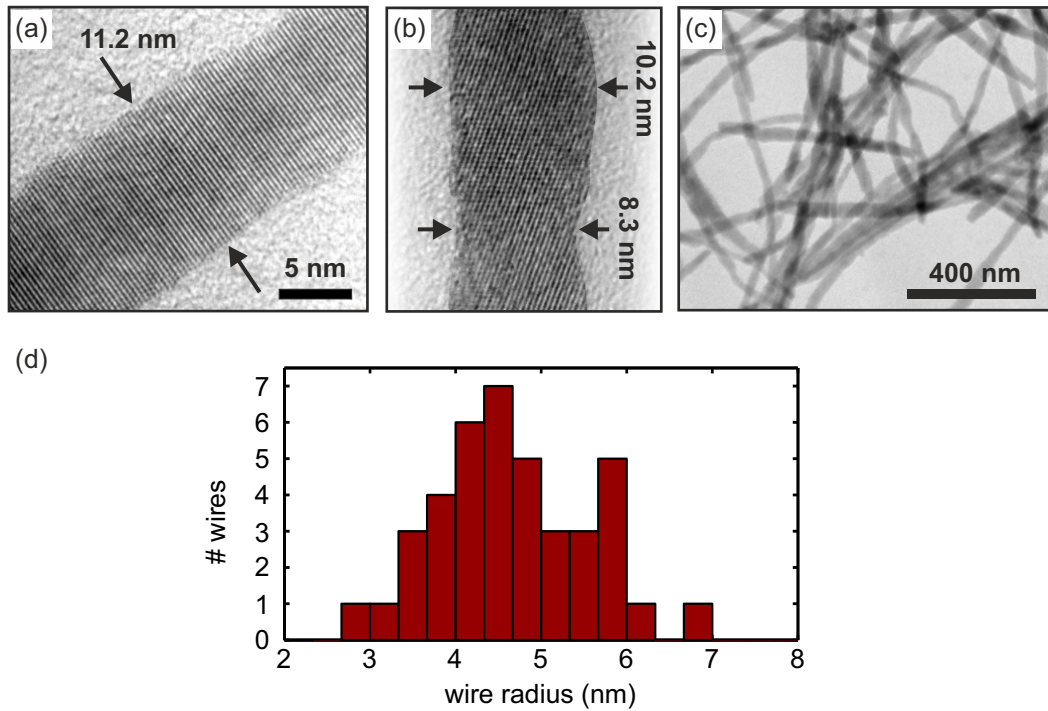


**Figure 5.4**

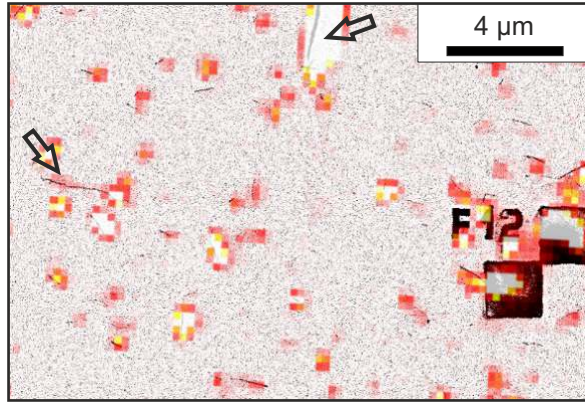
High resolution transmission electron microscopy images of different CdSe nanowires (a,b). Beside lattice defects, radius fluctuations within a single wire are observed. For better visibility we enhanced the contrast between the wire and carbon background in (b). Wire clusters (c) allow us to measure the radii of different wires with high accuracy. (d) The histogram of 40 measured wire radii follows a Gaussian distribution with its mean value at  $\approx 4.7$  nm.

### 5.3.1 Polarization dependent absorption of wires

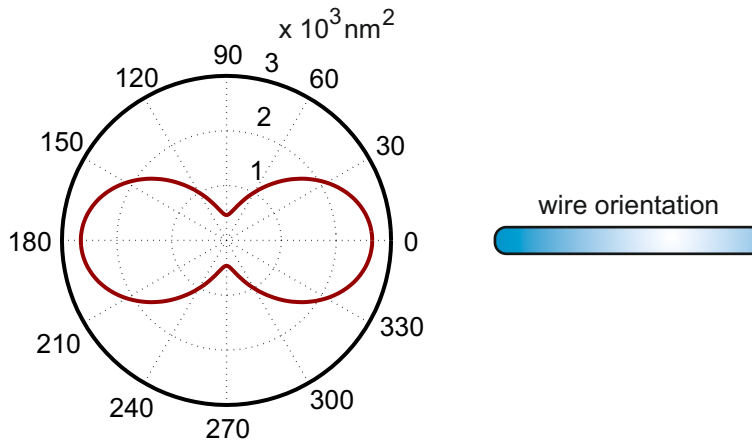
The sample of investigation consists of randomly dispersed single nanowires on a cover glass substrate of 200  $\mu\text{m}$  thickness. The fabrication steps are as follows. First, the substrate is cleaned with HPLC grade toluene and ethanol. Afterwards, a numbered grid of  $2 \times 2 \mu\text{m}^2$  gold markers is written by electron beam lithography in order to allow the localization and identification of certain wires. A diluted toluene-solution of the wires is prepared for 15 minutes in an ultrasonic bath. This reduces the amount of clusters and leads to a higher number of separated wires. Directly afterwards, the solution is slightly shaken and 20  $\mu\text{l}$  of it are spin-coated for 30 s at 3000 rpm onto the glass substrate. Figure 5.5 shows the overlay of high resolution SEM and photoluminescence map, measured in our experimental setup. The resolution and magnification of the SEM image is limited as carbon is deposited for too long exposure times but high enough to identify single wires. The photoluminescence map is resolved with the diffraction limit of the pump spotsize and measured with a vertical excitation polarization with respect to the image. The pump pulse energy is 15 fJ and we detect all polarizations of the emitted

**Figure 5.5**

Overlap of far field photoluminescence measurement and high resolution SEM image, to identify randomly distributed wires via the marker structure. The excitation polarization is vertical to the image, the emission detection is unpolarized.



photoluminescence. We find perfect overlap of both datasets and can identify several single wires, wire clusters, and a gold marker in the lower right corner of the image. Furthermore, for single wires as well as for clusters, we observe a strong orientation dependence of the photoluminescence intensity. The arrows in figure 5.5 show two almost orthogonally oriented wire clusters and wires. The lower left shows almost no photoluminescence, the upper one has a strong emission intensity. This is explained by the polarization dependent absorption cross section of the pump pulses and results from the cylindrical wire geometry [172, 186]. In order to compute this behavior, we apply the numerical model described in subsection 3.2.1. We use plane wave excitation at 390 nm wavelength and assume bulk optical properties of CdSe ( $n = 2.72 + 0.67i$ ). We neglect the glass substrate interface and use an effective medium with an index of refraction of  $n_{\text{eff}} = 1.4$ . The model wire has a length of 400 nm corresponding to the pump spotsize and a radius of 6 nm. The computed absorption cross section  $C_{\text{abs}}$  as a function of the plane wave polarization

**Figure 5.6**

Theoretical study of the polarization dependent absorption cross section  $C_{\text{abs}}$  at 390 nm of the wire. The effect is caused by the cylinder geometry. The maximum absorption of a plane wave is along the wire axis.

$\alpha$  is plotted in figure 5.6. For  $\alpha$  being  $0^\circ$  or  $180^\circ$ , the pump polarization is oriented along the wire. We find an approximately five times stronger excitation for the parallel polarization with respect to the orthogonal polarization. This behavior is found for all wavelengths from the near-UV to the near-IR but with changing ratio between the two polarization component. As a consequence, we align the sample parallel to the pump polarization to achieve maximum excitation.

#### 5.4 ULTRAFAST CARRIER DYNAMICS IN QUANTUM CONFINED STATES

In the following we investigate the ultrafast carrier dynamics of quantum confined states in a single CdSe nanowire by transient transmission spectroscopy. A high resolution SEM image of the investigated wire was taken after the measurements and is depicted on the left side of figure 5.7. Its length is approximately  $1.5 \mu\text{m}$  with a radius of  $5.8 \pm 0.75 \text{ nm}$  as determined by AFM. Pump and probe pulse polarization are aligned parallel to the wire axis, to achieve maximum excitation and probe signal contrast. The pump pulses are at  $390 \text{ nm}$  wavelength, have  $15 \text{ fJ}$  pulse energy at the sample, and are kept constant for all performed measurements. In order to obtain the transition bleaching between several electron-hole states, the probe pulses are tuned over the whole available spectrum from  $520 \text{ nm}$  to  $750 \text{ nm}$  in  $10 \text{ nm}$  steps. Their pulse energies are kept constant at  $130 \text{ fJ}$ . For this configuration of pump and probe pulses, we find negligible photobleaching over the required measurement time.

##### 5.4.1 *Nonlinear response of a single CdSe nanowire*

The nonlinear response is measured as a function of probe wavelength and time delay. The result is shown by the two dimensional dataset on the right side of figure 5.7. We observe relative transmission changes  $\Delta T/T$  on the order of some  $10^{-5}$ . Positive transmittance changes are colored in yellow and correspond to a decrease of the wire absorption or bleaching, respectively. Pump induced increase of the absorption is given by negative transmittance changes, colored in black. We compensate chirp for all wavelengths and adjusted the time axis to  $0 \text{ ps}$  delay, when pump and probe pulse are temporally overlapped. At negative time delays, when the system is probed before the pump excitation, we find no response over the whole spectrum what proves the excitation of an undisturbed system and full relaxation until the next pump pulse arrives after  $13 \text{ ns}$ . Directly after pump excitation, a significant signal with a dispersive lineshape can be observed (labeled 'plasma'). The feature ranges from  $570 \text{ nm}$  to  $740 \text{ nm}$  and disappears on a picosecond time scale. It changes into a much slower varying signal, following an absorptive line shape with its maximum at  $685 \text{ nm}$  wavelength. In the following we will discuss both phenomena in detail and attribute the fast feature to an electron-hole plasma and the slow feature to the bleaching of excitonic transitions.

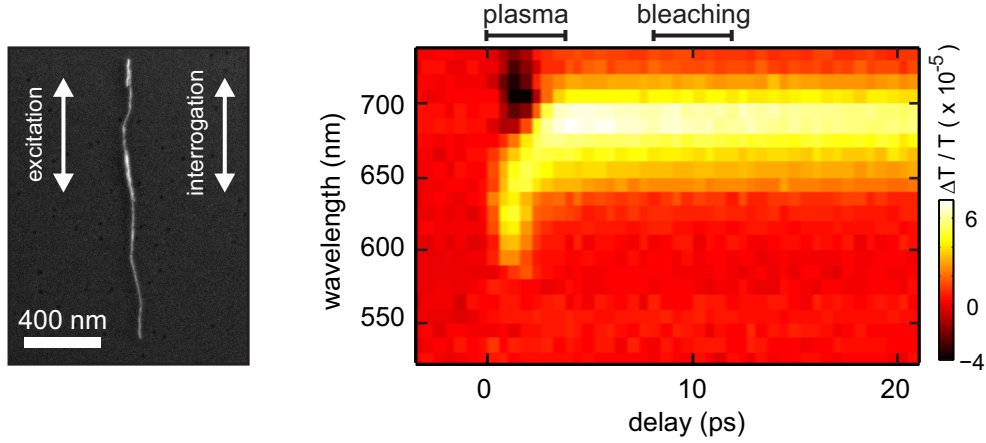


**Figure 5.7**

SEM image of the investigated single CdSe nanowire with a radius of 5.8 nm (left). Spectrally and temporally resolved nonlinear response around the pump excitation. We distinguish between a fast decaying electron-hole plasma response (0 – 4 ps), leading to a dispersive lineshape, and a slower decaying transition bleaching (> 4 ps). The zero delay position was corrected for the dispersion in the setup.

First, we consider the excitation process and approximate the number of photons absorbed out of the pump pulse at 390 nm wavelength. We apply the previously discussed model with the wire of 400 nm length and 6 nm radius to compute the ratio of its absorption and geometric cross section  $C_{geo}$ . For the excitation polarization parallel to the wire axis, we obtain an absorption cross section of 6600 nm<sup>2</sup> per  $\mu\text{m}$  and a conversion factor of

$$\left( \frac{\sigma_{abs}}{\sigma_{geo}} \right)_{parallel} = 0.55 \quad (5.21)$$

between the two cross sections. From the pump pulse energy of 15 fJ, we calculate the corresponding photons per pulse to  $30 \cdot 10^3$ . We consider the Gaussian intensity profile

$$I_{gauss}(x, y) = I_0 \cdot \exp\left(-\frac{1}{2} \frac{r^2}{\rho^2}\right) \quad , \quad (5.22)$$

with  $\rho = 185$  nm being the spot radius ( $\approx 436$  nm FWHM).  $I_0$  is normalized to match the number of photons in the laser pulse. We consider an infinite wire crossing the center of the beam and numerically calculate the number of photons  $N_{geo}$  impinging on the geometric cross section of the wire. With equation (5.21), we obtain the number  $N_{abs}$  of absorbed photons

$$N_{abs} = N_{geo} \cdot \left( \frac{\sigma_{abs}}{\sigma_{geo}} \right)_{parallel} \approx 400 \quad . \quad (5.23)$$

This corresponds to an average electron-hole density of  $1 \cdot 10^{19}$  cm<sup>-3</sup>. The carrier plasma leads to a density dependent renormalization of the band gap energy, causing

a shift of the optical transitions of the wire. This effect is also observed in wires of larger diameter, where the band gap change leads to a variation of the bulk complex refractive index [187, 188]. In order to investigate the plasma effect of our wire in greater detail, we plot the spectrally resolved time dependent nonlinear response in 500 fs steps in figure 5.8(a). We observe a rising dispersive signal within the first picosecond. In the following three picoseconds a transition from the dispersive to the absorptive line shape takes place. This strongly differs from the behavior of wires of larger diameter where the weak confinement seems to cause a much slower plasma decay and carrier recombination. However, for confined carriers we find no further fast changes for times  $> 4$  ps. Here, the remaining electron-hole pairs are relaxed into confined states leading to a bleaching of dipole allowed transitions within the wire. In order to guarantee a full relaxation of the plasma and the investigation of the bare bleaching signal, we analyse the experimental data 10 ps after excitation. The red datapoints in figure 5.8(b) show the average over the time interval labeled 'bleaching' in figure 5.7. We find the bleaching maximum at the lowest energy feature, indicating that most electrons and holes populate the lowest excited state. However, to interpret the complex behavior of the measured response, we use the dipole allowed transition energies between electron and hole states, calculated by the effective mass theory, discussed previously. For adjustment, we tune the wire radius in our simulation to fit the position of the ground state peak. We find a best fitting wire radius of 5.8 nm what is in excellent agreement with our AFM measurements. Higher energy transitions occur between more complex electron and hole states, bunching together into four effective states which we label  $\alpha$ ,  $\beta$ ,  $\gamma$  and  $\delta$  (see figure 5.8(c)). In order to fit the bleaching response with the calculated effective transition energies, we assume a linewidth broadening by exciton-phonon coupling following a Gaussian distribution. By only adjusting the amplitudes of the four Gaussian lines of equal width (fwhm 43 meV), these four states nicely describe our transient absorption signal. The model result is shown by the gray line in figure 5.8(b) and the fitting parameters are summarized in table 5.1. The determined amplitudes reflect the pump-induced population of the states, as depopulation of the crystal ground state can be neglected and the overlap matrix elements are almost identical. It further proves the origin of the detected signal being the expected excitonic transition bleaching.

state	$\alpha$	$\beta$	$\gamma$	$\delta$
energy (eV)	1.81	1.90	2.01	2.33
wavelength (nm)	685	653	616	533
amplitude ( $10^{-5}$ )	6.3	3.0	0.6	0.5

**Table 5.1**

Model parameters with the four calculated effective states energies and fitted bleaching amplitudes.

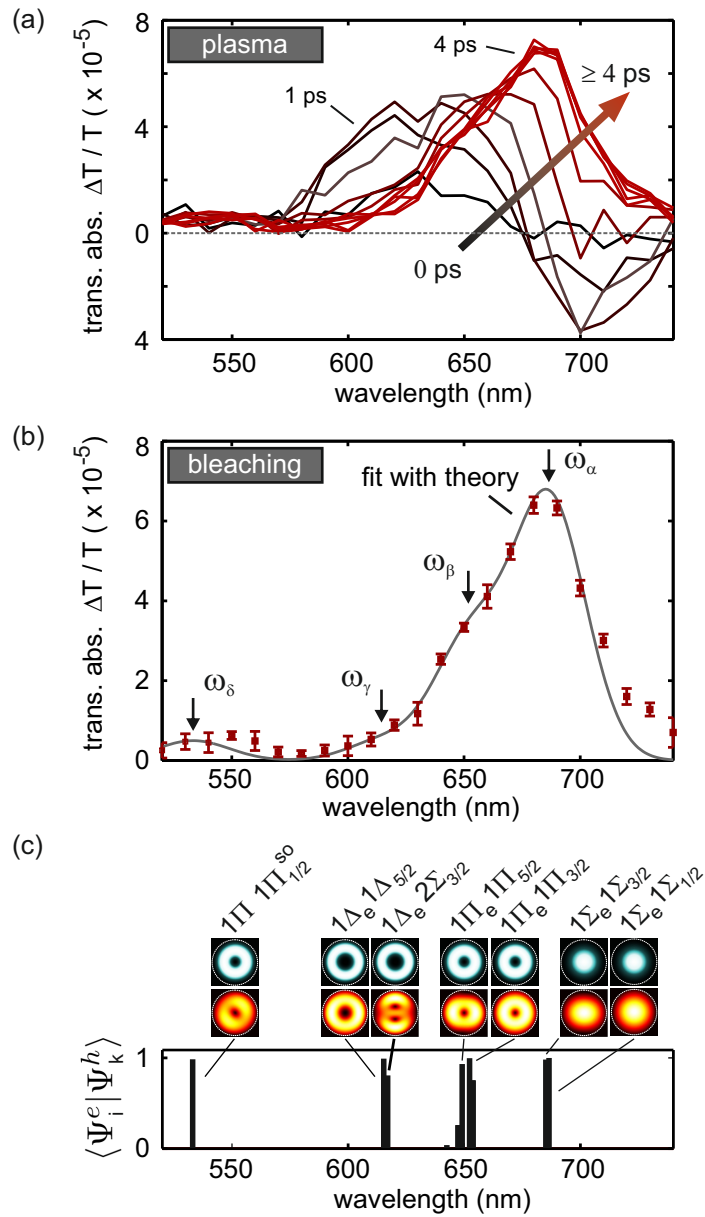


**Figure 5.8**

(a) Transient absorption spectra of the section labeled 'plasma' in figure 5.7, showing the build up and decay of the electron hole plasma. The color encodes the time of the nonlinear response from 0 fs (black) in constant steps of 500 fs to 7 ps (red) after excitation (b). The averaged transient transmission spectrum after 10 ps, labeled 'bleaching', shows several features. The gray curve is a fit with four Gaussians at center energies  $\omega_\alpha \cdots \omega_\delta$ , calculated with the six-band effective mass model for a wire radius of 5.8 nm. For comparison, the overlap matrix elements and the spectral position of the calculated transitions together with their corresponding electron-hole wavefunctions is shown in (c).

#### 5.4.2 Population of exciton states

The integral over an absorption line is connected with the transition dipole moment and the number of dipoles involved. This results, e.g., in the Strickler-Berg formula [189]. As a consequence, transient absorption spectroscopy gives direct insight to the ultrafast carrier dynamics in various quantized states of the wire, at any time after pump excitation. For comparison, photoluminescence measurements are related to spontaneous radiative decay and allow no direct access to the internal processes as the population of certain states. Furthermore, photoluminescence emission requires a high quantum efficiency which is defined as

$$\eta_Q = \frac{\Gamma_{rad}}{\Gamma_{nrad} + \Gamma_{rad}} \quad (5.24)$$

with  $\Gamma_{rad}$  being the radiative and  $\Gamma_{nrad}$  the nonradiative decay rate. As a consequence, a long living exciton state would appear dark, although it is populated and nonradiatively decaying.

In the following, we estimate the pump induced population of excitonic states, extracted from the previously discussed data. We follow R. Loudon [71] and consider the attenuation coefficient

$$K(\omega) = 2 \omega \kappa(\omega)/c \quad (5.25)$$

which is connected to the the Einstein  $B$  coefficient by

$$\int_0^\infty d\omega \frac{K(\omega) c}{\hbar \omega} = \frac{N}{V} B \quad , \quad (5.26)$$

with  $N$  being the number of emitters in the volume  $V$ . The Beer-Lamberts law

$$\frac{I(z)}{I(0)} = \exp(-K(\omega) z) \quad . \quad (5.27)$$

describes the intensity decay of light when propagating the distance  $z$  through a medium. Furthermore, the Einstein  $B$  coefficient is related to the dipole moment  $\mu_{single}$  of a single emitter and given by

$$B = \frac{\pi \mu_{single}^2}{3 \epsilon_0 \hbar^2} \quad , \quad (5.28)$$

where the factor  $1/3$  comes from averaging over all dipole orientations. From the combination of equation 5.26 and 5.28 we derive

$$N \mu_{single}^2 = \frac{3 \epsilon_0 \hbar^2}{\pi} V \int_0^\infty d\omega \frac{K(\omega) c}{\hbar \omega} \quad (5.29)$$

what gives a correlation between the number of emitters and the attenuation coefficient.

We experimentally determine the pump induced relative change in transmission  $\Delta T/T$ . From equation 5.27 we obtain the relation

$$z \Delta K(\omega) = -\ln \left( 1 - \frac{\Delta T}{T} \right) \quad (5.30)$$

which, in the limit of small absorption, can be approximated as

$$z \Delta K \approx \frac{\Delta T}{T} \quad . \quad (5.31)$$

We use  $V = A_{spot} \cdot z$  for the focal volume of our probe pulses and assume an invariant transition dipole moment, after pumping the wire. Consequently, we obtain

$$\Delta N \mu_{single}^2 = \frac{3 \epsilon_0 \hbar^2}{\pi} A_{spot} \int_0^\infty d\omega \frac{\frac{\Delta T}{T} c}{\hbar \omega} \quad . \quad (5.32)$$

by combining equations 5.29 and 5.31. The integral on the right hand side of equation 5.32 is separately solved for each transition ( $\alpha - \delta$ ), with  $\Delta T/T$  from the model fit discussed in the previous subsection. The computed values for  $\Delta N \cdot \mu_{single}^2$  are listed in table 5.2. In order to find the number  $\Delta N$  of excited excitons we calculate the single emitter dipole moment  $\mu_{single}$  as introduced in subsection 2.1.3 in the fundamental chapter. Oscillator strength  $f$  and dipole moment of a single emitter are given by

$$\mu_{single}(D) = 9.37 \sqrt{\frac{f}{\hbar\omega(eV)}} \quad (5.33)$$

$$\text{with } f = 45 \frac{\lambda^2(\mu m^2)}{n_{eff} \tau_{rad}(ns)} \quad (5.34)$$

where  $\lambda$  is the emitter wavelength,  $\tau_{rad}$  the purely radiative lifetime without non-radiative decay of the exciton, and  $n_{eff}$  the effective medium refractive index. A lower limit for the radiative lifetime is the measured luminescence lifetime  $\tau_{lumi} = 800$  ps of the wire. We assume a radiative lifetime of  $\tau_{rad} = 3$  ns, close to the lower limit and compute the oscillator strengths and dipole moments at the transition energies  $\omega_\alpha - \omega_\delta$ . We use a constant spot size area over the whole spectral range of  $A_{spot} = \pi r_{spot}^2$  with the radius  $r = \frac{\lambda}{2NA}$  and a numerical aperture of  $NA=0.9$ . The results are listed in table 5.2 and allow us to approximate the population number of the several states. We find the listed state populations and an overall number of  $\Delta N \approx 50$  excitons, created by the pump pulse. Distributed over a wire section within the probe focus of approximately 400 nm, this would lead to a volume averaged exciton-exciton distance of 12 nm. This is in the order of the exciton Bohr radius of 5.6 nm of bulk CdSe. Finally, we predict the photoluminescence intensity by the calculated values. As a consequence of the equations 5.32 and 5.33, we obtain with

$$\Delta N \propto \frac{1}{\mu_{single}^2} \propto \tau_{rad} \quad (5.35)$$

state	$\alpha$	$\beta$	$\gamma$	$\delta$
$\Delta N \cdot \mu_{single}^2$ (D <sup>2</sup> )	606	840	4450	9834
$\lambda$ (nm)	533	616	653	685
$f$	4.3	5.7	6.4	7.1
$\mu_{single}$ (D)	13	16	17	19
$\Delta N$	3.8	3.4	15.1	28.6
$N_{lumi}$	0.9	0.8	3.5	6.7

**Table 5.2**

Overview of the calculation results

the proportionality between excited excitons  $\Delta N$  and their purely radiative lifetime. However, the number  $N_{lumi}$  of emitted luminescence photons does not depend on the choice of  $\tau_{rad}$ , as it cancels out via the quantum efficiency  $\eta_Q$ . This is shown by

$$N_{lumi} = \Delta N \eta_Q = \Delta N \frac{\tau_{lumi}}{\tau_{rad}} \propto \tau_{lumi} \quad (5.36)$$

and allows us to approximate the emitted photons, listed in table 5.2. However, our photoluminescence measurements show a significantly smaller amount of emission. We attribute this phenomenon to reabsorption processes within the wire what will be discussed in greater detail in subsection 5.4.4.

#### 5.4.3 Investigation of transitions and photoemission lifetimes

In the following we investigate the lifetime of the carrier population. For this purpose, we increase the measured time delay to above 400 ps and change the observed wire. This allows us to prove the reproducibility of the measured data and its agreement with effective mass theory. By AFM, we determine the wire radius to  $3.7 \pm 0.5$  nm. The measured transient absorption spectra are shown in figure 5.9(a). As a consequence of the smaller radius and a stronger quantum confinement, the ground state and higher order transitions are blueshifted with respect to the wire investigated previously. In analogy to subsection 5.4.1, we determine the dominant optical transitions in the six-band effective mass model and find a best-fitting wire radius of 4.1 nm. The upper graph of figure 5.9(b) shows the computed transition wavelengths with corresponding probabilities. Again, we can clearly identify the blueshifted effective transitions. The  $\delta$  transition is predicted outside our spectral region around 500 nm. In order to describe the whole transient transmission spectra labeled 'early', we slightly shift the peak positions with respect to the six-band effective mass model. Again, we find a very good agreement between measurement and theory. However, different decay rates of the several transitions are found by scaling the fitted curve to match the measured bleaching signal at a later time, extracted around 380 ps (labeled 'late'). Especially the  $\beta$  state shows a significantly

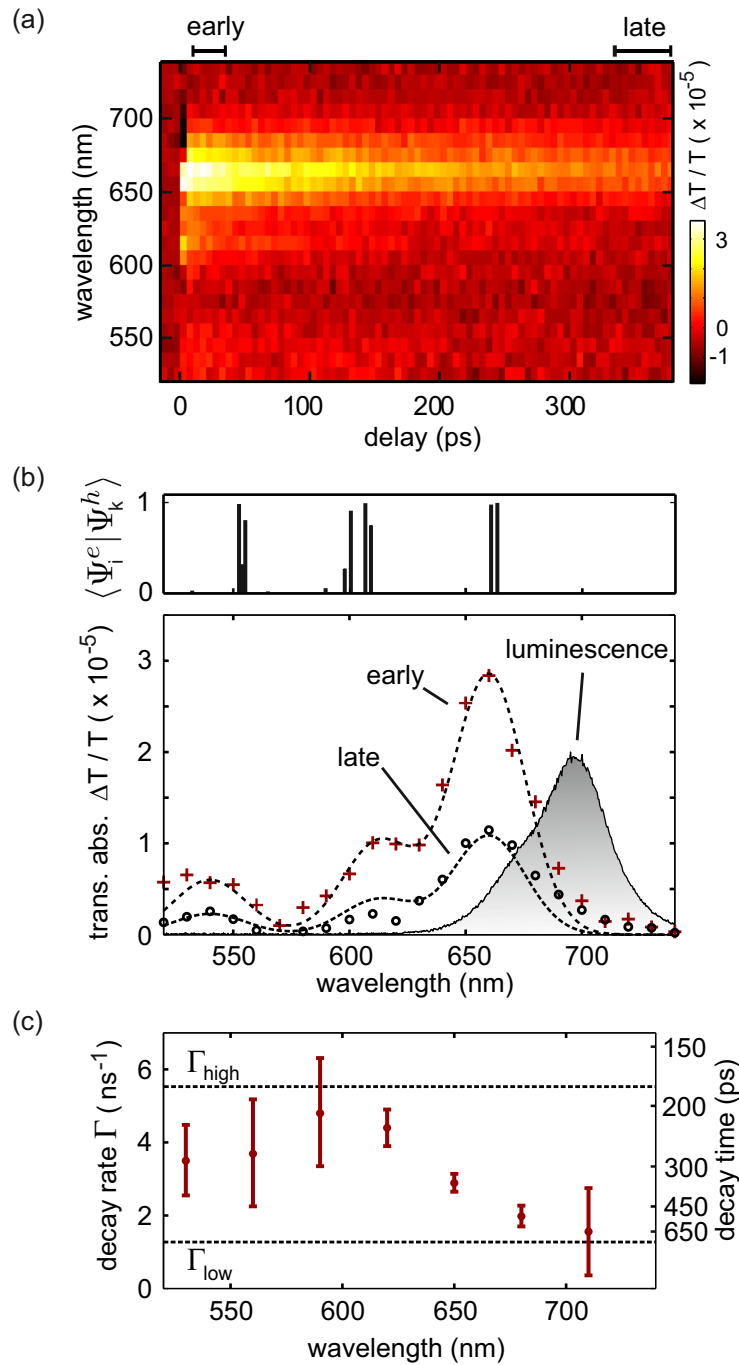


**Figure 5.9**

Nonlinear response of another wire with 4 nm in radius (a). We distinguish between early (red crosses) and late response (black crosses) in (b). The early response is fitted (4.1 nm) and scaled to fit the  $\alpha$  transition of the late response, implying different decay rates for the different transitions. The decay rates by averaging over 30 nm spectral width and fitting a single exponential decay are shown in (c). The error bars give the interval over which  $\chi_2$  increases by 10%. The dashed lines mark the photoluminescence decay rates, using a biexponential fit in the model 2.51.

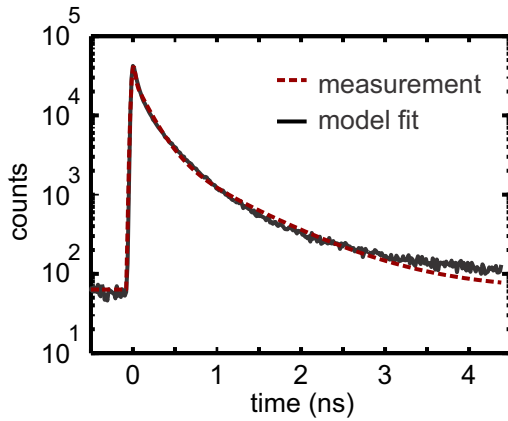


**Figure 5.10**

Time resolved photoluminescence (black) and overlaid the model fit (red), using a biexponential fit for the decay (see. equation 2.51). The fit yields decay times of 180 ps and 790 ps with integrated amplitudes of 4 and 2.5 when the instantaneous response is normalized to an integrated amplitude of 1.

shorter lifetime with respect to the  $\alpha$  and  $\gamma$  states. This is further analyzed, by fitting monoexponential functions to the delay traces as a function of wavelength. Figure 5.9(c) shows the fitted decay rates and lifetimes, respectively. We find decay rates between about  $2 \text{ ns}^{-1}$  around 700 nm and  $5 \text{ ns}^{-1}$  around 600 nm.

In the following we compare these findings with the photoluminescence properties of this wire. The emission spectrum of the wire is plotted as gray shaded curve in the graph 5.9(b). The emission peak is around 700 nm and approximately 40 nm (100 meV) redshifted from the transient absorption peak. However, a closer look to the bleaching response reveals a long wavelength tail spectrum that covers the luminescence emission. Furthermore, the time resolved photoluminescence signal is shown in figure 5.10 and fitted with the biexponential decay model, described in the fundamentals chapter in subsection 2.3.3. The extracted decay rates are plotted as vertically dashed lines in figure 5.9(c) and labeled  $\Gamma_{high}$  and  $\Gamma_{low}$ , respectively.

As the Einstein coefficients are identical for absorption and spontaneous emission, we measure the same process by transient absorption and luminescence emission spectroscopy. We find almost identical values for the emission decay rate  $\Gamma_{low}$  and the transition rate around the emitting states, determined by ultrafast pump-probe spectroscopy. However, the decay rate of the strong  $\alpha$  peak does not differ much. As a consequence, we assume only little population transfer from the  $\alpha$  state into lower lying emitting states, as this transfer would increase the decay rate. We conclude that the strong signal of  $\alpha$  and corresponding higher order transitions are defined by largest parts of the wire. But, some low energy states, which are present in the nanowire only at low density, cause the largest part of the emission. We attribute these states to lattice defects, surface states or fluctuation in the wire radius as shown in the TEM image 5.4(b). Here, short intervals of larger diameter lead to less confinement and thus a redshift of the ground and emission state.

#### 5.4.4 *Re-absorption processes in an individual nanowire*

The comparison of excitation and emission rate yields further insight. As discussed previously, we excite approximately 400 electron-hole pairs by each pump-pulse. After plasma recombination, around 50 excitons are created, of which about 30 populate the  $\alpha$  transition. Concerning our calculations of subsection 5.4.2 and the assumed purely radiative lifetime of 3 ns, we compute the luminescence quantum efficiency to about 25%. Consequently, we expect 8 – 12 photons being emitted per pump pulse, independent of the assumed radiative decay rate as shown by equation 5.36. However, by taking our detection efficiency of 1.5% into account, we find about 0.02 emitted photons in the optical far-field ( $1.5 \times 10^6$  per second). That means only one out of 500 emitted photons reaches the far-field. The required much lower quantum efficiency would correspond to a very short excited state lifetime, which is in contrast to our measurements. We propose reabsorption effects as reason for the low emission intensity of the nanowire.

We consider the recombination of an electron-hole pair. Directly after its emission, the photon is reabsorbed by other parts of the nanowire. From single nanowire extinction measurements, performed by Giblin et al., we estimate about 20000 absorbing dipole emitters per micrometer wire length for the  $\alpha$  peak [171]. Excitonic states in the near surroundings of the excited exciton are shifted out of resonance due to the Coulomb interaction. Consequently, short distance Förster type energy transfer is not possible and would also influence the decay rate what is not what we find [190]. Reabsorption of the emitted photon increases the overall probability of nonradiative recombination by the quantum efficiency of the wire. In order to support these assumptions, we apply a classical numerical model to calculate the emission properties of the photoluminescence intensity.

The recombination of an electron-hole pair is approximated by a classical emitting dipole. We estimate the ratio between emitted and reabsorbed photons by considering a dipolar emitter, embedded in a CdSe nanowire of 400 nm length and a radius of 6 nm. The essential components of the model are depicted in figure 5.11 and in analogy to the model discussed in subsection 3.2.1. The emission wavelength is chosen to 685 nm and we use the optical properties of bulk CdSe with vacuum ( $n_{eff} = 1$ ) as surrounding medium. Within the Bohr radius of 5.6 nm from the emitter, the wire absorption is neglected due to the transition energy shift by Coulomb interaction. The surface integral of the energy flux through a virtual inner sphere  $P_{inner}$  describes the power emitted by the dipole. The energy flux through the outer integration sphere gives the far-field emission strength. Corresponding to our model, the reabsorption exceeds the far-field emission by about a factor of 400. By taking into account that the exciton, excited by the reabsorbed photon, can emit another photon which itself can be reabsorbed again and so on, we compute an effective reabsorption coefficient. We find that  $\approx 0.33\%$  of the first emitted photons finally reach the far field. For comparison, in our experiments we found a factor of  $\approx 0.2\%$ ,

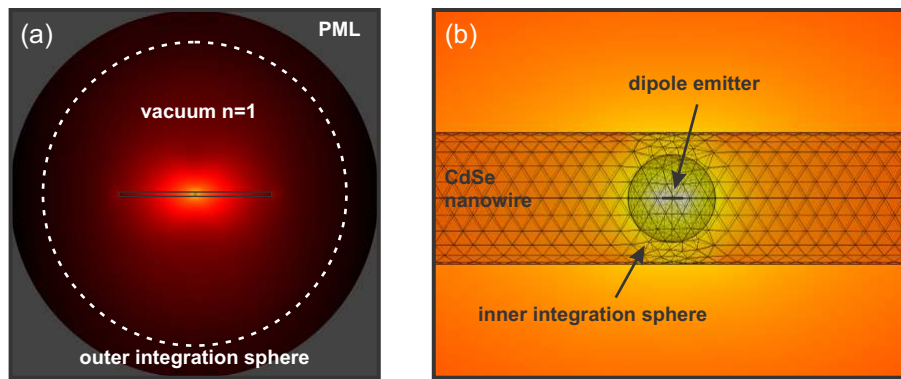


**Figure 5.11**

The numerical model is similar to the one introduced in section 3.2.1 but solving for the total field components, introduced in section 3.4. The CdSe nanowire together with the dipolar emitter is centered. The white dashed line marks the radius of the outer integration sphere where we extract the light emitted in the far-field. The structure is surrounded by a spherical PML. (b) Zoom into the model with a part of the wire, the dipolar emitter and the inner integration sphere.

what is in very good agreement with our model, although we fully neglect the quantum character of the wire. In addition, we performed the same calculations for different inner sphere radii, corresponding to different screening distances around the emitter due to the Stark shift. The calculated values stay in the same order of magnitude.

#### 5.4.5 Conclusion and outlook of single wire experiments

We discussed the equation system, derived from single and six-band effective mass theory, to compute the dipole allowed transition energies and probabilities of quantum confined carriers in a single CdSe nanowire. We theoretically predicted the absorption line energies as a function of the wire radius. Individual wires were characterized by transmission electron microscopy and time resolved photoluminescence measurements. The experimentally found polarization dependence of the excitation process was well described by our model, based on classical Maxwell's equations. After characterization, we presented the first time-resolved ultrafast nonlinear spectroscopy of the exciton dynamics in individual CdSe nanowires of radii well below 10 nm. We excite about 400 electron-hole pairs with our pump pulse, leading to a dispersive line shape of the transient absorption signal. This plasma decays within the first picoseconds after pump excitation. At time delays of more than 4 ps, we found clear peaks in the transient absorption spectra. This indicated the bleaching of excitonic states and is in very good agreement with the model predictions from effective mass theory. Via the integral over the absorption line, we were able to approximate the population of the different states. We found an overall number of about 50 excited excitons, of which about 30 populate the ground state. Further-

more, the lifetime of the carrier population was investigated. We found decay rates between  $2 \text{ ns}^{-1}$  and  $5 \text{ ns}^{-1}$ . By comparing these findings with time resolved photoluminescence measurements, we observed a large mismatch between the number of pump-induced excitations of the emitting state (about 10 per laser pulse) and the luminescence photon rate (about 0.02 per laser pulse). We explain this phenomenon by reabsorption of the emitted photons by other parts of the wire. This effect was supported by our numerical model, based on an emitting dipole in a CdSe nanowire with bulk optical properties. It further explained the strong redshift of the emission peak with respect to the ground state absorption line, determined by transient absorption spectroscopy. Here, the emission from low energy defect states is much less absorbed than emission from the nanowire itself and dominates the emission spectrum.

## 5.5 INTERACTION OF AN INDIVIDUAL CDSE NANOWIRE AND A PLASMONIC NANOOBJECT

Optical antennas can enhance the light matter interaction on a subwavelength scale and give access to previously unattainable nanosystems [80]. From our measurements of single CdSe nanowires, where we excite in the order of 30 excitons in the  $\alpha$  transition, we estimate a transient transition signal  $\Delta T/T$  for a single exciton being on the order of  $1/30 \cdot 6.3 \cdot 10^{-5} \approx 2 \cdot 10^{-6}$ . This corresponds to a change of the absorption cross section of approximately  $0.25 \text{ nm}^2$ , as discussed in section 2.1.3 of the fundamentals chapter. As a consequence, the expected signal amplitude is identical to the measured noise and thus almost impossible to resolve. Larger probe pulse intensities would destroy the nanocrystal while a longer integration time is not applicable due to stability conditions. In analogy to section 4.5 we aim for signal enhancement with a plasmonic antenna. However, the small dipole moment of the exciton reduces the hybridization effect with respect to the plasmon-plasmon interaction and we have to prove if the plasmon perturbation suffices to increase the nonlinear response of the nanocrystal. In the following we discuss our theoretical predictions and show first experimental data of a single CdSe nanostructure coupled to a plasmonic nanoantenna.

### 5.5.1 *Theoretical prediction of the nonlinear response*

In contrast to plasmons, excitons in nanocrystals show a much smaller dipole moment and highly nonlinear behavior due to saturation effects. As a consequence, experiments and especially the modeling of the plasmon-exciton interaction is challenging but treatable as long as we stay in the power regime where the excitonic response can be assumed as being linear. Furthermore in quantum theory, the gold particle modifies the environment of the nanocrystal [177]. This leads to changes in the properties of the exciton state, due to the quantum character of the semiconductor nanoparticle, and further complicates the modeling of the coupled system.

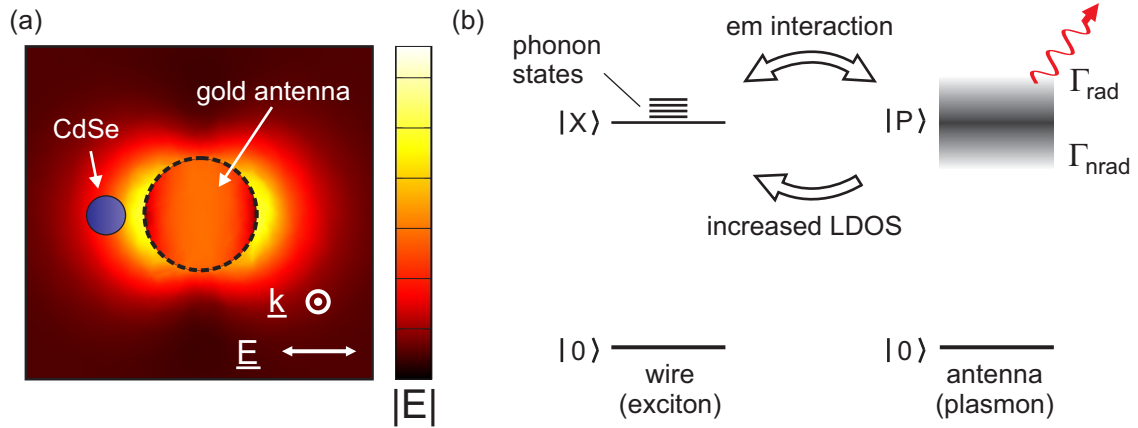


**Figure 5.12**

(a) The CdSe nanocrystal is placed into the near-field hot spot of a gold antenna to enhance the light matter interaction. Photons interact with the combined system, consisting of nanocrystal and antenna. The coupling is mediated by electromagnetic (em) fields (b) and leads to a change of the properties of exciton state due to the increased local density of states (LDOS).

For simplicity, we discuss the pump-probe experiment at the example of a single spherical CdSe nanocrystal in the hot spot of a plasmonic antenna, as depicted in figure 5.12(a).

First, we consider the pump excitation. In the spectral region where the d-band absorption of gold suppresses strong near-field amplitudes we expect negligible absorption or excitation enhancement of the nanocrystal. This changes for pump wavelengths above  $\approx 560$  nm where the field strength at the nanocrystal is increased and leads to a higher excitation efficiency as shown by Pfeiffer et al. [191]. However, this effect could be also achieved by increasing the pump pulse intensity at the corresponding excitation wavelengths. Furthermore, the pump enhancement is limited due to the nonlinearity and saturation of the nanocrystal. The antenna effect we are looking for is given by the probe response of the two combined systems. In order to describe the coupling between them we consider the two particle picture sketched in 5.12(b). The energy level scheme of the nanocrystal is shown on the left side and contains the crystal ground state  $|0\rangle$  and the excited exciton state  $|X\rangle$ . In case of the single nanocrystal, the probe absorption linewidth is broadened due to exciton-phonon scattering and the DC-Stark effect of carrier dynamics in the close environment [192, 193]. Furthermore, the exciton decay rate is given by the radiative and nonradiative decay rates  $\Gamma_{rad,0}$  and  $\Gamma_{nrad,0}$ , respectively. The energy scheme of the particle plasmon is sketched on the right side of figure 5.12(b). Its density of states (DOS) and possible excitations  $|P_i\rangle$  are visualized by the broad band and contains radiative and nonradiative plasmon states [194]. The coupling between semiconductor nanocrystal and gold nanoantenna is mediated by electromagnetic interaction. As a consequence, the two subsystems hybridize and photons

no longer interact with the single nanoobjects, but with the coupled structure with eigenstates  $|X\rangle|P\rangle$ . In analogy to the antenna introduced in chapter 4, the optical properties, as for example the absorption cross-section and lifetime, differs from the properties of the single nanoobjects. In the following we qualitatively discuss the different processes in the two particle picture by assuming purely electromagnetic interaction and neglect carrier tunneling or other interactions.

### *Carrier dynamics in a hybrid system*

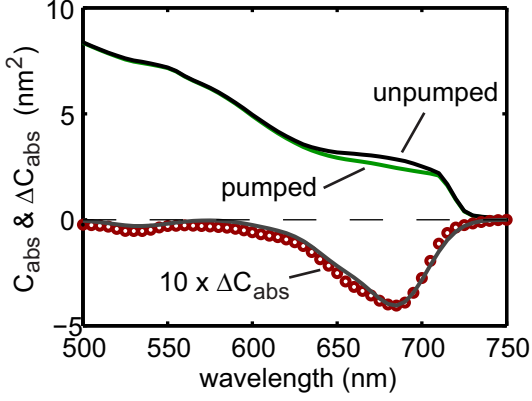
We assume coupling between the exciton state  $|X\rangle$  and the plasmonic nanoantenna, both being resonant at around 690 nm. A near-UV pump photon at 390 nm wavelength is absorbed by the off-resonant coupled system where exciton-plasmon interactions can be neglected. Supported by finite element simulations we expect no significant excitation (dissipation energy) change in the nanocrystal as the d-band absorption of the gold suppresses plasmonic and near-field effects. In analogy to the investigated wires, the electron hole pair decays from a higher order state into lower energetic eigenstates and populates the exciton state  $|X\rangle$ . While further non-radiative decay into the exciton ground or nanocrystal defect states is almost not influenced by the antenna, the radiative decay via photon emission requires the population of a photon state. Consequently,  $\Gamma_{rad,0}$  is a function of the photon mode density at the position of the nanocrystal. The plasmonic nanostructure increases the local density of states (LDOS) and gives further decay channels in addition to the photon vacuum states [194]. The balance between additional radiative and nonradiative decay channels is determined by the plasmon modes and corresponding mode density. For example, a dominantly scattering antenna can increase the emission intensity of the excitonic state, while an almost purely absorbing antenna increases the nonradiative decay and the emission is quenched [194, 195]. A common value to describe the increase of the overall decay rate is given by the effective Purcell factor

$$P_{eff} = \frac{\Gamma_{rad,c}}{\Gamma_{rad,0}} = \frac{\Gamma_{tot,c}/\Gamma_{tot,0} - 1 + \eta_Q}{\eta_Q} \quad (5.37)$$

with  $\Gamma_{rad,c}$  being the radiative decay rate of the coupled system. Furthermore,  $P_{eff}$  can be expressed from the ratio of the absolute decay rates  $\Gamma_{tot,c}$  and  $\Gamma_{tot,0}$  and the quantum efficiency  $\eta_Q$  of the nanocrystal. The time dependent population of the exciton state is interrogated by the resonant probe pulse. Here, electromagnetic interaction cannot be neglected and the coupled response has to be considered which leads to the desired antenna effect.

### *Modeling the antenna effect*

The nonlinear signal is given by the difference of pumped and unpumped optical response of the coupled system. Our model is based on the optical properties of bulk CdSe ( $n_{CdSe} + ik_{CdSe}$ ) to compute the quasi linear response of the nanocrystal [50]. Furthermore, the pump induced change of absorption of a single CdSe nanowire,

**Figure 5.13**

Linear and nonlinear response of a spherical single CdSe nanocrystal with a radius of 6 nm. The black and green curve show the response of the unpumped and pumped system. The nonlinear response, marked by the red circles, is multiplied by a factor of ten. The gray curve indicates the fit function which was used to modify the bulk optical properties.

as discussed in the previous section, allows us to estimate the perturbation of the optical properties after pump excitation at 390 nm and 15 fJ pulse energy. We use the attenuation coefficient  $K(\omega)$  as relation to model the optical properties ( $n'_{CdSe} + ik'_{CdSe}$ ) of the pumped CdSe nanowire. From equation 5.25 we derive

$$k'_{CdSe} = k_{CdSe} + \frac{\lambda}{4\pi} \Delta K(\lambda) \quad (5.38)$$

with  $\Delta K(\lambda)$  being negative due to the transition bleaching. The change is given by the fitting function, determined in section 5.4.1. Furthermore, we correct the real part  $n'_{CdSe}$  to keep the optical properties consistent with the Kramers Kronig relation. Figure 5.13 summarizes the finite element simulation results for a single CdSe nanosphere with 6 nm radius in an effective medium of  $n_{eff} = 1.4$ . The black curve shows the absorption spectrum of the unpumped nanocrystal. It is identical with the extinction spectrum as the scattering cross section is orders of magnitude smaller. The green curve shows the response of the pumped system. Consequently, we compute the nonlinear signal by the difference of pumped and unpumped response. For better visibility, the result is multiplied by a factor of ten and shown by the red circles. We obtain a maximum  $|\Delta C_{abs}|$  of  $\approx 0.4 \text{ nm}^2$  at the  $\alpha$  transition what is in very good agreement with the estimated  $0.25 \text{ nm}^2$  by dividing the wire response by 30 excitons. For comparison, the fitted function we used to modify the optical properties is overlaid as gray curve and in good agreement.

In the following we investigate the coupling to a plasmonic antenna. The disc shaped gold antenna has a height of 15 nm and the optical constants are given by the data of Johnson and Christy [49]. In order to tune the plasmon resonance over the  $\alpha$  transition of the nanocrystal, we perform a radius sweep of the antenna from 20 nm to 60 nm. The surface distance of nanocrystal and antenna is kept constant at 15 nm and the probe polarization is oriented along the long structure axis (see. figure 5.12). Figure 5.14(a) shows the absorption cross section of the coupled system. The dashed curve marks the resonance position of the single antenna, which is almost identical with the resonance of the coupled system. This is a consequence of the extremely weak oscillator strength of the CdSe nanocrystal

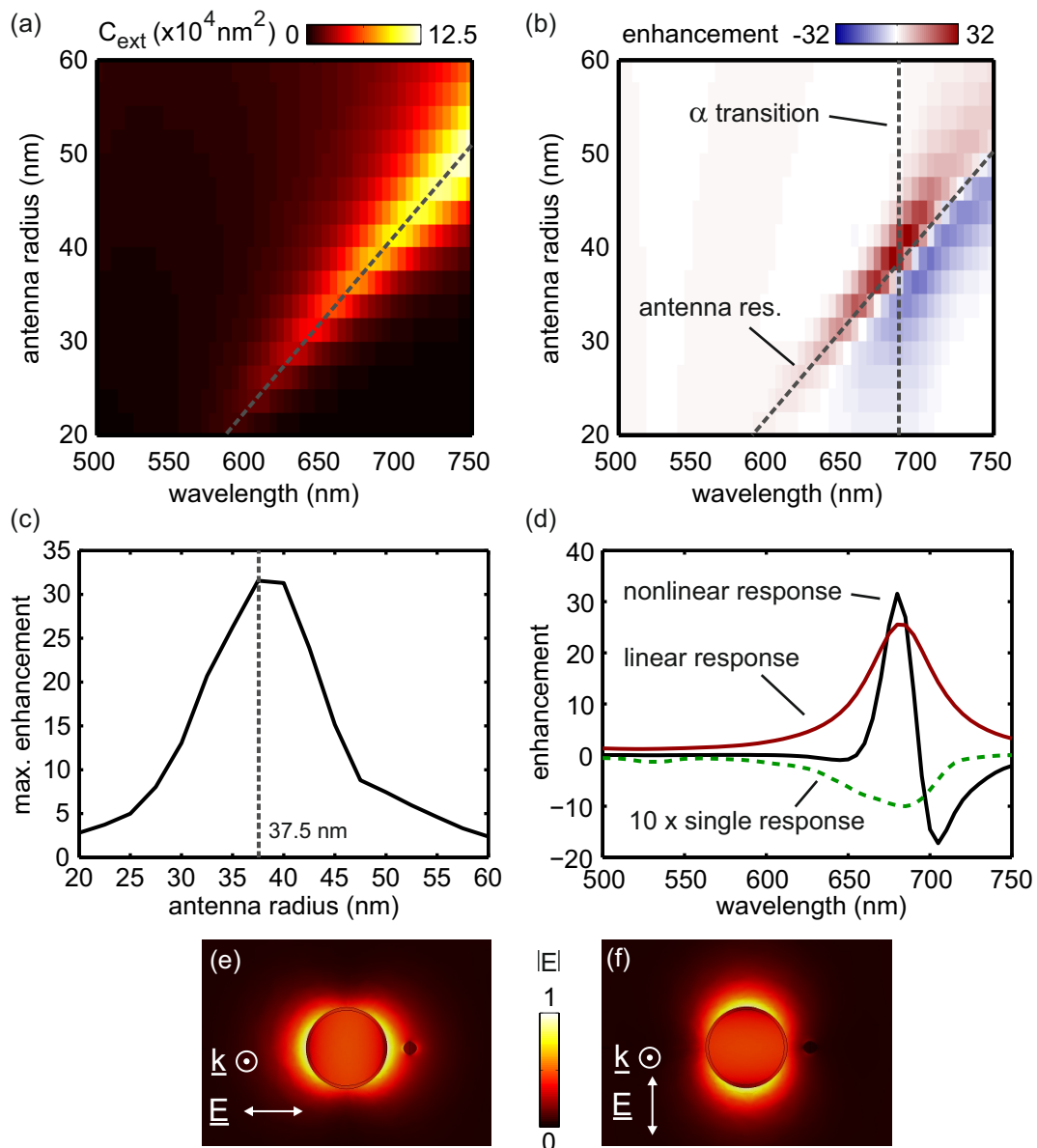


**Figure 5.14**

(a) Linear response of the hybrid system, for a polarization along the symmetry axis, as a function of antenna radius. The corresponding nonlinear response, normalized to the maximum response of the single nanocrystal, is shaped by the detuned plasmon resonance (b). The dashed vertical line shows the spectral position of the  $\alpha$ -transition. The other dashed curve marks the maximum extinction cross section of the antenna. We find maximum signal enhancement when the plasmon resonance matches the  $\alpha$ -transition wavelength. The maximum enhancement as a function of the antenna radius is shown in (c.) We find the optimum antenna radius at around 37.5 nm with an enhancement factor of  $\approx 30$ . The nonlinear response in case of the 37.5 nm antenna, normalized to the single crystal, is plotted in (d). For comparison, the linear response of the coupled system as well as the nonlinear response of the single nanocrystal, multiplied by a factor of ten, are plotted as well. Near-field distribution for the 37.5 nm antenna at its resonance position for parallel (e) and perpendicular (f) polarized excitation.

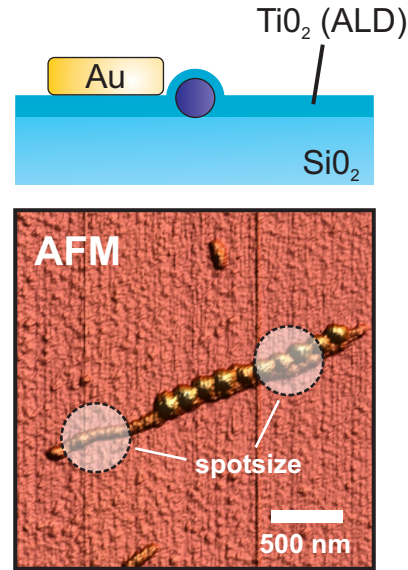
with respect to the plasmon. However, the computed nonlinear response, plotted in figure 5.14(b), shows that the transition bleaching of the nanocrystal and thus its reduced dipole moment is modulated onto the plasmon resonance. For comparison, the plasmon resonance and the  $\alpha$ -transition are marked by dashed lines. Maximum signal enhancement is achieved when the plasmon resonance matches the transition wavelength of the nanocrystal. This differs from the antenna effect we observed in the previous chapter and will be discussed in more detail in chapter 6. Furthermore, the maximum signal enhancement is plotted as a function of the antenna radius and shown in figure 5.14(c). We find the optimum antenna radius at 37.5 nm with a signal enhancement by a factor of  $\approx 30$ . The corresponding nonlinear response is shown in figure 5.14(d). For comparison, the normalized nonlinear response of the single nanocrystal, multiplied by a factor of ten, and the plasmon absorption spectrum in arbitrary units is plotted as well. Again we find the spectral overlap of the antenna and the  $\alpha$ -transition wavelength. The dispersive lineshape is characteristic for the perturbation of the plasmon and we expect a completely different response of the hybrid system, with respect to the single nanowire. Furthermore, the maximum signal contrast is enhanced by the factor of approximately 30 and thus similar to the response of the whole wire, analyzed previously. Consequently, we conclude that it is theoretically possible to measure and resolve the population of a single exciton state by coupling the nanocrystal to an optical antenna. However, the thermal decay of the electron-lattice temperature of the gold structure, described in section 4.2, shows a similar response as the exciton decay. As a consequence, the antenna response is superimposed on the desired signal, although the excitation power is much smaller than in the measurements for the acoustooptical properties of gold nanoparticles. As the antenna response cannot be separated from the nanocrystal signal, we limit the antenna volume to values where we detect no signal from the single antenna. In analogy to chapter 4, a rotation of the probe polarization reduces the interaction strength. Figure 5.14(e,f) shows the near field distribution of the resonant 37.5 nm antenna with the nanocrystal for parallel and perpendicularly polarized light. In (e) we find a strong near-field interaction. In (f), the interaction can be almost neglected and we find a drastic reduction of the calculated enhancement factor.

### 5.5.2 *Ultrafast spectroscopy of the hybrid system*

The positioning of a CdSe nanowire into the near field of a plasmonic nanostructure is done as follows. In the first step we prepare a single wire sample as described in section 5.3. Afterwards, the whole sample is covered with a 5 nm layer of TiO<sub>2</sub>, deposited by atomic layer deposition (ALD). This guarantees that the nanowire and antenna are not in direct contact. Furthermore, the sample is analyzed by SEM where we obtain high resolution images over large areas of the sample surface. The marker structures, written in advance, help to calibrate a grid which allows the design and definition of the antennas coordinates. Finally, the antennas are fabricated by electron beam lithography and gold evaporation. Here, I want to thank Daniela Ullrich for her great work and her contribution to my work.

**Figure 5.15**

A side view of the final structure geometry is sketched in the upper part of the figure. The wires are covered with a 5 nm layer of  $\text{TiO}_2$ . The antennas are written by electron beam lithography on top of it. The lower plot shows the AFM measurement of a single CdSe nanowire with several gold nanoantennas. The chosen antenna design allows the comparison between single wire and coupled system.



The upper sketch of figure 5.15 visualizes the cross section through the final structure. The atomic force microscopy image, depicted below, shows a single CdSe nanowire coupled to a plasmonic antenna. We use an antenna array to achieve the discussed antenna effect over a large part of the wire. In order to compare the uncoupled with the coupled system, the antenna is written over half the length of the wire. The spot size of our laser pulse is sketched in the AFM image. Furthermore, we estimate the gap distance between wire and antenna to  $\approx 15$  nm, by measuring the center to center distance and subtracting a 6 nm wire radius (measured AFM height) and 40 nm antenna radius (design radius). The antenna height is 15 nm. From our simulations we expect an almost resonant antenna and good signal enhancement. All experimental parameters are identical to the measurements of the single wires, discussed previously.

In comparison to the single wire results, we find a decreased photoluminescence intensity but comparable spectral response and lifetime for the wire region without neighboring antenna structure. We explain the decrease of intensity by the  $\text{TiO}_2$ -layer, slightly influencing the photophysical properties of the wire. Wire regions which are coupled to the optical antenna appear dark in photoluminescence scans. This is a consequence of the antenna design with its small volume to suppress the nonlinear signals of the gold itself. As a consequence, the absorption dominates over the scattering cross section of the antenna and thus almost all additional decay channels are nonradiative. Furthermore, the system is investigated by transient absorption spectroscopy. We limit ourselves to the  $\alpha$  and  $\beta$  transition and measure the response of the coupled and uncoupled wire between 660 nm and 740 nm over 400 ps, for a probe polarization parallel and perpendicular to the wire axis. In addition, a single antenna array is investigated where we find no nonlinear response. Figure 5.16 summarizes the results for the parallel polarization. The spectrally re-

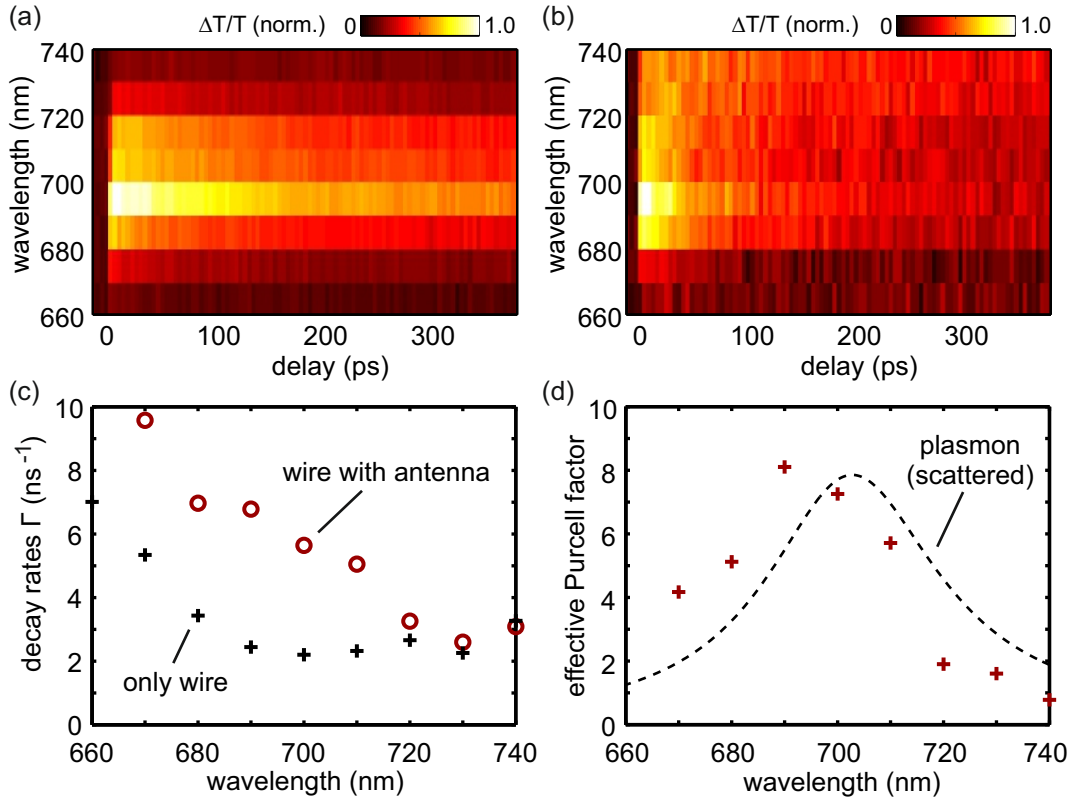


**Figure 5.16**

Normalized transient transmission spectra over 400 ps in the spectral region of the  $\alpha$  and  $\beta$  transition. In both cases, the pump and probe beam polarization is along the wire axis. The response of the uncoupled part (a) is similar to the first wire, discussed in subsection 5.4.1. The hybrid system (b) shows the same spectral behavior but with a decreased signal intensity and state lifetimes. Plot (c) depicts the decay rates of both wire sections as a function of probe wavelength. The calculated effective Purcell factor is plotted in (d). For comparison, a Lorentzian fit of the scattered plasmon resonance is plotted as black dashed curve.

solved response of the uncoupled wire and hybrid system is shown in the plots (a) and (b), respectively. In both cases, the transition energy and linewidth of the alpha state is in good agreement with the result of the wire investigated previously. The beta transition is merged with the ground state transition and cannot be resolved. In case of the uncoupled wire, the maximum bleaching response is  $\Delta T/T \approx 6 \cdot 10^{-6}$  and allows the conclusion that a similar amount of excitons is excited with respect to single wire experiment. We find the maximum signal intensity decreased to 1/3 when the wire is coupled to the antenna. This means that the plasmonic nanoparticle reduces the overall signal modulation, if we assume no excitation changes by the antenna. This can be explained by the weak coupling between antenna and nanocrystal for the parallel polarization. However, the data for perpendicular probe polarization, where we expect strong signal enhancement, cannot be evaluated. While the single wire part shows the expected (weak) response,

the coupled part appears dark in the transient transmission measurement. This differs from our theoretical prediction but was reproduced by other antenna-wire pairs. We explain this by the compromise in our antenna design to suppress its own nonlinear response. Furthermore, the position of the antenna on top of the wire could be not optimal and lead to a decreased dipole-dipole interaction. However, although the signal for the parallel polarization is not enhanced, we find interaction between the nanowire and antenna due to the enormous increase of the decay rate. Figure 5.16(c) shows the fitted decay rates of the single wire part and the antenna coupled part. We obtain a wavelength dependent increase of the decay rates. By equation 5.37, we calculate the corresponding effective Purcell factors which are plotted in figure 5.16(d). As the decay of each excitonic state depends on the local density of states, the lifetimes and thus the Purcell factors differ for the different transitions and wavelengths. For better comparability, a fit of the barely detectable scattered spectrum of the antenna is plotted as black dashed curve. We find the plasmon resonance mapped in the decay rate increase and Purcell factor, respectively. It has to be mentioned that the absorption resonance is slightly blueshifted with respect to the scattered response which offers the dominant amount of decay channels. Consequently, the  $\alpha$  transition, which is resonant with the antenna, shows a Purcell factor of  $\approx 8$ . The Purcell factor around the  $\beta$  transition is approximately 5. The one of the defect states, located at higher wavelength, is almost one and thus the decay rate not influenced by the off resonant antenna. This behavior proves interaction between the CdSe nanowire and the antenna array and is a first step towards ultrafast nonlinear optics of complex hybrid structures and tracking of carrier dynamics. In order to achieve the desired response enhancement, especially the antenna geometry and material gives space for improvement and further experiments have to be performed.

## 5.6 CONCLUSION AND OUTLOOK

In this chapter we investigated for the first time, ultrafast nonlinear carrier dynamics in quantum confined states of a single CdSe nanowire. The wires were characterized by transmission electron microscopy and time resolved photoluminescence measurements. We found lattice and geometrical defects as well as anisotropic properties which are supported by our classical model. Furthermore, transient transmission spectroscopy gave us insight into previously unattainable processes and information. We excite about 400 electron-hole pairs with our near-UV pump-pulse from which about 50 survive the fast recombination of the carrier plasma and populate the ground state or higher order excitonic states. The experimentally determined bleaching signal is nicely supported by six-band effective mass theory. We investigated several transitions and found decay rates between  $2 \text{ ns}^{-1}$  and  $5 \text{ ns}^{-1}$ . The comparison of the ground state population, determined by the integral over the absorption line, with photoluminescence measurements revealed a gigantic mismatch between excited excitons and emitted photons and cannot be explained by the quantum efficiency of the wire. Furthermore, the emission is strongly redshifted with

respect to the ground state absorption line. Our presented model covers the relevant physical properties of the wire and is based on classical calculations, what allows us to attribute these effects to re-absorption processes and the wire defects.

Furthermore, we discussed the interaction between a single CdSe nanoobject and a plasmonic antenna. In the limit of small pulse energies where the response of the nanocrystal can be assumed being linear, the electromagnetic interaction with a plasmonic nanoantenna can be described by classical dipole-dipole interaction or Maxwell's equations, respectively. In our model, the nonlinear response of the CdSe nanoobject is described via the change of the attenuation coefficient. In our simulations we showed that the response of a single exciton can be enhanced into an experimentally accessible regime. Furthermore, we performed first measurements of a hybrid system, where we couple a part of a single wire to an antenna array. The elongated wire geometry in combination with the small spot sizes allows the direct comparison between uncoupled and coupled quantum system. We find no signal enhancement and explain this behavior by the compromise of a resonant antenna geometry with negligible own nonlinear response. Furthermore, the luminescence intensity is almost zero at wire parts which are coupled to the antenna what we attribute to the nonradiative decay via the plasmon. The effective Purcell factor, which quantifies the modified decay rates of the  $\alpha, \beta$ , and defect state transitions, maps the additional local density of states given by the plasmon absorption resonance. This proves the interaction between the quantum system and the plasmon. In order to increase the signal, further measurements have to be performed. Here, other antenna geometries and materials may help to obtain the desired signal enhancement. An alternative could be also the usage of dielectric microcavities [160, 161]. They also influence the properties of the quantum system by their mode density but show no own nonlinear response what simplifies the development of optimized systems. Furthermore, we hope that our work can be continued and also applied at coherent low temperature experiments. The investigation of the coherent interaction of coupled quantum dots is fundamental for future quantum information and network applications [15, 196, 197].



## A POINT DIPOLE APPROACH FOR THE FAST COMPUTATION AND OPTIMIZATION OF MANY-PARTICLE ANTENNAS

---

Several numerical methods such as FEM, FDTD, or multiple multipoles (MMP) are available to compute the linear optical behavior of plasmonic nanostructures [90, 94]. The accuracy of the solution depends on the considered system and its boundary conditions [92]. In general, all these methods require high computational effort but predict the linear optical response of a system by solving Maxwell's equations. However, a deeper understanding of the coupling behavior is not obtained and gets lost in the complexity of the algorithm. Furthermore, large parameter and optimization studies require long computation times. In this chapter, we introduce a point-dipole approximation method (PDA) which gives a very fast alternative to these methods and helps to understand the fundamental processes in complex plasmonic structures. Furthermore, it can be used in the development of optical nanoantennas for single nanoparticle spectroscopy [11, 80].

In section 6.1 we discuss the implementation of our method and investigate the limitations for complex structures consisting of various particles with different optical properties. Our aim is to quantitatively predict the linear as well as the nonlinear response of coupled nanostructures by a minimum of computational effort. We use

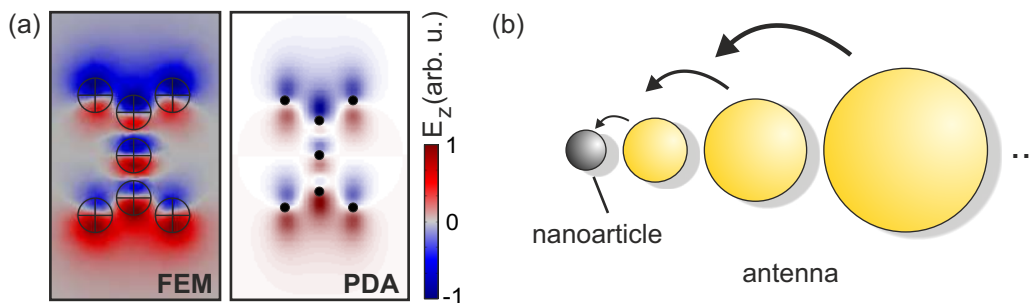


**Figure 6.1**

Comparison of finite element simulation and our discrete dipole approximation which will be introduced in this chapter. As an example we show the  $z$ -component of the scattered electric field, extracted 15 nm above the structure surface, of seven coupled nanospheres and dipoles, respectively. (b) Sketch of an optical antenna which consists of several particles. Intuitively, one expects a cascade effect in the enhancement by adding optical antennas to the previous nanoparticle-antenna systems.

the fundamentals of the discrete dipole approximation (DDA) [91, 198], but maximally reduce the number of considered dipoles as illustrated in figure 6.1(a). As a consequence, the influence and contribution of each particle to the overall response can be separated and reveals deeper insight to the hybrid system. Furthermore, the computation effort is drastically reduced with respect to common DDA calculations and allows the simulation of huge and previously unattainable parameter spaces. We use our method to investigate the crucial properties for optimum and most efficient optical antennas as discussed in section 6.2. In addition, we answer the question if more complex antenna designs with several antenna particles, as sketched in figure 6.1(b), may help to further increase the antenna efficiency. In section 6.3, we apply an evolutionary algorithm as optimization technique to find optimum antenna geometries.

## 6.1 POINT DIPOLE APPROXIMATION

Our point dipole approximation method is based on the discrete dipole approximation with a maximum reduction of used dipoles. In the following we introduce the fundamentals of DDA [198]. Furthermore, we discuss the modifications for our PDA approach and the corresponding properties.

### 6.1.1 Fundamentals and the discrete dipole approximation

We consider the scattering of an arbitrary system of classical nanoobjects in the incident electric field

$$\mathbf{E}_{inc}(\mathbf{r}) = \mathbf{E}_0 \exp(i(\mathbf{k}\mathbf{r} - \omega t)) \quad (6.1)$$

with  $\mathbf{E}_0 = (E_{0,x}, E_{0,y}, E_{0,z})^T$  and wavevector  $\mathbf{k}$ . In the discrete dipole approximation, matter is replaced by a large number  $N$  of discrete dipoles as sketched in

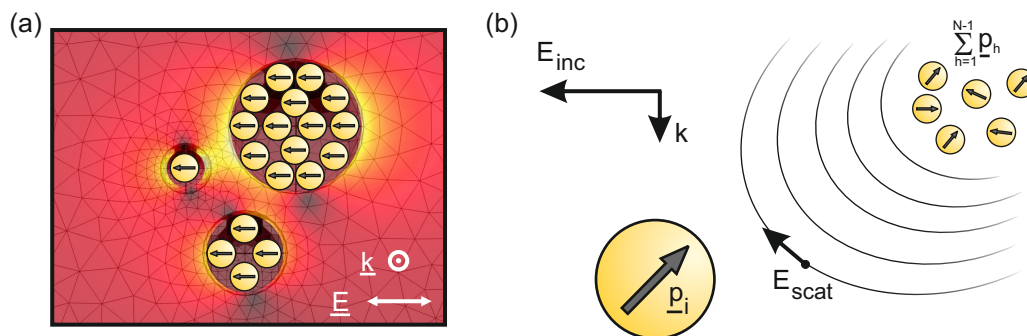


**Figure 6.2**

In the discrete dipole approximation, matter is represented by many small dipoles with polarizability, dependent on the material (a). Each dipole is polarized by the incident electric field and the scattered field of the surrounding dipoles (b).

figure 6.2(a). In analogy to other methods, the accuracy of the solution depends on the discretization or number of considered dipoles, respectively [198, 199]. Typical values for the overall number  $N$  of used dipoles are on the order of  $10^3$  to  $10^5$ . Each dipole  $i \in N$  has a specific isotropic polarizability

$$\alpha_i = 4\pi\epsilon_0 R^3 \frac{\epsilon - \epsilon_m}{\epsilon + 2\epsilon_m} \quad (6.2)$$

dependent on the optical properties of the target material  $\epsilon$  and the environment  $\epsilon_m$ . Furthermore, as depicted in figure 6.2(b), each dipole is polarized by the incident electric field  $\mathbf{E}_{inc}$  plus the contribution of the scattered field of the remaining  $N - 1$  dipoles. Consequently, we write

$$\mathbf{p}_i = \alpha_i \mathbf{E}_{inc}(\mathbf{r}_i) + \sum_{h \neq i}^{N-1} \underbrace{\alpha_h \mathbf{E}_{scat,h}(\mathbf{r}_i)}_{\stackrel{\text{def}}{=} \mathbf{A}_{i,h} \mathbf{p}_h} \quad (6.3)$$

for the polarization  $\mathbf{p}_i$  of the dipole at  $\mathbf{r}_i$ , with  $\mathbf{E}_{scat,h}(\mathbf{r}_i)$  being the scattered field of the dipole  $h$  at the position  $\mathbf{r}_i$ . Neglecting retardation effects, the scattered field vector  $\mathbf{E}_{scat,h}^{noret}(\mathbf{r}_i)$  of the dipole  $h$  with polarization  $\mathbf{p}_h$  is given by

$$\mathbf{E}_{scat,h}^{noret}(\mathbf{r}_i) = \frac{1}{4\pi\epsilon_0\epsilon_r} \frac{1}{\Delta r_{i,h}^3} \left( 3 \frac{\Delta \mathbf{r}_{i,h} \mathbf{p}_h}{\Delta r_{i,h}^2} \Delta \mathbf{r}_{i,h} - \mathbf{p}_h \right) \quad (6.4)$$

with  $\Delta \mathbf{r}_{i,h} = \mathbf{r}_i - \mathbf{r}_h$  being the distance vector between the dipoles  $h$  and  $i$ . The distance is its absolute value  $\Delta r_{i,h} = |\Delta \mathbf{r}_{i,h}|$ . However, the investigated systems reach sizes which are comparable to the wavelength and we have to consider retardation so that equation 6.4 changes to

$$\begin{aligned} \mathbf{E}_{scat,h}^{ret}(\mathbf{r}_i) = \frac{1}{4\pi\epsilon_0\epsilon_r} \cdot \left[ - \frac{\exp(ik\Delta r_{i,h})}{\Delta r_{i,h}} \left( \frac{k^2 \Delta \mathbf{r}_{i,h} \mathbf{p}_h}{\Delta r_{i,h}^2} \Delta \mathbf{r}_{i,h} - \mathbf{p}_h \right) + \dots \right. \\ \left. \dots + \frac{\exp(ik\Delta r_{i,h})}{\Delta r_{i,h}^3} (1 - ik\Delta r_{i,h}) \left( 3 \frac{\Delta \mathbf{r}_{i,h} \mathbf{p}_h}{\Delta r_{i,h}^2} \Delta \mathbf{r}_{i,h} - \mathbf{p}_h \right) \right] . \quad (6.5) \end{aligned}$$

As the scattered field depends on the dipole polarization, we define a scattering matrix  $\underline{\underline{A}}$  with elements  $\mathbf{A}_{i,h}$ , containing the polarizability as introduced in equation 6.3. This allows the transformation of equation 6.3 into the linear inhomogeneous equation system

$$\sum_{i=1}^N \sum_{h=1}^N (\underline{\underline{E}} - \underline{\underline{A}})_{i,h} \mathbf{p}_i = \sum_{i=1}^N \alpha_i \mathbf{E}_{inc}(\mathbf{r}_i) \quad (6.6)$$

with  $\underline{\underline{E}}$  being the identity matrix. In our calculations we define the polarization vector to  $\mathbf{p} = (p_{1,x}, p_{1,y}, p_{1,z}, p_{2,x}, \dots, p_{N,z})^T$ , containing the  $x, y, z$ -components of the dipoles. This leads to

$$\begin{pmatrix} \begin{pmatrix} 1 & 0 & 0 \\ 0 & 1 & 0 \\ 0 & 0 & 1 \end{pmatrix}_{1,1} & -\mathbf{A}_{1,2}^{3 \times 3} & \dots & -\mathbf{A}_{1,N}^{3 \times 3} \\ -\mathbf{A}_{2,1}^{3 \times 3} & \begin{pmatrix} 1 & 0 & 0 \\ 0 & 1 & 0 \\ 0 & 0 & 1 \end{pmatrix}_{2,2} & \dots & -\mathbf{A}_{2,N}^{3 \times 3} \\ \vdots & \vdots & \ddots & \vdots \\ -\mathbf{A}_{N,1}^{3 \times 3} & -\mathbf{A}_{N,2}^{3 \times 3} & \dots & \begin{pmatrix} 1 & 0 & 0 \\ 0 & 1 & 0 \\ 0 & 0 & 1 \end{pmatrix}_{N,N} \end{pmatrix} \begin{pmatrix} p_{1,x} \\ p_{1,y} \\ p_{1,z} \\ p_{2,x} \\ p_{2,y} \\ p_{2,z} \\ \vdots \end{pmatrix} = \dots \\ \dots = \begin{pmatrix} \alpha_{1,x} E_{inc,x}(\mathbf{r}_1) \\ \alpha_{1,y} E_{inc,y}(\mathbf{r}_1) \\ \alpha_{1,z} E_{inc,z}(\mathbf{r}_1) \\ \alpha_{2,x} E_{inc,x}(\mathbf{r}_2) \\ \alpha_{2,y} E_{inc,y}(\mathbf{r}_2) \\ \alpha_{2,z} E_{inc,z}(\mathbf{r}_2) \\ \vdots \end{pmatrix} \quad (6.7)$$

where the  $3 \times 3$  identity matrices ensure that different components of each separate dipole do not influence each other. The  $3 \times 3$  sub-matrices  $A_{i,h}$  define the influence of dipole  $h$  to the response of dipole  $i$ . The system is solved numerically via the inversion of the system matrix

$$\mathbf{p} = (\underline{\underline{E}} - \underline{\underline{A}})^{-1} \mathbf{b} \quad (6.8)$$

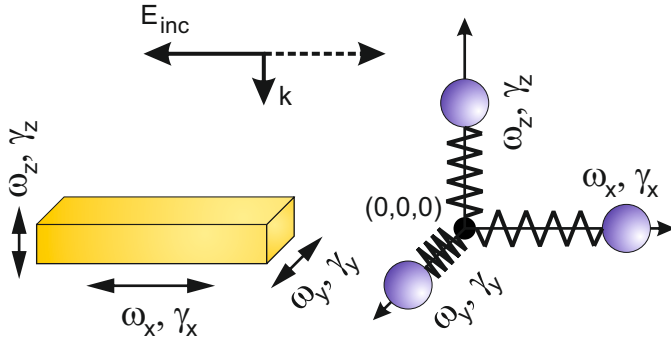
with  $\mathbf{b}$  being the inhomogeneous part of equation 6.7. After computation of the polarizations  $\mathbf{p}_i$ , the extinction cross section is calculated by the optical theorem, given by

$$C_{ext} = \frac{4\pi k}{|\mathbf{E}_0|^2} \sum_{i=1}^N \text{Im} [\mathbf{E}_{inc,i}^* \cdot \mathbf{p}_i] \quad (6.9)$$

with

$$E_0 = \sqrt{|E_{0,x}|^2 + |E_{0,y}|^2 + |E_{0,z}|^2} \quad (6.10)$$

being the incident electric field amplitude [199]. As a consequence of the flexible discretisation, the discrete dipole approximation allows to simulate the scattering

**Figure 6.3**

The polarization dependent linear plasmonic resonances, concerning their resonances and linewidths, are modeled by an anisotropic polarizability tensor and Lorentz oscillators.

properties of particles and structures with almost arbitrary shape and different material decompositions. However, the huge amount of used dipoles requires long computation times.

We aim for the fast computation and insight to electromagnetically coupled nanoobjects and plasmonic structures. Both can be achieved by drastically reducing the number of overall dipoles. The smaller equation system requires less computation effort. Furthermore, if each particle is reproduced by one single dipole, the interaction between two objects is completely described by the coupling matrices  $A_{i,h}$  and  $A_{h,i}$  and gives the desired insight into their roles in complex many particle systems. However, in order to describe anisotropic particle shapes we have to introduce polarizability tensors  $\underline{\underline{\alpha}}_i$  for each particle, as sketched in figure 6.3. A rod-type geometry for example can be expressed by

$$\underline{\underline{\alpha}}_i = \begin{pmatrix} \alpha_{i,xx} & 0 & 0 \\ 0 & \alpha_{i,yy} & 0 \\ 0 & 0 & \alpha_{i,zz} \end{pmatrix} \quad (6.11)$$

with  $\alpha_{i,kk}$  being the polarizability along the  $k \in \{x, y, z\}$  axis. In the discrete dipole approximation, the anisotropic response is determined by the geometry and the huge amount of dipoles. In order to model plasmonic or optical transitions of the particles along the different orientations we apply harmonic oscillators

$$\alpha_{i,kk} = \frac{\Theta_{i,k}}{(\omega_{0,i,k}^2 - \omega^2) - i\omega\gamma_{i,k}} \quad (6.12)$$

for the polarizability, with  $\Theta_{i,k}$ ,  $\omega_{0,i,k}$ , and  $\gamma_{i,k}$  being the oscillator strength, eigenfrequency, and damping, respectively. In our calculations we assume that the oscillator strength is defined by the particle volume and the resonance position by its geometry [200]. For the damping we use constant phenomenological values, or if necessary imitate the material properties via an intrinsic damping constant based on the attenuation coefficient  $K$  of the material. We argue that the dissipative losses, given by the Beer-Lambert law, lead to the damping of the plasma oscillation. In this case, we use  $\gamma_i = 2 \cdot K$  as phenomenological fit for which we find good agreement with finite element simulations as shown in figure 6.4. In the FEM simulation we

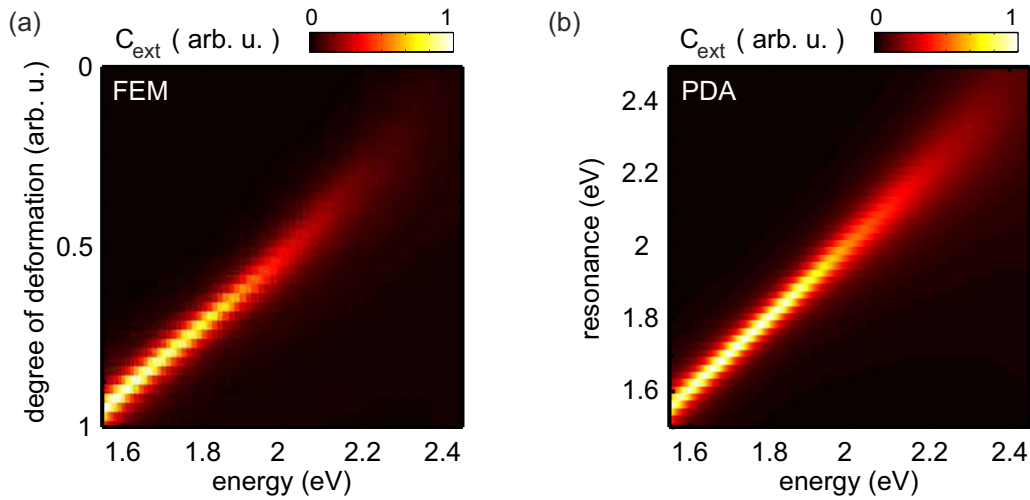


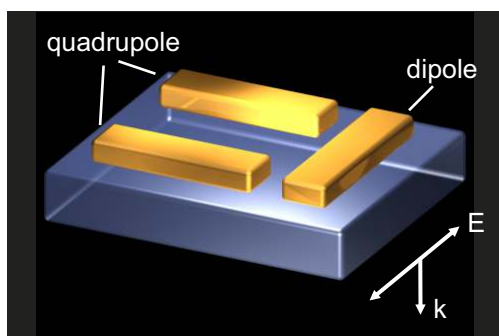
**Figure 6.4**

(a) Extinction spectra of a tiny gold ellipsoid with negligible scattering as a function of deformation to shift its purely absorptive plasmon resonance. The d-band absorption damps resonances below  $\approx 2$  eV. The phenomenological model of the PDA is in good agreement (b), where we directly shift the plasmon oscillator eigenfrequency.

computed the extinction spectrum of a gold nanoellipsoid in an effective medium of  $n_{eff} = 1.4$ . The semiaxes are all in the sub-nanometer range to avoid influences by radiation damping. In order to shift the plasmon resonance we tune the aspect ratio between the two semiaxes, which are perpendicular to the incident light propagation direction, while keeping the ellipsoid volume and height constant. Consequently, we expect an almost constant oscillator strength. Figure 6.4(a) shows the simulated purely absorptive extinction cross section as a function of the used deformation parameter. For a deformation parameter of 0, both perpendicular semiaxes are identical. An increase of the degree of deformation leads to an elongated shape of the ellipsoid and results in a redshift of the plasmon resonance which is also found for other geometries [201]. For comparison, figure 6.4(b) shows the extinction spectra, computed by the point dipole approximation, where we tune the resonance of a single dipole with constant oscillator strength and the effective damping, discussed previously. Both results are in good agreement and support our phenomenological damping model.

### 6.1.2 Range of validity

The introduced point dipole model combines the discrete dipole approximation and coupled harmonic oscillators. While the DDA supports the coupling properties mediated via dipole radiation, the harmonic oscillators define the polarizability of the dipoles and phenomenologically imitate plasmonic resonances or optical transitions. The anisotropic polarizability of each dipole allows the investigation of different geometries without using many hundreds or thousands of dipoles and leads to a

**Figure 6.5**

Sketch of the investigated structure. We couple a dark plasmon mode (quadrupole) to a bright one (dipole).

drastic reduction of required computation time. Of course, the applied approximation is not able to replace accurate simulation methods such as finite elements, but it helps to understand coupling behavior and allows the investigation of fundamental mechanisms within certain limits.

The time averaged radiated power  $P_{rad}$  of a dipole with dipole moment  $p$  is given by

$$P_{rad} = \frac{\omega^4 |p|^2}{12\pi\epsilon c^3} \quad (6.13)$$

with  $\omega$  being the radiation frequency,  $\epsilon$  and  $c$  the dielectric constant and velocity of light, respectively [47]. Consequently, radiation damping is a function of the dipole moment and thus not considered in a harmonic oscillator model with only linear terms. In order to demonstrate the possibilities and limits of our model, we apply the example of the plasmonic analogue of electromagnetically induced transparency, similar to the one we discussed in subsection 3.2.2 of the numerics chapter [104]. Figure 6.5 depicts a sketch of the investigated structure. In our FEM model, we use cylindrical shaped nanorods as substructures. The dipole has a length of 10 nm and a diameter of 3.75 nm. The quadrupole arms have the same size but are rotated by  $\pi/2$  and are separated by 3.125 nm from the dipole. Furthermore we use an effective medium of  $n_{eff} = 1.4$  and plane wave excitation, polarized along the long axis of the dipole. The upper graph of figure 6.6(a) shows the computed normalized extinction spectrum as black curve. We find the typical transparency window between the two hybrid modes of the coupled bright and dark plasmon. For comparison, the response of the single dipole is plotted as red dashed curve. The lower graph shows the corresponding result, calculated with our point dipole approximation model. We use the effective damping model of gold and set the resonance of the dipole to 1.7 eV as extracted from the FEM data. The dipole resonances along the two short axes are set to 2.5 eV. For both quadrupole arms we use slightly redshifted resonances at 1.68 eV along the long axis and again 2.5 eV for the other short axes. The dipole positions are placed into the center points of the particles and the excitation is along the long axis of the dipole. The oscillator strengths of all dipoles are identical and are used as fit parameter to achieve comparable coupling with respect to the real plasmonic structure. As summarized in figure 6.4(b), we find a very

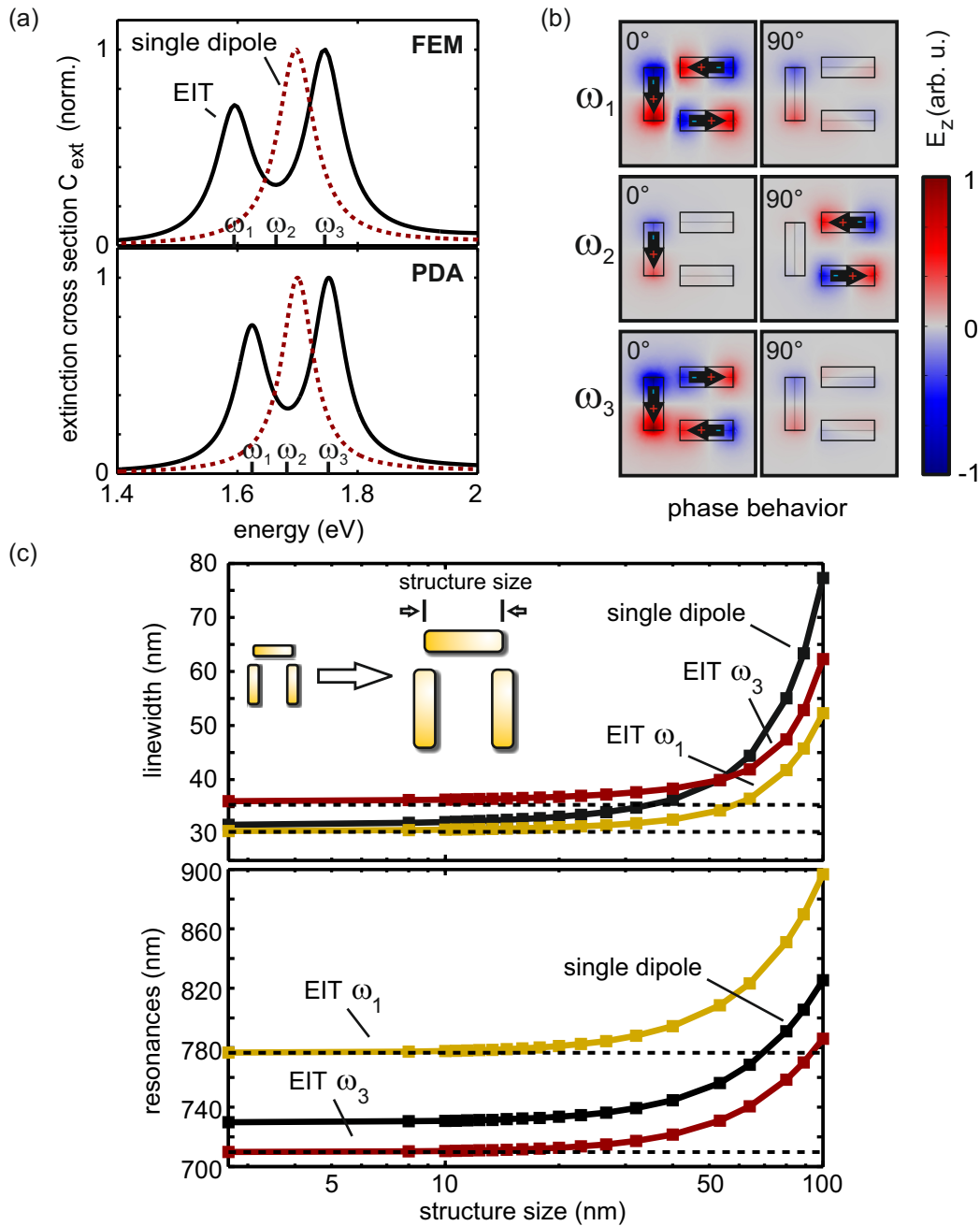


**Figure 6.6**

Comparison between the finite element method and the PDA (a). We use the example of EIT as discussed in subsection 3.2.2 of the numerics chapter. We tune the oscillator strengths in the PDA model to fit the interaction strength and find a very good agreement with respect to the finite element method. The phase dependent z-component of the electric field, taken at the three labeled energies, is plotted in (b). The data is extracted 20 nm above the structure surface. For comparison, the corresponding dipole orientations and amplitudes are superimposed and again in good agreement. In (c) we plot the resonances and linewidths of the single dipole and the EIT modes as a function of the structure size, determined by Lorentzian fits. For the considered geometry, we find negligible radiation effects below  $\approx 30$  nm.

good agreement for the extinction spectra and the phase dependence of the dipole polarizations. We obtain the frequency dependent modes and find the expected behavior of the coupled dark-bright oscillator. However, the assumed tiny structure size cannot be fabricated. In order to investigate the system behavior on different lengthscales we define the structure size by the length of the dipole and scale the whole geometry in our FEM calculation. Figure 6.4(c) shows the resonances and linewidths of the EIT double-peak feature (yellow and red) and the single dipole as a function of the structure size. We find an almost invariant response for structures below  $\approx 30$  nm. For larger lengthscales, the linewidths broaden and the resonances start to shift. This is a consequence of the increased scattering which can no longer be neglected. Here, the point dipole model fails to predict the reduced linewidths in the EIT geometry due to the reduced radiation losses of the quadrupole. We conclude that the point dipole approximation neglects radiation effects and fails to consider influences of higher order modes if a particle is modeled by one single dipole. We expect large deviations if the particle surface shows artifacts or sharp corners. Furthermore, only dipolar modes are considered. However, this is not what we aim for. The model allows us to gain insight into many particle interactions and the individual role of each particle. Furthermore, the computation time of the FEM model with approximately 80 frequency steps is on the order of 60 minutes. For comparison, the system with ten times more frequency points is solved by the point dipole model within roughly 400 ms. This is a factor of  $\approx 10^4$  faster. Of course it does not replace the accurate calculation but gives a fast and detailed picture of dipole coupled systems within the discussed limits.

## 6.2 SIGNAL ENHANCEMENT VIA AN OPTICAL ANTENNA

In the chapters 4 and 5 we applied optical nanoantennas to enhance the light matter interaction of tiny nanoobjects. Although both chapters consider different nonlinear systems, namely the acousto-optical response of a single gold nanoparticle and the transition bleaching of quantum confined states of a semiconductor nanowire, the electromagnetic coupling between antenna and nanoobject follows the same physics. In general, the optical and geometric properties of the involved subsystems shape the overall coupled response. As a consequence, nonlinear effects of the nanoparticle and the antenna modulate the hybrid response and are not directly separable. Antenna enhancement is achieved if the nonlinear response of the nanoobject is amplified by the perturbation of a much stronger carrier signal, provided by the antenna. Intuitively, the question for the optimum antenna arises. In the previous chapters we used numerical methods to answer this question for a single particle antenna. However, the results for the optimum antenna sizes and resonances are not well understood, phenomenologically differ from each other, and their prediction required long computation times.

In the following we use our point dipole approximation model to discuss and investigate the crucial parameters which are required for an optimum antenna. In analogy

to the chapters 4 and 5 we distinguish between two cases which we discuss separately. The first one is the general 'strong perturbation case', where the backscattering of the nanoobject noticeably influences the hybrid response. In subsection 6.2.2, we investigate the 'weak perturbation case', where the oscillator strength of the nanoobject is much smaller with respect to the antenna and its influence is not directly observable in the hybrid response.

### 6.2.1 Strong perturbation case

An example for the strong perturbation case is given in chapter 4, where the nanoparticle and the antenna have a comparable dipole moment [80]. Consequently, the hybrid response strongly differs from the response of the individual subsystems. In subsection 4.5.2 we performed numerical calculations to find the optimum radius for a 30 nm high disc shaped antenna to enhance the nonlinear response of a smaller gold disc with 20 nm radius and identical height. Figure 6.7(a) shows the predicted nonlinear signal of the nanoparticle as a function of the antenna radius as already discussed in subsection 4.5.2. The black cross marks the maximum nonlinear response at an antenna radius of  $\approx 35$  nm which was successfully used in the experiment. In analogy, one could expect that an antenna radius of approximately 70 nm most efficiently enhances the nonlinear response of a disc with a radius of 40 nm. Figure 6.7(b) shows the corresponding simulation result and predicts maximum signal enhancement for an antenna radius of approximately 30 nm. Consequently, the antenna is smaller than the particle of interest and counterintuitively to the antenna picture. In order to understand this behavior, additional parameters have to be studied. However, as the computation time for each of the presented nanoparticles

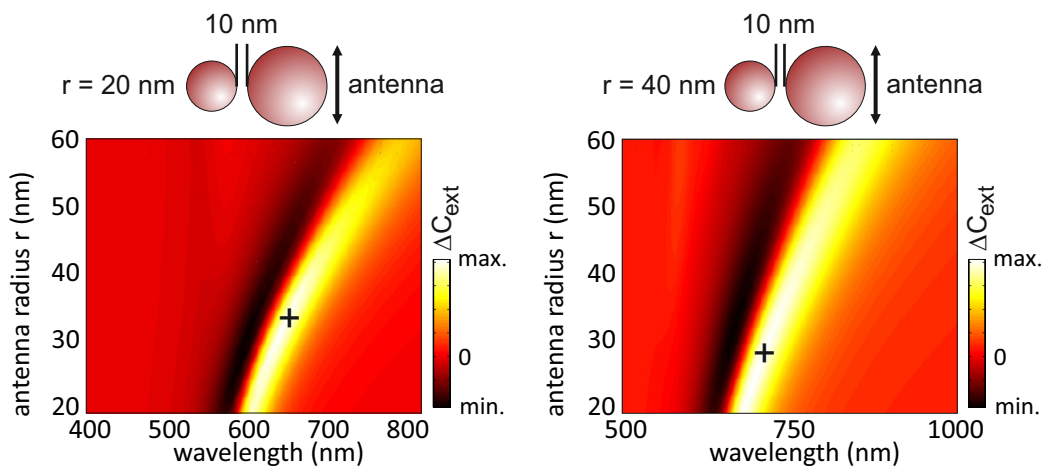


**Figure 6.7**

T-Matrix calculations to determine the optimum antenna sizes to enhance the nonlinear response of a 20 nm diameter (left) and a 40 nm radius particle (right). The distance between nanoparticle and antenna is kept constant at 10 nm. The black cross in the plots mark the maximum nonlinear response.

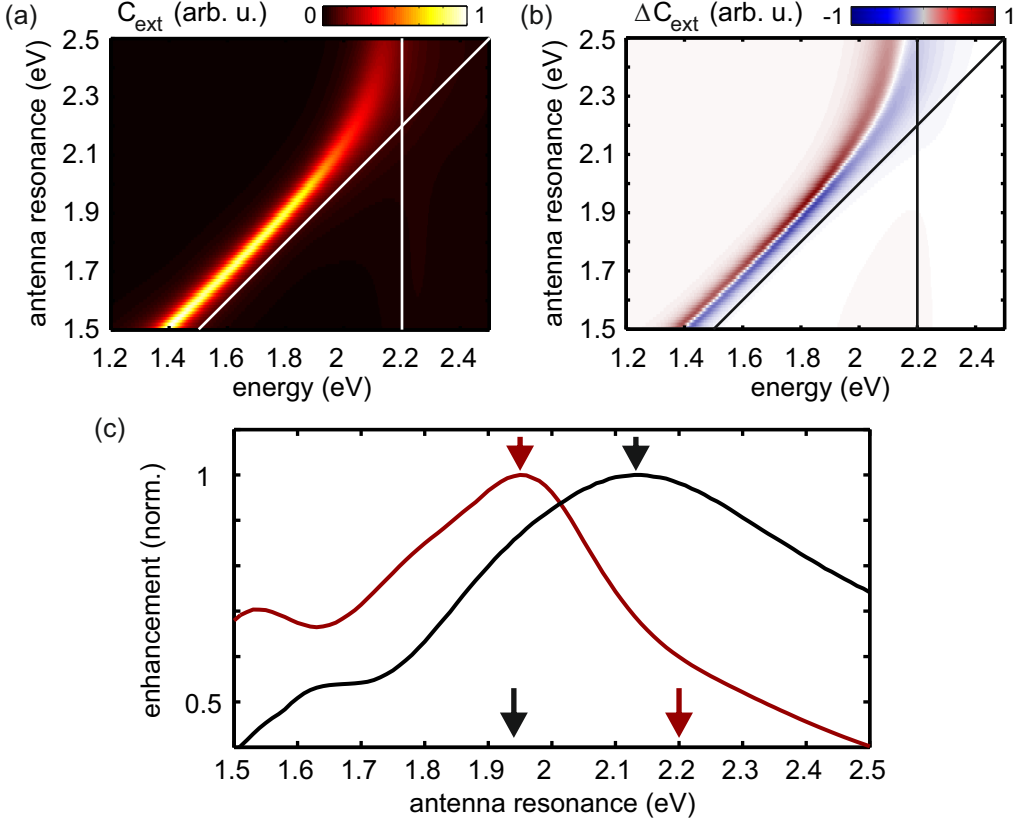


**Figure 6.8**

Linear and nonlinear response of a small nanoparticle at 2.2 eV as a function of antenna resonance (a,b). For orientation, the corresponding resonance positions of the subsystems are marked by the lines. The enhancement as a function of the antenna resonance is plotted as red curve in (c). The red arrows mark the resonances of the nanoparticle (2.2 eV) and the optimum antenna, respectively. For comparison, the black curve and arrows show the example for a bigger nanoparticle at 1.94 eV. For better visibility, both curves are normalized to their maximum.

is on the order of 24 hours we apply our point dipole model and investigate the large parameter space to obtain better insight into the involved processes. We use a constant dipole-dipole distance of 20 nm and excite along the distance vector. We isotropically tune the antenna resonance between 1.5 eV and 2.5 eV in 0.01 eV steps. The oscillator strengths of nanoparticle and antenna fulfill the strong coupling case. In order to include the size and resonance dependent oscillator strength we assume an inverse proportionality between the fundamental resonance energy  $\omega_a$  and the disc diameter. As the oscillator strength  $A$  is proportional to its volume and thus to its radius squared, we write

$$A_i \propto \frac{1}{\omega_i^2} \quad (6.14)$$

for each dipole  $i$ . The small nanoparticle of interest has its isotropic resonance at 2.2 eV ( $\approx 560$  nm) which corresponds to the disc with a radius of 20 nm. Fig-

ure 6.8(a) shows the linear response of the coupled system as a function of the antenna resonance energy. For orientation, the resonances of the antenna and the nanoparticle are given by the white lines. We find the strong coupling case where the bright hybrid mode is significantly shifted to lower energies. The weaker antisymmetric mode at higher energies is suppressed by the d-band absorption what is in very good agreement with our numerical simulations, discussed in subsection 4.5.2. In order to compute the nonlinear response of the nanoparticle, we modify its eigenfrequency with a phenomenological shift of 10 meV. The result for the nonlinear response is shown in figure 6.8(b). In analogy to our T-Matrix simulations we find the perturbation of the hybrid mode for all considered antennas. The normalized maximum signal enhancement as a function of the antenna eigenfrequency is plotted as red curve in figure 6.8(c). The lower red arrow marks the resonance of the nanoparticle, the upper red arrow gives the optimum antenna frequency at  $\approx 1.94$  eV. This corresponds to an antenna with a radius of roughly 40 nm and is in good agreement with our numerical predictions, discussed previously. We explain the slight deviation by the assumed coupling strength and the neglect of radiation damping and thus resonance broadening what reduces the sensitivity of antennas with larger radii. We repeat the simulation for a nanoparticle with its eigenfrequency at 1.94 eV, corresponding to the nanodisc with a radius of 40 nm. The result is plotted as black curve in figure 6.8(c). Again, the upper and lower black arrow mark the optimum antenna resonance and nanoparticle eigenfrequency, respectively. We observe the same behavior with respect to our T-Matrix simulations, where the small antenna enhances the nonlinear response of a larger nanoparticle.

In order to obtain more insight, we compute the maximum enhancement as a function of the antenna resonance and the nanoparticle resonance, by taking the size dependent oscillator strengths into account. Figure 6.9(a) shows the result where each datapoint corresponds to the absolute maximum of the nonlinear response of a given nanoparticle-antenna pair. For comparison, the calculation took on the order of one hour while the corresponding simulation with our finite element model would have taken roughly four years. The black curve marks the spectral overlap of antenna and nanoparticle. The white curve follows the optimum antenna resonance. We find no clear correlation between the two curves and a crossing behavior. Furthermore we predict that the signal of a nanoparticle at 2.05 eV is most efficiently enhanced by an antenna with the same eigenfrequency. Larger nanoparticles require smaller antennas and vice versa. This behavior seems chaotic but is a consequence of the optical properties of gold. The dashed black curve marks the hybrid mode resonance in the case of the optimum antenna. For particles with resonances above 2 eV we find an almost constant carrier mode frequency at approximately 1.85 eV. For particles with lower energies, the response is parallel to the spectral overlap. This is an outcome of the absorption band of gold at around 2 eV, which leads to a strong damping of the plasmon resonance. Consequently, the nonlinear response of a small gold nanoparticle is modulated on a broad and weak plasmon and thus the desired signal is further reduced. The optimum antenna for these particles is a

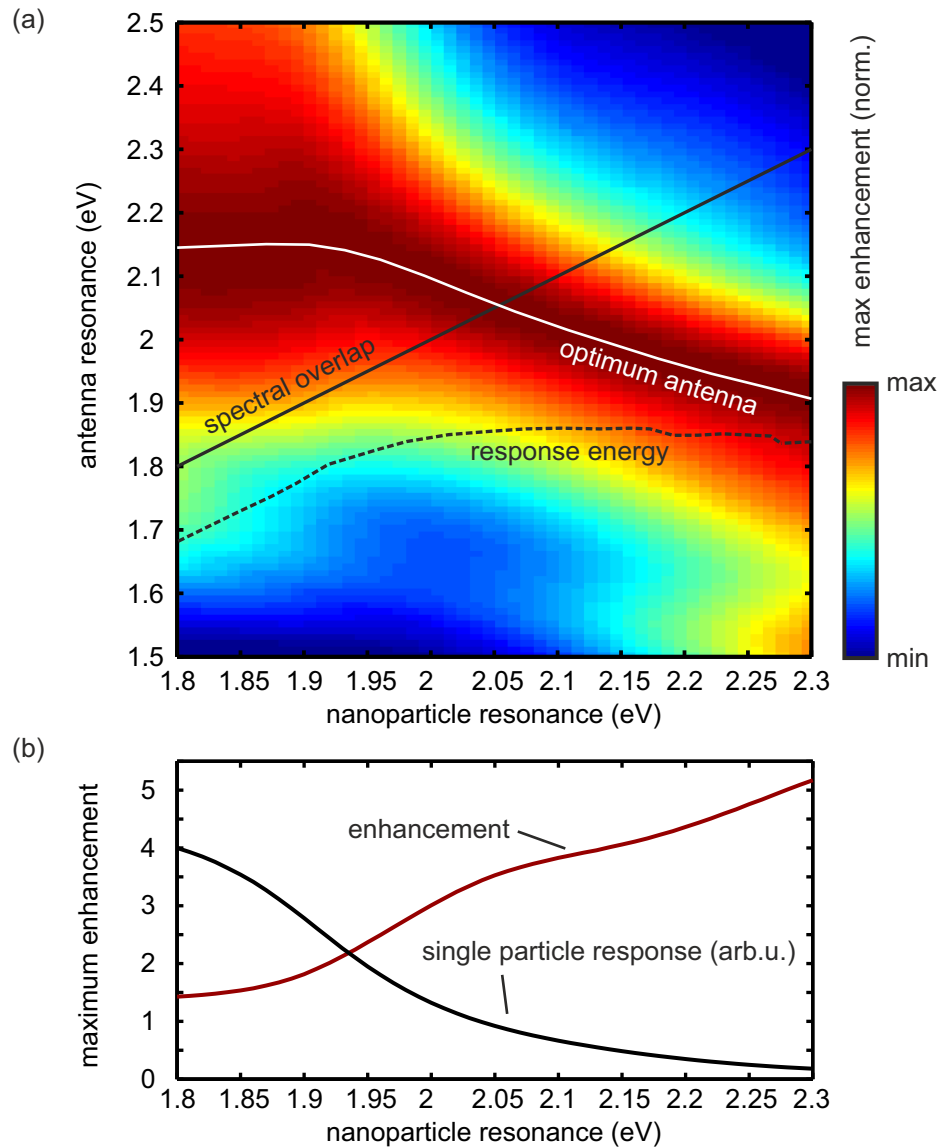


**Figure 6.9**

(a) Maximum enhancement for the strong coupling case as a function of the nanoparticle resonance and the antenna resonance. For better comparability, the antenna resonance dependent enhancement for each nanoparticle is normalized to the maximum hybrid response. The black curve marks the spectral overlap of antenna and nanoparticle. The white curve shows the resonance of the optimum antenna with highest signal enhancement. The coupling between the optimum antenna and the nanoparticle shifts the coupled response resonance, marked by the dashed curve. Subfigure (b) shows the signal enhancement along the optimum antenna curve in (a). For comparison, the black curve in (b) gives the maximum nonlinear response of the single nanoparticles in arbitrary units.

compromise of spectral overlap and oscillator strength to shift the hybrid response outside the d-band and will be discussed in the following.

Independent on the nanoparticle energy, spectral overlap is required to achieve a strong hybridization and thus modulation of the nonlinear response onto the hybrid mode. The oscillator strengths define the coupling strength, the spectral shift, and the nonlinear response amplitude by the perturbation of the overall strong carrier signal. If we consider larger nanoparticles below 2 eV, the antenna resonance is blue shifted into the d-band to avoid strong resonance redshifts of the hybrid mode into spectral regions with increasing losses due to the Drude damping and especially radiation losses which we neglected in our calculations [49, 202]. As a consequence, the symmetric hybrid mode is red-shifted but follows the nanoparticle resonance. However, for particles with energies above approximately 2 eV, the hybrid mode would enter the d-band absorption spectrum. The compromise to achieve signal enhancement is to reduce the spectral overlap but overcompensate the detuning by the larger oscillator strength and the reduced resonance broadening outside the absorption band. This argumentation is supported by the red curve in figure 6.9(b) which shows the maximum enhancement as a function of the nanoparticle resonance. While the signal of larger nanoparticles is slightly enhanced, the resonance shift outside the d-band leads to strong enhancement for the smaller nanoparticles.

In order to support the further discussed interpretations, we perform the identical calculation without the effective damping model of gold and assume a constant resonance damping of  $\gamma = 0.1$  eV for all particles. Figure 6.10 shows the computation result. For comparison, we plotted the optimum antenna resonance, spectral overlap, and the optimum hybrid response energy as white, black, and dashed black curve, respectively. We find a clear correlation between optimum antenna resonance and the spectral overlap which underlines the importance of the spectral similarity between nanoparticle and antenna. In analogy to the previous discussion for particle resonances outside the absorption band of gold, we predict maximum enhancement by a blueshifted antenna with smaller oscillator strength. However, the analyzed systems without effective damping model are idealized and do not represent realistic material properties. A more reliable example was numerically investigated in the work of Daniela Ullrich [150]. She discussed the optimum parameters for a disc shaped silver antenna, without absorption band in the visible, to enhance the nonlinear response of a gold nanoparticle. The results show that the silver nanoantenna with slightly higher plasmon resonance energy than the nanoparticle resonance, but much larger oscillator strength leads to maximum signal enhancement. The coupled nonlinear response is at the lower energetic symmetric mode and supports our model although radiation losses cannot be fully neglected and the antenna oscillator strength is much larger with respect to the smaller gold antenna, discussed previously. We conclude that in the strong perturbation case the strong influence and backscattering of the nanoparticle to the hybrid response is important and has to be taken into account in the antenna design. It can be a powerful method to shift

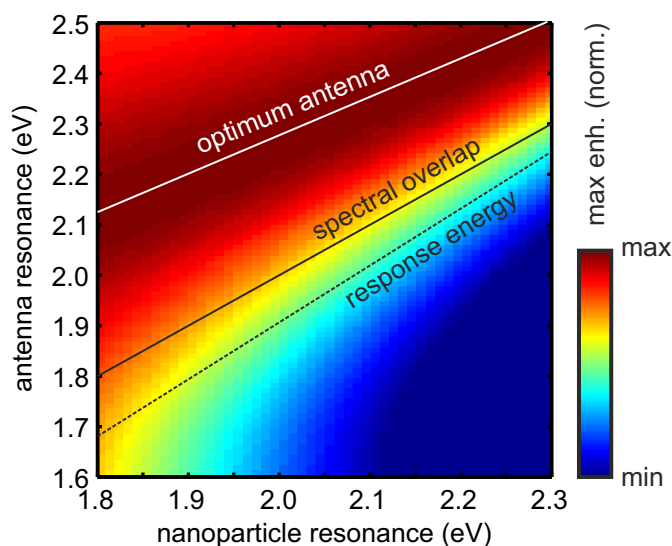


**Figure 6.10**

In analogy to figure 6.9 but without phenomenological damping coefficient. We find a clear correlation between the spectral overlap of antenna and nanoparticle and the optimum antenna resonance.

the hybrid response into spectral regions with advantageous optical properties what allows high efficient enhancement of the nonlinear signal amplitude. This is of great importance if the response is damped by absorption bands or other suppressing mechanisms. Furthermore, the usage of different antenna materials or geometries can help to optimize the antenna properties by optimizing the spectral overlap by simultaneously increasing the antenna's oscillator strength [150].

### 6.2.2 Weak perturbation case

In the following we consider the weak perturbation case where the small oscillator strength of the nanoparticle is not able to significantly influence the linear response of the coupled system. An example for this is given in chapter 5 where we couple a single CdSe nanowire to a plasmonic antenna. As already mentioned, this is only a special case of the strong perturbation case and cannot be strictly separated. However, for the weak perturbation we find a more disentangled behavior of the optimum antenna parameters as we discuss in the following.

The simulation parameters are identical to the previous subsection. We apply the effective gold damping for all particles but reduce the oscillator strength of the nanoparticle by four orders of magnitude. Consequently, we couple a very weak dipole moment of the nanocrystal to the strong dipole moment of the plasmonic nanoantenna. Again, we assume a perturbation of 10 meV of the nanoparticle's resonance. This differs from the transition bleaching where we observe a reduced dipole moment but it allows the direct comparison with the previous discussion. In order to consider transition bleaching, we repeat the calculation with a pure perturbation of the oscillator strength. We find no mentionable differences which would require a separate discussion. Figure 6.11(a) shows the maximum nonlinear response as a function of the antenna and the nanoparticle resonance. In contrast to the strong perturbation case we find the optimum antenna being resonant to the nanoobject

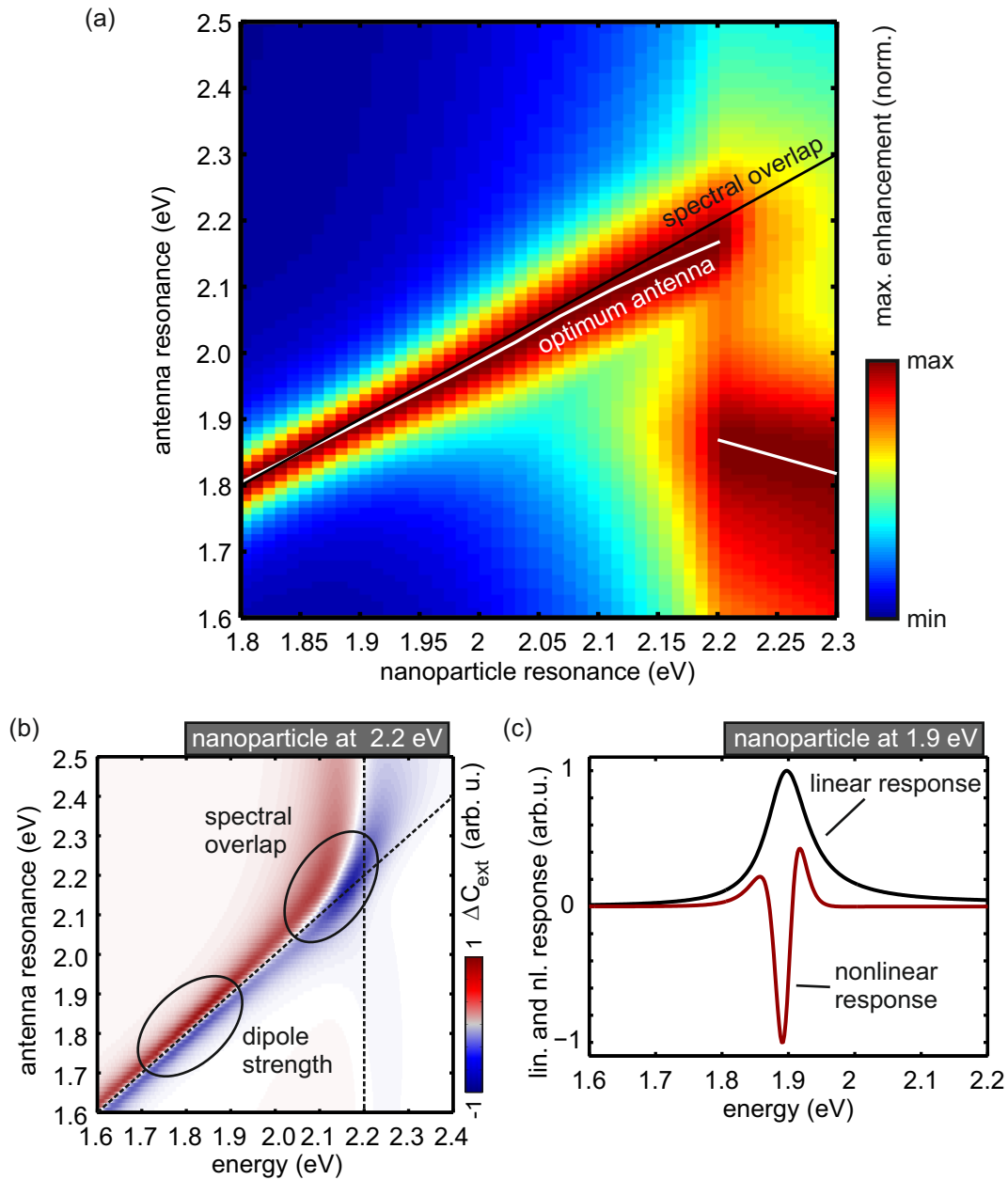


**Figure 6.11**

(a) Normalized maximum enhancement for the weak coupling case as a function of the nanoparticle resonance and antenna resonance. The black and white curves mark the spectral overlap of antenna and nanoparticle and the optimum antenna resonance, respectively. The response energy is identical with the optimum antenna resonance. The nonlinear response of the nanoparticle at 2.2 eV as a function of antenna resonance is plotted in (b). The dashed lines show the corresponding resonance energies. The markers highlight two different areas of high nonlinear response. The maximum nonlinear response of the nanoparticle at 1.9 eV is plotted as red curve in (c). For orientation, the linear response is plotted as black curve.

of interest. Furthermore, the hybrid response energy is identical with the optimum antenna resonance and not plotted separately. This is a consequence of the weak coupling where off-resonant particles show neglectable interaction and thus no or neglectable hybridization. In case of resonant particles, the nonlinear response of the nanoparticle is modulated onto the much stronger antenna response and leads to a much higher enhancement factor, compared to the strong perturbation case. However, for nanoparticles with resonances above  $\approx 2.2$  eV, the optimum antenna resonance jumps to lower energies. This is a consequence of the d-band absorption of the gold antenna as shown in figure 6.11(b). Here, we plot the spectrally resolved nonlinear response for the nanoparticle at 2.2 eV, where we observe the resonance jump of the optimum antenna, as a function of the antenna resonance. The two markers highlight the regions with strongest enhancement, one for an antenna resonance at around 1.8 eV and the other at 2.15 eV. The antenna at higher energy has a smaller oscillator strength but good spectral overlap. For the antenna with lower eigenenergy it is vice versa and the nonlinear response of the nanoparticle leads to a tiny perturbation of the far off-resonant antenna resonance with large oscillator strength. For nanoparticles at higher eigenenergies, the increasing antenna plasmon damping, caused by the absorption band, suppresses the desired enhancement effect and the off resonant antennas become more efficient. However, the design of a gold antenna which operates within the d-band absorption spectrum should be avoided and other materials such as silver or aluminum should be applied. Finally, we consider the nonlinear response for a nanoobject outside the absorption band of the gold antenna at 1.9 eV. The red curve in figure 6.11(b) shows the spectrally resolved nonlinear response of the hybrid system with the maximum achieved nonlinear signal amplitude. For comparison, the linear response of the antenna with its resonance at 1.9 eV is plotted as black curve. The behavior of linear and nonlinear response nicely reproduce the calculation results, discussed in subsection 5.5.1, where we investigated the coupling of a CdSe nanocrystal with a gold nanoantenna.

### 6.2.3 Conclusion

In this section we investigate the crucial parameters for an optical nanoantenna in the limits of our point dipole approximation method. In our discussions we distinguished between two cases. In the 'strong perturbation case', the backcoupling of the nanoparticle of interest to the antenna cannot be neglected and leads to a spectral shift of the hybrid response. For demonstration, we used the example of chapter 4 where we enhanced the nonlinear response of a small gold nanoparticle with a slightly larger gold antenna. However, our numerical simulations show that in contrast to intuitive expectations, the signal of a larger nanoparticle is most efficiently enhanced by a nanoantenna of smaller size. This seems counterintuitive but can be explained by the optical properties of gold and the harmonic oscillator model polarizability. Furthermore, the d-band absorption of gold above approximately 2 eV suppresses plasmon resonances of small nanoparticles and thus the modulated nonlinear response. In this case, the optimum antenna is a compromise

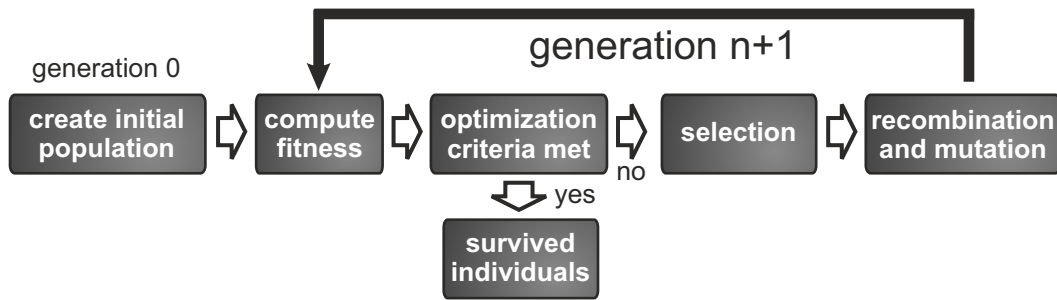
of spectral overlap and oscillator strength, leading to a shift of the hybrid mode outside the absorption band. Here, larger antennas cannot overcompensate the off-resonance by their additional dipole moment. The hybrid response with smaller antennas is damped by the d-band and thus inefficient as carrier mode.

In the weak perturbation case, the dipole moment of the nanoparticle is much smaller with respect to the antenna. Consequently the coupled response seems almost unaffected by the nanoobject. We found the spectral overlap of nanoparticle and antenna as most important condition for optimum signal enhancement. Furthermore, we obtained good agreement with our predictions of subsection 5.5.1 where we consider a single CdSe nanocrystal with tiny dipole moment, coupled to a gold nanoantenna.

We conclude that in the case where the nanoparticle shows neglectable influence on the antenna resonance, spectral overlap seems to be the most important value. Consequently, the antenna material and geometry should be chosen for the maximum oscillator strength but simultaneous spectral overlap. Just for cases where an absorption band, for example of gold, suppresses the plasmon resonance of the antenna, off-resonant antennas can enhance the nonlinear response with poor efficiency. Here, other materials such as silver or aluminum should be applied. In cases where the nanoparticle has a strong dipole moment, its backscattering and influence on the overall response cannot be neglected and an optical nanoantenna can help to shift the hybrid response into spectral positions with better response properties. This can be a powerful method to shift resonances outside an absorption band into spectral regions with advantageous optical properties.

### 6.3 OPTIMIZATION OF MANY-PARTICLE OPTICAL ANTENNAS

In the previous section we investigated the crucial conditions for maximum signal enhancement of a nanoparticle coupled to a single particle nanoantenna. However, optical nanoantennas can consist of more than one particle [110, 133, 159]. Furthermore, the several antenna particles can have individual optical properties. Plenty of antenna configurations such as the Yagi-Uda or the bow tie geometry are suggested to achieve high efficiency by directivity or near-field enhancement [24, 203]. Eventually, one can ask for an optimum arrangement and optimum optical properties of many particle antennas to achieve the maximum signal enhancement of a tiny nanoparticle. However, the huge parameter space opens an unlimited amount of possibilities to design optical antennas. In this section we give a short outlook for the design of optimum antennas by using our point dipole method in combination with evolutionary computation.

**Figure 6.12**

Structure of the applied single population evolutionary algorithm.

### 6.3.1 *Evolutionary computation as optimization routine*

Our point dipole approximation allows the fast computation of the linear and non-linear response of coupled nanostructures. This is an elementary property and allows us to apply stochastic numerical optimization techniques such as evolutionary algorithms [204]. In order to approximate the solution of a complex problem, evolutionary computation applies the principle of the survival of the fittest. A certain population is iteratively analyzed, selected and developed to approximate and reach the solution within a previously defined accuracy or optimization criteria. In our case, the 'fittest' is the antenna with its optical and geometric properties which leads to maximum signal enhancement of the nanoparticle's nonlinear response.

The several steps of the applied algorithm are sketched in figure 6.12. In the first step, an initial random population in the defined solution space is created. Afterwards, the fitness of each individual of the population is computed and gives quantitative values for the quality of the reached solutions. If the population reaches the defined optimization criteria, the evolution ends and the survived individuals of the population represent the computation results that fulfill the defined optimization condition. For the case that the population does not reach the desired accuracy, the population is selected and developed by recombination. This means that the 'fittest' individuals are used to breed new individuals to form a new generation of individuals and population, respectively. The reproduction is realized by crossover and mutation operations. Finally, the next generation is finished and analyzed for their fitness. The evolution continues until the population reaches the defined optimization criteria or the computation is aborted. In the following we discuss the implementation of the algorithm in our point dipole approximation method and use the example of an antenna which consists of one particle. In analogy, the optimization of many-particle antennas is realized.

We optimize for the optimum antenna geometry which consists of a single particles with previously defined optical properties. Furthermore, we define a closest dipole-dipole distance which cannot be undershot and keep the z-component of the

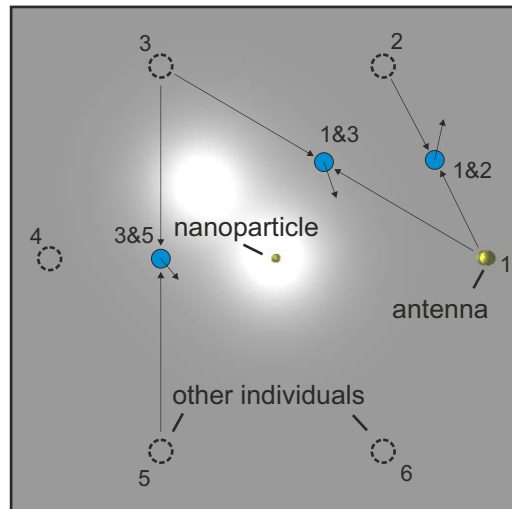


**Figure 6.13**

The initial population in case of a single particle antenna. The nanoparticle is located in the center. The antenna population consists of six individuals, symmetrically distributed around the nanoobject. The blue circles mark an example for the offspring positions, based on recombination and mutation.

position always zero to imitate particles with finite sizes on a surface. The system under optimization is sketched in figure 6.13. The nanoparticle is centered at  $\mathbf{r} = (0 \ 0 \ 0)^T$ . In analogy to the previous section, its resonance perturbation is defined to 10 meV to imitate the nonlinear perturbation. Independent on the overall number of antenna particles, we typically use populations with a number between 3 and 8 individuals. Each individual carries the properties of the whole system with all antenna particles. In the first step, the initial population is created, either by random positions of the antenna particles or by a symmetric distribution with a small mutation around the nanoparticle as depicted in figure 6.13. The random initial population has the larger variety. Per definition, the symmetric one covers a larger area around the nanoparticle and allows the antenna particle approximation from all directions. The sketch shows one of the six individuals of the population in the first generation and the symmetric distribution. The other individuals are represented by the dashed circles and labeled  $2 \dots 6$ . As fitness of each individual we use the achieved maximum nonlinear response. We cannot clearly define an optimization criterion and use a previously defined number of overall generations. The offspring of individual '1' is either generated by crossbreed with other individuals or just by mutation. Three examples for crossbreeds of different parent individuals are shown as blue circles in figure 6.13. We apply a random mutation, based on a normal distribution with scattering amplitude  $\sigma$ , on all offspring positions which is visualized by the black arrows. This avoids systematic iterations and increases the variety of the population. The fitness of the offspring is computed and compared to the fitness of the parents. In case of a higher fitness, the parents are replaced by the best offspring. Otherwise, the old individuals survive and can recombine

with eventually other replaced individuals or the next mutation helps to develop the population. This evolution can be continued until the population shows no further optimization. However, already the single particle antenna shows that refinement steps of the mutation are required to find the optimum particle position with high accuracy. Consequently, we split the algorithm into three parts. In the first part we apply the development as described above with strong mutation amplitude  $\sigma$  to cover a large parameter space. After the rough positions are found, we stop the development and separately mutate the particle positions within each individual. This further optimized the overall antenna response in the case of many particle antennas. Finally, we optimize the several individuals in analogy to the first step, but just by random mutation which decrease with the number of generations. All three steps are fully automatized and controlled by various parameters such as rough scattering amplitude, refinement steps of the scattering amplitude in the fine mutation, and the overall number of generations in the rough, fine, and single antenna particle optimization sections. Figure 6.14(a) shows the fitness of a population with 3 individuals as a function of the generation in the strong mutation (left) and fine mutation (right) section. For the strong mutation we find a large scattering of the fitness what is a consequence of the strong mutation to cover a huge parameter space and to escape local maxima. Afterwards, the position of the individuals is slightly optimized and the fine mutation algorithm further optimizes the antenna particle positions, in analogy to the strong mutation. We obtain the desired optimization trace. The three solutions are sketched in figure 6.14(b). We find two different solution. The strongest enhancement is achieved for the antenna

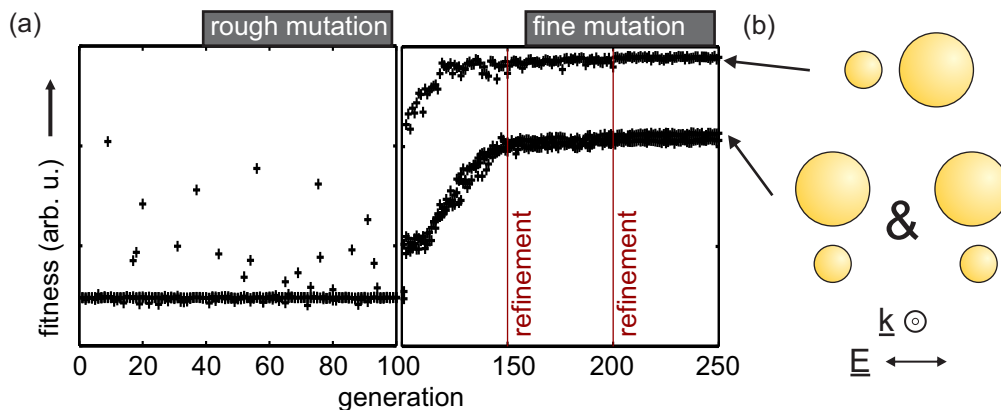


**Figure 6.14**

The rough mutation algorithm shows a strong scattering of the fitness over the whole evolution (left section of (a)). After the rough positions are found, the fine mutation algorithm optimized the antenna structure until the fitness saturates (right section of (a)). In the shown case, the mutation amplitude is two times refined at the marked generations. The optimum geometries which were found for the antenna are shown in (b). One of the two degenerated solutions is slightly detuned, what results to the smaller signal enhancement, as shown by the final fitness.

which is displaced parallel to the excitation field. The other antenna with smaller enhancement is perpendicular to it. This is in agreement with what we found in our simulation in subsection 4.5.2 of the nanomechanics chapter. Of course there is much room for optimization of the applied algorithm, especially in the recombination and crossbreed operations, but we risk a first try to find optimum antenna geometries.

### 6.3.2 *Optimum antenna geometries*

We consider the case of the strong perturbation of subsection 6.2.1 where the nanoparticle influences the hybrid response. Consequently, the computation covers a broad spectrum, with 1 meV resolution, to achieve a high accuracy and maximum enhancement, independent on the frequency of the carrier mode. Furthermore, we use the effective damping model of gold and search for an optimum nanoantenna for a nanoparticle with its resonance at 2.3 eV. All antenna particles are identical and have a plasmon resonance at 2.0 eV. The smallest allowed dipole-dipole distance is 20 nm. Figure 6.15(a) shows the results for one and two particle antennas and the most efficient three and four particle antennas. The efficiency decreases from left to right. While the one and two particle antennas are intuitive solutions, one would expect a stronger enhancement efficiency if the third antenna particle would be closer to the remaining nanostructure. However, this is not what we find. Furthermore, for the antenna which consists of 4 discs we find the highest efficiency for the shortest distances between the antenna particles. This phenomenon is a consequence of the unbalanced eigenresonances of the left antenna particle and the hybrid response of the antenna particle pair on the right side. The decreased coupling between the several subsystems leads to a reduction of the nonlinear signal enhancement. We conclude that symmetry plays an important role in the design of plasmonic nanoantennas and implement symmetry conditions around the nanoparticle of interest. Consequently, a particle at  $\mathbf{r}_i$  has always its mirrored particle at  $\mathbf{r}_k = -\mathbf{r}_i$ . Finally, we apply this additional condition and use the example of a tiny nanoparticle with its resonance at 2.3 eV and an antenna which consists of nanodiscs with their resonance at 2 eV. Furthermore, the smallest allowed dipole-dipole distance is 30 nm. We search for the antenna geometry with highest signal enhancement at a frequency of 1.8 eV. This can be interesting, if the nonlinear response must be maximized at a certain laser energy. Figure 6.15(b) shows the result of our algorithm for an antenna geometry which consists of 14 antenna particles. The found compromise between the overall oscillator strength and spectral overlap with the nanoparticle is not directly intuitive what supports our method and the necessity of efficient optimization algorithms. Furthermore, the overall antenna geometry reaches sizes where retardation effects can no longer be neglected what leads to further complications. Additional antenna particles can further amplify the response as the best compromise of overall oscillator strength and spectral overlap is not yet reached. Finally, we demonstrated that the huge parameter space of many particle antennas complicates the design of efficient antenna geometries.

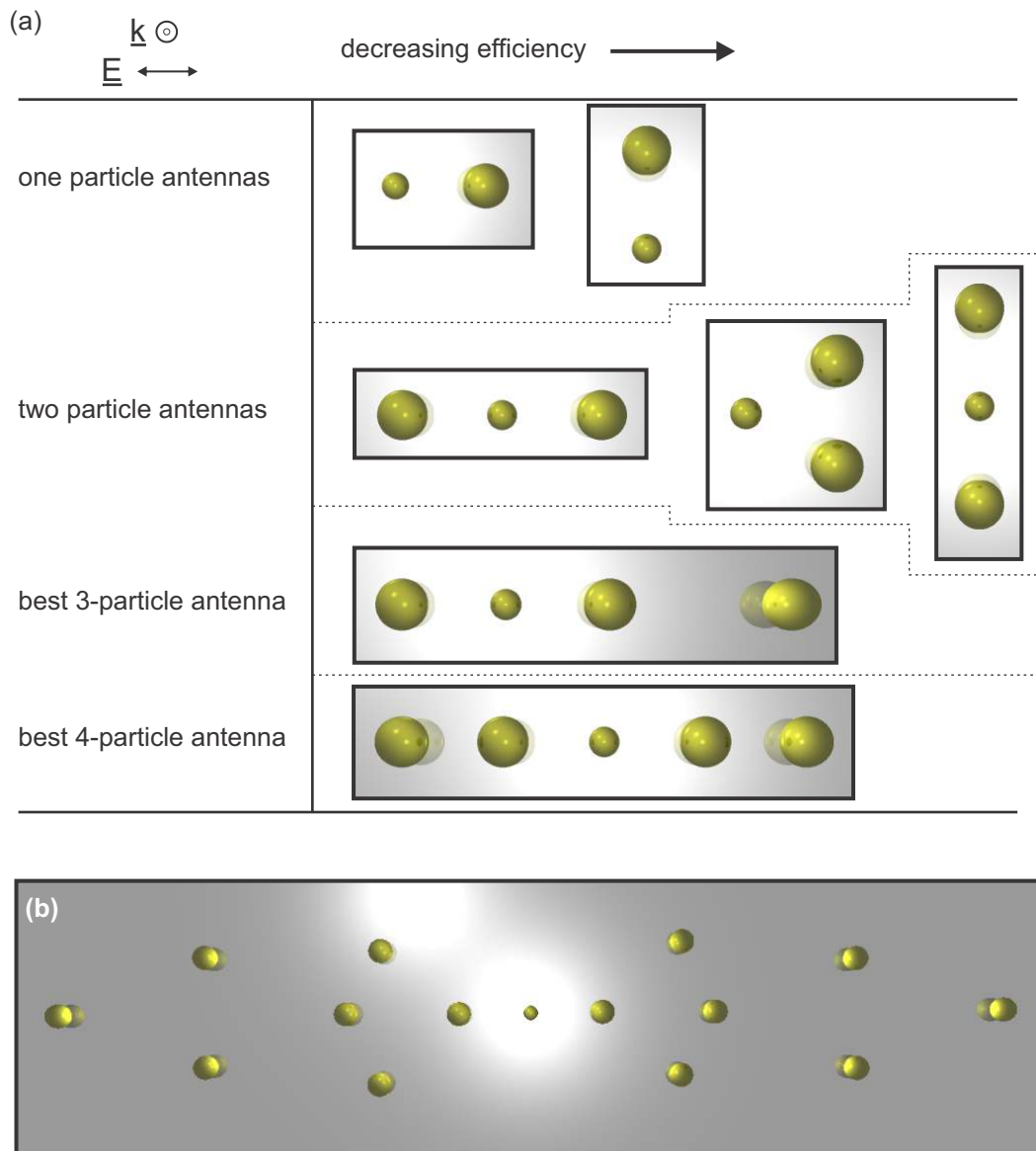


**Figure 6.15**

Solutions for optimum antenna geometries found by the evolutionary algorithm in combination with our point dipole approximation model (a). The excitation field is horizontally aligned and the antennas are placed by their efficiency from left to right. The small sphere represents the static nanoparticle. The larger particles mark the positions of the antenna dipoles. All graphs were directly generated by a raytracing script (POV-Ray) and represent with the result of the strongest individual. (b) An example for a complex antenna, which consists of 14 identical antenna particles, to achieve maximum signal enhancement at a certain frequency.

An approach is done by combining an evolutionary algorithm with our introduced point dipole approximation which helps to find complex nanoantennas, consisting of many coupled particles.

#### 6.4 CONCLUSION

In this chapter we introduced a point dipole approximation method, based on the discrete dipole approximation, for the fast computation and optimization of complex plasmonic structures. In contrast to DDA, each particle is replaced by one dipole. We apply harmonic oscillators and anisotropic polarizability tensors to imitate different geometries and particle sizes. While all parameters for the optical properties are given by the particle size and orientation dependent plasmon resonances, the only free fitting parameter is the overall oscillator strength. We find good agreement of our model with FEM and T-Matrix simulations. However, radiation damping is fully neglected in our method as we discussed at the example of the plasmonic analogue of EIT [202]. Consequently, the point dipole approximation model allows a very good prediction of the linear and nonlinear response and access to all relevant properties of complex many particle nanosystems as long as radiation damping can be neglected.

In section 6.2 we discussed the crucial parameters for optimum antenna enhancement. We distinguished between the 'strong perturbation' and the 'weak perturbation' case. In the first one, the oscillator strength of the nanoobject is on the same order of magnitude with respect to the antenna. As a consequence, its contribution and influence to the overall system response cannot be neglected. We discussed the complex behavior and partially counterintuitive parameters for the optimum antenna. Furthermore we demonstrated that the hybridization of nanoparticle and antenna mode can shift the nonlinear response into spectral regions with better optical properties. An example for this is given in chapter 4 where the optimum antenna, a compromise of spectral overlap with the nanoparticle and oscillator strength, shifts the nonlinear response of a tiny nanoparticle outside the absorption band of gold. In the 'weak perturbation case' we found a clear correlation between spectral overlap and the optimum antenna resonance. This is in good agreement with our calculation results, discussed in chapter 5. We conclude that the optimum antenna is resonant with the nanoobject of interest with simultaneous maximum oscillator strength, as long as the antenna does not operate within an absorption band.

The last section of the chapter shows our work on combining an evolutionary computation method with our point dipole approximation method to find optimum antenna geometries of many particle antennas. We gave a brief introduction into the applied algorithm and presented first results for optimum antenna geometries which consist between one and four antenna particles. While the one, two, and four particle antennas show intuitive results, the optimum three particle antenna geometry surprises and is a consequence of the broken symmetry. Furthermore, we showed an example for a 14 nanoparticle antenna, optimized for a certain laser wavelength. This can be important, if the nonlinear response of a nanosystem has to be efficiently

transferred to a certain carrier frequency. The complex and not intuitive solution supports our fast computation method and the necessity of advanced computation techniques.



## CONCLUSION AND OUTLOOK

---

Nanoobjects with a few nanometers in size show fascinating optical properties which make them to promising candidates for future applications and attractive for fundamental research. Nonlinear spectroscopy investigates the small deviations from linear light-matter interaction and reveals physical processes on ultrafast timescales. The weak nonlinear response is reduced further when single nanoobjects such as quantum dots or nanoparticles are investigated. Resonant optical nanoantennas concentrate their near-field in subwavelength volumes and promise signal enhancement by increasing the light-matter interaction in their feed gap. This study aimed at the investigation of various ultrafast nonlinear processes in single metallic and semiconductor nanostructures as well as the development and realization of optical nanoantennas to enhance the otherwise barely detectable nonlinear response.

The fundamentals of linear and nonlinear light-matter interaction on the nanoscale have been introduced in chapter 2. We characterized and discussed the applied experimental techniques of transient transmission spectroscopy, time resolved photoluminescence, and dark-field spectroscopy. We demonstrated the ability to perform shot-noise limited experiments with sub-picosecond temporal resolution and single particle photoluminescence and dark-field spectroscopy. Finite element models, as discussed in chapter 3, allowed us to compute the scattering of electromagnetic waves by arbitrary nanostructures and provided the basis of our theoretical work in the several chapters. In particular, we developed a theoretical model for the polarization resolved higher harmonic generation in complex plasmonic nanostructures and supported the work of Bernd Metzger [103, 112]. In future, the model could be further optimized by taking re-absorption and radiation properties of the structures into account. Furthermore, we supported Christian Dicken in his work about magnetoplasmonics and provided the numerical model to compute the scattering phase of nanostructures in complex multilayer structures [205]. This plays an important role in common path interferometry and allows the design and investigation of optical antennas to tweak the phase response into optimum conditions. Finally, we implemented the constitutive equations for optical chirality what allows the theoretical investigation and optimization of optical antennas for chiral sensing. This was done to support the work of Daniel Dregely and coworker about glucose and fructose sensing with planar gold nanostructures. First calculations showed that these planar antennas can slightly enhance the response amplitude of thin chiral layers. However, the interaction between chiral media and three dimensional chiral antennas is still under investigation and the next step in future work.

In chapter 4, the acousto-plasmonic properties of single gold nanodiscs with radii ranging from 20 nm to 45 nm and heights of 30 nm have been studied. The samples were fabricated by electron beam lithography. We computed the absorption cross section, shaped by the plasmon resonance, and applied a two-temperature model to describe the pump wavelength and particle size dependent excitation process. We found that for the experimentally used parameters, the particle lattice temperatures are increased by a few hundreds of Kelvin and impulsively launch mechanical vibrations. The caused perturbation of the particle plasmon resonance was modeled via the modification of the dielectric properties of gold, based on a combination of the Drude model and linear thermal expansion. The predicted nonlinear response showed a dispersive lineshape and signal intensities between  $10^{-6}$  and  $10^{-3}$ . We verified the theoretical predictions by ultrafast nonlinear spectroscopy where we excited in the near infrared at 800 nm wavelength and recorded the spectrally resolved temporal evolution of the mechanical oscillations. Fourier analyses allowed us to investigate the mechanical mode spectra of the disc shaped particles where we observed two eigenmodes, corresponding to an extensional mode and a drum mode. The size dependent mechanical eigenfrequency of the dominating drum mode was nicely reproduced by a simple model based on the sound velocity of gold. Furthermore, we investigated the probe wavelength dependent signal strength of the oscillation and found good agreement with our theoretical predictions, as long as the spectral response is outside the absorption band of gold which is not taken into account in our model. Outgoing from this preparatory work, we were able to perform theoretical studies about the nonlinear response of a single gold nanoparticle coupled to an optical antenna. We used the example of a nanodisc with 20 nm diameter, which is at the limit of our detection range, and theoretically predicted the optimum enhancement with a disc shaped nanoantenna with a radius of approximately 35 nm. We found the antenna effect being a consequence of plasmon hybridization of the nanoparticle and the antenna, where the desired nonlinear response modulates a very strong carrier mode of the hybrid system. The experimentally investigated nanoparticle-antenna pair was separated by 12.5 nm. Fourier decomposition allowed us to distinguish between the response contributions of the antenna and the nanoparticle under investigation. We found the nonlinear response of the nanoparticle redshifted to the symmetric hybrid mode resonance and enhanced by one order of magnitude [80]. Our method provides a powerful tool in linear and nonlinear spectroscopy of single nanoobjects, especially in simplifying such challenging experiments as transient absorption or multiphoton excitation. However, more complex antenna geometries which could further increase the efficiency are mostly not applicable due to their multiple mechanical resonances and strong background signal, both limiting the Fourier decomposition. For future work, we suggest the combination of plasmonic nanoantenna and simple dielectric cavity structures to increase the light matter interaction of small nanoparticles and to reach particle sizes of 10 nm and below where the atomistic character of the mechanical oscillations should become observable.

In chapter 5 we presented for the first time ultrafast nonlinear spectroscopy of exciton dynamics in quantum confined states of individual CdSe nanowires with radii well below 10 nm. The small wire radii on the order of the Bohr radius (5.6 nm) lead to quantum confinement and discrete energy levels of the electron and hole states. Consequently the absorption line is shaped by the dipole allowed discrete transitions which we computed as a function of the radius by applying six-band effective mass theory. Our samples were synthesized by the groups of G.V.Hartland and M.Kuno and afterwards spin-coated onto a glass substrate. We used near-UV pump pulses to excite higher order transitions and performed time resolved photoluminescence spectroscopy measurements. The absorption cross section showed a strong polarization dependence which is a consequence of the wire geometry and well described by our finite element model. Ultrafast nonlinear spectroscopy revealed short and long living effects, distributed over the visible and near infrared spectrum. The first picoseconds after excitation are dominated by an electron-hole plasma, leading to a dispersive line shape of the transient signal. At later times, we found clear peaks in the transient absorption spectra, indicating the bleaching of different excitonic states which are in excellent spectral agreement with the predictions from effective mass theory. The population of these states decays with spectrally rather independent rates between 2 and 5 ns<sup>-1</sup>. Furthermore, we used the integral over the absorption line to estimate the pump induced population of several states. We found approximately 50 excitons being created by each pump pulse. Furthermore, we perceived a large mismatch between the number of pump-induced excitations of the emitting state (about 10 per laser pulse) and the luminescence photon rate (about 0.02 per laser pulse). Numerical simulations of the power flow of an emitting dipole in a CdSe nanowire revealed that the mismatch is caused by re-absorption of emitted photons by other parts of the nanowire. Emission from low energy defect states is much less absorbed than emission from the nanowire itself. The former thus dominates the emission spectrum. The combination of single wire transient absorption spectroscopy with luminescence spectroscopy allowed us to track the excitation and emission dynamics [81]. Finally, we presented our work on the coupling between an individual CdSe nanowire and a plasmonic antenna. We provided a classical model and described the interaction at the example of a single nanocrystal and a disc shaped gold nanoantenna. From theory, we predicted the desired signal enhancement to be in an experimentally accessible regime. First experimental results showed interaction between wire and antenna, indicated by the increase of the transition decay rates which follow the absorption line of the antenna plasmon due to additional (nonradiative) decay channels. This was further supported by the measured reduction of the photoluminescence intensity. However, in contrast to our predictions concerning a single CdSe dot, the nonlinear response amplitude of the wire-antenna system is decreased with respect to the single wire. We explained this by the compromise in the antenna design, which was chosen to avoid a strong superimposed nonlinear response of the antenna itself. To overcome this background signal, we suggest dielectric microcavities which also increase the light matter interaction without an own nonlinear response. However, both meth-

ods distort the properties of the quantum system and complicate its investigation by the increased local density of states.

Finally, in chapter 6 we generally discussed the antenna nanoparticle interaction based on our point dipole approximation model where each scatterer is replaced by a single dipole. We combined the fundamentals of the discrete dipole approximation and anisotropic polarizability for the nanoobjects, based on harmonic oscillators. The dramatic reduction of computational effort allowed the fast computation of complex many particle nanostructures and the investigation of previously unattainable, large parameter spaces. At the example of the electromagnetic analogue of EIT, where a dark plasmon is coupled to a bright one, we discussed the limitations due to the neglect of radiation losses and broadening. For the general discussion about maximum antenna efficiency and enhancement, we distinguished between two cases with different oscillator strengths of the nanoobject under investigation, in analogy to the systems discussed in the chapters 4 and 5, respectively. In the strong perturbation case, the influence of the nanoobject cannot be neglected in the hybrid response of the nanoparticle-antenna pair. Consequently, the hybrid mode resonance energies strongly depend on the properties of the nanoparticle as discussed in chapter 4 where the coupled response in case of the optimum antenna is redshifted with respect to the resonances of nanoparticle and antenna. In addition, we found that in this case the optimum antenna is a compromise of spectral overlap with the nanoparticle and high oscillator strength which shifts the spectral response of the nanoparticle outside the absorption band of gold. Consequently, the larger antenna structure with respect to the nanoparticle is not a general constellation but more a result of the optical properties of the used material. In contrast, the weak perturbation case, where the influence of the nanoobject can be almost neglected in the hybrid response, shows a more disentangled behavior with spectral overlap being the most crucial parameter for an efficient antenna. An example was discussed in chapter 5, where we computed the optimum antenna for a single CdSe nanocrystal. At the end of the chapter, we presented first results about the implementation of an evolutionary algorithm to find optimum many particle antenna geometries and found symmetry as an important condition.

In conclusion, we investigated the acousto-optical response of single gold nanoparticles and applied for the first time an optical nanoantenna for ultrafast nonlinear spectroscopy of a single nanoobject. Furthermore, we tracked the ultrafast carrier dynamics in quantum confined exciton states of a single CdSe nanowire and investigated a hybrid system, consisting of semiconductor nanowire and plasmonic nanoantenna. Our point dipole approximation approach allows the fast computation of complex response of many particle antennas and is a first step towards optimum antenna geometries. Optical nanoantennas can enhance the nonlinear response of individual nanoobjects but may influence the object under investigation. We expect this dissertation to give detailed insight into ultrafast processes in metallic and semiconductor nanostructures. We envision that the provided numerical

models and methods help to study and optimize antenna structures for higher harmonic phenomena and optical chirality and that our antenna-technique provides a powerful tool for linear and nonlinear spectroscopy on the nanoscale.



## BIBLIOGRAPHY

---

- [1] Fan, J. A. *et al.* Self-Assembled Plasmonic Nanoparticle Clusters. *Science* **328**, 1135–1138 (2010).
- [2] Barnes, W., Dereux, A. & Ebbesen, T. Surface plasmon subwavelength optics. *Nature* **424**, 824–830 (2003).
- [3] Ergin, T., Stenger, N., Brenner, P., Pendry, J. B. & Wegener, M. Three-Dimensional Invisibility Cloak at Optical Wavelengths. *Science* **328**, 337–339 (2010).
- [4] Alivisatos, A. Semiconductor clusters, nanocrystals, and quantum dots. *Science* **271**, 933–937 (1996).
- [5] Murray, C., Kagan, C. & Bawendi, M. Synthesis and characterization of monodisperse nanocrystals and close-packed nanocrystal assemblies. *Annual Review of Materials Science* **30**, 545–610 (2000).
- [6] Baughman, R., Zakhidov, A. & de Heer, W. Carbon nanotubes - the route toward applications. *Science* **297**, 787–792 (2002).
- [7] Baker, S. N. & Baker, G. A. Luminescent Carbon Nanodots: Emergent Nanolights. *Angewandte Chemie-International Edition* **49**, 6726–6744 (2010).
- [8] Moerner, W. E. & Orrit, M. Illuminating single molecules in condensed matter. *Science* **283**, 1670–1676 (1999).
- [9] Vahala, K. Optical microcavities. *Nature* **424**, 839–846 (2003).
- [10] Willets, K. A. & Van Duyne, R. P. Localized surface plasmon resonance spectroscopy and sensing. *Annual Review of Physical Chemistry* **58**, 267–297 (2007).
- [11] Liu, N., Tang, M. L., Hentschel, M., Giessen, H. & Alivisatos, A. P. Nanoantenna-enhanced gas sensing in a single tailored nanofocus. *Nature Materials* **10**, 631–636 (2011).
- [12] Liu, N., Mesch, M., Weiss, T., Hentschel, M. & Giessen, H. Infrared Perfect Absorber and Its Application As Plasmonic Sensor. *Nano Letters* **10**, 2342–2348 (2010).
- [13] Michalet, X. *et al.* Quantum dots for live cells, in vivo imaging, and diagnostics. *Science* **307**, 538–544 (2005).

- [14] Medintz, I., Uyeda, H., Goldman, E. & Mattoussi, H. Quantum dot bioconjugates for imaging, labelling and sensing. *Nature Materials* **4**, 435–446 (2005).
- [15] Loss, D. & DiVincenzo, D. Quantum computation with quantum dots. *Physical Review A* **57**, 120–126 (1998).
- [16] Michler, P. *et al.* A quantum dot single-photon turnstile device. *Science* **290**, 2282–2285 (2000).
- [17] Li, X. *et al.* An all-optical quantum gate in a semiconductor quantum dot. *Science* **301**, 809–811 (2003).
- [18] Reithmaier, J. *et al.* Strong coupling in a single quantum dot-semiconductor microcavity system. *Nature* **432**, 197–200 (2004).
- [19] Piccione, B., Cho, C.-H., van Vugt, L. K. & Agarwal, R. All-optical active switching in individual semiconductor nanowires. *Nature Nanotechnology* **7**, 640–645 (2012).
- [20] Kempa, T. J. *et al.* Coaxial multishell nanowires with high-quality electronic interfaces and tunable optical cavities for ultrathin photovoltaics. *Proceedings of the National Academy of Sciences of the United States of America* **109**, 1407–1412 (2012).
- [21] Cho, C.-H. *et al.* Tailoring hot-exciton emission and lifetimes in semiconducting nanowires via whispering-gallery nanocavity plasmons. *Nature Materials* **10**, 1–7 (2011).
- [22] Yan, R., Pausauskie, P., Huang, J. & Yang, P. Direct photonic-plasmonic coupling and routing in single nanowires. *Proceedings of the National Academy of Sciences of the United States of America* **106**, 21045–21050 (2009).
- [23] Myroshnychenko, V. *et al.* Modelling the optical response of gold nanoparticles. *Chem. Soc. Rev.* **37**, 1792–1805 (2008).
- [24] Novotny, L. & van Hulst, N. Antennas for light. *Nature Photonics* **5**, 83–90 (2011).
- [25] Hentschel, M., Schaeferling, M., Weiss, T., Liu, N. & Giessen, H. Three-Dimensional Chiral Plasmonic Oligomers. *Nano Letters* **12**, 2542–2547 (2012).
- [26] Hentschel, M., Dregely, D., Vogelgesang, R., Giessen, H. & Liu, N. Plasmonic Oligomers: The Role of Individual Particles in Collective Behavior. *ACS Nano* **5**, 2042–2050 (2011).
- [27] Prodan, E., Radloff, C., Halas, N. J. & Nordlander, P. A hybridization model for the plasmon response of complex nanostructures. *Science* **302**, 419–422 (2003).

- [28] Nordlander, P., Oubre, C., Prodan, E., Li, K. & Stockman, M. I. Plasmon hybridization in nanoparticle dimers. *Nano Letters* **4**, 899–903 (2004).
- [29] Liu, N., Hentschel, M., Weiss, T., Alivisatos, A. P. & Giessen, H. Three-Dimensional Plasmon Rulers. *Science* **332**, 1407–1410 (2011).
- [30] Zhang, S., Genov, D. A., Wang, Y., Liu, M. & Zhang, X. Plasmon-induced transparency in metamaterials. *Physical Review Letters* **101**, 047401 (2008).
- [31] Shalaev, V. M. Optical negative-index metamaterials. *Nature Photonics* **1**, 41–48 (2007).
- [32] Pendry, J. Negative refraction makes a perfect lens. *Physical Review Letters* **85**, 3966–3969 (2000).
- [33] Liu, Y., Zentgraf, T., Bartal, G. & Zhang, X. Transformational Plasmon Optics. *Nano Letters* **10**, 1991–1997 (2010).
- [34] Haes, A., Zou, S., Schatz, G. & Van Duyne, R. Nanoscale optical biosensor: Short range distance dependence of the localized surface plasmon resonance of noble metal nanoparticles. *Journal of Physical Chemistry B* **108**, 6961–6968 (2004).
- [35] Anker, J. N. *et al.* Biosensing with plasmonic nanosensors. *Nature Materials* **7**, 442–453 (2008).
- [36] Stievater, T. H. *et al.* Rabi oscillations of excitons in single quantum dots. *Physical Review Letters* **87**, 133603 (2001).
- [37] Hartschuh, A., Pedrosa, H. N., Novotny, L. & Krauss, T. D. Simultaneous fluorescence and raman scattering from single carbon nanotubes. *Science* **301**, 1354–1356 (2003).
- [38] Lippitz, M., van Dijk, M. & Orrit, M. Third-harmonic generation from single gold nanoparticles. *Nano Letters* **5**, 799–802 (2005).
- [39] van Dijk, M. A., Lippitz, M. & Orrit, M. Detection of acoustic oscillations of single gold nanospheres by time-resolved interferometry. *Physical Review Letters* **95**, 267406 (2005).
- [40] Nie, S. & Emery, S. Probing single molecules and single nanoparticles by surface-enhanced Raman scattering. *Science* **275**, 1102–1106 (1997).
- [41] Champion, A. & Kambhampati, P. Surface-enhanced Raman scattering. *Chemical Society Reviews* **27**, 241–250 (1998).
- [42] Farahani, J., Pohl, D., Eisler, H. & Hecht, B. Single quantum dot coupled to a scanning optical antenna: A tunable superemitter. *Physical Review Letters* **95** (2005).

- [43] Kinkhabwala, A. *et al.* Large single-molecule fluorescence enhancements produced by a bowtie nanoantenna. *Nature Photonics* **3**, 654–657 (2009).
- [44] Taminiau, T. H., Stefani, F. D. & van Hulst, N. F. Enhanced directional excitation and emission of single emitters by a nano-optical Yagi-Uda antenna. *Optics Express* **16**, 10858–10866 (2008).
- [45] Curto, A. G. *et al.* Unidirectional emission of a quantum dot coupled to a nanoantenna. *Science* **329**, 930–933 (2010).
- [46] Dorfmüller, J. *et al.* Plasmonic Nanowire Antennas: Experiment, Simulation, and Theory. *Nano Letters* **10**, 3596–3603 (2010).
- [47] Jackson, J. D. *Classical Electrodynamics* (Wiley, New York, 1998).
- [48] Novotny, L. & Hecht, B. *Principles of Nano-Optics* (Cambridge University Press, Cambridge, 2012).
- [49] Johnson, P. B. & Christy, R. W. Optical constants of noble metals. *Phys. Rev. B* **6**, 4370–4379 (1972).
- [50] Sopra n&k database. <http://refractiveindex.info> (2013). Aug. 10, 2013.
- [51] Sommerfeld, A. & H. Bethe. *Elektronentheorie der Metalle* (Springer-Verlag, Berlin Heidelberg New York, 1967).
- [52] Ashcroft, N. W. & Mermin, N. D. *Solid state physics* (Saunders College, 1976).
- [53] Rangel, T. *et al.* Band structure of gold from many-body perturbation theory. *Physical Review B* **86**, 125125 (2012).
- [54] Pitarke, J. M., Silkin, V. M., Chulkov, E. V. & Echenique, P. M. Theory of surface plasmons and surface-plasmon polaritons. *Reports on Progress in Physics* **70**, 1–87 (2007).
- [55] Mie, G. Articles on the optical characteristics of turbid tubes, especially colloidal metal solutions. *Annalen der Physik* **25**, 377–445 (1908).
- [56] Myroshnychenko, V. *et al.* Modelling the optical response of gold nanoparticles. *Chemical Society Reviews* **37**, 1792–1805 (2008).
- [57] Maier, S. *et al.* Local detection of electromagnetic energy transport below the diffraction limit in metal nanoparticle plasmon waveguides. *Nature Materials* **2**, 229–232 (2003).
- [58] Gramotnev, D. K. & Bozhevolnyi, S. I. Plasmonics beyond the diffraction limit. *Nature Photonics* **4**, 83–91 (2010).

- [59] Krenn, J. Nanoparticle waveguides - Watching energy transfer. *Nature Materials* **2**, 210–211 (2003).
- [60] Yguerabide, J. & Yguerabide, E. Light-scattering submicroscopic particles as highly fluorescent analogs and their use as tracer labels in clinical and biological applications - I. Theory. *Analytical Biochemistry* **262**, 137–156 (1998).
- [61] Yguerabide, J. & Yguerabide, E. Light-scattering submicroscopic particles as highly fluorescent analogs and their use as tracer labels in clinical and biological applications - II. Experimental characterization. *Analytical Biochemistry* **262**, 157–176 (1998).
- [62] Raschke, G. *et al.* Biomolecular recognition based on single gold nanoparticle light scattering. *Nano Letters* **3**, 935–938 (2003).
- [63] Streetman, B. G. & Banerjee, S. *Solid State Electronic Devices* - (Prentice Hall PTR, New Jersey, 2000).
- [64] Kittel, C. *Einführung in die Festkörperphysik* (Oldenbourg Wissensch.Vlg, München, 2002).
- [65] Burns, A., Ow, H. & Wiesner, U. Fluorescent core-shell silica nanoparticles: towards “Lab on a Particle” architectures for nanobiotechnology. *Chemical Society Reviews* **35**, 1028–1042 (2006).
- [66] Michler, P. *et al.* A quantum dot single-photon turnstile device. *Science* **290**, 2282–2285 (2000).
- [67] Santori, C., Pelton, M., Solomon, G., Dale, Y. & Yamamoto, E. Triggered single photons from a quantum dot. *Physical Review Letters* **86**, 1502–1505 (2001).
- [68] Karrai, K. & Warburton, R. Optical transmission and reflection spectroscopy of single quantum dots. *Superlattices and Microstructures* **33**, 311–337 (2003).
- [69] Cohen-Tannoudji, C., Diu, B. & Laloe, F. *Quantum Mechanics* (Wiley, New York, 1992).
- [70] Feynman, R., Leighton, R. & Sands, M. *The Feynman Lectures on Physics, vol. 1* (Addison Wesley, Amsterdam, 1977).
- [71] Loudon, R. *The Quantum Theory Of Light* (Oxford University Press, New York, 2000).
- [72] Lee, H., Yang, W. & Sercel, P. Temperature and excitation dependence of photoluminescence line shape in InAs/GaAs quantum-dot structures. *Physical Review B* **55**, 9757–9762 (1997).

- [73] SHEN, Y. Surface-Properties Probed by 2nd-Harmonic and Sum-Frequency Generation. *Nature* **337**, 519–525 (1989).
- [74] Franken, P. A., Hill, A. E., Weinreich, G. & Peters, C. W. Generation of optical harmonics. *Physical Review Letters* **7**, 118–119 (1961).
- [75] Metzger, B., Hentschel, M., Lippitz, M. & Giessen, H. Third-harmonic spectroscopy and modeling of the nonlinear response of plasmonic nanoantennas. *Optics Letters* **37**, 4741–4743 (2012).
- [76] Brinks, D. *et al.* Visualizing and controlling vibrational wave packets of single molecules. *Nature* **465**, 905–909 (2010).
- [77] Butet, J. *et al.* Optical second harmonic generation of single metallic nanoparticles embedded in a homogeneous medium. *Nano Letters* **10**, 1717–1721 (2010).
- [78] Mukamel, S. *Nonlinear Optical Spectroscopy* (Oxford University Press, New York, 1995).
- [79] Hamm, P. & Zanni, M. *Concepts and Methods of 2D Infrared Spectroscopy* (Cambridge University Press, Cambridge, 2011).
- [80] Schumacher, T. *et al.* Nanoantenna-enhanced ultrafast nonlinear spectroscopy of a single gold nanoparticle. *Nature Communications* **2**, 333 (2011).
- [81] Schumacher, T., Giessen, H. & Lippitz, M. Ultrafast Spectroscopy of Quantum Confined States in a Single CdSe Nanowire. *Nano Letters* **13**, 1706–1710 (2013).
- [82] *Manual: MODEL SR830 DSP Lock - In Amplifier* (Stanford Research Systems, 2011). Revision 2.5 (10/2011).
- [83] Schmidt, M. *et al.* General Atomic and Molecular Electronic-Structure System. *Journal of Computational Chemistry* **14**, 1347–1363 (1993).
- [84] Scholl, J. A., Koh, A. L. & Dionne, J. A. Quantum plasmon resonances of individual metallic nanoparticles. *Nature* **483**, 421–U68 (2012).
- [85] Zuloaga, J., Prodan, E. & Nordlander, P. Quantum Plasmonics: Optical Properties and Tunability of Metallic Nanorods. *ACS NANO* **4**, 5269–5276 (2010).
- [86] Quijada, M., Borisov, A. G. & Muino, R. D. Time-dependent density functional calculation of the energy loss of antiprotons colliding with metallic nanoshells. *Physica Status Solidi A-Applications and Materials Science* **205**, 1312–1316 (2008).

- [87] Song, P., Nordlander, P. & Gao, S. Quantum mechanical study of the coupling of plasmon excitations to atomic-scale electron transport. *Journal of Chemical Physics* **134**, 074701 (2011).
- [88] Pastoriza-Santos, I., Gomez, D., Perez-Juste, J., Liz-Marzan, L. & Mulvaney, P. Optical properties of metal nanoparticle coated silica spheres: a simple effective medium approach. *Physical Chemistry Chemical Physics* **6**, 5056–5060 (2004).
- [89] *Comsol Multiphysics RF Module - User's Guide* (Comsol, 2012). Version: 4.3.
- [90] Oskooi, A. F. *et al.* MEEP: A flexible free-software package for electromagnetic simulations by the FDTD method. *Computer Physics Communications* **181**, 687–702 (2010).
- [91] Kelly, K., Coronado, E., Zhao, L. & Schatz, G. The optical properties of metal nanoparticles: The influence of size, shape, and dielectric environment. *Journal of Physical Chemistry B* **107**, 668–677 (2003).
- [92] Zhao, J. *et al.* Methods for Describing the Electromagnetic Properties of Silver and Gold Nanoparticles. *Accounts of Chemical Research* **41**, 1710–1720 (2008).
- [93] Zienkiewicz, O. C., Taylor, R. L. & Zhu, J. Z. *The finite element method: its basis and fundamentals* (Butterworth-Heinemann, 2005).
- [94] Gedney, S. & Navsariwala, U. An Unconditionally Stable Finite-Element Time-Domain Solution of the Vector Wave-Equation. *IEEE Microwave and Guided Wave Letters* **5**, 332–334 (1995).
- [95] Um, E. S., Harris, J. M. & Alumbaugh, D. L. 3D time-domain simulation of electromagnetic diffusion phenomena: A finite-element electric-field approach. *Geophysics* **75**, F115–F126 (2010).
- [96] Schwarzbach, C. *Stability of Finite Element Solutions to Maxwell's Equations in Frequency Domain*. Phd-thesis, Universiteit Leiden (2009).
- [97] Smith, D., Padilla, W., Vier, D., Nemat-Nasser, S. & Schultz, S. Composite medium with simultaneously negative permeability and permittivity. *Physical Review Letters* **84**, 4184–4187 (2000).
- [98] Valentine, J. *et al.* Three-dimensional optical metamaterial with a negative refractive index. *Nature* **455**, 376 (2008).
- [99] Wu, D. *et al.* Terahertz plasmonic high pass filter. *Applied Physical Letters* **83**, 201–203 (2003).
- [100] Gansel, J. K. *et al.* Gold Helix Photonic Metamaterial as Broadband Circular Polarizer. *Science* **325**, 1513–1515 (2009).

- [101] O'Hara, J. F. *et al.* Thin-film sensing with planar terahertz metamaterials: sensitivity and limitations. *Optics Express* **16**, 1786–1795 (2008).
- [102] Schurig, D. *et al.* Metamaterial electromagnetic cloak at microwave frequencies. *Science* **314**, 977–980 (2006).
- [103] Metzger, B., Schumacher, T., Hentschel, M., Lippitz, M. & Giessen, H. Third Harmonic Mechanism in Complex Plasmonic Fano Structures. *ACS Photonics* **1**, 471–476 (2014).
- [104] Liu, N. *et al.* Planar Metamaterial Analogue of Electromagnetically Induced Transparency for Plasmonic Sensing. *Nano Letters* **10**, 1103–1107 (2010).
- [105] Kauranen, M. & Zayats, A. V. Nonlinear plasmonics. *Nature Photonics* **6**, 737–748 (2012).
- [106] Husu, H. *et al.* Metamaterials with Tailored Nonlinear Optical Response. *Nano Letters* **12**, 673–677 (2012).
- [107] Thyagarajan, K., Rivier, S., Lovera, A. & Martin, O. J. F. Enhanced second-harmonic generation from double resonant plasmonic antennae. *Optics Express* **20**, 12860–12865 (2012).
- [108] Harutyunyan, H., Volpe, G., Quidant, R. & Novotny, L. Enhancing the nonlinear optical response using multifrequency gold-nanowire antennas. *Physical Review Letters* **108**, 217403 (2012).
- [109] Zeng, Y., Hoyer, W., Liu, J., Koch, S. W. & Moloney, J. V. Classical theory for second-harmonic generation from metallic nanoparticles. *Phys. Rev. B* **79**, 235109 (2009).
- [110] Hentschel, M., Utikal, T., Giessen, H. & Lippitz, M. Quantitative Modeling of the Third Harmonic Emission Spectrum of Plasmonic Nanoantennas. *Nano Letters* **12**, 3778–3782 (2012).
- [111] Metzger, B., Steinmann, A. & Giessen, H. High-power widely tunable sub-20 fs Gaussian laser pulses for ultrafast nonlinear spectroscopy. *Optics Express* **19**, 24354–24360 (2011).
- [112] Metzger, B. *et al.* Doubling the Efficiency of Third Harmonic Generation by Positioning ITO Nanocrystals into the Hot-Spot of Plasmonic Gap-Antennas. *Nano Letters* **14**, 2867–2872 (2014).
- [113] Lindfors, K., Kalkbrenner, T., Stoller, P. & Sandoghdar, V. Detection and spectroscopy of gold nanoparticles using supercontinuum white light confocal microscopy. *Physical Review Letters* **93**, 037401 (2004).

- [114] Xia, J., Beyersdorf, P. T., Fejer, M. M. & Kapitulnik, A. Modified Sagnac interferometer for high-sensitivity magneto-optic measurements at cryogenic temperatures. *Applied Physics Letters* **89**, 062508 (2006).
- [115] Sihvola, A. H. Electromagnetic modeling of bi-isotropic media. *Progress in electromagnetics research* **9**, 45–86 (1994).
- [116] Wang, B., Zhou, J., Koschny, T., Kafesaki, M. & Soukoulis, C. M. Chiral metamaterials: simulations and experiments. *Journal of Optics A-Pure and Applied Optics* **11**, 114003 (2009).
- [117] Hecht, E. *Optics* (Pearson Education, 2008).
- [118] Lin, J.-Y. Determination of the refractive index and the chiral parameter of a chiral solution based on chiral reflection equations and heterodyne interferometry. *Applied Optics* **47**, 3828–3834 (2008).
- [119] Shemer, G. *et al.* Chirality of silver nanoparticles synthesized on DNA. *Journal of the American Chemical Society* **128**, 11006–11007 (2006).
- [120] Gautier, C. & Buergi, T. Chiral Gold Nanoparticles. *ChemPhysChem* **10**, 483–492 (2009).
- [121] *Comsol Multiphysics Structural Mechanics - User's Guide* (Comsol, 2012). Version: 4.3.
- [122] Hodak, J. H., Henglein, A. & Hartland, G. V. Size dependent properties of au particles: Coherent excitation and dephasing of acoustic vibrational modes. *J. Chem. Phys.* **111**, 8613–8621 (1999).
- [123] Perner, M. *et al.* Observation of hot-electron pressure in the vibration dynamics of metal nanoparticles. *Physical Review Letters* **85**, 792–795 (2000).
- [124] Tang, Y. & Ouyang, M. Tailoring properties and functionalities of metal nanoparticles through crystallinity engineering. *Nature Materials* **6**, 754–759 (2007).
- [125] Saucedo, H. E. *et al.* Vibrational Properties of Metal Nanoparticles: Atomistic Simulation and Comparison with Time-Resolved Investigation. *Journal of Physical Chemistry C* **116**, 25147–25156 (2012).
- [126] Gilbert, B., Huang, F., Zhang, H., Waychunas, G. & Banfield, J. Nanoparticles: Strained and stiff. *Science* **305**, 651–654 (2004).
- [127] Staleva, H. & Hartland, G. V. Vibrational dynamics of silver nanocubes and nanowires studied by single-particle transient absorption spectroscopy. *Adv. Funct. Mater.* **18**, 3809–3817 (2008).

- [128] Voisin, C., Christofilos, D., Del Fatti, N. & Vallee, F. Environment effect on the acoustic vibration of metal nanoparticles. *Physica B-Condensed Matter* **316**, 89–94 (2002).
- [129] Zijlstra, P., Tchebotareva, A. L., Chon, J. W. M., Gu, M. & Orrit, M. Acoustic Oscillations and Elastic Moduli of Single Gold Nanorods. *Nano Letters* **8**, 3493–3497 (2008).
- [130] Perner, M. *et al.* Observation of hot-electron pressure in the vibration dynamics of metal nanoparticles. *Physical Review Letters* **85**, 792–795 (2000).
- [131] Huang, W., Qian, W. & El-Sayed, M. The optically detected coherent lattice oscillations in silver and gold monolayer periodic nanoprism arrays: The effect of interparticle coupling. *Journal of Physical Chemistry B* **109**, 18881–18888 (2005).
- [132] Farahani, J. N., Pohl, D. W., Eisler, H. J. & Hecht, B. Single quantum dot coupled to a scanning optical antenna: A tunable superemitter. *Physical Review Letters* **95**, 017402 (2005).
- [133] Kinkhabwala, A. *et al.* Large single-molecule fluorescence enhancements produced by a bowtie nanoantenna. *Nature Photonics* **3**, 654–657 (2009).
- [134] Bigot, J., Halte, V., Merle, J. & Daunois, A. Electron dynamics in metallic nanoparticles. *Chemical Physics* **251**, 181–203 (2000).
- [135] Perner, M. *et al.* Optically induced damping of the surface plasmon resonance in gold colloids. *Physical Review Letters* **78**, 2192–2195 (1997).
- [136] Utikal, T. *Ultrafast Nonlinear Spectroscopy of Hybrid Plasmonic Systems*. Phd-thesis, Universität Stuttgart (2011).
- [137] Bosbach, J., Hendrich, C., Stietz, F., Vartanyan, T. & Trager, F. Ultrafast dephasing of surface plasmon excitation in silver nanoparticles: Influence of particle size, shape, and chemical surrounding. *Physical Review Letters* **89**, 257404 (2002).
- [138] Sönnichsen, C. *et al.* Drastic reduction of plasmon damping in gold nanorods. *Physical Review Letters* **88**, 077402 (2002).
- [139] Hartland, G. V. Coherent excitation of vibrational modes in metallic nanoparticles. *Annual Review of Physical Chemistry* **57**, 403–430 (2006).
- [140] Doicu, A., Wriedt, T. & Eremin, Y. *Light Scattering by Systems of Particles. Null-Field Method with Discrete Sources – Theory and Programs* (Springer, 2006).
- [141] Otter, M. Temperaturabhängigkeit der Optischen Konstanten Massiver Metalle. *Zeitschrift Für Physik* **161**, 539 (1961).

- [142] Haynes, W. M. *CRC Handbook of Chemistry and Physics 2011-2012* (Taylor and Francis Limited, 2011).
- [143] Cumming, D., Thoms, S., Weaver, J. & Beaumont, S. 3 nm NiCr wires made using electron beam lithography and PMMA resist. *Microelectronic Engineering* **30**, 423–425 (1996).
- [144] Hentschel, M., Schaeferling, M., Metzger, B. & Giessen, H. Plasmonic Diastereomers: Adding up Chiral Centers. *Nano Letters* **13**, 600–606 (2013).
- [145] Jiao, X., Goeckeritz, J., Blair, S. & Oldham, M. Localization of Near-Field Resonances in Bowtie Antennae: Influence of Adhesion Layers. *Plasmonics* **4**, 37–50 (2009).
- [146] Hentschel, M. *Complex 2D and 3D Plasmonic Nanostructures: Fano Resonances, Chirality, and Nonlinearities*. Phd-thesis, University of Stuttgart (2013).
- [147] MATLAB. *version 7.10.0 (R2010a)* (The MathWorks Inc., Natick, Massachusetts, 2010).
- [148] Butz, T. *Fouriertransformation Für Fußgänger* (Springer DE, Berlin, 2009).
- [149] Kratzer, K. *Nonlinear Spectroscopy using Nanoantennas*. Diplomarbeit, Max Planck Institute for Solid State Research (2010).
- [150] Ullrich, D. *Optimization of Optical Nanoantennas for Nonlinear Spectroscopy*. Diplomarbeit, Max Planck Institute for Solid State Research (2011).
- [151] Lide, D. *CRC handbook of chemistry and physics : a ready-reference book of chemical and physical data* (CRC Press, Boca Raton, Fla, 2003).
- [152] Thongrattanasiri, S. & Javier Garcia de Abajo, F. Optical Field Enhancement by Strong Plasmon Interaction in Graphene Nanostructures. *Physical Review Letters* **110**, 187401 (2013).
- [153] Esteban, R., Borisov, A. G., Nordlander, P. & Aizpurua, J. Bridging quantum and classical plasmonics with a quantum-corrected model. *Nature Communications* **3**, 825 (2012).
- [154] Mühlischlegel, P., Eisler, H. J., Martin, O. J. F., Hecht, B. & Pohl, D. W. Resonant optical antennas. *Science* **308**, 1607–1609 (2005).
- [155] Bharadwaj, P., Deutsch, B. & Novotny, L. Optical antennas. *Advances in Optics and Photonics* **1**, 438–83 (2009).
- [156] Merlein, J. *et al.* Nanomechanical control of an optical antenna. *Nature Photonics* **2**, 230–233 (2008).

- [157] Kosako, T., Kadoya, Y. & Hofmann, H. F. Directional control of light by a nano-optical Yagi-Uda antenna. *Nature Photonics* **4**, 312–315 (2010).
- [158] Liu, N. & Giessen, H. Coupling effects in optical metamaterials. *Angew. Chemie Int. Ed.* **49**, 9838 (2010).
- [159] Castro-Lopez, M., Brinks, D., Sapienza, R. & van Hulst, N. F. Aluminum for Nonlinear Plasmonics: Resonance-Driven Polarized Luminescence of Al, Ag, and Au Nanoantennas. *Nano Letters* **11**, 4674–4678 (2011).
- [160] Armani, D., Kippenberg, T., Spillane, S. & Vahala, K. Ultra-high-Q toroid microcavity on a chip. *Nature* **421**, 925–928 (2003).
- [161] Ates, S. *et al.* Non-resonant dot-cavity coupling and its potential for resonant single-quantum-dot spectroscopy. *Nature Photonics* **3**, 724–728 (2009).
- [162] Lu, W. & Lieber, C. M. Nanoelectronics from the bottom up. *Nature Materials* **6**, 841–850 (2007).
- [163] Peidong Yang, M. F., Ruoxue Yan. Semiconductor nanowire: what's next? *Nano letters* **10**, 1529–1536 (2010).
- [164] McDonald, M. P., Vietmeyer, F. & Kuno, M. Direct Measurement of Single CdSe Nanowire Extinction Polarization Anisotropies. *The Journal of Physical Chemistry Letters* **3**, 2215–2220 (2012).
- [165] Vietmeyer, F., McDonald, M. P. & Kuno, M. Single Nanowire Microscopy and Spectroscopy. *The Journal of Physical Chemistry C* **116**, 12379–12396 (2012).
- [166] Achtstein, A. W., Schoeps, O., Artemyev, M. V. & Woggon, U. Excitonic properties of single CdSe nanowires and coupling to plasmonic nanocavities. *Physica Status Solidi (b)* **247**, 2498–2508 (2010).
- [167] Fedutik, Y., Temnov, V. V., Schoeps, O., Woggon, U. & Artemyev, M. V. Exciton-plasmon-photon conversion in plasmonic nanostructures. *Physical Review Letters* **99**, 136802 (2007).
- [168] Protasenko, V. V., Hull, K. L. & Kuno, M. Disorder-Induced Optical Heterogeneity in Single CdSe Nanowires. *Advanced Materials* **17**, 2942–2949 (2005).
- [169] Kulzer, F. & Orrit, M. Single-Molecule Optics. *Annual Review of Physical Chemistry* **55**, 585–611 (2004).
- [170] Myalitsin, A. *et al.* Diameter Scaling of the Optical Band Gap in Individual CdSe Nanowires. *ACS Nano* **5**, 7920–7927 (2011).
- [171] Giblin, J., Vietmeyer, F., McDonald, M. P. & Kuno, M. Single Nanowire Extinction Spectroscopy. *Nano Letters* **11**, 3307–3311 (2011).

- [172] Giblin, J., Syed, M., Banning, M. T., Kuno, M. & Hartland, G. Experimental Determination of Single CdSe Nanowire Absorption Cross Sections through Photothermal Imaging. *ACS Nano* **4**, 358–364 (2010).
- [173] Carey, C. R. *et al.* Imaging and Absolute Extinction Cross-Section Measurements of Nanorods and Nanowires through Polarization Modulation Microscopy. *The Journal of Physical Chemistry C* **114**, 16029–16036 (2010).
- [174] Carey, C., Yu, Y., Kuno, M. & Hartland, G. Ultrafast Transient Absorption Measurements of Charge Carrier Dynamics in Single II-VI Nanowires. *The Journal of Physical Chemistry C* **113**, 19077–19081 (2009).
- [175] Lo, S. S. *et al.* Charge Carrier Trapping and Acoustic Phonon Modes in Single CdTe Nanowires. *ACS Nano* **6**, 5274–5282 (2012).
- [176] Proceedings of the american physical society. *Phys. Rev.* **69**, 674–674 (1946).
- [177] Vuckovic, J., Loncar, M. & Scherer, A. Surface plasmon enhanced light-emitting diode. *IEEE Journal of Quantum Electronics* **36**, 1131–1144 (2000).
- [178] Robel, I., Bunker, B. A., Kamat, P. V. & Kuno, M. Exciton Recombination Dynamics in CdSe Nanowires: Bimolecular to Three-Carrier Auger Kinetics. *Nano Letters* **6**, 1344–1349 (2006).
- [179] Rabani, E., Hetenyi, B., Berne, B. & Brus, L. Electronic properties of CdSe nanocrystals in the absence and presence of a dielectric medium. *Journal of Chemical Physics* **110**, 5355–5369 (1999).
- [180] Vogel, D., Kruger, P. & Pollmann, J. Ab-Initio Electronic-Structure Calculations for II-VI Semiconductors Using Self-Interaction-Corrected Pseudopotentials. *Physical Review B* **52**, 14316–14319 (1995).
- [181] Dresselhaus, G. Effective Mass Approximation for Excitons. *Journal of Physics and Chemistry of Solids* **1**, 14–22 (1956).
- [182] Luttinger, J. & Kohn, W. Motion of Electrons and Holes in Perturbed Periodic Fields. *Physical Review* **97**, 869–883 (1955).
- [183] Kane, E. Band Structure of Indium Antimonide. *Journal of Physics and Chemistry of Solids* **1**, 249–261 (1957).
- [184] Shabaev, A. & Efros, A. L. 1D Exciton Spectroscopy of Semiconductor Nanorods. *Nano Letters* **4**, 1821–1825 (2004).
- [185] Puthussery, J., Kosel, T. H. & Kuno, M. Facile Synthesis and Size Control of II-VI Nanowires Using Bismuth Salts. *Small* **5**, 1112–1116 (2009).
- [186] Giblin, J. & Kuno, M. Nanostructure Absorption: A Comparative Study of Nanowire and Colloidal Quantum Dot Absorption Cross Sections. *The Journal of Physical Chemistry Letters* **1**, 3340–3348 (2010).

- [187] Montazeri, M. *et al.* Transient Rayleigh Scattering: A New Probe of Picosecond Carrier Dynamics in a Single Semiconductor Nanowire. *Nano Letters* **12**, 5389–5395 (2012).
- [188] Banyai, L. & Koch, S. A Simple Theory for the Effects of Plasma Screening on the Optical-Spectra of Highly Excited Semiconductors. *Zeitschrift Für Physik B-Condensed Matter* **63**, 283–291 (1986).
- [189] Strickler, S. & Berg, R. Relationship Between Absorption Intensity and Fluorescence Lifetime of Molecules. *Journal of Chemical Physics* **37**, 814 (1962).
- [190] Forster, T. Zwischenmolekulare Energiewanderung und Fluoreszenz. *Annalen der Physik* **2**, 55–75 (1948).
- [191] Pfeiffer, M. *et al.* Enhancing the Optical Excitation Efficiency of a Single Self-Assembled Quantum Dot with a Plasmonic Nanoantenna. *Nano Letters* **10**, 4555–4558 (2010).
- [192] Jeong, T., Yu, P. & Kim, T. Temperature dependence of the free excitons in a CdS single crystal. *Journal of the Korean Physical Society* **36**, 102–105 (2000).
- [193] Muller, J. *et al.* Monitoring surface charge migration in the spectral dynamics of single CdSe/CdS nanodot/nanorod heterostructures. *Physical Review B* **72**, 205339 (2005).
- [194] Anger, P., Bharadwaj, P. & Novotny, L. Enhancement and quenching of single-molecule fluorescence. *Physical Review Letters* **96**, 113002 (2006).
- [195] Goffard, J. *et al.* Plasmonic engineering of spontaneous emission from silicon nanocrystals. *Scientific Reports* **3**, 2672 (2013).
- [196] Mariani, M. *et al.* Implementing the Quantum von Neumann Architecture with Superconducting Circuits. *Science* **334**, 61–65 (2011).
- [197] Wolpert, C. *Ultrafast Spectroscopy of Single Quantum Dots*. Phd-thesis, Max Planck Institute for Solid State Research (2012).
- [198] Draine, B. & Flatau, P. Discrete-Dipole Approximation for Scattering Calculations. *Journal of the Optical Society of America A-Optics Image Science and Vision* **11**, 1491–1499 (1994).
- [199] Draine, B. The Discrete-Dipole Approximation and its Application to Interstellar Graphite Grains. *Astrophysical Journal* **333**, 848–872 (1988).
- [200] Li, Y., Zhao, K., Sobhani, H., Bao, K. & Nordlander, P. Geometric Dependence of the Line Width of Localized Surface Plasmon Resonances. *Journal of Physical Chemistry Letters* **4**, 1352–1357 (2013).

- [201] Grand, J. *et al.* Optical extinction Spectroscopy of oblate, prolate and ellipsoid shaped gold nanoparticles: Experiments and theory. *Plasmonics* **1**, 135–140 (2006).
- [202] Na Liu *et al.* Plasmonic analogue of electromagnetically induced transparency at the Drude damping limit. *Nature Materials* **8**, 758–62 (2009).
- [203] Kim, S. *et al.* High-harmonic generation by resonant plasmon field enhancement. *Nature* **453**, 757–760 (2008).
- [204] Simon, D. *Evolutionary Optimization Algorithms* (John Wiley and Sons, New York, 2013).
- [205] Dicken, C. *et al.* The Role of the scattering phase in the interferometric detection of single nanomagnets. *in preparation* (2013).



## APPENDIX

## COMPARISON BETWEEN THE ULTRAFAST RESPONSE OF SINGLE WIRE AND WIRE AGGREGATE

As written in the supplemental material of [81]. We perform transient absorption measurements of wire clusters and compare them with our single wire experiments. Figure A.1(a) shows the ultrafast response of a small cluster, consisting of  $\approx 5$  touching wires. On the left side, the high temporal resolution data in the range from  $-20$  to  $+20$  ps is shown. Similar to the single wire response, we find a fast plasma effect, as well as decaying excitonic state bleaching, shown in the scans from 20 to 400 ps on the right side of figure A.1(a). The maximum transient absorption signal is increased by a factor of 3 to 5, indicating the number of wires over which we average. Figure A.1(b) shows the comparison between the transient absorption spectrum of single wire and wire aggregate, both extracted 10 ps after excitation. We find significant changes of the line shape. While the single wire signal is dominated by a broad bleaching signal, the cluster shows a different behavior. We attribute these changes mainly to wire-wire connections or crossings, reducing the quantum confinement, leading to the observed transition redshifts. The extracted lifetimes are longer compared to the single wire results. In addition, we observe pump induced absorbance, indicated by spectral regions with negative  $\Delta T/T$ . This can

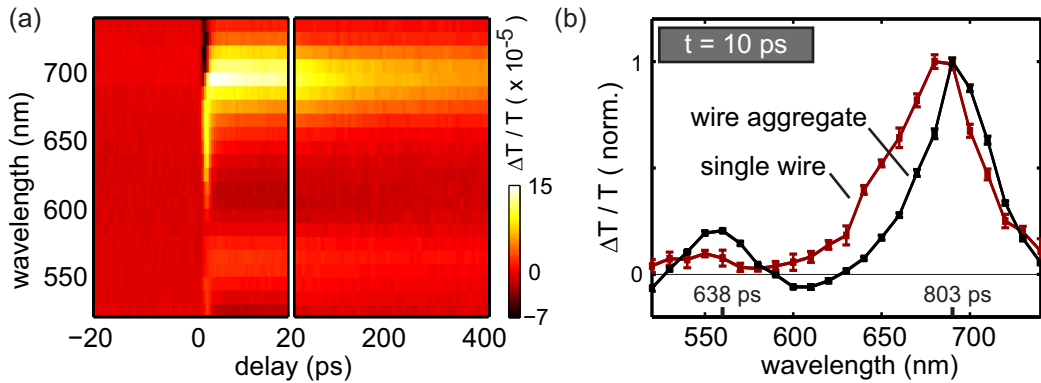


**Figure A.1**

(a) Transient absorption spectrum as a function of time delay of a wire aggregate. Both parts have different linear time scales. While the left part covers the fast features when pump and probe pulse overlap, the right part shows the decay of the states. For comparison, the transition bleaching, 10 ps after excitation, of the wire aggregate and the single wire of subsection 5.4.1 is shown in (b).

be explained by higher order excitations, or by an overlapp of partially single wire and plasma response, coming from broad cluster areas. In conclusion, single wire measurements are necessary to resolve their unaveraged character and to minimize effects due to connections between wires, in addition to inhomogeneous broadening.

## ERKLÄRUNG

---

Hiermit versichere ich an Eides statt, dass ich die vorliegende Arbeit selbständig verfasst und keine anderen als die angegebenen Quellen und Hilfsmittel verwendet habe. Ich erkläre, dass ich bisher keinen anderweitigen Promotionsversuch unternommen habe und die Hilfe von gewerblichen Promotionsberatern bzw. -vermittlern oder ähnlichen Dienstleistern weder bisher in Anspruch genommen habe noch künftig in Anspruch nehmen werde.

Bayreuth, den 2. September 2014

---

Thorsten Schumacher

## COLOPHON

This document was typeset with L<sup>A</sup>T<sub>E</sub>X using a modified version of "classicthesis" by André Miede. The style was inspired by Robert Bringhurst's seminal book on typography "*The Elements of Typographic Style*". It is available via CTAN.